Spring 5-15-2015

Ion Interactions at the Mineral-Water Interface During Biogeochemical Iron and Manganese Cycling

Margaret A. G. Hinkle
Washington University in St. Louis

WASHINGTON UNIVERSITY IN ST. LOUIS

Department of Earth and Planetary Sciences

Dissertation Examination Committee:
Jeffrey G. Catalano, Chair
Alex S. Bradley
David E. Fike
Daniel E. Giammar
Jill D. Pasteris

Ion Interactions at the Mineral-Water Interface During Biogeochemical Iron and Manganese Cycling

by

Margaret A. G. Hinkle

A dissertation presented to the
Graduate School of Arts & Sciences
of Washington University in
partial fulfillment of the
requirements for the degree
of Doctor of Philosophy

May 2015
St. Louis, Missouri

TABLE OF CONTENTS

LIST OF FIGURES

CHAPTER 2

CHAPTER 4

CHAPTER 5

LIST OF TABLES

CHAPTER 2

CHAPTER 3

CHAPTER 4

CHAPTER 5

ACKNOWLEDGEMENTS

This dissertation is the culmination of many years of training in scientific thought and practice. I am deeply indebted to those who provided support and advice as I embarked on this scientific adventure. In particular, I would like to thank my advisor, Jeff Catalano, for teaching me how to be a better scientist, for introducing me to synchrotron techniques, and for always supporting my career plans. I truly appreciate his support of my desire to become a better teacher, even when it came at the expense of productivity in other arenas. His continual support for my aspirations has been inspiring and humbling. I have been financially supported largely through the U.S. National Science Foundation, Division of Earth Sciences, Geobiology and Low-temperature Geochemistry program through award no. EAR-1056480. I would also like to thank my advisory committee for their thoughtful discussions and insight into this work.

My undergraduate chemistry professors, in particular Rob Bachman, Deon Miles, and John Shibata were instrumental in imparting both the desire to pursue a scientific career and the confidence that I could be successful doing so. A special thank you to Rob Bachman for allowing me to work in his lab, providing my first real experience in the successes and failures inherent in scientific research.

I am thankful for the support of my fellow lab-mates in the Aqueous Geochemistry and Mineralogy Laboratory, past and present. Beamtimes were made infinitely more tolerable, and occasionally even enjoyable, by your presence. I should also thank Pepperidge Farm, because your double chocolate Milanos are truly the best beamtime food, and were quite handy bargaining tools when I inevitably had to push everyone's dinner time back to get one more set of samples up and running. Although I am loathe to admit it, I should give credit where credit is due; so I say thank you, Rockstars, for keeping me going during beamtime prep, data collection,

and – most importantly – awake during many drives home from the APS. I will forever be thankful for Katherine Becker's late night company in the lab during crunch time.

My family has been unwaveringly supportive through these past 5 years. I thank them for always being there when I needed them, and understanding when I would 'go dark' for months during crunch time. I thank my dog Gonzo for taking me on walks every day and for his contagious excitement about life. I thank my cat Whittakers for always keeping me company during long data fitting sessions, and especially for figuring out how to sit in my lap without obstructing my access to the keyboard. Most cats would not be so accommodating. Now comes the time for thanking my husband Daniel, who has been on the frontlines through it all. I cannot thank him enough for all the support he has given me – making sure I ate real food, learning how to brew the best coffee, understanding late nights and early mornings, keeping me sane, and encouraging me every step of the way. Daniel, I dedicate this dissertation to you, as this dissertation would not have come into being without you supporting me each and every day.

Margaret A. G. Hinkle

Washington University in St. Louis

May 2015

ABSTRACT OF THE DISSERTATION

Ion Interactions at the Mineral-Water Interface During Biogeochemical Iron and Manganese Cycling

by

Margaret A. G. Hinkle
Doctor of Philosophy in Earth and Planetary Sciences
Washington University in St. Louis, 2014
Professor Jeffrey G. Catalano, Chair

The biogeochemical cycling of iron and manganese involves the reductive dissolution and oxidative precipitation of Fe(III) and Mn(IV/III) oxides. Biogenic Fe(III) and Mn(IV/III) oxides are often characterized by high surface areas and therefore high sorptive capacities. As a result, these minerals can substantially alter the chemistry of natural waters and the availability of micronutrients in soils and sediments by scavenging trace metals. Recent research indicates that the adsorption of aqueous Fe(II) onto Fe(III) oxides involves oxidative adsorption, electron transfer, and subsequent reductive dissolution at another surface site [a process collectively referred to as 'electron transfer-atom exchange' (ET-AE)]. Aqueous Mn(II) adsorption onto Mn(IV/III) oxides likely also involves oxidation, but because of the potential for Mn(II)-Mn(IV) comproportionation reactions and the accessibility of nearly all atoms in Mn(IV/III) oxide sheets to reaction with aqueous solution, aqueous Mn(II)-solid Mn(IV/III) interactions are expected to differ substantially from the analogous Fe system. These complex interactions between reduced and oxidized forms of Fe (and Mn) occur at redox interfaces and can exert substantial effects on trace metal fate. These processes may, in turn, be affected by ions common in natural systems. The main objective of this dissertation is to determine how interactions between ions commonly present during biogeochemical Fe or Mn cycling in natural systems [e.g., phosphate, sulfate, Ni, Zn, Fe(II), or Mn(II)] alter one another's interactions with Fe and Mn oxide surfaces. This

research specifically seeks to (1) identify the mechanisms through which the oxoanions phosphate and sulfate alter Fe(II) adsorption onto Fe oxides; (2) determine how oxoanion-Fe(II) interactions alter trace metal partitioning between the mineral surface, bulk mineral structure, and aqueous phase; (3) characterize the effect of Mn(II) on phyllomanganate sheet structures; and (4) examine the effect of Mn(II) on trace metal sorption on phyllomanganates.

Macroscopic adsorption edges show that Fe(II) cooperatively co-adsorbs with sulfate and phosphate on Fe(III) oxide surfaces. Both attenuated total reflectance Fourier transform infrared spectroscopy and surface complexation modeling indicate that this cooperative adsorption behavior arises from a combination of ternary complexation and electrostatic interactions. The formation Fe(II)-oxoanion ternary complexes suggests that processes associated with Fe(II)-Fe(III) ET-AE reactions may be altered in the presence of oxoanions, depending on the stability and identity of the ternary complex that forms. The effect of these oxoanions on one such process, trace metal repartitioning, was investigated in detail. Sulfate and, to a larger degree, phosphate suppress Ni cycling through hematite during Fe(II)-catalyzed recrystallization by altering Ni adsorption, structural incorporation, and release back into solution. Conversely, Ni cycling through goethite is unaffected or enhanced by phosphate and sulfate.

This dissertation also investigated Mn(II) effects on phyllomanganate structure and the fate of associated trace metals. Powder X-ray diffraction and X-ray absorption fine structure spectroscopic measurements indicate that Mn(II) causes distortion of the sheet structure of Mn(IV/III) oxides and alters sheet stacking at low pH, but has a minimal effect on phyllomanganate structures at circumneutral pH. As a result, Ni and Zn adsorption mechanisms on phyllomanganates are altered in the presence of aqueous Mn(II) at pH 4, but exhibit few

changes at pH 7. The Ni and Zn adsorption behaviors with aqueous Mn(II) suggests that Mn(II) alters phyllomanganate reactivities by decreasing phyllomanganate vacancy content.

These results emphasize the importance of understanding adsorbate interactions in systems with coexisting reduced and oxidized Fe or Mn, as under such conditions Fe and Mn oxide minerals undergo dynamic structural transformations. Trace metal uptake and partitioning between Fe oxide surfaces can be altered in systems with appreciable amounts of phosphate or sulfate (e.g., riparian zones, estuaries, or marine sediments). The complex interactions at iron oxide surfaces must be considered when evaluating trace metal fate at redox interfaces or interpreting trace metal proxies in the rock record to reconstruct ancient water compositions. The Mn(II)-induced phyllomanganate structural changes observed here suggest a relationship between water composition and the reactivity of Mn oxides as adsorbent materials. The identified phyllomanganate restructuring may also modify the capacity of Mn oxides to serve as oxidants of inorganic and organic compounds in aquatic systems. This dissertation highlights the complex structural and chemical processes that occur via cooperative and competitive interactions of ion at iron and manganese oxide surfaces.

“God made the bulk; surfaces were invented by the devil.”

– Wolfgang Pauli

CHAPTER 1

INTRODUCTION

1.1 BACKGROUND

Iron (Fe) and manganese (Mn) oxide minerals are important constituents in many natural systems, including soils, marine and lacustrine sediments, ocean crusts and nodules, and desert varnishes (Potter and Rossman, 1979; Krumbein and Jens, 1981; Burdige, 1993; Thamdrup et al., 1994; Van Cappellen et al., 1998; Cornell and Schwertmann, 2003; van der Zee et al., 2003; Templeton et al., 2009). Abiotic Mn(II) oxidation by O_2 is kinetically limited (Diem and Stumm, 1984; Von Langen et al., 1997; Morgan, 2005). Therefore most naturally occurring Mn(IV/III) oxides form through microbially-mediated Mn oxidation (Nealson et al., 1988; Tebo, 1991; Grote and Krumbein, 1992; Wehrli et al., 1995; Tebo et al., 1997; Bargar et al., 2000; Nelson and Lion, 2003; Northup et al., 2003). Although abiotic aqueous Fe(II) oxidation may occur rapidly under oxic conditions (Millero, 1989), microbial Fe oxidation plays a large role in the formation of Fe(III) oxides in both oxic environments as well as anoxic ones (Krumbein and Jens, 1981; Sobolev and Roden, 2002; Northup et al., 2003; Kappler and Straub, 2005; Weber et al., 2006).

Biogenic Fe and Mn oxides typically have large surface areas (Cornell and Schwertmann, 2003; Liu et al., 2004) and therefore are highly reactive materials with large sorptive capacities. Most naturally occurring and biogenic Mn oxides are phyllomanganates, in which edge-linked MnO_6 octahedra form negatively charged sheets separated by hydrated interlayers (Krumbein and Jens, 1981; Emerson et al., 1982; Villalobos et al., 2003; Bargar et al., 2005; Webb et al.,

2005; Saratovsky et al., 2006; Bargar et al., 2009; Clement et al., 2009; Dick et al., 2009; Grangeon et al., 2010; Tan et al., 2010; Santelli et al., 2011). The negative charge arises from Mn(IV) vacancies or Mn(III) substitutions for Mn(IV), and is compensated by exchangeable cations in the interlayer (Toner et al., 2006; Manceau et al., 2007; Peacock and Sherman, 2007b; Peacock, 2009; Zhu et al., 2010b). Fe oxides are similarly comprised of $Fe(OH,O)_6$ octahedra, but do not form charged sheets, with the exception of the mixed valence phase green rust.

As a result, Fe and Mn oxides adsorb cations (e.g., Ni, Zn, Pb) and oxoanions (e.g., selenate, chromate, sulfate, phosphate) differently from one another, with each mineral system adsorbing these ions through different adsorption mechanisms (Manceau et al., 1992; Lefèvre, 2004). For example, cations typically adsorb over Mn(IV) vacancies within the phyllomanganate interlayer to balance the negative sheet charges (Manceau et al., 1992; Manceau et al., 2002); thus, Mn(IV/III) oxides exhibit a high affinity for cations (McKenzie, 1980; Manceau et al., 1992). As a result, many cations that do not exhibit strong adsorption behaviors on other metal oxides are strongly adsorbed by phyllomanganates and are associated with Mn(IV/III) oxides in natural systems (Whitney, 1975; Koschinsky and Halbach, 1995; Manceau et al., 2002a; Manceau et al., 2007). Because of repulsion from the negatively-charged interlayers, oxoanions are relegated to adsorption at phyllomanganate edge sites (Manceau et al., 1992; Vergeer, 2013). Fe(III) oxides, however, exhibit strong affinities for oxoanions, which adsorb as either outer- or inner-sphere complexes on Fe oxide surface sites at $Fe(O,OH)_6$ corners (Benjamin and Leckie, 1981; Manceau et al., 1992; Peak et al., 2001; Lefèvre, 2004). Fe(III) oxides also have strong affinities for many cations (Benjamin and Leckie, 1981; Balistrieri and Murray, 1982; Rose and Bianchi-Mosquera, 1993; Coughlin and Stone, 1995), although cation adsorption onto Fe(III) oxides exhibits a stronger pH dependence than the Mn(IV/III) oxide system due to their differing

structures (McKenzie, 1980). Fe and Mn oxides, therefore, exhibit differing effects on trace metal and oxoanion concentrations in natural systems (McKenzie, 1980; Manceau et al., 1992; Koschinsky and Halbach, 1995), although both minerals often exert substantial controls on the concentrations of trace metals (Jenne, 1968; Smith and Longmore, 1980; Lion et al., 1982; Young and Harvey, 1992; Tebo et al., 1997; Fuller and Harvey, 2000; Hlawatsch et al., 2002; Manceau et al., 2002b; Nelson and Lion, 2003; Peacock and Sherman, 2007a; Kumar et al., 2014). Aqueous Fe(II) and Mn(II), like other cations, can also adsorb onto Fe(III) and Mn(IV/III) oxide surfaces, but recent research indicates that interactions between reduced and oxidized Fe (or Mn) are more complex than simple surface adsorption processes.

1.2. AQUEOUS FE(II)-SOLID FE(III) OXIDE REACTIONS

Aqueous Fe(II) reaction with the surfaces of solid Fe(III) oxide involves the oxidative adsorption of Fe(II) and the subsequent reduction of a spatially-separated surficial Fe(III) site through interfacial electron transfer and atom exchange (ET-AE) processes (Williams and Scherer, 2004; Larese-Casanova and Scherer, 2007; Yanina and Rosso, 2008; Handler et al., 2009; Rosso et al., 2010). Isotope exchange studies indicate that these Fe(II)-Fe(III) ET-AE reactions can lead to substantial Fe(III) oxide recrystallization, with the extent of recrystallization dependent on the amount of added aqueous Fe(II) and the Fe(III) oxide mineral identity. For example, reacting isotopically labeled aqueous ^{57}Fe(II) with goethite leads to near-complete isotope mixing between the aqueous and mineral phases (Handler et al., 2009; Frierdich et al., 2014), but no observable changes in the mineral phase or crystal morphologies. Metastable Fe oxides such as ferrihydrite and lepidocrocite, however, do undergo mineral phase transformations upon reaction with aqueous Fe(II) (Tronc et al., 1992; Hansel et al., 2003;

Hansel et al., 2004; Pedersen et al., 2005; Hansel et al., 2005). These results indicate that Fe(II) acts as a catalyst during the self-recrystallization of thermodynamically stable Fe(III) oxides. Taken together, these studies have wide-ranging implications for our understanding of Fe(III) oxide mineral behaviors in natural systems; Fe(III) oxides should not be considered static solids in the presence of aqueous Fe(II).

1.3 AQUEOUS MN(II)-SOLID MN(IV/III) OXIDE REACTIONS

The unique capacity for Mn(II)-Mn(IV) comproportionation reactions, resulting in the formation of Jahn-Teller distorted Mn(III), suggests that aqueous Mn(II)-solid Mn(IV/III) oxide interactions differ from the analogous Fe(II)-Fe(III) interactions described above. Research indicates that aqueous Mn(II) alters Mn(IV/III) oxide structures (Bargar et al., 2005; Zhu et al., 2010a) or causes Mn(IV/III) oxide phase transformations to Mn(II/III) oxides (Elzinga, 2011; Lefkowitz et al., 2013). The extent of Mn(II)-induced Mn(IV/III) oxide mineral recrystallization is unclear, however, as the Mössbauer spectroscopy studies that confirmed atom exchange between aqueous Fe(II)-solid Fe(III) oxides cannot be conducted with the Mössbauer-inactive Mn, and isotope exchange studies have thus far focused on conditions resulting in manganese oxide phase transformations (Elzinga and Kustka, 2015).

Mn(II), like other cations, likely adsorbs above vacancies within the phyllomanganate interlayer. If adsorbed Mn(II)-layer Mn(IV) comproporationation occurs, the formation of Jahn-Teller distorted Mn(III) sites may lead to increased sheet strain. As a result, phyllomanganates may exhibit different sheet symmetries or sheet stacking behavior in the presence of aqueous Mn(II). Changes in phyllomanganate sheet structures and stacking can have important ramifications on the reactivity and sorptive capacity of Mn oxides (Post, 1999).

Aqueous Mn(II)-solid Mn(IV/III) interactions may therefore be an important control on trace metal fate in natural soil, sedimentary, and aquatic systems.

1.4 ION INTERACTIONS ON FE AND MN OXIDE SURFACES: IMPLICATIONS FOR TRACE ELEMENT FATE

As a result of Fe(II)-catalyzed Fe(III) oxide recrystallization, adsorbate partitioning between the solid, surface, and aqueous phases can be altered. For example, structurally compatible adsorbates (e.g., Ni and Zn) become progressively incorporated into hematite and goethite with increasing aqueous Fe(II) concentrations or reaction times (Frierdich et al., 2011), likely because of surficial overgrowth in regions of Fe(III) oxidative adsorption. Conversely, trace metals preincorporated into hematite or goethite are released back into solution in the presence of aqueous Fe(II) (Frierdich et al., 2011; Latta et al., 2012b; Frierdich and Catalano, 2012). Because these processes are fundamentally the result of Fe(II) adsorption and subsequent Fe(III) oxide recrystallization, conditions that alter cation adsorption mechanisms or Fe(III) oxide precipitation/dissolution may affect Fe(II)-Fe(III) ET-AE reactions or trace element partitioning.

Oxoanions such as phosphate and sulfate likely affect both the extent and mechanism(s) of cation adsorption onto Fe(III) oxide surfaces. Oxoanions may enhance cation adsorption onto mineral surfaces through electrostatic effects or ternary complexation, or may suppress cation adsorption through surface site competition. Phosphate and sulfate typically enhance the adsorption of divalent metal cations on Fe oxide surfaces (e.g., Cd, Co, Cu, Pb, and Zn) (Benjamin and Bloom, 1981; Balistrieri and Murray, 1982; Diaz-Barrientos et al., 1990; Madrid et al., 1991; Hoins, 1993; Venema et al., 1997; Collins et al., 1999; Juang and Wu, 2002;

Swedlund et al., 2003). Many modeling, spectroscopic, and macroscopic adsorption studies have found that ternary complexation explains this cooperative oxoanion-cation adsorption behavior on Fe oxides (Benjamin and Leckie, 1982; Hoins, 1993; Ostergren et al., 2000; Elzinga et al., 2001; Swedlund and Webster, 2001; Zhang and Peak, 2007; Swedlund et al., 2009; Elzinga and Kretzschmar, 2013).

The effect of oxoanions on aqueous Fe(II) adsorption onto Fe(III) oxides is currently unclear. If oxoanions alter the amount or mechanism of Fe(II) adsorption, Fe(II)-Fe(III) ET-AE reactions may be altered, as the extent of Fe(II)-catalyzed Fe(III) oxide recrystallization appears to scale with Fe(II) adsorption. Recent research indicates that phosphate enhances the rate and extent of Fe(II)-Fe(III) atom exchange (Latta et al., 2012a), although the causal mechanism is unknown. Because phosphate and sulfate can also affect Fe(III) oxide nucleation, precipitation, and dissolution reactions (Bondietti et al., 1993; Stumm, 1993; Stumm, 1997; Eggleston et al., 1998; Majzlan and Myneni, 2005; Borch et al., 2007), these oxoanions may exert substantial effects on processes associated with Fe(II)-Fe(III) ET-AE. Fe(II)-catalyzed trace element partitioning may be especially altered by sulfate and phosphate, as these oxoanions can affect trace element adsorption onto the Fe oxide surface, likely an important intermediate step during trace element incorporation, as well as Fe(II)-Fe(III) ET-AE. Understanding the effects of phosphate and sulfate on Fe(II)-Fe(III) oxide interactions and associated processes is vitally important, as these reactions may alter trace metal uptake in regions with high sulfate and Fe(II) contents (e.g., marine sediments, hydrothermal vents), or with high phosphate and Fe(II) contents (e.g., riparian soils and wetlands).

Interactions between ions on Mn(IV/III) oxides are similarly complex, but likely exhibit different effects from the Fe system due to differing adsorption mechanisms and the unique

phyllomanganate structure. Because oxoanion adsorption onto phyllomanganates is typically restricted to edge-sites, oxoanions likely have a minimal effect on aqueous Mn(II)-Mn(IV/III) oxide interactions. Most trace metal cations (e.g., Ni and Zn), however, adsorb within phyllomanganate interlayers by capping vacant sites (Marcus et al., 2004; Manceau et al., 2005; Toner et al., 2006; Peacock and Sherman, 2007a; Peacock and Sherman, 2007b; Peacock, 2009). Structurally compatible cations such as Ni become incorporated into the phyllomanganate sheet by capping or filling these Mn(IV) vacancies (Peacock, 2009). There is a current dearth of knowledge of aqueous Mn(II) interactions with other adsorbates on phyllomanganate sheets, although recent research indicates that Ni and Zn may effectively compete with Mn(II) for vacant sites during biogenic Mn(II) oxidation (Zhu et al., 2010a; Grangeon et al., 2012). If competitive adsorption between Mn(II) and trace metals occurs on pre-formed phyllomanganate sheets, Mn(II)-induced structural changes may be inhibited, or Mn(II) may alter trace metal adsorption mechanisms. Trace metal incorporation into the phyllomanganate sheet may increase due to Mn(II)-catalyzed Mn(IV/III) recrystallization, or trace metals may be ejected from the phyllomanganate sheet as a result of Mn(II)-induced structural changes. A comprehensive understanding of the interactions of adsorbates, such as phosphate, sulfate, Ni, Zn, Fe(II) and Mn(II), is critical to our ability to predict the behavior of micronutrient and contaminant fate in systems with coexisting reduced and oxidized Fe (or Mn), such as euxinic soils and sediments, marine and lacustrine environments, riparian zones, and acid and coal mine drainage sites.

1.5 RESEARCH OBJECTIVES

The goal of this research is to characterize interactions between ions common in natural aquatic, soil, and sedimentary systems at Fe and Mn oxide surfaces during biogeochemical Fe

and Mn cycling to assess the potential impact of such interactions on micronutrient and contaminant fate. This dissertation consists of four specific research projects, outlined in the following chapters:

CHAPTER 2: Interaction of Fe(II) with phosphate and sulfate on iron oxide surfaces (Hinkle, M.A.G., Wang, Z., Giammar, D.E., Catalano, J.G.)

This chapter consists of a detailed analysis of the co-adsorption behavior of aqueous Fe(II) and sulfate, and aqueous Fe(II) and phosphate, on hematite and goethite surfaces. The effect of aqueous Fe(II) on sulfate and phosphate macroscopic adsorption behavior, as well as the effects of sulfate and phosphate on aqueous Fe(II) macroscopic adsorption behavior is investigated. To elucidate the specific interactions occurring between Fe(II) and these oxoanions, attenuated total reflectance Fourier transform infrared (ATR-FTIR) spectroscopic measurements of adsorbed sulfate and phosphate in the presence and absence of aqueous Fe(II) were conducted. Adsorbed sulfate and phosphate exhibited altered adsorption behaviors upon Fe(II) addition, indicating that Fe(II)-oxoanion interactions on hematite and goethite involve ternary complexation as well as electrostatic interactions. A surface complexation model (SCM) was developed (courtesy of Dr. Zimeng Wang and Prof. Daniel Giammar in the Department of Energy, Environmental, and Chemical Engineering) to explain the macroscopic adsorption data, providing further evidence that ternary complexation between oxoanions and aqueous Fe(II) occurs on Fe oxide surfaces. The ATR-FTIR spectroscopic experiments and the SCM results both confirm that mixed ternary complexation and electrostatic effects are responsible for the cooperative co-adsorption behavior observed in the macroscopic data.

CHAPTER 3: Effect of phosphate and sulfate on Ni repartitioning during Fe(II)-catalyzed Fe(III) oxide mineral recrystallization (Hinkle, M.A.G., Catalano, J.G.)

In this chapter, the impact of phosphate and sulfate on Fe(II)-catalyzed Ni repartitioning between aqueous, adsorbed, and bulk mineral pools in hematite and goethite was examined. The effect of phosphate and sulfate on time-dependent Fe(II)-catalyzed Ni release from Ni-substituted hematite and goethite was explored both macroscopically and with X-ray absorption near edge structure (XANES) measurements to quantify the amount of Ni adsorbed, incorporated, or in the aqueous phase. Ni incorporation after reaction with aqueous Fe(II) and Fe oxides in the absence and presence of oxoanions was also explored using XANES spectroscopy. These measurements show that sulfate and phosphate have different effects on Ni partitioning during Fe(II)-catalyzed hematite and goethite recrystallization and that these effects vary with mineral identity.

CHAPTER 4: Effect of Mn(II) on manganese oxide sheet structures (Hinkle, M.A.G., Catalano, J.G.)

Phyllomanganate structural changes after aging in the absence and presence of aqueous Mn(II) were investigated using a combination of powder X-ray diffraction analyses and X-ray absorption fine structure (XAFS) spectroscopy. The roles of initial phyllomanganate vacancy content and pH were explored because Mn(II) likely binds over vacant sites in the interlayer, and Mn(II) macroscopic adsorption exhibits pH dependence. Three Mn(IV/III) oxide minerals were used in this study, each with differing vacancy content: δ-MnO_2, hexagonal birnessite, and triclinic birnessite. Fitting to extended X-ray absorption fine structure (EXAFS) spectra to a

phyllomanganate structural model, which accounted for changes in vacancy content and distortions in sheet structure associated with formation of structural Jahn-Teller distorted Mn(III), were used to characterize the Mn oxide sheet structures. This study finds that Mn(II) alters Mn(IV/III) oxide structures, with differing effects depending on the pH and the initial phyllomanganate vacancy content.

CHAPTER 5: Impact of Mn(II)-manganese oxide reactions on trace element fate

(Hinkle, M.A.G., Becker, K.G., Catalano, J.G.)

Chapter 5 explores the role of Mn(II) and pH on controlling Ni and Zn uptake and adsorption behavior on phyllomanganates of varying vacancy content. Although macroscopic Ni adsorption experiments suggest that Mn(II)-metal competitive adsorption effects are minimal, EXAFS spectroscopic results find that Mn(II) has a substantial effect on Ni and Zn adsorption mechanisms at pH 4, promoting Ni and Zn adsorption at edge sites rather than vacancies. XAFS spectroscopy also indicates that Zn coordination becomes increasingly tetrahedral upon Mn(II) addition at pH 4. Conversely, Ni and Zn sorption behaviors in the pH 7 system are minimally affected by aqueous Mn(II), with only a slight effect observed on incorporated Ni bonding environments in one mineral system. The results of this research suggests that both pH and Mn(II) are important controlling factors on the dominant Ni and Zn adsorption behavior.

1.6 REFERENCES

Balistrieri L. S. and Murray J. W. (1982) The adsorption of Cu, Pb, Zn, and Cd on goethite from major ion seawater. *Geochimica et Cosmochimica Acta* **40,** 1253-1265.

Bargar J. R., Fuller C. C., Marcus M. A., Brearley A. J., de la Rosa M. P., Webb S. M. and Caldwell W. A. (2009) Structural characterization of terrestrial microbial Mn oxides from Pinal Creek, AZ. *Geochimica et Cosmochimica Acta* **73,** 889-910.

Bargar J. R., Tebo B. M., Bergmann U., Webb S. M., Glatzel P., Chiu V. Q. and Villalobos M. (2005) Biotic and abiotic products of Mn(II) oxidation by spores of the marine *Bacillus sp.* strain SG-1. *American Mineralogist* **90,** 143-154.

Bargar J. R., Tebo B. M. and Villinski J. E. (2000) In situ characterization of Mn (II) oxidation by spores of the marine *Bacillus* sp. strain SG-1. *Geochimica et Cosmochimica Acta* **64,** 2775-2778.

Benjamin M. M. and Bloom N. S. Effects of strong binding of anionic adsorbates on adsorption of trace metals on amorphous iron oxyhydroxide, In *Adsorption From Aqueous Solutions,* P.H. Tewari (Ed.), Plenum Press, New York, 1981; pp. 41-60.

Benjamin M. M. and Leckie J. O. (1981) Multiple-site adsorption of Cd, Cu, Zn, and Pb on amorphous iron oxyhydroxide. *Journal of Colloid and Interface Science* **79,** 209-221.

Benjamin M. M. and Leckie J. O. (1982) Effects of complexation by Cl, SO_4, and S_2O_3 on adsorption behavior of Cd on oxide-surfaces. *Environmental Science & Technology* **16,** 162-170.

Bondietti G., Sinniger J. and Stumm W. (1993) The reactivity of Fe(III) (hydr)oxides: effects of ligands in inhibiting the dissolution. *Colloids and Surfaces A: Physicochemical and Engineering Aspects* **79,** 157-167.

Borch T., Masue, Y., Kukkadapu R. K. and Fendorf S. (2007) Phosphate imposed limitations on biological reduction and alteration of ferrihydrite. *Environmental Science & Technology* **41,** 166-172.

Burdige D. J. (1993) The biogeochemistry of manganese and iron reduction in marine sediments. *Earth-Science Reviews* **35,** 249-284.

Clement B. G., Luther III G. W. and Tebo B. M. (2009) Rapid, oxygen-dependent microbial Mn(II) oxidation kinetics at sub-micromolar oxygen concentrations in the Black Sea suboxic zone. *Geochimica et Cosmochimica Acta* **73,** 1878-1889.

Collins C. R., Ragnarsdottir K. V. and Sherman D. M. (1999) Effect of inorganic and organic ligands on the mechanism of cadmium sorption to goethite. *Geochimica et Cosmochimica Acta* **63,** 2989-3002.

Cornell R. M. and Schwertmann U. The iron oxides: Structure, properties, reactions, occurrences and uses, WILEY-VCH Verlag GmbH & Co. KGaA, Weinheim, 2003.

Coughlin B. R. and Stone A. T. (1995) Nonreversible adsorption of divalent metal ions (Mn^{II}, Co^{II}, Ni^{II}, Cu^{II}, and Pb^{II}) onto goethite: Effects of acidification, Fe^{II} addition, and picolinic acid addition. *Environmental Science & Technology* **29,** 2445-2455.

Diaz-Barrientos E., Madrid L., Contreras M. C. and Morillo E. (1990) Simultaneous adsorption of zinc and phosphate on synthetic lepidocrocite. *Australian Journal of Soil Research* **28,** 549-557.

Dick G. J., Clement B. G., Webb S. M., Fodrie F. J., Bargar J. R. and Tebo B. M. (2009) Enzymatic microbial Mn(II) oxidation and Mn biooxide production in the Guaymas Basin deep-sea hydrothermal plume. *Geochimica et Cosmochimica Acta* **73,** 6517-6530.

Diem D. and Stumm W. (1984) Is dissolved Mn2+ being oxidized by O2 in absence of Mn-bacteria or surface catalysts? *Geochimica et Cosmochimica Acta* **48,** 1571-1573.

Eggleston C. M., Hug S., Stumm W., Sulzberger B. and Dos Santos Afonso M. (1998) Surface complexation of sulfate by hematite surfaces: FTIR and STM observations. *Geochimica et Cosmochimica Acta* **62,** 585-593.

Elzinga E. J. (2011) Reductive transformation of birnessite by aqueous Mn (II). *Environmental Science & Technology* **45,** 6366-6372.

Elzinga E. J. and Kustka A. B. (2015) A Mn-54 radiotracer study of Mn isotope solid-liquid exchange during reductive transformation of vernadite (δ-MnO2) by aqueous Mn (II). *Environmental Science & Technology* doi: 10.1021/acs.est.5b00022.

Elzinga E. J. and Kretzschmar R. (2013) *In situ* ATR-FTIR spectroscopic analysis of the co-adsorption of orthophosphate and Cd(II) onto hematite. *Geochimica et Cosmochimica Acta* **117,** 53-64.

Elzinga E. J., Peak D. and Sparks D. L. (2001) Spectroscopic studies of Pb(II)-sulfate interactions at the goethite-water interface. *Geochimica et Cosmochimica Acta* **65,** 2219-2230.

Emerson S., Kalhorn S., Jacobs L., Tebo B. M., Nealson K. H. and Rosson R. A. (1982) Environmental oxidation rate of manganese(II): bacterial catalysis. *Geochimica et Cosmochimica Acta* **46,** 1073-1079.

Frierdich A. J., Beard B. L., Reddy T. R., Scherer M. M. and Johnson C. M. (2014) Iron isotope fractionation between aqueous Fe(II) and goethite revisited: New insights based on a multi-direction approach to equilibrium and isotopic exchange rate modification. *Geochimica et Cosmochimica Acta* **139,** 383-398.

Frierdich A. J. and Catalano J. G. (2012) Controls on Fe(II)-activated trace element release from goethite and hematite. *Environmental Science & Technology* **46,** 1519-1526.

Frierdich A. J., Luo Y. and Catalano J. G. (2011) Trace element cycling through iron oxide minerals during redox-driven dynamic recrystallization. *Geology* **39,** 1083-1086.

Fuller C. C. and Harvey J. W. (2000) Reactive uptake of trace metals in the hyporheic zone of a mining-contaminated stream, Pinal Creek, Arizona. *Environmental Science & Technology* **34,** 1150-1155.

Grangeon S., Lanson B., Miyata N., Tani Y. and Manceau A. (2010) Structure of nanocrystalline phyllomanganates produced by freshwater fungi. *American Mineralogist* **95,** 1608-1616.

Grangeon S., Manceau A., Guilhermet J., Gaillot A. C., Lanson M. and Lanson B. (2012) Zn sorption modifies dynamically the layer and interlayer structure of vernadite. *Geochimica et Cosmochimica Acta* **85,** 302-313.

Grote G. and Krumbein W. E. (1992) Microbial precipitation of manganese by bacteria and fungi from desert rock and rock varnish. *Geomicrobiology Journal* **10,** 49-57.

Handler R. M., Beard B. L., Johnson C. M. and Scherer M. M. (2009) Atom exchange between aqueous Fe(II) and goethite: an Fe isotope tracer study. *Environmental Science & Technology* **43,** 1102-1107.

Hansel C. M., Benner S. G. and Fendorf S. (2005) Competing Fe(II)-induced mineralization pathways of ferrihydrite. *Environmental Science & Technology* **39,** 7147-7153.

Hansel C. M., Benner S. G., Neiss J., Dohnalkova A., Kukkadapu R. K. and Fendorf S. (2003) Secondary mineralization pathways induced by dissimilatory iron reduction of ferrihydrite under advective flow. *Geochimica et Cosmochimica Acta* **67,** 2977-2992.

Hansel C. M., Benner S. G., Nico P. and Fendorf S. (2004) Structural constrains of ferric (hydr)oxides on dissimilatory iron reduction and the fate of Fe(II). *Geochimica et Cosmochimica Acta* **68,** 3217-3229.

Hlawatsch S., Garbe-Schönberg C. D., Lechtenberg F., Manceau A., Tamura N., Kulik D. A. and Kersten M. (2002) Trace metal fluxes to ferromanganese nodules from the western Baltic Sea as a record for long-term environmental changes. *Chemical Geology* **182,** 697-709.

Hoins U. (1993) Ligand effect on the adsorption of heavy metals: The sulfate-cadmium-goethite case. *Water, Air, and Soil Pollution* **68,** 241-255.

Jenne E. A. Controls on Mn, Fe, Co, Ni, Cu, and Zn concentrations in soils and water: The significant role of hydrous Mn and Fe oxides, In *Advances in Chemistry,* American Chemical Society, 1968; pp. 337-387.

Juang R. and Wu W. (2002) Adsorption of sulfate and copper(II) on goethite in relation to the changes of zeta potentials. *Journal of Colloid and Interface Science* **249,** 22-29.

Kappler A. and Straub K. L. (2005) Geomicrobiological cycling of iron. *Reviews in Mineralogy and Geochemistry* **59,** 85-108.

Koschinsky A. and Halbach P. (1995) Sequential leaching of marine ferromanganese precipitates: Genetic implications. *Geochimica et Cosmochimica Acta* **59,** 5113-5132.

Krumbein W. E. and Jens K. (1981) Biogenic rock varnishes of the Negev Desert (Israel) and ecological study of iron and magnanese transformation by cyanobacteria and fungi. *Oceologia* **50,** 25-38.

Kumar E., Bhatnagar A., Hogland W., Marques M. and Sillanpää M. (2014) Interaction of inorganic anions with iron-mineral adsorbents in aqueous media— A review. *Advances in Colloid and Interface Science* **203,** 11-21.

Larese-Casanova P. and Scherer M. M. (2007) Fe(II) sorption on hematite: new insights based on spectroscopic measurements. *Environmental Science & Technology* **41,** 471-477.

Latta D. E., Bachman J. E. and Scherer M. M. (2012a) Fe electron transfer and atom exchange in goethite: Influence of Al-substitution and anion sorption. *Environmental Science & Technology* **46,** 10614-10623.

Latta D. E., Gorski C. A. and Scherer M. M. (2012b) Influence of Fe^{2+}-catalysed iron oxide recrystallization on metal cycling. *Biochemical Society Transactions* **40,** 1191-7.

Lefèvre G. (2004) In situ Fourier-transform infrared spectroscopy studies of inorganic ions adsorption on metal oxides and hydroxides. *Advances in Colloid and Interface Science* **107,** 109-123.

Lefkowitz J. P., Rouff A. A. and Elzinga E. J. (2013) Influence of pH on the reductive transformation of birnessite by aqueous Mn(II). *Environmental Science & Technology* **47,** 10364-10371.

Lion L. W., Altmann R. S. and Leckie J. O. (1982) Trace-metal adsorption characteristics of estuarine particulate matter: evaluation of contributions of iron/manganese oxide and organic surface coatings. *Environmental Science & Technology* **16,** 660-666.

Liu J., Durand J. P., Espinal L., Garces L. -J., Gomez S., Son Y. -C., Villegas J. and Suib S. L. (2004) Layered Manganese Oxides: Synthesis, Properties, and Applications, In *Handbook of Layered Materials*, pp. 475.

Madrid L., Diaz-Barrientos E. and Contreras M. C. (1991) Relationships between zinc and phosphate adsorption on montmorillonite and an iron oxyhydroxide. *Australian Journal of Soil Research* **29,** 239-247.

Majzlan J. and Myneni S. C. B. (2005) Speciation of iron and sulfate in acid waters: Aqueous clusters to mineral precipitates. *Environmental Science & Technology* **39,** 188-194.

Manceau A., Charlet L., Boisset M. C., Didier B. and Spadini L. (1992) Sorption and speciation of heavy metals on hydrous Fe and Mn oxides. From microscopic to macroscopic. *Applied Clay Science* **7,** 201-223.

Manceau A., Lanson B. and Drits V. A. (2002) Structure of heavy metal sorbed birnessite. Part III: Results from powder and polarized extended X-ray absorption fine structure spectroscopy. *Geochimica et Cosmochimica Acta* **66,** 2639-2663.

Manceau A., Lanson M. and Geoffroy N. (2007) Natural speciation of Ni, Zn, Ba, and As in ferromanganese coatings on quartz using X-ray fluorescence, absorption, and diffraction. *Geochimica et Cosmochimica Acta* **71,** 95-128.

Manceau A., Tamura N., Celestre R. S., MacDowell A. A., Geoffroy N., Sposito G. and Padmore H. A. (2002a) Molecular-Scale Speciation of Zn and Ni in Soil Ferromanganese Nodules from Loess Soils of the Mississippi Basin. *Environmental Science & Technology* **37,** 75-80.

Manceau A., Tamura N., Marcus M. A., MacDowell A. A., Celestre R. S., Sublett R. E., Sposito G. and Padmore H. A. (2002b) Deciphering Ni sequestration in soil ferromanganese nodules by combining X-ray fluorescence, absorption, and diffraction at micrometer scales of resolution. *American Mineralogist* **87,** 1494-1499.

Manceau A., Tommaseo C., Rihs S., Geoffroy N., Chateigner D., Schlegel M., Tisserand D., Marcus M. A., Tamura N. and Chen Z. -S. (2005) Natural speciation of Mn, Ni, and Zn at the micrometer scale in a clayey paddy soil using X-ray fluorescence, absorption, and diffraction. *Geochimica et Cosmochimica Acta* **69,** 4007-4034.

Marcus M. A., Manceau A. and Kersten M. (2004) Mn, Fe, Zn and As speciation in a fast-growing ferromanganese marine nodule. *Geochimica et Cosmochimica Acta* **68,** 3125-3136.

McKenzie R. M. (1980) The adsorption of lead and other heavy metals on oxides of manganese and iron. *Soil Research* **18,** 61-73.

Millero F. J. (1989) Effect of ionic interactions on the oxidation of Fe(II) and Cu(I) in natural waters. *Marine Chemistry* **28,** 1-18.

Morgan J. J. (2005) Kinetics of reaction between O_2 and Mn (II) species in aqueous solutions. *Geochimica et Cosmochimica Acta* **69,** 35-48.

Nealson K. H., Tebo B. M. and Rosson R. A. (1988) Occurrence and mechanisms of microbial oxidation of manganese. *Advances in Applied Microbiology* **33,** 2027-2035.

Nelson Y. M. and Lion L. W. (2003) Formation of biogenic manganese oxides and their influence on the scavenging of toxic trace elements. *Geochemical and Hydrological Reactivity of Heavy Metals in Soils. CRC Press* **200,** 169-186.

Northup D. E., Barns S. M., Yu L. E., Spilde M. N., Schelble R. T., Dano K. E., Crossey L. J., Connolly C. A., Boston P. J., Natvig D. O. and Dahm C. N. (2003) Diverse microbial communities inhabiting ferromanganese deposits in Lechuguilla and Spider Caves. *Environmental Microbiology* **5,** 1071-1086.

Ostergren J. D., Brown G. E., Parks G. A. and Persson P. (2000) Inorganic ligand effects on Pb(II) sorption to goethite (α-FeOOH): II. Sulfate. *Journal of Colloid and Interface Science* **225,** 483-493.

Peacock C. L. (2009) Physiochemical controls on the crystal-chemistry of Ni in birnessite: Genetic implications for ferromanganese precipitates. *Geochimica et Cosmochimica Acta* **73,** 3568-3578.

Peacock C. L. and Sherman D. M. (2007a) Crystal-chemistry of Ni in marine ferromanganese crusts and nodules. *American Mineralogist* **92,** 1087-1092.

Peacock C. L. and Sherman D. M. (2007b) Sorption of Ni by birnessite: Equilibrium controls on Ni in seawater. *Chemical Geology* **238,** 94-106.

Peak D., Elzinga E. J. and Sparks D. L. Understanding sulfate adsorption mechanisms on iron(III) oxides and hydroxides: Results from ATR-FTIR spectroscopy, In *Heavy Metals Release in Soils,* H.M. Selim (Ed.), CRC Press LLC, Boca Raton, 2001; pp. 167-190.

Pedersen H. D., Postma D., Jakobsen R. and Larsen O. (2005) Fast transformation of iron oxyhydroxides by the catalytic action of aqueous Fe(II). *Geochimica et Cosmochimica Acta* **69,** 3967-3977.

Post J. E. (1999) Manganese oxide minerals: Crystal structures and economic and environmental significance. *Proceedings of the National Academy of Sciences of the United States of America* **96,** 3447-3454.

Potter R. M. and Rossman G. R. (1979) The manganese-and iron-oxide mineralogy of desert varnish. *Chemical Geology* **25,** 79-94.

Rose A. W. and Bianchi-Mosquera G. C. (1993) Adsorption of Cu, Pb, Zn, Co, Ni, and Ag on goethite and hematite; a control on metal mobilization from red beds into stratiform copper deposits. *Economic Geology* **88,** 1226-1236.

Rosso K. M., Yanina S. V., Gorski C. A., Larese-Casanova P. and Scherer M. M. (2010) Connecting observations of hematite (α-Fe_2O_3) growth catalyzed by Fe(II). *Environmental Science & Technology* **44,** 61-67.

Santelli C. M., Webb S. M., Dohnalkova A. C. and Hansel C. M. (2011) Diversity of Mn oxides produced by Mn(II)-oxidizing fungi. *Geochimica et Cosmochimica Acta* **75,** 2762-2776.

Saratovsky I., Wightman P. G., Pasten P. A., Gaillard J. F. and Poeppelmeier K. R. (2006) Manganese oxides: Parallels between abiotic and biotic structures. *Journal of the American Chemical Society* **128,** 11188-11198.

Smith J. D. and Longmore A. R. (1980) Behaviour of phosphate in estuarine water. *Nature* **287,** 532-534.

Sobolev D. and Roden E. E. (2002) Evidence for rapid microscale bacterial redox cycling of iron in circumneutral environments. *Antonie Van Leeuwenhoek* **81,** 587-97.

Stumm W. (1993) From surface acidity to surface reactivity; inhibition of oxide dissolution. *Aquatic Sciences* **55,** 273-280.

Stumm W. (1997) Reactivity at the mineral-water interface: dissolution and inhibition. *Colloids and Surfaces A: Physicochemical and Engineering Aspects* **120,** 143-166.

Swedlund P. J. and Webster J. G. (2001) Cu and Zn ternary surface complex formation with SO_4 on ferrihydrite and schwertmannite. *Applied Geochemistry* **16,** 503-511.

Swedlund P. J., Webster J. G. and Miskelly G. M. (2003) The effect of SO_4 on the ferrihydrite adsorption of Co, Pb and Cd: ternary complexes and site heterogeneity. *Applied Geochemistry* **18,** 1671-1689.

Swedlund P. J., Webster J. G. and Miskelly G. M. (2009) Goethite adsorption of Cu (II), Pb (II), Cd (II), and Zn (II) in the presence of sulfate: Properties of the ternary complex. *Geochimica et Cosmochimica Acta* **73,** 1548-1562.

Tan H., Zhang G., Heaney P. J., Webb S. M. and Burgos W. D. (2010) Characterization of manganese oxide precipitates from Appalachian coal mine drainage treatment systems. *Applied Geochemistry* **25,** 389-399.

Tebo B. M. (1991) Manganese (II) oxidation in the suboxic zone of the Black Sea. *Deep Sea Research Part A. Oceanographic Research Papers* **38,** S883-S905.

Tebo B. M., Ghiorse W. C., van Waasbergen L. G., Siering P. L. and Caspi R. (1997) Bacterially mediated mineral formation; insights into manganese (II) oxidation from molecular genetic and biochemical studies. *Reviews in Mineralogy and Geochemistry* **35,** 225-266.

Templeton A. S., Knowles E. J., Eldridge D. L., Arey B. W., Dohnalkova A. C., Webb S. M., Bailey B. E., Tebo B. M. and Staudigel H. (2009) A seafloor microbial biome hosted within incipient ferromanganese crusts. *Nature Geoscience* **2,** 872-876.

Thamdrup B., Fossing H. and Jørgensen B. B. (1994) Manganese, iron and sulfur cycling in a coastal marine sediment, Aarhus Bay, Denmark. *Geochimica et Cosmochimica Acta* **58,** 5115-5129.

Toner B., Manceau A., Webb S. M. and Sposito G. (2006) Zinc sorption by biogenic hexagonal birnessite particles within a hydrated bacterial biofilm. *Geochimica et Cosmochimica Acta* **70,** 27-43.

Tronc E., Belleville P., Jolivet J. P. and Livage J. (1992) Transformation of ferric hydroxide into spinel by iron(II) adsorption. *Langmuir* **8,** 313-319.

Van Cappellen P., Viollier E., Roychoudhury A., Clark L., Ingall E., Lowe K. and Dichristina T. (1998) Biogeochemical cycles of manganese and iron at the oxic-anoxic transition of a

stratified marine basin (Orca Basin, Gulf of Mexico). *Environmental Science & Technology* **32,** 2931-2939.

van der Zee C., Roberts D. R., Rancourt D. G. and Slomp C. P. (2003) Nanogoethite is the dominant reactive oxyhydroxide phase in lake and marine sediments. *Geology* **31,** 993-996.

Venema P., Hiemstra T. and van Riemsdijk WH (1997) Interaction of Cadmium with Phosphate on Goethite. *Journal of Colloid and Interface Science* **192,** 94-103.

Vergeer K. A. (2013) Adsorption of Antimony by Birnessite and the Impact of Antimony on the Electrostatic Surface Properties of Variable-Charge Soil Minerals. Master's Thesis, University of Tennessee.

Villalobos M., Toner B., Bargar J. R. and Sposito G. (2003) Characterization of the manganese oxide produced by *pseudomonas putida* strain MnB1. *Geochimica et Cosmochimica Acta* **67,** 2649-2662.

Von Langen P. J., Johnson K. S., Coale K. H. and Elrod V. A. (1997) Oxidation kinetics of manganese (II) in seawater at nanomolar concentrations. *Geochimica et Cosmochimica Acta* **61,** 4945-4954.

Webb S. M., Dick G. J., Bargar J. R. and Tebo B. M. (2005) Evidence for the presence of Mn(III) intermediates in the bacterial oxidations of Mn(II). *Proceedings of the National Academy of Sciences of the United States of America* **102,** 5558-55563.

Weber K. A., Achenbach L. A. and Coates J. D. (2006) Microorganisms pumping iron: anaerobic microbial iron oxidation and reduction. *Nature Reviews Microbiology* **4,** 752-64.

Wehrli B., Friedl G. and Manceau A. (1995) Reaction rates and products of manganese oxidation at the sediment-water interface. In *Advances in Chemistry* pp. 111-134.

Whitney P. R. (1975) Relationship of manganese-iron oxides and associated heavy metals to grain size in stream sediments. *Journal of Geochemical Exploration* **4,** 251-263.

Williams A. G. B. and Scherer M. M. (2004) Spectroscopic evidence for Fe(II)-Fe(III) electron transfer at the iron oxide-water interface. *Environ Sci Technol* **38,** 4782-90.

Yanina S. V. and Rosso K. M. (2008) Linked reactivity at mineral-water interfaces through bulk crystal conduction. *Science* **320,** 218-22.

Young L. B. and Harvey H. H. (1992) The relative importance of manganese and iron oxides and organic matter in the sorption of trace metals by surficial lake sediments. *Geochimica et Cosmochimica Acta* **56,** 1175-1186.

Zhang G. Y. and Peak D. (2007) Studies of Cd (II)--sulfate interactions at the goethite--water interface by ATR-FTIR spectroscopy. *Geochimica et Cosmochimica Acta* **71,** 2158-2169.

Zhu M., Ginder-Vogel M., Parikh S. J., Feng X. H. and Sparks D. L. (2010a) Cation effects on the layer structure of biogenic Mn-oxides. *Environmental Science & Technology* **44,** 4465-4471.

Zhu M., Ginder-Vogel M. and Sparks D. L. (2010b) Ni(II) sorption on biogenic Mn-oxides with varying Mn octahedral layer structure. *Environmental Science & Technology* **44,** 4472-4478.

CHAPTER 2

INTERACTION OF FE(II) WITH PHOSPHATE AND SULFATE ON IRON OXIDE SURFACES

Published in *Geochimica et Cosmochimica Acta* as:
Hinkle, M.A.G., Wang, Z., Giammar, D.E., Catalano, J.G. (2015) Interaction of Fe(II) with phosphate and sulfate on iron oxide surfaces, **158**, 130-146.

2.1 ABSTRACT

Sulfate and phosphate, oxoanions common in natural systems, affect iron oxide growth and dissolution processes, the adsorption behavior of divalent cations, and iron oxide phase transformations. These oxoanions may thus influence Fe(II) adsorption behavior and subsequently alter the mechanisms and products of Fe(II)-catalyzed Fe(III) oxide recrystallization processes, such as trace metal repartitioning. In this study, the macroscopic and molecular-scale effects of the coadsorption of Fe(II) and sulfate or phosphate onto Fe(III) oxide surfaces were investigated. Macroscopic adsorption edges show that both sulfate and phosphate increase Fe(II) adsorption and that Fe(II) increases sulfate and phosphate adsorption. Attenuated total reflectance Fourier transform infrared spectroscopy shows that the cooperative adsorption behavior of oxoanions and aqueous Fe(II) likely results from a combination of ternary complexation and electrostatic interactions. Surface complexation modeling requires the inclusion of ternary complexes to simulate all conditions of the macroscopic data, further suggesting that these oxoanions and Fe(II) form ternary complexes on Fe(III) oxide surfaces. Despite clear evidence in previous research for Fe(II) oxidation upon adsorption on iron oxide surfaces, this work shows that Fe(II) also displays macroscopic and molecular-scale behaviors associated with divalent (i.e., non-oxidative) cation adsorption. Prior work has shown that metal release from iron oxides caused by ET-AE reactions is directly proportional to the macroscopically-determined Fe(II) surface coverage. Predicting the effects of sulfate and phosphate on processes controlled by ET-AE reactions at redox interfaces, such as mineral phase transformations and trace element repartitioning, may thus not require the explicit consideration of electron transfer processes.

2.2 INTRODUCTION

Biogeochemical iron cycling occurs in many environments, including sediments, estuaries, wetlands, acid mine and rock drainage sites, carbonate springs and caves, and soils (Tugel et al., 1986; Canfield et al., 1993; Johnson et al., 1993; Sobolev and Roden, 2002; Northup et al., 2003; Kappler and Straub, 2005; Weber et al., 2006; Thompson et al., 2006; Baskar et al., 2008), leading to the coexistence of aqueous Fe(II) and solid Fe(III) oxide minerals. Reactions between these iron species result in mineral phase transitions from metastable iron oxides to more thermodynamically stable forms, iron isotope fractionation, and simultaneous growth and dissolution of crystalline iron oxide surfaces (Williams and Scherer, 2004; Crosby et al., 2005; Hansel et al., 2005; Catalano et al., 2010). Recent studies have shown that aqueous Fe(II) and solid Fe(III) oxides react via interfacial electron transfer and atom exchange (ET-AE) processes, involving the coupled oxidative adsorption of aqueous Fe(II) and the reductive dissolution of a spatially separated Fe(III) surface site, resulting in mineral recrystallization (Williams and Scherer, 2004; Larese-Casanova and Scherer, 2007; Yanina and Rosso, 2008; Handler et al., 2009; Rosso et al., 2010).

Oxoanions such as phosphate and sulfate can influence mineral surface reactions, affecting mineral nucleation, precipitation, and dissolution. Oxoanion surface complexes may block reactive surface sites (e.g., steps, defects, kinks) involved in iron oxide dissolution and growth (Bondietti et al., 1993; Stumm, 1997; Eggleston et al., 1998; Majzlan and Myneni, 2005; Borch et al., 2007). Phosphate adsorption decreases the reductive dissolution of ferrihydrite by dissimilatory iron reducing bacterium (Borch et al., 2007), suppresses the reductive dissolution of goethite (Stumm, 1993) and hematite (Stumm, 1997) by H_2S, and inhibits the ligand promoted dissolution of lepidocrocite by ethylenediaminetetraacetic acid (Stumm, 1997). Sulfate can alter

Fe(III) oxide nucleation and precipitation processes, affecting Fe(III) oxide formation under acid drainage conditions (Majzlan and Myneni, 2005).

The presence of oxoanions can also affect the adsorption mechanism of cations on iron oxide surfaces through the formation of ternary complexes, enhanced electrostatic effects, or competitive adsorption. Previous studies indicate that sulfate increases Cd(II) adsorption onto goethite (Balistrieri and Murray, 1982; Hoins, 1993; Zhang and Peak, 2007; Swedlund et al., 2009) and ferrihydrite (Swedlund et al., 2003), Cu(II) adsorption onto goethite (Balistrieri and Murray, 1982; Ali and Dzombak, 1996; Juang and Wu, 2002; Swedlund et al., 2009) and ferrihydrite (Swedlund and Webster, 2001), Pb(II) adsorption onto goethite (Ostergren et al., 2000) and ferrihydrite (Swedlund et al., 2003), and Zn(II) adsorption onto goethite (Balistrieri and Murray, 1982; Swedlund et al., 2009) and ferrihydrite (Swedlund and Webster, 2001). Phosphate has also been found to enhance cation adsorption onto iron oxide surfaces, such as Cd(II) (Venema et al., 1997; Collins et al., 1999) and Zn(II) (Diaz-Barrientos et al., 1990; Madrid et al., 1991). Although there are disparities between some X-ray absorption fine structure (XAFS) and Fourier transform infrared (FTIR) spectroscopic studies (e.g., Collins et al., 1999; Zhang and Peak, 2007), many spectroscopic, macroscopic, and modeling studies have indicated that cations and oxoanions commonly form ternary complexes on Fe(III) oxide surfaces (Benjamin and Leckie, 1982; Hoins, 1993; Ali and Dzombak, 1996; Ostergren et al., 2000; Elzinga et al., 2001; Swedlund and Webster, 2001; Zhang and Peak, 2007; Swedlund et al., 2009; Elzinga and Kretzschmar, 2013).

Studies specifically focused on Fe(II)-oxoanion coadsorption are limited. Jeon et al. (2001) found that sulfate substantially enhanced Fe(II) adsorption onto hematite, with 1.0 mM sulfate shifting the Fe(II) adsorption edge by more than two pH units. The effect of Fe(II) on

sulfate adsorption, however, has not been studied macroscopically or spectroscopically and the Fe(II)-sulfate coadsorption mechanism(s) remains uncertain. A study of Fe(II) and arsenate coadsorption onto goethite and hematite indicates that while the adsorption of both species is somewhat increased there is no change in arsenate adsorption mechanisms, suggesting that Fe(II) and arsenate do not directly interact (Catalano et al., 2011). A recent study probing the effect of silicate, bicarbonate, and phosphate on Fe(II)-Fe(III) ET-AE reactions demonstrated that phosphate has a small enhancing effect on the rate and extent of Fe atom exchange with goethite and does not prevent electron transfer; the mechanism through which phosphate enhances Fe atom exchange, however, is unknown (Latta et al., 2012). These studies suggest that oxoanions may affect Fe(II) adsorption, which could impact a wide array of subsequent processes, such as mineral recrystallization and trace element repartitioning. However, the nature and extent of Fe(II)-oxoanion coadsorption reactions are currently unclear.

This paper describes an investigation of the coadsorption behavior of Fe(II) and two oxoanions common in natural systems, phosphate and sulfate, on hematite and goethite. The macroscopic effects of coadsorption were investigated in batch experiments that examined a wide pH range and varying adsorbate concentrations. The effect of Fe(II) on sulfate and phosphate adsorption mechanisms was further probed by attenuated total reflectance-Fourier transform infrared (ATR-FTIR) spectroscopy to determine if specific molecular interactions occur between these species on iron oxide surfaces. A surface complexation model (SCM) was also developed to determine if the molecular-scale processes inferred from spectroscopic measurements could explain the observed macroscopic behavior.

2.3 MATERIALS AND METHODS

2.3.1. Iron Oxide Syntheses

Iron oxide minerals were prepared following modified procedures outlined by Schwertmann and Cornell (2000). Goethite was synthesized by hydrolysis of 100 mL of a 1 M $Fe(NO_3)_3 \cdot 9H_2O$ solution with 180 mL of a 5 M NaOH solution in a 1 L polypropylene bottle, resulting in the rapid precipitation of ferrihydrite. The resulting suspension was diluted to 1 L with deionized water (>18.2 MΩ·cm), and aged for 60 hours at 70 ^{o}C, forming a yellow precipitate. Hematite was synthesized by the addition of 40 g of $Fe(NO_3)_3 \cdot 9H_2O$ to 500 mL deionized water, 300 mL of a 1 M KOH solution, and 50 mL of a 1 M $NaHCO_3$ solution in a 1 L polypropylene bottle. The pH of the solution was checked to ensure it was above 8 but below 8.5. The suspension was then aged for 5 days at 98 ^{o}C, forming a red precipitate. Excess electrolytes were removed from both final solids by vacuum filtration and rinsing with deionized water. The resulting wet pastes were resuspended in deionized water and stored in clear polypropylene bottles wrapped with aluminum foil.

After synthesis, the mineral suspensions were transferred to an anaerobic chamber (Coy Laboratory Products, Inc.) with a 3% H_2/97% N_2 atmosphere and Pd catalysts to limit O_2(g). Suspensions were sparged with the gas stream from a gas filtration system comprised of chamber atmosphere pumped through two gas washing bottles. The first bottle contained a 10% pyrogallol ($C_6H_6O_3$) and 40% KOH solution, removing O_2(g) and CO_2(g), and the second bottle contained deionized water, hydrating the gas stream (to minimize evaporation of the suspension), and preventing pyrogallol and KOH from entering the gas stream to the suspension. Sparging continued until the dissolved oxygen content of the mineral suspension was below the detection limit (2.5 ppb O_2) of a colorimetric indicator (CHEMets® Kit K-7540). After sparging, the

concentrations of the hematite and goethite mineral suspensions were determined through gravimetric analysis. A sample of each mineral suspension was dried in a convection oven at 70 ^{o}C for characterization. Powder X-ray diffraction (XRD) patterns were collected to confirm the formation of hematite and goethite and the absence of impurities (Rigaku Geigerflex D-MAX/A diffractometer, Cu Kα radiation). Brunauer-Emmett-Teller (BET) specific surface areas of the synthesized hematite and goethite are 30.1 and 42.0 m^2 g^{-1}, respectively (N_2 adsorption, Quantachrome Instruments Autosorb-1).

2.3.2. Reagents

All solutions were prepared in the anaerobic chamber using deoxygenated deionized water, which was sparged using the gas filtration system until the dissolved oxygen content was below the detection limit. A stock solution of 10^{-2} M Fe(II) was prepared with $FeCl_2$•$4H_2O$, acidified to a pH of 2 with HCl and stored in an amber polypropylene bottle to prevent photooxidation. Stock solutions for 10^{-2} M phosphate and 10^{-2} M sulfate were made with Na_2HPO_4 and Na_2SO_4, respectively. NaCl, 2-(4-morpholino)ethanesulfonic acid (MES) and 3-[4-(2-hydroxyethyl)-1-piperazinyl]propanesulfonic acid (EPPS) stock solutions were also prepared. Dilute HCl and NaOH solutions for pH adjustment were brought into the anaerobic chamber and sparged at least 90 days prior to use.

2.3.3. Macroscopic Fe(II) and Oxoanion Adsorption

A series of adsorption experiments were conducted to investigate the coadsorption of Fe(II) and phosphate or sulfate. The initial conditions studied were 0, 0.1 mM, or 1.0 mM phosphate or sulfate and 0, 0.1 mM, or 1.0 mM aqueous Fe(II). Each experiment consisted of

samples ranging from pH 3.0 - 9.0, with samples at pH intervals of ~0.5, with mineral-free blanks and triplicate samples at pH 3.0, 6.0, and 9.0. All phosphate experiment samples contained 4 g L^{-1} goethite or hematite, 10^{-2} M NaCl to buffer ionic strength, and 10^{-3} M MES (for samples with pH of 3.0-6.0) or EPPS (for samples with pH of 6.5-9.0) to buffer the pH. The sulfate experiments were conducted without a pH buffer because most buffers with appropriate pK_a values that are known to not substantially complex metal cations are sulfonic acids, preventing determination of sulfate adsorption via inductively coupled plasma-optical emission spectroscopy (ICP-OES).

Samples were prepared within the anaerobic chamber by first adding the appropriate aliquot of mineral suspension, NaCl, buffer (if used), and deoxygenated deionized water in a 15 mL conical centrifuge tube. The sample pH was adjusted to below pH 7.0 to prevent the precipitation of secondary mineral phases during the addition of Fe(II) and phosphate or sulfate. Once the oxoanion and Fe(II) solutions were added to the samples (with Fe(II) added approximately 30 seconds after the oxoanion in dual-sorbate systems), the pH of each sample was adjusted to within ±0.1 units of the target pH using HCl and NaOH. The centrifuge tubes were wrapped in aluminum foil to prevent photooxidation of Fe(II) and placed on end-over-end rotators for 5 days. After 24 hours, the pH of each sample was checked and adjusted for any pH drift greater than ±0.5 from the target pH. The pH of the samples for the unbuffered sulfate experiments were checked daily and adjusted, if necessary. At the end of each experiment, the final pH of each sample was recorded and the samples were filtered using 0.22 μm mixed cellulose ester (MCE) syringe filters (Fisher Scientific). The samples for the 1.0 mM phosphate and 0.1 mM Fe(II) experiments were filtered using 0.02 μm alumina-based syringe filters (Anotop) because the iron oxide particles were highly dispersed under these conditions and

passed through the larger pore-size filters. The samples were then removed from the anaerobic chamber and acidified to 2% HNO_3 using trace metal grade concentrated HNO_3.

Dissolved iron, phosphorus, and sulfur concentrations remaining in solution at the end of the experiments were determined using ICP-OES (Perkin Elmer Optima 7300 DV). These concentrations were used to calculate the percentage of adsorbed Fe(II), phosphate, and sulfate. Sets of 8 - 11 calibration standards were used for each analysis, with check standards and blanks throughout. ICP-OES measurements were made in triplicate and were averaged. Uncertainty for the percentage of adsorbed Fe(II), phosphate, and sulfate calculations was determined as the percent relative uncertainty for a 95% confidence level, using standard deviations from both the triplicate ICP-OES measurements and the triplicate samples at pH 3.0, 6.0, and 9.0.

2.3.4. ATR-FTIR Experiments

The effect of aqueous Fe(II) on oxoanion adsorption mechanisms onto hematite and goethite was investigated by ATR-FTIR spectroscopy using a Thermo Nicolet Nexus 470 ESP FTIR spectrometer (Nexus DTGS detector with a KBr window) and a PIKE Technologies Horizontal ATR (HATR) accessory. Sample preparation was conducted in a ZnSe HATR flow through cell (45^{o}; thickness, 4 mm; upper face dimensions, 80 mm x 10 mm; 10 internal reflections; refractive index, 2.4) within the anaerobic chamber, using solutions deoxygenated and prepared through the processes outlined above. Previous studies have indicated that adsorbed species on dried solids undergo structural changes that affect the ATR-FTIR spectra (Arai and Sparks, 2001; Paul et al., 2005), therefore these experiments were performed in situ.

The samples consisted of a hematite or goethite coating on the crystal, equilibrated with a solution of 10^{-2} M NaCl, phosphate (or sulfate), and Fe(II) at pH 7.00 ±0.05. The hematite and

goethite coatings were prepared by pipetting 1.5 mL of a 2 g L^{-1} hematite or goethite suspension onto the crystal (Rubasinghege et al., 2010). The mineral suspension was allowed to partially dry, after which the crystal was placed under vacuum (~0.2 atm) for 8-15 minutes to increase contact between the iron oxide particles and the crystal (Beattie et al., 2008). The mineral coated crystal was rinsed with deoxygenated deionized water at least 5 times to remove particles not well adhered to the crystal. Most solids remained adhered to the cell post washing. The resulting layer thickness was estimated to be less than 1.7 μm and 2.4 μm for hematite and goethite, respectively, assuming a film with 60% porosity (Hug, 1997). The evanescent wave penetration depth (d_p, the depth at which 63% of the electric field has decayed) at 1200 cm^{-1} is ~0.86 μm for a ZnSe HATR crystal coated with water, therefore the actual depth sampled ($d_s=3\times d_p$) for a ZnSe HATR crystal coated with an iron oxide, which has a higher refractive index than water, is greater than 2.6 μm (Tickanen et al., 1991; Lefèvre, 2004). The spectra obtained in these experiments thus likely sampled the entire solid layer, including species adsorbed to the mineral surface.

All spectra for the hematite experiments were referenced to a background consisting of the hematite coated crystal equilibrated with 10^{-2} M NaCl at pH 7.00. The goethite spectra were processed differently, as the sulfate and phosphate IR regions were affected by the strong goethite –OH stretching bands between 800 and 900 cm^{-1}. The goethite spectra were referenced against a background of deoxygenated deionized water; a spectrum of the goethite coated crystal equilibrated with 10^{-2} M NaCl at pH 7.00 was subtracted from the experimental spectra with the subtraction factor, as has been done in previous work (Persson and Lövgren, 1996; Liger et al., 1999), consistently between 0.95 and 1.05. All spectra (background and sample) were collected by sealing the ports on the flow through cell, heat sealing the cell in a polyethylene bag,

transferring the cell from the anaerobic chamber to the ATR-FTIR spectrometer, and removing the sealed flow through cell from the polyethylene bag immediately prior to analysis. Both background and sample spectra were obtained as the average of 2000 scans with a 4 cm^{-1} resolution, requiring approximately one hour of analysis time. Once the spectrum for the hematite or goethite coated crystal equilibrated with the 10^{-2} M NaCl solution was collected, the cell was returned to the anaerobic chamber and equilibrated for a minimum of 5 hours with a 10^{-2} M NaCl and 4 μM phosphate or 50 μM sulfate solution at pH 7.00 using a flow rate of 0.5 mL min^{-1}. After collecting the spectrum, the cell was returned to the anaerobic chamber and equilibrated with a solution with the same conditions as the initial experiments, but with the addition of 4 μM Fe(II) (for the phosphate system) or 50 μM Fe(II) (for the sulfate system) while maintaining the same mineral coating. The procedure was repeated for the final set of conditions with higher Fe(II) concentrations: 400 μM Fe(II) (for the phosphate system) or 500 μM Fe(II) (for the sulfate system). The phosphate, sulfate, and Fe(II) concentrations were chosen based on the equilibrium concentrations at pH 7.0 for the 0.1 mM oxoanion macroscopic adsorption experiments, and were undersaturated with respect to secondary mineral phases containing Fe(II) and the oxoanions (e.g., vivianite).

Additional IR experiments were conducted with goethite and hematite reacted with higher phosphate or sulfate concentrations (16 μM phosphate or 200 μM sulfate) following the same procedure, including the collection of a background spectrum with a fresh mineral coating and the initial equilibration and collection of an IR spectrum with 4 μM phosphate or 50 μM sulfate. Experiments conducted with different mineral coatings cannot be directly compared on the same absorbance scale, due to the potential for deviations in the degree of contact between the mineral and the ZnSe HATR crystal and the amount of mineral surface area between mineral

coatings. Instead, experiments with different mineral coatings can be compared by changes in their difference spectra, normalized absorbance, and their band positions and relative areas, as has been discussed in previous studies (Beattie et al., 2008).

An IR spectrum of synthetic vivianite was also collected for reference. Vivianite was synthesized in the anaerobic chamber following the procedure outlined in Eynard et al. (1992), at pH 6 with a Fe(II) to KOH ratio of 1:1. After drying, the vivianite was ground with an agate mortar and pestle, distributed across the ZnSe HATR crystal, and an IR spectrum was collected following the procedures described above to maintain anaerobic conditions. The spectrum was referenced against a background of the blank ZnSe crystal. An XRD pattern of the synthesized vivianite was also collected for phase identification using a sealed XRD slide to prevent Fe(II) oxidation (Bruker D8 Advance powder X-ray diffractometer using Cu Kα radiation).

The final FTIR spectra were baseline corrected following previously published protocols (Tejedor-Tejedor and Anderson, 1990; Peak et al., 1999; Elzinga and Sparks, 2007) using OMNIC software (Thermo Scientific^{TM}). Normalized FTIR spectra were obtained by ratioing the spectra to the highest absorbance in the region of interest. Gaussians were fit to the absorbance spectra using the least squares fitting routine in the program SIXPack (Webb, 2005); peak positions were allowed to vary. Spectral subtractions for the difference spectra were obtained by subtracting the original spectra (i.e., not normalized spectra) from one another. These difference spectra isolate the contributions of the complexes that adsorb upon addition of Fe(II), assuming that no complexes desorb.

2.3.5. Surface Complexation Modeling

A SCM was developed for Fe(II), phosphate, and sulfate adsorption onto goethite. A

diffuse double-layer (DDL) model (Dzombak and Morel, 1990) was implemented in MINEQL+ 4.6 (Schecher and McAvoy, 2007). This model incorporated the surface acid-base reactions of goethite, adsorption reactions of Fe(II), phosphate, and sulfate to form binary (i.e., one sorbate and one surface site) surface complexes, and adsorption to form ternary Fe(II)-oxoanion-goethite surface complexes. The full equilibrium model also included relevant precipitation reactions and aqueous acid-base and complexation reactions (Table A2.1).

The SCM was developed by first setting the surface reactions and properties of goethite. The surface acid-base equilibrium constants were taken from Mathur and Dzombak (2006) and modified to account for differences in specific surface areas and site densities through the approach described by Sverjensky (2003). A wide range of goethite site densities (2.3 - 8.0 sites nm^{-2}) has been reported in literature (Villalobos et al., 2003); crystallographic calculations of surface hydroxyl groups on goethite yield approximately 3 sites nm^{-2} (Sposito, 1989). Lützenkirchen et al. (2002) suggested a lower bound of the goethite site density of 2.5 sites nm^{-2}, and this value was found to successfully fit all the data in this study. The 1.0 mM phosphate data suggested surface site saturation (with a maximum of 30% phosphate adsorbing), and these data were consistent with a site density of 2.5 sites nm^{-2}. If the complete uptake of 1.0 mM Fe(II) at neutral pH is solely attributed to adsorption, then a site density ≥ 3.7 sites nm^{-2} would have been required. However, such a high site density consistently led to overestimation of phosphate adsorption, and the loss of Fe(II) from solution in experiments with 1.0 mM total Fe(II) can be partially attributed to the precipitation of Fe(II) as $Fe(OH)_2(s)$ in addition to adsorption.

In the second step, Fe(II), phosphate, and sulfate adsorption in isolation were simulated to identify the surface reactions and equilibrium constants needed in the model. Fe(II) adsorption was modeled using two Fe(II) surface complexes [$(FeO)Fe^+$ and (FeO)FeOH] with

stoichiometries that have been used in modeling the adsorption of Fe(II) (Liger et al., 1999) and other divalent cations to goethite (Mathur and Dzombak, 2006). For sulfate adsorption, surface complexes were selected based on prior modeling and IR spectroscopy studies, which indicate that sulfate adsorbs as a mixture of inner- and outer-sphere complexes on goethite (Peak et al., 1999; Peak et al., 2001; Zhang and Peak, 2007; Fukushi and Sverjensky, 2007; Beattie et al., 2008). A deprotonated monodentate inner-sphere sulfate surface complex with the same stoichiometry used in Xu et al. (2006) and Fukushi and Sverjensky (2007) was included. An outer-sphere sulfate species was selected to have a bidentate configuration similar to that studied computationally by Paul et al. (2006) and employed by Fukushi and Sverjensky (2007). The charge state of this outer-sphere complex was altered to best match the current macroscopic adsorption data. The phosphate surface complexation reactions were selected based on the study of Kanematsu et al. (2010). The values of the equilibrium constants for these reactions that provided the optimal fits to the adsorption percentage data with the minimal residual sum of squares were identified by systematically performing multiple forward calculations of the models. A grid-search approach was followed to find the best fit when multiple combinations of equilibrium constants were involved.

After constraining the surface complex equilibrium constants and reactions for Fe(II), phosphate, and sulfate in isolation, the model was applied to the coadsorption experiments using the combined set of binary surface complexation reactions. This combined model accounted for the competition between the Fe(II) and the oxoanions for surface sites, possible precipitation of the Fe(II)-phosphate mineral vivianite, and electrostatic interactions that may alter the thermodynamic driving forces of the surface complexation reactions. Ternary surface complexation reactions were then incorporated in the model to examine if their inclusion could

improve the fit of the model to the experimental data. In the present study, the ternary surface complexes were modeled as bidentate binuclear phosphate (or sulfate) bridging structures, with the specific surface complex selected based on the best fit to the macroscopic data. With the equilibrium constants for the binary surface complexation reactions kept constant at this stage, the optimized equilibrium constants for the ternary surface complexes were obtained by performing multiple forward calculations (Table 2.1; Figure A2.1). To enable the application of the present models to other conditions with different goethite concentrations, site densities and specific surface areas, the MINEQL input molar-based constants (K^0) were converted to the site occupancy based equilibrium constants (K^θ) using the corrections proposed by Sverjensky (2003).

2.4. RESULTS AND DISCUSSION

2.4.1. Macroscopic Sorption

Fe(II) enhances sulfate adsorption onto hematite and goethite at circumneutral pH (Figure 2.1). This effect is less substantial at high (1.0 mM) sulfate concentrations and on hematite compared to goethite. The effects of Fe(II) on phosphate adsorption are more limited because of the nearly complete phosphate adsorption in systems containing 0.1 mM initial phosphate (Figure 2.2). At 1.0 mM initial phosphate some enhancement in adsorption is seen upon addition of Fe(II), but at the higher Fe(II) concentration a large increase in phosphate uptake occurs above pH 6 that is more consistent with the precipitation of an Fe(II)-phosphate solid, e.g., vivianite.

Coadsorption with oxoanions also enhances the sorption of Fe(II) onto hematite and goethite. Fe(II) adsorption increases in the presence of sulfate at circumneutral pH (Figure 2.3); this effect is more substantial on goethite than on hematite. Similarly, the addition of phosphate

enhances Fe(II) adsorption onto both hematite and goethite between pH 4 and 8. For hematite, the effect of phosphate on Fe(II) adsorption is greater than that of sulfate, but the oxoanions enhance Fe(II) adsorption similarly on goethite (Figure 2.4). For the highest phosphate and Fe(II) concentrations a sharp rise in sorption of both species is observed at pH > 6 (Figures 2.2,2.4). The simultaneous and sharp increase in phosphate and aqueous Fe(II) sorption suggests that a secondary ferrous phosphate mineral precipitated. In fact, vivianite saturation index (SI) calculations for the goethite experiment samples with an initial 1.0 mM phosphate and 1.0 mM Fe(II) (Table A2.2) show that the suspensions at pH ≤ 5.5 are undersaturated, while those at pH ≥ 6 are supersaturated with respect to vivianite. The XRD patterns of goethite and hematite reacted with 1.0 mM phosphate and 1.0 mM Fe(II) at pH 6.5 both show a clear peak near 13.2^{o} 2θ, corresponding to the (020) reflection of vivianite, $Fe_3(PO_4)_2 \cdot 8H_2O$ (Figure A2.2).

2.4.2. Oxoanion Adsorption Mechanisms

Sulfate and Fe(II) Adsorption Mechanisms on Hematite

The IR spectra of sulfate adsorbed onto hematite show increased absorbance with the addition of Fe(II), indicating greater surface coverage, consistent with the observed macroscopic adsorption behavior of sulfate (Figure 2.5). Previous studies have provided detailed overviews of the IR active bands and symmetry arguments that are used to interpret adsorbed sulfate IR spectra (Hug, 1997; Peak et al., 1999). The IR spectrum for 50 μM sulfate adsorbed onto hematite (Figure 2.5a) requires four Gaussians to fit the data (Table 2.2), in close agreement with those reported by Paul et al. (2005), who attributed the bands as belonging to a sulfate complex with C_{2v} symmetry (e.g., monodentate bisulfate, bidentate binuclear, or bidentate mononuclear sulfate). Based on the symmetry arguments discussed in past studies (Hug, 1997; Peak et al.,

1999; Paul et al., 2005), the sulfate IR spectrum presented here is consistent with an H-bonded or an inner-sphere surface complex with C_{2v} symmetry.

The area of each band increases with increasing aqueous Fe(II) concentrations, except for the band centered at ~1066 cm^{-1}. The relative areas of the ~1116, 1033, and 978 cm^{-1} bands were consistently 1.0:0.2:0.03. Increasing sulfate concentrations to 200 μM sulfate produces an IR spectrum distinct from both the 50 - 0 and the 500 - 50 μM Fe(II) difference spectra (Figure 2.5). The distinct spectral changes induced by increasing sulfate and adding Fe(II) and the anomalous behavior of the band at ~1066 cm^{-1} indicate one of two scenarios: (1) that a portion of the C_{2v} symmetric sulfate surface species are forming ternary complexes with Fe(II) without affecting the relative areas of three of the bands, or (2) that two inner-sphere complexes are initially present and 50 μM Fe(II) alters their relative concentrations, causing one complex to desorb but the other to increase adsorption.

Sulfate and Fe(II) Adsorption Mechanisms on Goethite

Sulfate-Fe(II) interactions on goethite surfaces are similarly complex. Four Gaussians are required to fit the IR spectrum of 50 μM sulfate adsorbed onto goethite at pH 7 (Table 2.2; Figure 2.6a). The bands at 1120 and 979 cm^{-1} (Figure 2.6a) are consistent with outer-sphere sulfate (Persson and Lövgren, 1996; Peak et al., 1999; Zhang and Peak, 2007; Beattie et al., 2008), while the bands at 1073 cm^{-1} and 1004 cm^{-1} are indicative of an inner-sphere complex (Peak et al., 2001; Zhang and Peak, 2007) with C_{2v} symmetry [only C_{2v} complexes induce substantial shifts (~30 cm^{-1}) in the v_1 band position (Hezel and Ross, 1968)]. Sulfate thus adsorbs onto goethite at pH 7 as a mixture of outer-sphere sulfate and an inner-sphere or H-bonded outer-sphere sulfate complex with C_{2v} symmetry.

Analogous to hematite, the addition of Fe(II) increases sulfate IR absorbance (Figure 2.6a). Increasing Fe(II) shifts the C_{2v} band positions, while the outer-sphere sulfate bands remain relatively stable (Table 2.2). The peak areas increase with increasing aqueous Fe(II), with the exception of the band at ~1066 cm^{-1}, which is largely unchanged in the presence of 50 μM Fe(II) and decreases by ~30% with 500 μM Fe(II). The band at ~1010 cm^{-1}, conversely, increases substantially relative to the other bands in the presence of Fe(II). The differing behaviors of the bands associated with the inner-sphere or H-bonded C_{2v} symmetric complex at ~1066 cm^{-1} and ~1010 cm^{-1} suggests that Fe(II) alters the adsorption behavior of the C_{2v} complex or that the two bands are associated with two different complexes that desorb or are promoted, respectively, by aqueous Fe(II).

The difference spectra (Figure 2.6c) also show that Fe(II) increases the bands at ~1115 cm^{-1} and ~1015 cm^{-1}, but causes a decrease in the band at ~1066 cm^{-1}, similar to the changes observed for Cd-sulfate ternary complexation on goethite (Zhang and Peak, 2007). These changes differ from those induced by increasing the sulfate concentration 200 μM sulfate (Figures 2.6a,c), which produces an IR spectrum with inner-sphere or H-bonded sulfate bands at positions different from the bands that appear in the 50 μM sulfate-Fe(II)-goethite system (Table 2.2). The 200 - 50 μM sulfate difference spectrum makes clear that the additional sulfate surface complexes that adsorb due to increased equilibrium sulfate concentrations are not the same complexes that adsorb in the presence of aqueous Fe(II). IR experiments have indicated that aqueous Fe(II) does not specifically interact with aqueous sulfate (Majzlan and Myneni, 2005), thus outer-sphere Fe(II)-sulfate ternary complexes are not likely and cannot be responsible for the spectral changes induced by Fe(II). These results indicate that aqueous Fe(II) increases outer-sphere sulfate adsorption through electrostatic interactions and also either forms a ternary

complex with sulfate or increases the adsorption of an inner-sphere or H-bonded sulfate surface complex with C_{2v} symmetry while causing another inner-sphere complex to desorb from goethite.

Phosphate and Fe(II) Adsorption Mechanisms on Hematite

Phosphate IR absorbance also increases for hematite upon addition of aqueous Fe(II) (Figure 2.7), consistent with the macroscopic phosphate adsorption data (Figure 2.2). The vivianite IR spectrum (Figure A2.3) is clearly distinct from the IR spectra of phosphate adsorbed onto hematite and goethite (Figures 2.7,2.8) in the presence of Fe(II), confirming that the conditions investigated do not induce precipitation. Comprehensive summaries of phosphate IR spectral interpretations can be found in Elzinga and Sparks (2007) and Tejedor-Tejedor and Anderson (1990), among others. FTIR spectra cannot distinguish changes in arsenate symmetry from protonation versus surface complexation to an iron oxide (Myneni et al., 1998) and it is likely that FTIR spectroscopy is similarly ambiguous for phosphate. The interpretations of phosphate coordination are thus based on past D_2O studies when possible, as these studies can differentiate between protonation and surficial Fe complexation.

Six bands are required to adequately fit the IR spectrum of 4 μM phosphate adsorbed onto hematite (Table 2.2; Figure 2.7). This fit is consistent with previous studies that identified both a monodentate monoprotonated complex [$(FeO)PO_2(OH)$] (Elzinga and Sparks, 2007) and a bidentate monoprotonated [$(FeO)_2PO(OH)$] complex (Elzinga and Kretzschmar, 2013) on hematite surfaces at circumneutral pH. Two distinct bands at 980 and 950 cm^{-1} associated with the $(FeO)_2PO(OH)$ and $(FeO)PO_2(OH)$ complexes, respectively, could not be fit to the spectrum in this study, which instead required one band at 972 cm^{-1}. Previous research has shown that not

all bands associated with all surface species present can be fit to the spectra of phosphate adsorbed at circumneutral pH due to spectral overlap (Arai and Sparks, 2001; Luengo et al., 2006; Elzinga and Sparks, 2007).

The spectral fits (Table 2.2) show that every band increases in area with increasing aqueous Fe(II). The relative areas of the ~1083 and 1046 cm^{-1} bands are consistently 1.0:0.3 across all experiments, confirming that these bands are indicative of the same complex [$(FeO)PO_2(OH)$]. The apparent decrease in the normalized ~1046 cm^{-1} band (Figure 2.7b) is due to an increase in the ~1119 cm^{-1} band, which increases the apparent peak height of the overall spectrum, affecting the normalization. The $(FeO)_2PO(OH)$ band centered at ~1119 cm^{-1}, commonly attributed to ν(P=O), shifts to higher wavenumbers with Fe(II) (1115 cm^{-1}-1122 cm^{-1}). This band, however, is weak in the Fe(II)-free spectrum and there is thus a large uncertainty in that band position.

Difference spectra (Figure 2.7c) also indicate that Fe(II) promotes the adsorption of both phosphate surface species, although the $(FeO)PO_2(OH)$ complex continues to be the dominant surface species. The spectral changes observed with Fe(II) (in both the IR and the difference spectra) are different than those associated with a higher phosphate coverage as observed in this study and in previous research (Elzinga and Sparks, 2007; Tejedor-Tejedor and Anderson, 1990). The 16 - 4 μM phosphate difference spectrum (Figure 2.7c) shows that adsorption of the $(FeO)_2PO(OH)$ complex is enhanced less than when 400 μM Fe(II) is added. In addition, the band at 1115 cm^{-1} does not shift in position when equilibrium phosphate concentration is increased to 16 μM (Table 2.2). These measurements suggest that aqueous Fe(II) specifically affects the adsorption of the $(FeO)_2PO(OH)$ species, potentially through the formation of a ternary complex.

Phosphate and Fe(II) Adsorption Mechanisms on Goethite

The spectra of phosphate adsorbed onto goethite (Figure 2.8) show similar bands as those observed for phosphate adsorbed onto hematite, although bands below 940 cm^{-1} are obscured by the strong goethite –OH stretching bands. The observed bands in the goethite 4 μM phosphate spectrum (Figure 2.8a) are in agreement with Luengo et al. (2006), which found that phosphate adsorbed onto goethite at pH 7.5-9 exhibits IR bands corresponding to two different complexes. Bands centered at ~1090, 1045, and 950 cm^{-1} have often been interpreted in iron oxide systems as coming from a nonprotonated bidentate phosphate complex [$(FeO)_2PO_2$] (Tejedor-Tejedor and Anderson, 1990; Arai and Sparks, 2001; Luengo et al., 2006), but recent D_2O studies of phosphate adsorbed onto hematite interpreted those three bands as belonging to the $(FeO)PO_2(OH)$ complex (Elzinga and Sparks, 2007). To maintain consistency with our phosphate-hematite results, which also exhibit bands at similar positions, we assign the bands at 1089, 1046, and 951 cm^{-1} to the $(FeO)PO_2(OH)$ complex identified by Elzinga and Sparks (2007). The band centered at 1037 cm^{-1} in this study is indicative of the presence of an inner-sphere or an outer-sphere H-bonded complex.

The addition of 4 μM aqueous Fe(II) leads to an increase in absorbance of all peaks and the appearance of a fifth band at 1127 cm^{-1} (Figure 2.8a). The addition of 400 μM Fe(II) increases the peak areas for all bands except those at ~1032 and 948 cm^{-1}. The relative peak areas for the ~1086 and 1045 cm^{-1} bands are consistently 1.00:0.34, respectively, for all spectra, confirming that these bands are representative of the same complex [$(FeO)PO_2(OH)$]. No clear correlation in intensities is observed for the other bands.

The difference spectra (Figure 2.8c) are consistent with the spectral fits (Figure 2.8a),

confirming that another phosphate surface species (band ~1121 cm^{-1}) forms and that every band increases in IR absorbance upon Fe(II) addition, except the ~1032 cm^{-1} band in the presence of 400 μM Fe(II). The difference spectra are clearly distinct from the 16 μM phosphate IR spectrum (Figure 2.8a), which shows an increase in the ~1032 cm^{-1} band and no detectable band at ~1124 cm^{-1} (Table 2.2). The lack of a band at ~948 cm^{-1} in the 16 μM phosphate IR spectrum and fit (Table 2.2; Figure 2.8a) is likely due to the processing issues associated with OH bands in goethite as described by Luengo et al. (2006) rather than an actual absence of that band.

Previous studies have demonstrated that increasing phosphate loading can also shift the dominant adsorbing phosphate species to the $(FeO)_2PO(OH)$ complex, which exhibits IR bands of roughly equal intensity at ~1120-1128 and 1004-1010 cm^{-1} and a weaker band at ~975-988 cm^{-1} (Tejedor-Tejedor and Anderson, 1990; Luengo et al., 2006). While the appearance of the band at ~1124 cm^{-1} in our spectra is consistent with one of the bands associated with the $(FeO)_2PO(OH)$ complex, our difference spectra clearly show that the two other $(FeO)_2PO(OH)$ bands centered at ~1004-1010 and 975-988 cm^{-1} do not appear upon Fe(II) addition. These results thus indicate that Fe(II) leads to the formation of a new phosphate surface species, likely a ternary complex with Fe(II), and promotes the adsorption of two preexisting phosphate surface species [$(FeO)PO_2(OH)$ and the complex with the band at ~1032 cm^{-1}].

2.4.3. Predicted Oxoanion and Fe(II) Behavior by Surface Complexation Models

The SCM provides additional support for the formation of Fe(II)-oxoanion ternary complexes on Fe(III) oxide surfaces. Given the similarities between goethite and hematite in the macroscopic adsorption experiments, it is anticipated that the processes identified for goethite are similar to those occurring in the hematite system. Due to the limited additional insight and

the substantial extra effort involved in developing another model for the hematite system, only the goethite system was subject to modeling. The surface complexes used in the SCM are largely consistent with the species identified in the goethite IR measurements. The relative predominance of the individual surface complexes over the pH range simulated by the present model is also consistent with previous studies (Liger et al., 1999; Kanematsu et al., 2010). In this study, the positively charged Fe(II) surface complex [$(FeO)Fe^{+}$] is predicted to dominate at lower pH, and the neutral Fe(II) surface complex [(FeO)FeOH] emerges at higher pH and higher surface coverage (Figures A2.4,A2.5). For 1.0 mM initial Fe(II), $Fe(OH)_2(s)$ is predicted to precipitate at pH > 8.2. Green rust [e.g., chloride green rust, $Fe(II)_3Fe(III)(OH)_8Cl(s)$] might also be supersaturated under some conditions, but it was not seen in solid characterizations (not shown) and its inclusion did not improve the fitting of the model to the adsorption data. However, the model accurately predicts the precipitation of vivianite with 1.0 mM initial Fe(II) and 1.0 mM phosphate at pH > 5.8 (Figure A2.4). The possibility that phosphate might react with the Fe(III) released from goethite or hematite, forming Fe(III)-phosphate precipitates (e.g., strengite) was considered; strengite precipitation could have interfered with our modeling interpretation of phosphate adsorption data. However, careful examinations based on equilibrium calculations excluded this possibility (details included in the Appendix).

Based on the reaction frameworks developed individually for Fe(II) and the oxoanions in isolation, electrostatic interactions can only partially account for the promotional effect of oxoanions on Fe(II) adsorption to goethite. The 0.1 mM Fe(II) and 1.0 mM oxoanion experiments illustrate the importance of ternary complexes in the coadsorption systems (Figures 2.9,2.10). The ternary complex-free model accurately predicts the Fe(II) adsorption edge shift to lower pH upon addition of 1.0 mM oxoanion and was able to fit the data above pH 6. However,

below pH 6 the ternary complex-free model still underestimates Fe(II) adsorption. The addition of ternary complexes to the model substantially improves the SCM fits of the data. These phenomena are similar for both phosphate and sulfate systems, while the extent of underestimation by the ternary complex-free model is larger for the phosphate system. These results are consistent with the FTIR spectral results, both indicating the presence of Fe(II)-oxoanion ternary complexes.

2.4.4. Comparison to Prior Studies of Oxoanion-Cation Surface Interactions

A number of studies have found that sulfate enhances divalent cation adsorption onto iron oxides (Balistrieri and Murray, 1982; Hoins, 1993; Ali and Dzombak, 1996; Ostergren et al., 2000; Swedlund and Webster, 2001; Juang and Wu, 2002; Swedlund et al., 2003; Zhang and Peak, 2007; Swedlund et al., 2009). These studies all demonstrated a shift in the cation adsorption edge to lower pH by roughly 0.5 units, similar to what was observed for Fe(II) in the present study (Figure 2.3). One prior study observed a more substantial effect of sulfate on Fe(II) adsorption to hematite (Jeon et al., 2001), with the adsorption edge shifting 2 pH units lower. This clearly contrasts with the present measurements and the much smaller shift in divalent cation adsorption edges upon sulfate addition seen in a wide array of prior studies. The origin of the discrepancy between the present study and that of Jeon et al. (2001) are not clear, but it should be noted that major sources of potential artifacts in experiments involving Fe(II) are associated with oxidation by trace levels of O_2. Such errors would lead to greater apparent Fe sorption because of the lower solubility of Fe(III).

FTIR spectroscopic studies have shown that sulfate adsorbs onto iron oxides as both outer- and inner-sphere complexes (Lefèvre, 2004), which is consistent with the observations of

this current study. Here, we found that sulfate adsorbs onto goethite at pH 7 through a mixture of outer-sphere and H-bonded or inner-sphere complexes, while no outer-sphere sulfate complexes were observed in the hematite system. The inner-sphere or H-bonded surface species in both the hematite and goethite systems has a C_{2v} symmetry (e.g., bidentate structure) if there is only one inner-sphere or H-bonded sulfate complex initially present. The C_{2v} symmetry of the inner-sphere or H-bonded sulfate surface complex is in agreement with several sulfate adsorption studies, including FTIR (Paul et al., 2005) and total internal reflectance-Raman (Jubb et al., 2013) spectroscopic studies of hematite, a FTIR study of goethite (Peak et al., 1999), and a recent XAFS and FTIR spectroscopic study of sulfate adsorption onto ferrihydrite (Zhu et al., 2014).

Although sulfate adsorption mechanisms differ, the current study found evidence for similar Fe(II)-sulfate interactions on hematite and goethite. Fe(II) promotes outer-sphere sulfate adsorption onto goethite through electrostatic interactions as well as inner-sphere or H-bonded surface complex formation through ternary complexation. Addition of Fe(II) also promotes inner-sphere or H-bonded sulfate adsorption onto hematite, likely through ternary complexation. Interestingly, the inner-sphere sulfate IR band at ~1063 cm^{-1} in both mineral systems behaves anomalously relative to the other bands (decreasing in peak area with Fe(II) while others increase), indicating that this band is affected through ternary complexation with Fe(II) or represents a second inner-sphere or H-bonded surface species that desorbs in the presence of Fe(II). These results are largely consistent with previous studies that observed that sulfate forms ternary complexes with Pb(II) and Cd(II) on goethite surfaces (Ostergren et al., 2000; Elzinga et al., 2001; Zhang and Peak, 2007).

Similar to sulfate, phosphate adsorption behavior differs slightly on hematite and goethite

surfaces. Here, phosphate was found to adsorb onto hematite and goethite through a mixture of two inner-sphere surface complexes. The dominant adsorbed species in both the hematite and goethite systems is a monodentate monoprotonated surface complex [$(FeO)PO_2(OH)$] with bands at ~1085 and 1046 cm^{-1} and similar band area ratios in both systems (1.0:0.3 and 1.00:0.34, respectively), consistent with the findings of a recent D_2O study of phosphate adsorbed onto hematite (Elzinga and Sparks, 2007). The additional phosphate surface complex adsorbed onto hematite, a bidentate complex [$(FeO)_2PO(OH)$], has also been observed previously (Elzinga and Kretzschmar, 2013). The additional surface complex adsorbed onto goethite, however, cannot be conclusively identified; this issue has been discussed in a previous study (Luengo et al., 2006).

Consistent with our macroscopic adsorption experiments, phosphate has typically been observed to increase the adsorption of divalent cations on iron oxide surfaces (Diaz-Barrientos et al., 1990; Madrid et al., 1991; Venema et al., 1997; Collins et al., 1999). In this study, phosphate and Fe(II) were found to cooperatively adsorb, with both species enhancing one another's adsorption. Although the $(FeO)PO_2(OH)$ complex remains the dominant adsorbed phosphate molecular configuration for both hematite and goethite systems with the addition of Fe(II), the FTIR difference spectra show that the surface species affected by Fe(II) (e.g., $(FeO)_2PO(OH)$ and the species with the band at ~1124 cm^{-1} in the hematite and goethite systems, respectively) increase substantially. Increases in phosphate adsorption have also been observed in FTIR studies with the addition of Cd(II) on hematite surfaces (Elzinga and Kretzschmar, 2013), and Ca(II) on TiO_2 surfaces (Ronson and McQuillan, 2002). A recent FTIR spectroscopic study has shown that Cd(II)-phosphate interactions on hematite involve ternary complexation (Elzinga and Kretzschmar, 2013). XAFS spectroscopy, however, has shown that phosphate does not form ternary complexes with Cd(II) on goethite surfaces (Collins et al., 1999). In this study, the

appearance of a new band in the goethite system and a possible shift of a band associated with the bidentate surface complex in the hematite system with the addition of Fe(II) indicates the formation of an Fe(II)-phosphate-iron oxide ternary complex. Although weak lateral interactions between adsorbed Fe(II) and adsorbed oxoanions may also give rise to the observed changes in oxoanion FTIR spectra, the SCM results support the conclusion that oxoanions interact with Fe(II) on iron oxide surfaces through combined electrostatic interactions and ternary complexation.

2.4.5. Nature of Adsorbed Fe(II) and Implications for ET-AE Processes

Although recent studies have shown that aqueous Fe(II) oxidizes and undergoes atom exchange upon adsorption onto Fe(III) oxide surfaces (Williams and Scherer, 2004; Crosby et al., 2005; Handler et al., 2009), aqueous Fe(II) behaves macroscopically as an adsorbing divalent cation. Previous research has shown that Fe(II) adsorption increases with increasing pH like most divalent cations, and Fe(II) adsorbs more strongly onto goethite than hematite (Liger et al., 1999), consistent with our results. In addition, Fe(II) shows competitive adsorption effects, with its adsorption suppressed in the presence of other cations, e.g., Co(II), Cd(II), Ni(II), and Zn(II) (Jeon et al., 2003) and its presence reducing the adsorption of Ni(II) (Frierdich et al., 2011). The present study further demonstrates that Fe(II) macroscopically behaves like an adsorbing divalent cation, with sulfate and phosphate promoting its adsorption through ternary complexation. This is confirmed by the spectroscopic measurements, which demonstrate that the effects of Fe(II) on sulfate and phosphate adsorption mechanisms are similar to those of other divalent cations. Such molecular-scale interactions suggests that unoxidized Fe(II) participates in interfacial reactions at iron oxide surfaces.

The results of this study further indicate that phosphate and sulfate may affect ET-AE reactions. Enhanced Fe(II) adsorption by electrostatic interactions, as indicated by the SCM results and the sulfate-goethite FTIR experiments, may increase the amount of Fe(II) undergoing oxidative adsorption at the surface, and thereby promote ET-AE reactions. Ternary complexation with oxoanions also increases the Fe(II) surface coverage, which may enhance ET-AE processes, but such binding may also stabilize Fe(II) on the surface, inhibiting ET-AE. Recent research suggests that phosphate slightly enhances the rate and extent of atom exchange between Fe(II) and goethite at pH 7.5 (Latta et al., 2012), although further work is needed to determine whether electron transfer processes are altered. The effects of sulfate on such reactions are currently unclear.

Oxoanions may also impact numerous processes caused by ET-AE reactions at redox interfaces. For example, ET-AE reactions promote continued Fe(III) oxide recrystallization, which leads to the incorporation of adsorbed metal cations into Fe(III) oxides as well as the release of preincorporated metal cations back to solution (Frierdich et al., 2011); the rate of Fe(II)-catalyzed metal release is proportional to the Fe(II) surface coverage (Frierdich and Catalano, 2012). Because Fe(II) behaves both macroscopically and molecularly as an adsorbing divalent cation in the presence of sulfate and phosphate, predicting the effects of these oxoanions on Fe(II)-catalyzed trace metal repartitioning may not require the specific consideration of electron transfer processes. The impact of these oxoanions may be well described solely by their macroscopic co-adsorption behavior with Fe(II).

The present work also suggests that the effects of sulfate and phosphate on Fe(II)-catalyzed mineral recrystallization and trace metal repartitioning differ for distinct oxoanion-mineral systems. The FTIR results indicate that sulfate and phosphate enhance Fe(II) surface

coverage and alter Fe(II) adsorption behavior by mechanisms that depend on both the oxoanion and mineral identity. For example, the FTIR spectra do not provide any evidence of the formation of a bidentate phosphate surface species on goethite at pH 7, while Fe(II) specifically interacts with the bidentate $(FeO)_2PO(OH)$ surface species on hematite. Such phosphate surface complexes may block steps and kinks and other reactive surface sites commonly involved in iron oxide recrystallization processes (Bondietti et al., 1993; Stumm, 1997). Therefore, phosphate may affect Fe(II)-catalyzed mineral recrystallization and associated processes differently in the goethite and hematite systems. This study demonstrates the complex relationship between oxoanion-cation-mineral surface interactions that may occur at redox interfaces. A fundamental understanding of these interactions is necessary to predict how these common aqueous oxoanions alter important processes affecting mineral stability, nutrient bioavailability, and contaminant sequestration.

2.5 ACKNOWLEDGMENTS

This project was supported by the U.S. National Science Foundation (NSF), Division of Earth Sciences, Geobiology and Low-temperature Geochemistry Program through award no. EAR-1056480. ICP-OES data was collected at the Nano Research Facility at Washington University in St. Louis, supported by the NSF through award no. ECS-0335765. Use of the Bruker D8 Advance X-ray diffractometer at Washington University in St. Louis was supported by the NSF through award no. EAR-1161543. ATR-FTIR spectra were obtained using the instrumentation and resources of the Jens Environmental Molecular and Nanoscale Analysis Laboratory at Washington University in St. Louis. The authors would like to thank Kate Nelson for her assistance with obtaining ICP-OES measurements, Patty Wurm for support with data

collection, Alison Beehr for helpful discussions, and Yun Luo and Andrew Frierdich for advice on experimental procedures in the early stages of this study. Comments from Satish Myneni and two anonymous reviewers improved this manuscript.

Table 2.1 Equilibrium reactions and constants for surface species and precipitates.

Equilibrium Reactions	LogK^{0a}	LogK^{0b}	Reference
Goethite (de)protonation and Fe(II) adsorption			
$\equiv FeOH + H^+ \rightleftharpoons \equiv FeOH_2^+$	6.99	7.01	(Mathur and Dzombak, 2006)[c]
$\equiv FeOH \rightleftharpoons \equiv FeO^- + H^+$	−9.95	−9.92	(Mathur and Dzombak, 2006)[c]
$\equiv FeOH + Fe^{2+} \rightleftharpoons \equiv FeOFe^+ + H^+$	−1.02	−1.00	This study
$\equiv FeOH + Fe^{2+} + H_2O \rightleftharpoons \equiv FeOFeOH + 2H^+$	−11.3	−11.28	This study
Phosphate adsorption and P-Fe(II) ternary surface complex			
$2\equiv FeOH + 2H^+ + PO_4^{3-} \rightleftharpoons (\equiv FeO)_2PO_2^- + 2H_2O$	29.2	31.84	This study
$2\equiv FeOH + 3H^+ + PO_4^{3-} \rightleftharpoons (\equiv FeO)_2POOH + 2H_2O$	35.2	37.84	This study
$\equiv FeOH + H^+ + PO_4^{3-} \rightleftharpoons \equiv FeOPO_3^{2-} + H_2O$	19.95	19.98	This study
$2\equiv FeOH + H^+ + Fe^{2+} + PO_4^{3-} \rightleftharpoons (\equiv FeO)_2PO_2FeOH + H_2O$	28.8	31.44	This study
Sulfate adsorption and S-Fe(II) ternary surface complex			
$2\equiv FeOH + SO_4^{2-} \rightleftharpoons (\equiv FeOH)_2{:::}SO_4^{2-}$	4.56	7.20	This study[d]
$\equiv FeOH + SO_4^{2-} + H^+ \rightleftharpoons \equiv FeOSO_3^- + H_2O$	5.88	5.90	This study
$2\equiv FeOH + H^+ + Fe^{2+} + SO_4^{2-} \rightleftharpoons (\equiv FeO)_2SO_2FeOH^+ + H_2O$	17.5	20.14	This study
Solid precipitation			
$Fe^{2+} + 2H_2O \rightleftharpoons Fe(OH)_{2(s)} + 2H^+$	−12.9	N.A.	(Stumm and Lee, 1961)
$3Fe^{2+} + 2PO_4^{3-} + 8H_2O \rightleftharpoons Fe_3(PO_4)_2{\bullet}8H_2O_{(s)}$	33.04	N.A.	(Al-Borno and Tomson, 1994; Singer, 1972)

[a] Molar concentration based equilibrium constants, as input in MINEQL. These constants for surface reactions are corresponding to the site density ($N = 2.5$ sites nm^{-2}), specific surface area ($A = 42$ m^2 g^{-1}) and goethite concentration ($C_s = 4$ g L^{-1}).

[b] Equilibrium constants (K^{θ}) calculated based on the correction established by Sverjensky (2003). Note that the molar concentration based equilibrium constants as input in MINEQL are dependent on solid concentration for bidentate surface complexation reactions (Wang and Giammar, 2013).

[c] The goethite database compiled by Mathur and Dzombak was based on the specific conditions of $A = 60$ m^2 g^{-1} and $N = 2$ sites nm^{-2}. The adaption of their constants in the present study was subject to corrections for site density and specific surface area.

[d] The ::: symbol denotes outer-sphere adsorption, which was needed to produce a plausible reaction stoichiometry.

Table 2.2. Band positions (cm^{-1}) and areas determined from fits to the FTIR spectra.

Sample	Band 1		Band 2		Band 3		Band 4		Band 5		Band 6		R-factor
	Position	Area	Position	Area	Position	Area	Position	Area	Position	Area	Position	Area	
Hematite-Sulfate													
50 μM SO_4^{2-}, 0 μM Fe(II)	977	0.19	1036	1.1	1064	1.0	1117	6.0	-	-	-	-	2.0e-4
50 μM SO_4^{2-}, 50 μM Fe(II)	978	0.32	1030	1.7	1067	0.6	1115	9.3	-	-	-	-	7.4e-5
50 μM SO_4^{2-}, 500 μM Fe(II)	977	0.35	1032	2.6	1067	1.1	1117	13	-	-	-	-	4.4e-5
200 μM SO_4^{2-}, 0 μM Fe(II)	979	0.16	1017	0.8	1062	0.5	1114	4.2	-	-	-	-	3.5e-4
Goethite-Sulfate													
50 μM SO_4^{2-}, 0 μM Fe(II)	979	0.008	1004	0.01	1073	0.23	1120	0.6	-	-	-	-	7.3e-5
50 μM SO_4^{2-}, 50 μM Fe(II)	978	0.029	1007	0.04	1062	0.23	1118	1.0	-	-	-	-	4.7e-5
50 μM SO_4^{2-}, 500 μM Fe(II)	977	0.027	1018	0.11	1062	0.17	1118	1.6	-	-	-	-	1.4e-4
200 μM SO_4^{2-}, 0 μM Fe(II)	981	0.034	1024	0.06	1044	0.02	1104	0.8	1132	0.09	-	-	5.5e-5
Hematite-Phosphate													
4 μM PO_4^{3-}, 0 μM Fe(II)	916	0.3	972	1.6	1031	1.0	1046	0.6	1081	2.4	1115	0.4	3.2e-4
4 μM PO_4^{3-}, 4 μM Fe(II)	916	0.7	974	1.9	1029	1.5	1047	1.2	1083	4.4	1119	0.7	4.2e-4
4 μM PO_4^{3-}, 400 μM Fe(II)	918	1.3	973	2.2	1030	2.5	1047	1.4	1086	5.6	1122	1.8	6.1e-4
16 μM PO_4^{3-}, 0 μM Fe(II)	914	0.4	955	0.8	1032	3.6	1046	1.1	1086	2.5	1115	1.1	6.5e-4
Goethite-Phosphate													
4 μM PO_4^{3-}, 0 μM Fe(II)	951	0.0006	1037	0.12	1046	0.01	1089	0.04	-	-	-	-	8.1e-4
4 μM PO_4^{3-}, 4 μM Fe(II)	945	0.0029	1030	0.13	1044	0.07	1085	0.19	1127	0.014	-	-	2.0e-4
4 μM PO_4^{3-}, 400 μM Fe(II)	949	0.0027	1029	0.13	1045	0.09	1083	0.22	1120	0.054	-	-	3.0e-4
16 μM PO_4^{3-}, 0 μM Fe(II)	-	-	1022	0.15	1047	0.17	1087	0.47	-	-	-	-	5.0e-4

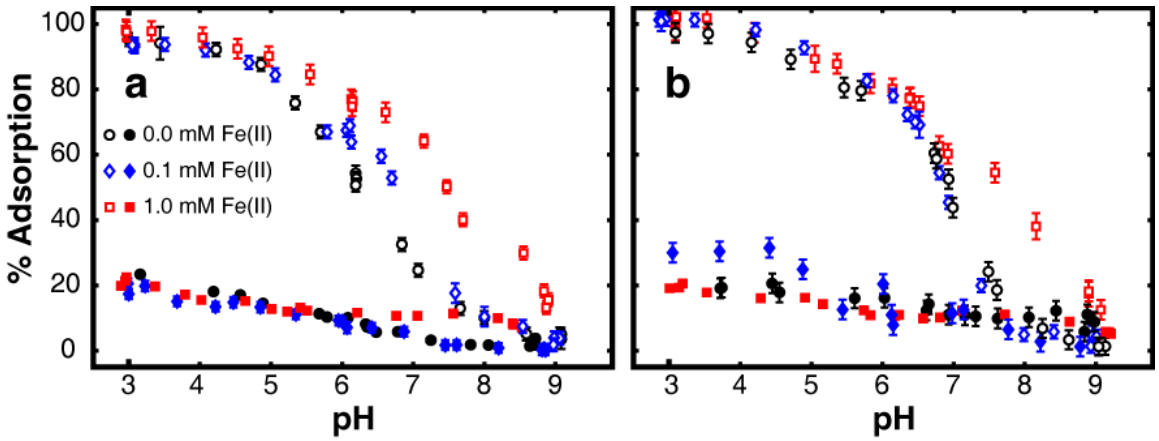

Figure 2.1. Sulfate sorption on (a) goethite and (b) hematite in the absence and presence of aqueous Fe(II), with 0.1 mM (open symbols) or 1.0 mM (filled symbols) initial sulfate.

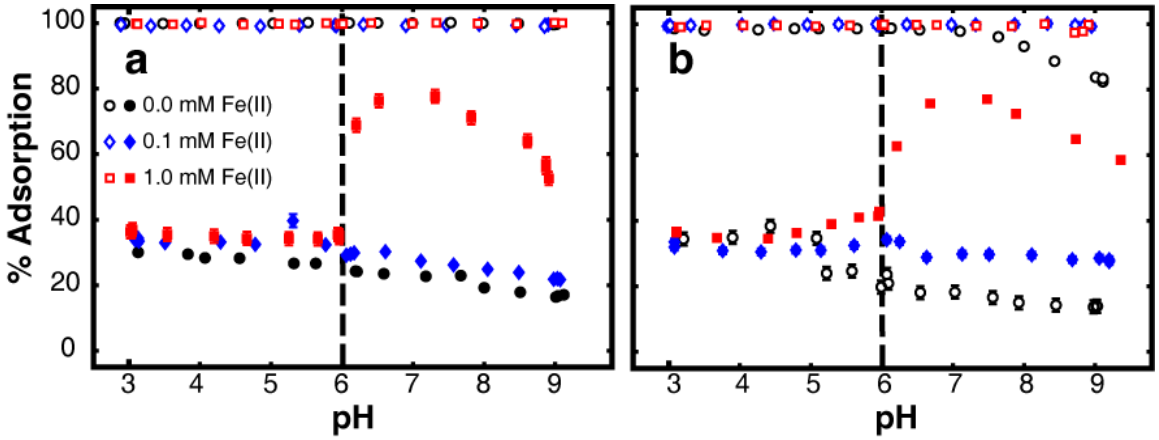

Figure 2.2. Phosphate sorption on (a) goethite and (b) hematite in the absence and presence of aqueous Fe(II), with 0.1 mM (open symbols) and 1.0 mM (filled symbols) initial phosphate. Dashed line indicates the abrupt change in sorption behavior for experiments conducted with 1.0 mM Fe(II) and phosphate.

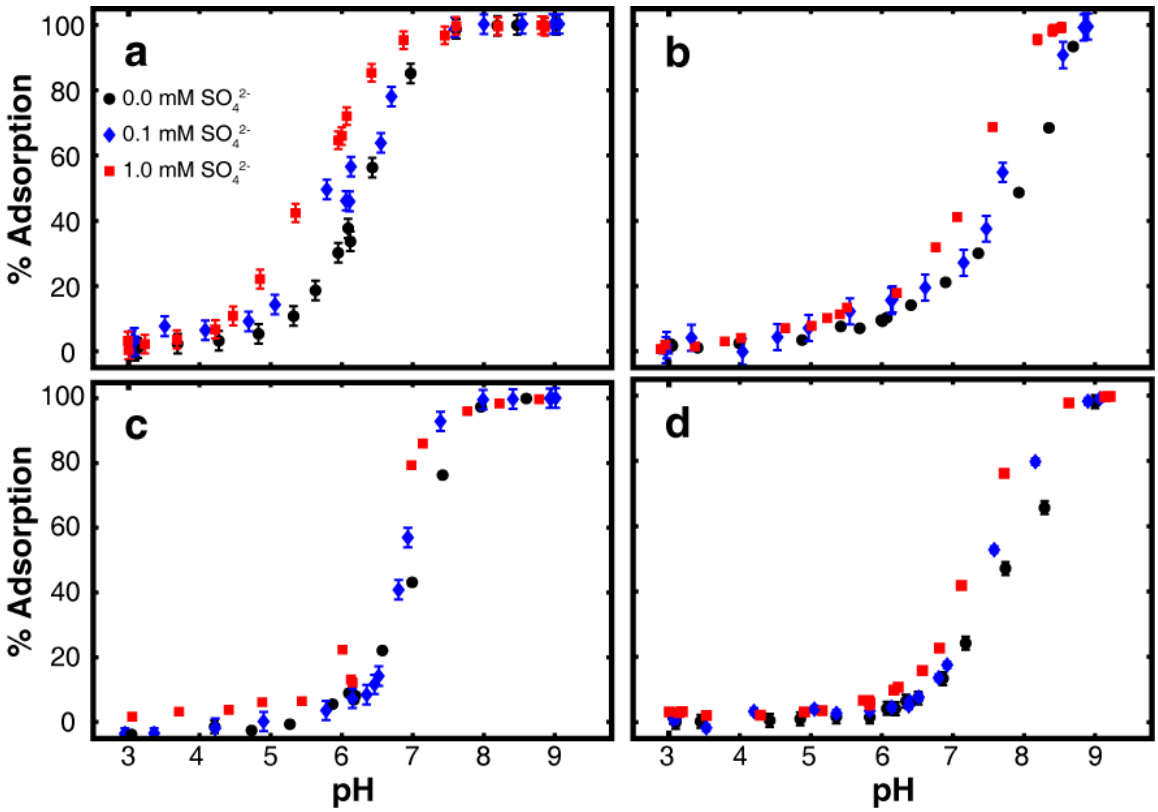

Figure 2.3. Fe(II) sorption in the absence and presence of sulfate: goethite with (a) 0.1 mM or (b) 1.0 mM initial aqueous Fe(II) and hematite with (c) 0.1 mM or (d) 1.0 mM initial aqueous Fe(II).

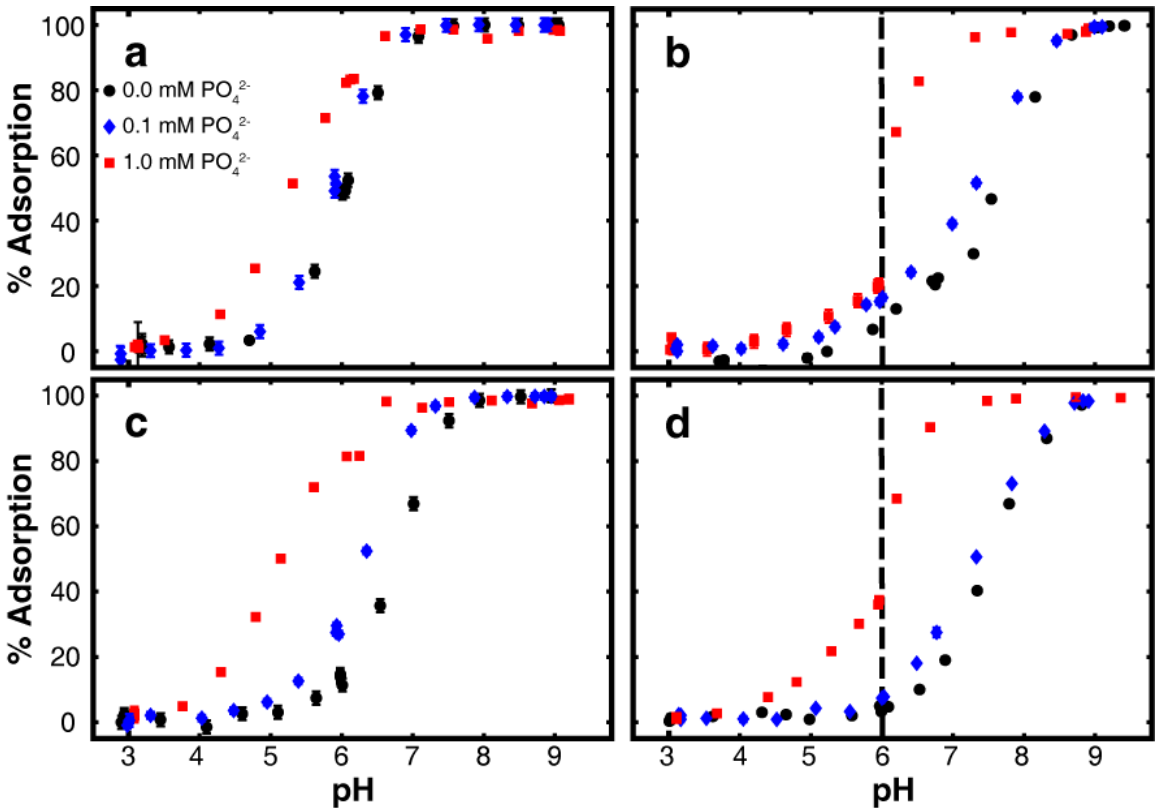

Figure 2.4. Fe(II) sorption in the absence and presence of phosphate: goethite with (a) 0.1 mM or (b) 1.0 mM initial aqueous Fe(II) and hematite with (c) 0.1 mM or (d) 1.0 mM initial aqueous Fe(II). Dashed line indicates the abrupt change in sorption behavior for experiments conducted with 1.0 mM Fe(II) and phosphate.

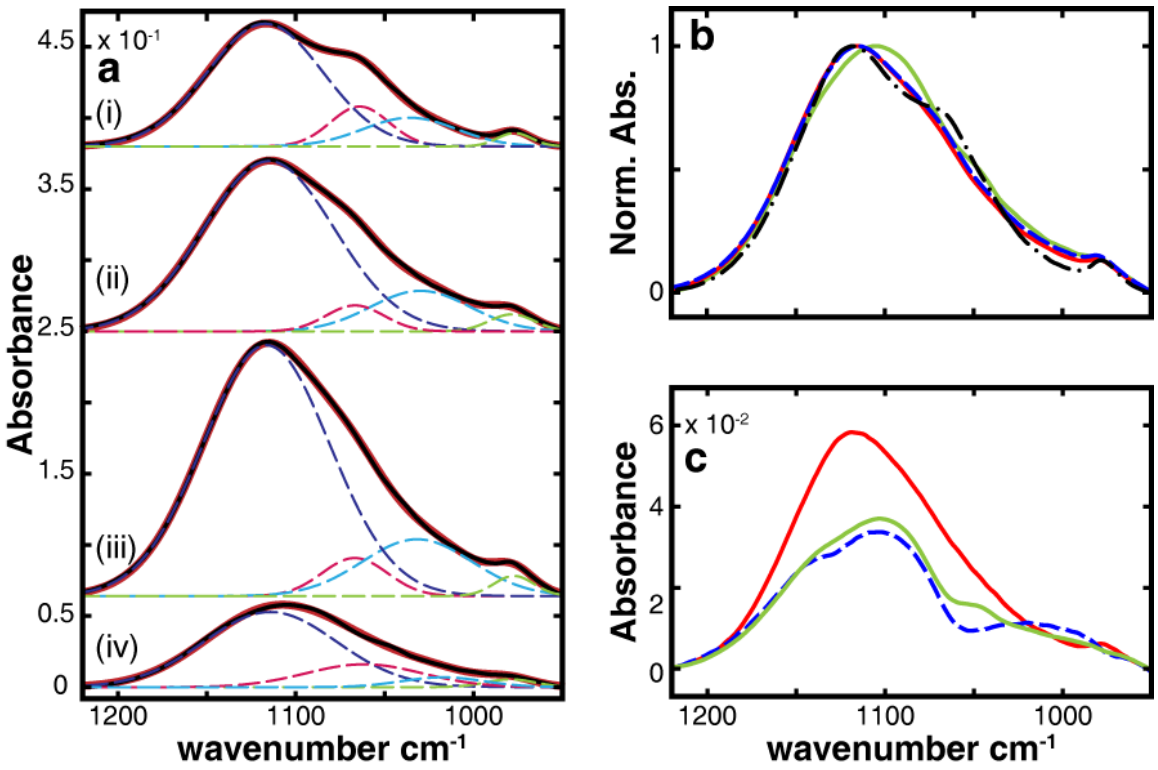

Figure 2.5. ATR-FTIR spectra of sulfate adsorbed onto hematite at pH 7. (a) Sulfate absorbance (black) and fits (red) with corresponding components (dashed) for equilibrium conditions of 50 μM SO_4^{2-} with no Fe(II) (i), 50 μM Fe(II) (ii), or 500 μM Fe(II) (iii), and 200 μM SO_4^{2-} with no Fe(II) (iv). The spectra are offset for clarity. (b) Normalized ATR-FTIR spectra of 50 μM SO_4^{2-} with no Fe(II) (dashed-dotted), 50 μM Fe(II) (dashed), or 500 μM Fe(II) (red solid), and 200 μM SO_4^{2-} with no Fe(II) (green solid). (c) Difference spectra of 50 μM Fe(II) – 0 μM Fe(II) with 50 μM SO_4^{2-} (dashed), 500 μM Fe(II) – 50 μM Fe(II) with 50 μM SO_4^{2-} (red solid), and 200 μM SO_4^{2-} - 50 μM SO_4^{2-} with no Fe(II) (green solid).

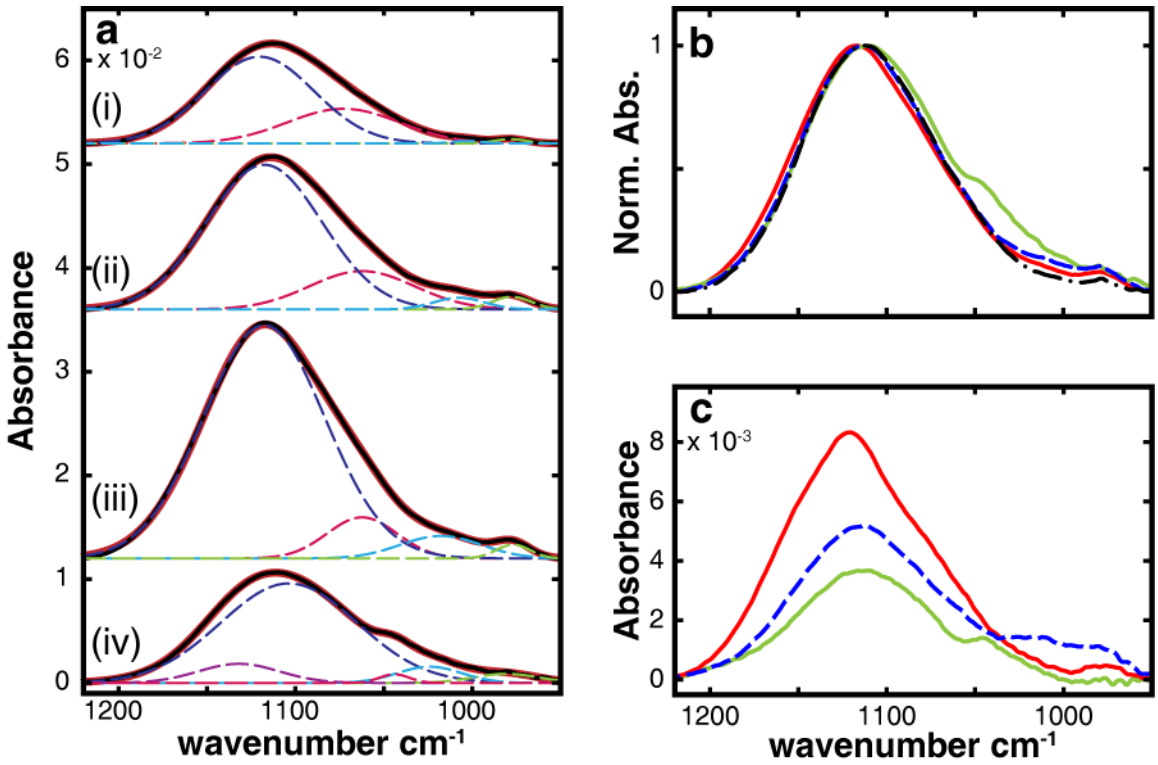

Figure 2.6. ATR-FTIR spectra of sulfate adsorbed onto goethite at pH 7. (a) Sulfate absorbance (black) and fits (red) with corresponding components (dashed) for equilibrium conditions of 50 μM SO_4^{2-} with no Fe(II) (i), 50 μM Fe(II) (ii), or 500 μM Fe(II) (iii), and 200 μM SO_4^{2-} with no Fe(II) (iv). Spectra are offset for clarity. (b) Normalized ATR-FTIR spectra of 50 μM SO_4^{2-} with no Fe(II) (black dashed-dotted lines), 50 μM Fe(II) (dashed), or 500 μM Fe(II) (red solid), and 200 μM SO_4^{2-} with no Fe(II) (green solid). (c) Difference spectra of 50 μM Fe(II) – 0 μM Fe(II) with 50 μM SO_4^{2-} (dashed), 500 μM Fe(II) – 50 μM Fe(II) with 50 μM SO_4^{2-} (red solid), and 200 μM SO_4^{2-} - 50 μM SO_4^{2-} with no Fe(II) (green solid).

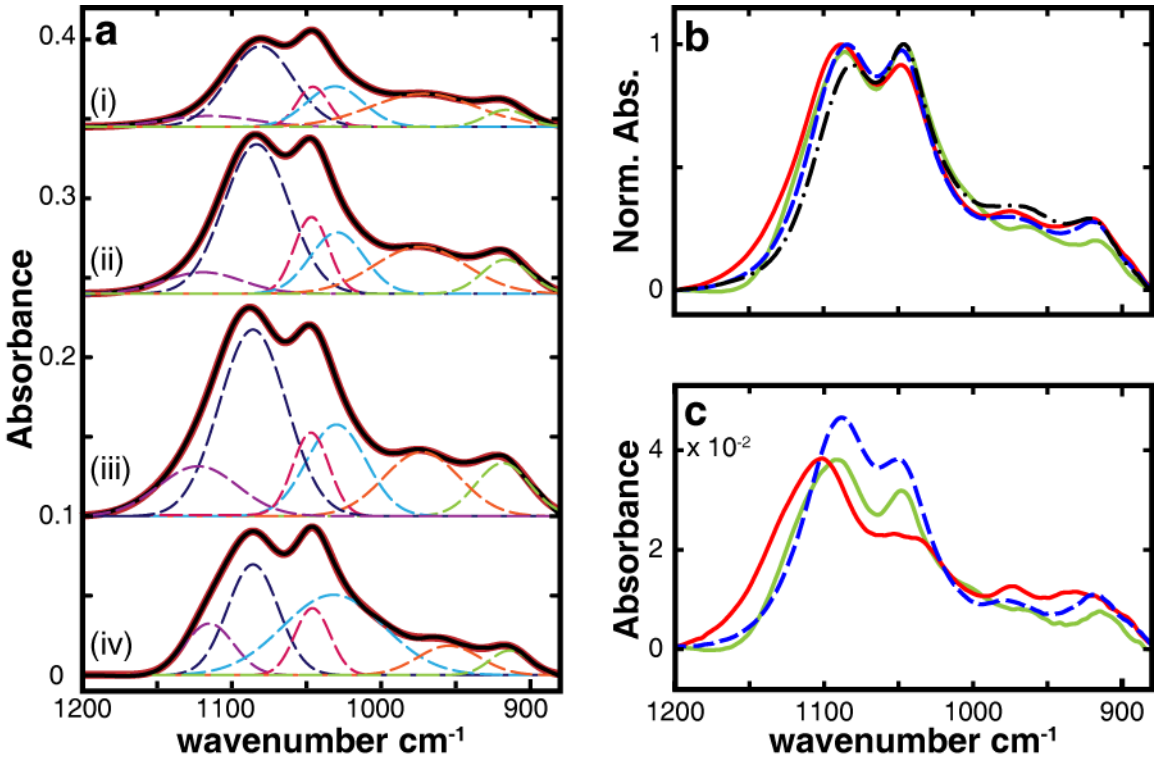

Figure 2.7. ATR-FTIR spectra of phosphate adsorbed onto hematite at pH 7. (a) Phosphate absorbance (black) and fits (red) with corresponding components (dashed) for equilibrium conditions of 4 μM PO_4^{3-} with no Fe(II) (i), 4 μM Fe(II) (ii), or 400 μM Fe(II) (iii), and 16 μM PO_4^{3-} with no Fe(II) (iv). Spectra are offset for clarity. (b) Normalized ATR-FTIR spectra of 4 μM PO_4^{3-} with no Fe(II) (dashed-dotted), 4 μM Fe(II) (dashed), or 400 μM Fe(II) (red solid), and 16 μM PO_4^{3-} with no Fe(II) (green solid). (c) Difference spectra of 4 μM Fe(II) – 0 μM Fe(II) with 4 μM PO_4^{3-} (dashed), 400 μM Fe(II) – 4 μM Fe(II) with 4 μM PO_4^{3-} (red solid), and 16 μM PO_4^{3-} - 4 μM PO_4^{3-} with no Fe(II) (green solid).

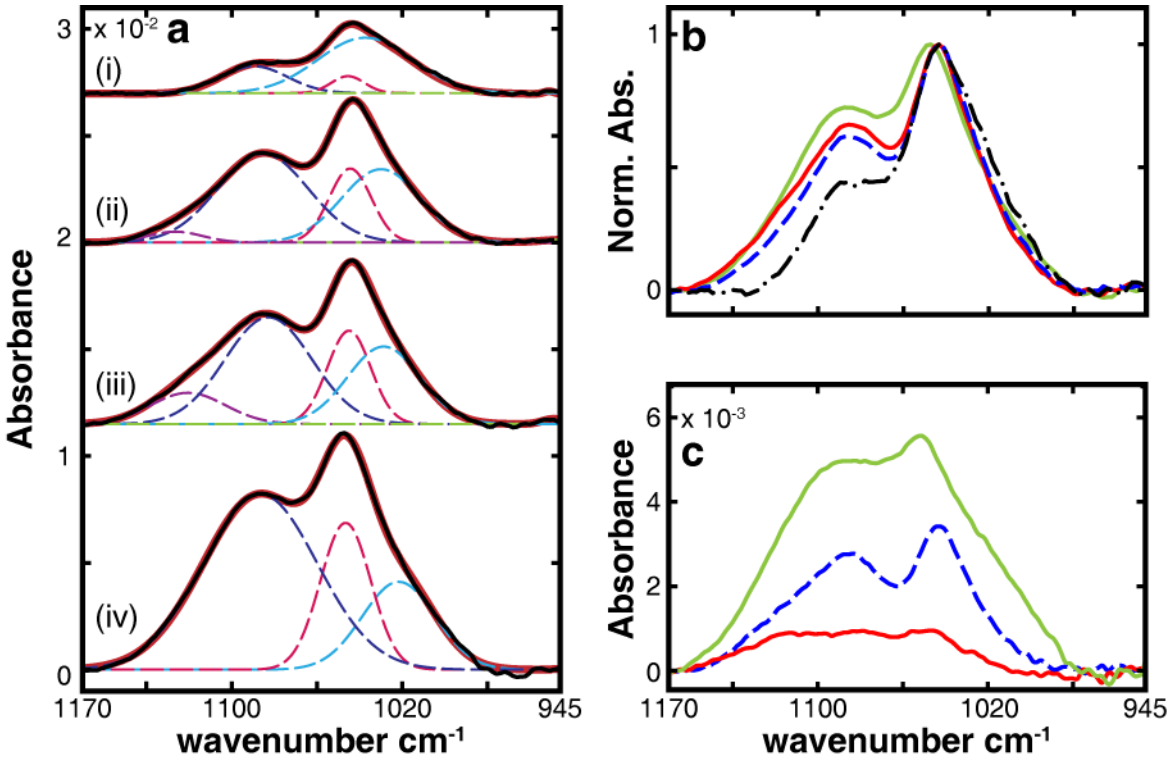

Figure 2.8. ATR-FTIR spectra of phosphate adsorbed onto goethite at pH 7. (a) Phosphate absorbance (black) and fits (red) with corresponding Gaussians (dashed) for equilibrium conditions of 4 μM PO_4^{3-} with no Fe(II) (i), 4 μM Fe(II) (ii), or 400 μM Fe(II) (iii), and 16 μM PO_4^{3-} with no Fe(II) (iv). Spectra are offset for clarity. (b) Normalized ATR-FTIR spectra of 4 μM PO_4^{3-} with no Fe(II) (dashed-dotted), 4 μM Fe(II) (dashed), or 400 μM Fe(II) (red solid), and 16 μM PO_4^{3-} with no Fe(II) (green solid). (c) Difference spectra of 4 μM Fe(II) – 0 μM Fe(II) with 4 μM PO_4^{3-} (dashed), 400 μM Fe(II) – 4 μM Fe(II) with 4 μM PO_4^{3-} (red solid), and 16 μM PO_4^{3-} - 4 μM PO_4^{3-} with no Fe(II) (green solid).

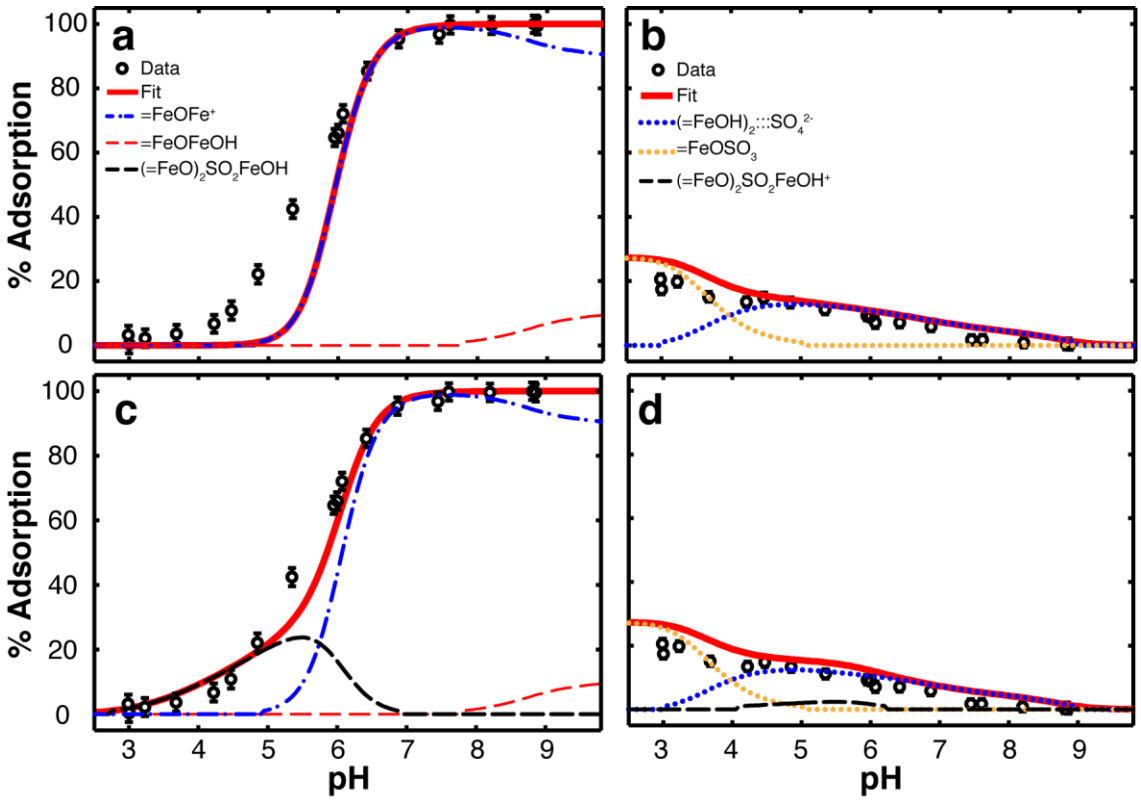

Figure 2.9. Optimized SCM for 0.1 mM Fe(II) and 1.0 mM sulfate adsorption onto goethite. Fe(II) (a,c) and sulfate (b,d) adsorption data and SCM fits with corresponding surface complexes without (a,b) and with (c,d) inclusion of ternary surface complexation.

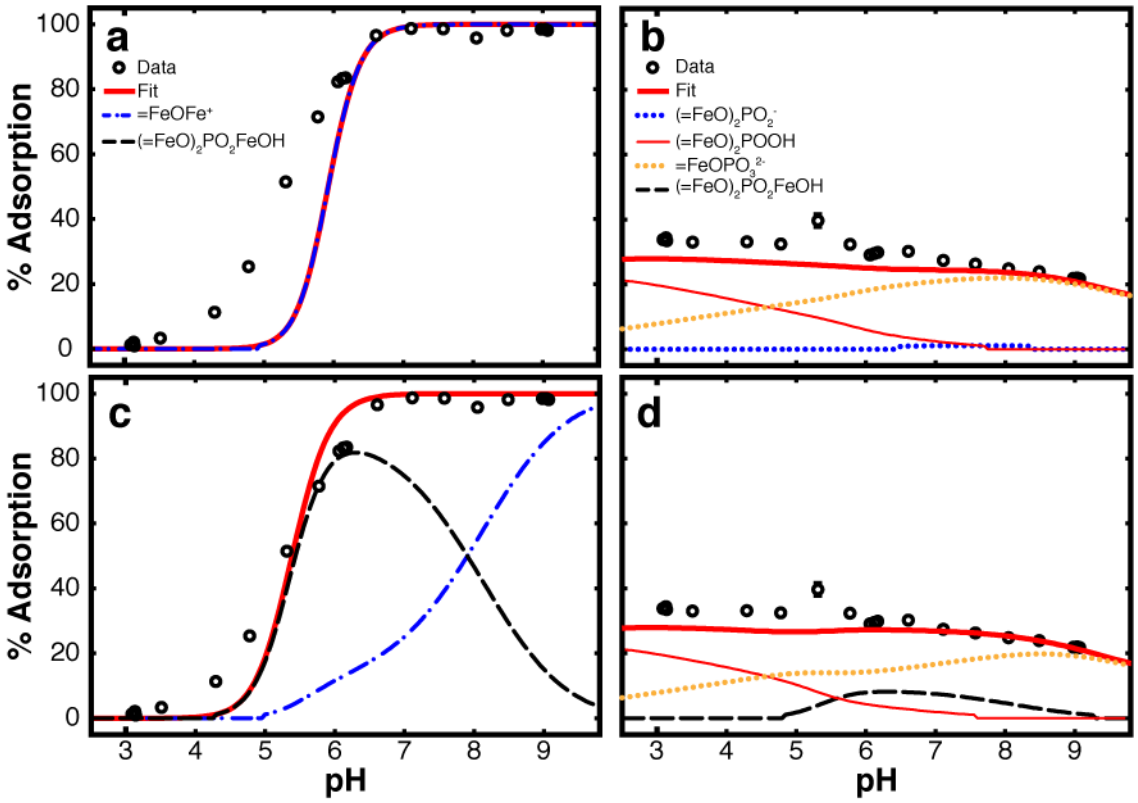

Figure 2.10. Optimized SCM for 0.1 mM Fe(II) and 1.0 mM phosphate adsorption onto goethite. Fe(II) (a,c) and phosphate (b,d) data and fits with corresponding surface complexes without (a,b) and with (c,d) inclusion of ternary surface complexation.

2.6 APPENDIX

2.6.1 Vivianite Formation

Vivianite ($Fe_3(PO_4)_2 \cdot 8H_2O$) was synthesized and characterized by powder XRD and ATR-FTIR spectroscopy following the procedures described in the paper (Figure A2.3). The PO_4-active region of the vivianite FTIR spectrum does not match any of the spectra of phosphate reacted with hematite or goethite (Figures 2.7,2.8), thus we are confident that the experimental spectra are of adsorbed phosphate with no ferrous phosphate precipitates present.

Vivianite was found to precipitate in samples reacted with 1.0 mM initial phosphate and 1.0 mM Fe(II) above pH 6 in both the goethite and the hematite systems. Vivianite saturation index (SI) calculations for the goethite samples reacted at pH 5.5 – 9.0 (Table A2.2) show that the system is supersaturated with respect to vivianite at pH $\geq$ 6.0. The fact that the system becomes more supersaturated with increasing pH may be due to a flaw in the thermodynamic data or due to slow precipitation kinetics.

2.6.2 Surface Complexation Modeling

The SCM could simulate the observed Fe(II), sulfate, and phosphate adsorption data well except for the 1.0 mM Fe(II) and 0.1 mM sulfate experiment (Figure A2.5j), where an enhancement in adsorption is simulated between pH 6-7.5 that deviates from the data. The FTIR spectra are consistent with the presence of an outer-sphere sulfate surface complex on goethite. The electrostatic activity correction for such a species requires a weaker columbic correction term associated with adsorption at a β-plane. The diffuse double layer (DDL) model used in the present study cannot determine such a correction as all adsorption occurs at the o-plane, so the present model may overestimate the impact of Fe(II) adsorption (increasing positive surface charge) on sulfate uptake. The calculated surface charge – pH relationship for the condition

where excessive adsorption is predicted, 1.0 mM Fe(II) and 0.1 mM sulfate, illustrates that the high uptake of Fe(II) as a positively charged surface complex leads to a local maximum in positive charge at pH 8 (Figure A2.6). The non-monotonic trend of surface charge as a function of pH and the inability to make proper activity corrections for outer-sphere surface complexes may explain the failure of the DDL model to predict sulfate adsorption at this particular condition.

2.6.3 Discussion Ruling Out Fe(III)-Phosphate Precipitation

The dissolved Fe(III) concentration should be very low when the system is in equilibrium with goethite or hematite. However, phosphate is also known to form insoluble minerals with Fe(III), such as strengite. First, we did not see any evidence of phosphate precipitates in the IR spectra. In addition, we performed chemical equilibrium modeling to identify under what conditions strengite may precipitate. We calculated the speciation of Fe(III) in the presence of 0.1 mM and 1.0 mM phosphate in equilibrium with goethite or hematite. The thermodynamic constants we used for the minerals are as follows:

Reactions	Log K
$Fe^{3+} + 2H_2O \rightleftharpoons$ Goethite(s) $+ 3H^+$	−0.36
$2Fe^{3+} + 3H_2O \rightleftharpoons$ Hematite(s) $+ 6H^+$	1.42
$Fe^{3+} + 2H_2O + PO_4^{3-} \rightleftharpoons$ Strengite(s)	26.4

For the goethite system with 1 mM phosphate, strengite is only supersaturated at pH < 4.2. With 0.1 mM phosphate, the critical pH is 3.3. For the hematite system with 1.0 mM phosphate, the critical pH is 3.0. With 0.1 mM phosphate in equilibrium with hematite, strengite is always undersaturated. The possibility of Fe(III)-phosphate mineral formation was limited to

the very acidic pH range. The calculated saturation index (SI) was never > 1 (Figure A2.7a), so precipitation of strengite likely never occurs in our short-term experiments due to kinetic limitations from slow goethite and hematite dissolution.

If precipitation of strengite was allowed in the equilibrium calculations, then the calculated phosphate speciation (total 1.0 mM) in equilibrium with goethite at pH 3 was 93% precipitated as strengite and 7 % as dissolved phosphate (Figure A2.7b). The experimental results showed less than 30% phosphate uptake, which is more likely to be attributed to adsorption. With the analysis above, we have confidence to conclude that adsorption was the dominant uptake mechanism.

2.6.4 Discussion Ruling Out Potential Impurities in FTIR Spectra

Variable amounts of adsorbed water and other impurities may conceivably alter FTIR spectra of adsorbed oxoanions. CO_3^{2-} in particular may affect the FTIR spectra, but it is not likely this species is present due to the fact the flow-through cells maintain anaerobic conditions during FTIR analyses. Figure A2.8 shows the full FTIR spectrum (4000 – 400 cm^{-1}) for the goethite-phosphate system. The variations in the water and –OH bending modes (3600 – 2800 cm^{-1} and 1700 – 1500 cm^{-1}, respectively) are slight at best and are consistent with those previously observed for goethite (Prasad et al. 2006). The large bands around 890 and 790 cm^{-1} correspond with goethite –OH bands. The changes in the FTIR spectra with increasing Fe(II) are inconsistent with those induced by carbonate adsorption onto goethite (Villalobos and Leckie, 2001; Wijnja and Schultess, 2001). Thus, we are confident that the changes in oxoanion FTIR spectra induced by Fe(II) in our experiments are not the result of impurities or artifacts.

Table A2.1. Equilibrium constants for aqueous species used in the SCM. (Source: MINEQL+)

Equilibrium Reactions for Aqueous Species	LogK
Phosphate speciation	
$PO_4^{3-} + 3H^+ \rightleftharpoons H_3PO_4$	21.7
$PO_4^{3-} + 2H^+ \rightleftharpoons H_2PO_4^-$	19.56
$PO_4^{3-} + H^+ \rightleftharpoons HPO_4^{2-}$	12.35
$PO_4^{3-} + H^+ + Na^+ \rightleftharpoons NaHPO_4^-$	13.455
$PO_4^{3-} + H^+ + Fe^{2+} \rightleftharpoons FeHPO_{4(aq)}$	15.975
$PO_4^{3-} + 2H^+ + Fe^{2+} \rightleftharpoons FeH_2PO_4^+$	22.273
Sulfate speciation	
$SO_4^{2-} + H^+ \rightleftharpoons HSO_4^-$	1.99
$SO_4^{2-} + Na^+ \rightleftharpoons NaSO_4^-$	0.73
$SO_4^{2-} + Fe^{2+} \rightleftharpoons FeSO_{4(aq)}$	2.39
Fe(II) speciation with background electrolyte	
$Fe^{2+} + H_2O = FeOH^+ + H^+$	−9.397
$Fe^{2+} + 2H_2O = Fe(OH)_{2(aq)} + 2H^+$	−20.494
$Fe^{2+} + 3H_2O = Fe(OH)_3^- + 3H^+$	−28.991
$Fe^{2+} + Cl^- = FeCl^+$	−0.2

Table A2.2. Vivianite saturation index (SI) calculations and final aqueous Fe and P concentrations for goethite reacted with 1.0 mM initial phosphate and 1.0 mM Fe(II).

pH	$[Fe]_{aq}$ (mM)	[P]aq (mM)	SI (vivianite)
5.66	0.829(5)[a]	0.645(2)	-0.19
5.96	0.782(5)	0.642(2)	0.87
6.2	0.321(5)	0.312(2)	0.18
6.52	0.168(5)	0.240(2)	0.31
7.31	0.035(5)	0.227(2)	0.61
7.82	0.021(5)	0.289(2)	1.25
8.61	0.026(5)	0.357(2)	3.17
8.87	0.017(5)	0.436(2)	3.23

[a]Absolute uncertainties of the least significant digit are in parentheses (95% confidence value, includes standard deviation of triplicate samples and triplicate ICP-OES measurements).

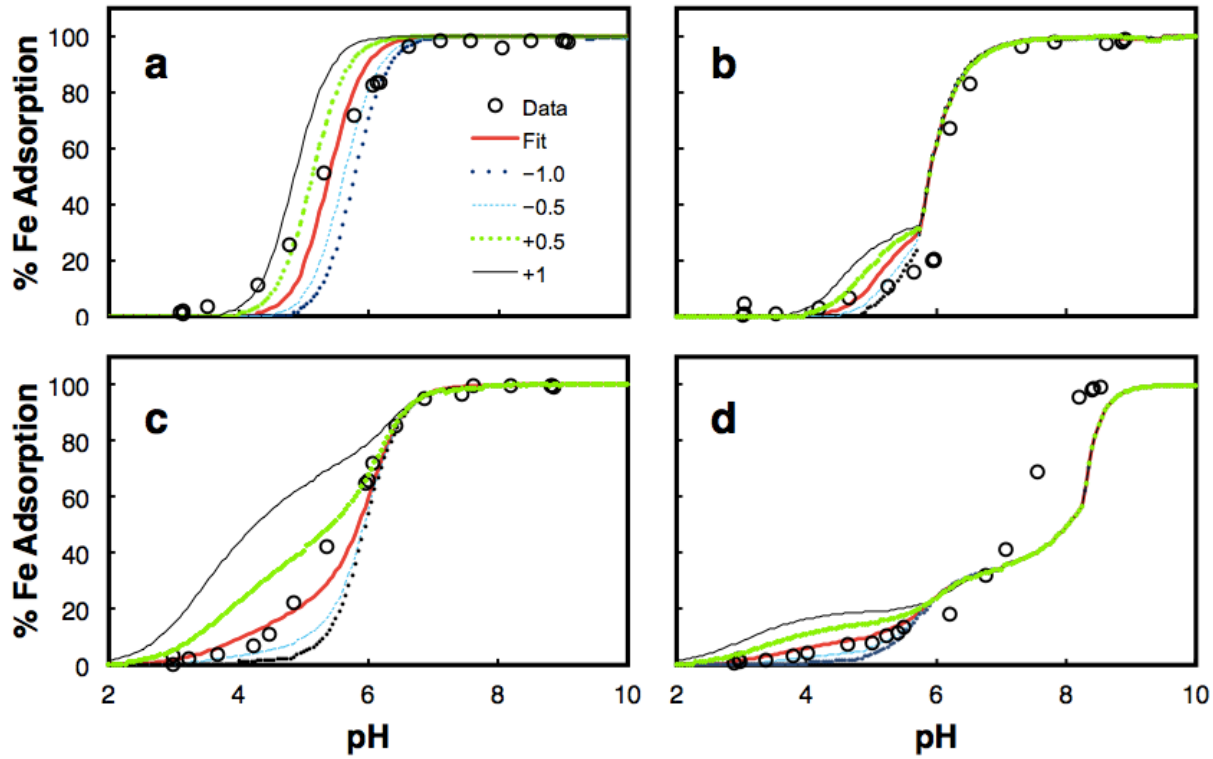

Figure A2.1. Sensitivity test of the model with respect to the variation of equilibrium constants for the ternary surface complexation reactions on goethite. (a) 0.1 mM Fe(II) + 1.0 mM phosphate, (b) 1.0 mM Fe(II) + 1.0 mM phosphate, (c) 0.1 mM Fe(II) + 1.0 mM sulfate, (d) 1.0 mM Fe(II) + 1.0 mM sulfate. The red solid lines represents the best fit. Other lines were simulated by increasing or decreasing the log K values (molar based) of the ternary surface complexes by 0.5 or 1.0.

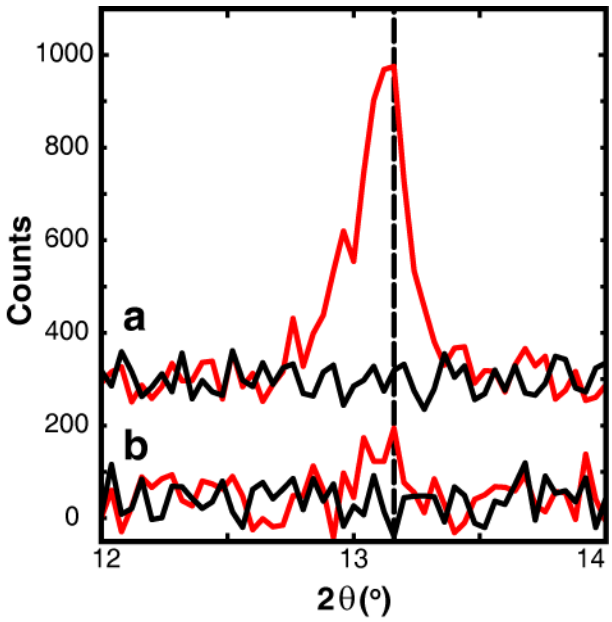

Figure A2.2. Powder XRD patterns of samples reacted with 4 g L^{-1} goethite (a) or hematite (b) reacted with 1.0 mM phosphate and 1.0 mM Fe(II) at pH 6.5 (red) compared with unreacted goethite or hematite (black solid) in the region of the strongest vivianite line, the (020) reflection (dashed).

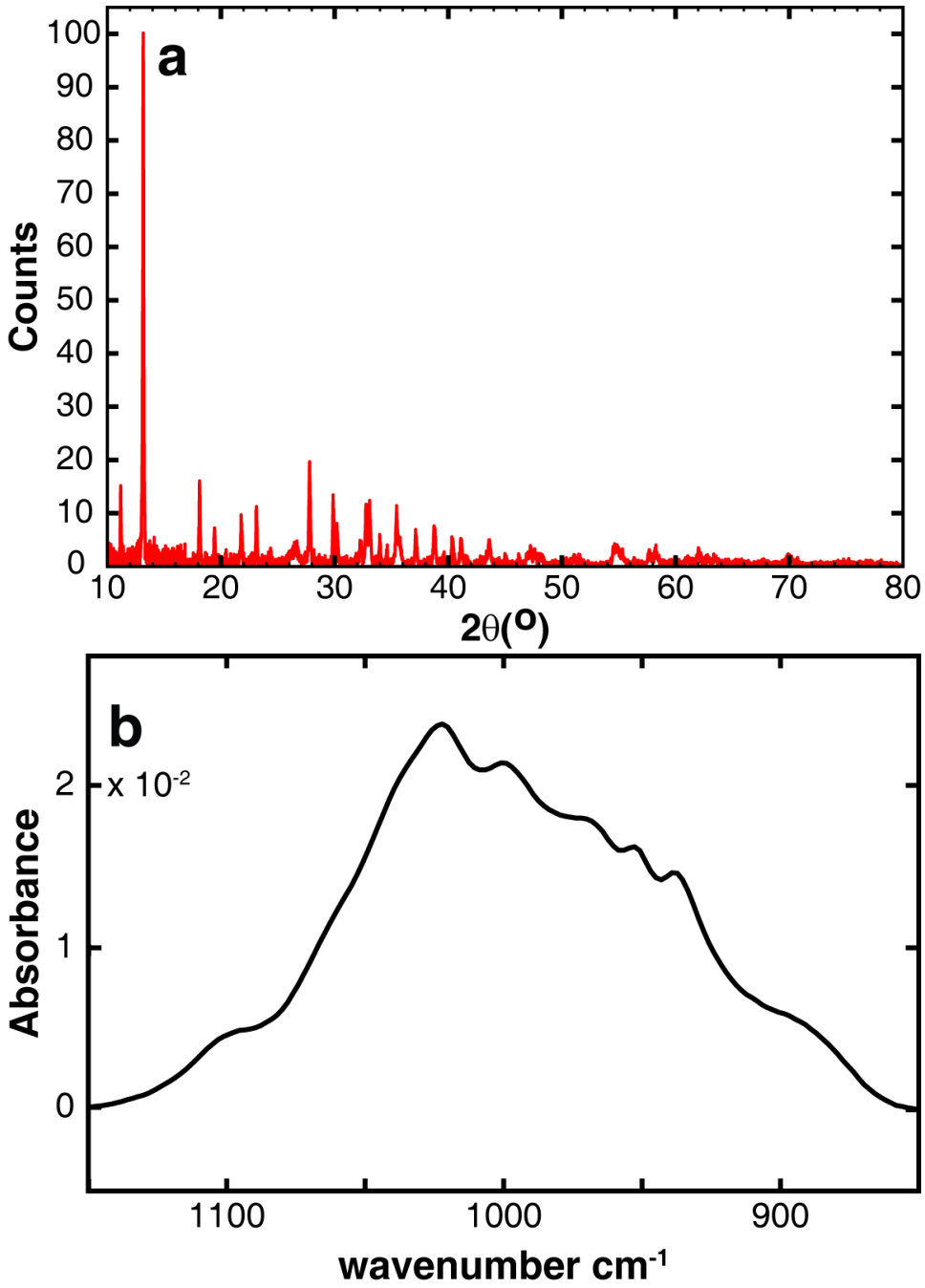

Figure A2.3. Powder XRD pattern (a) and ATR-FTIR spectrum in the P-O stretching region (b) of synthetic vivianite.

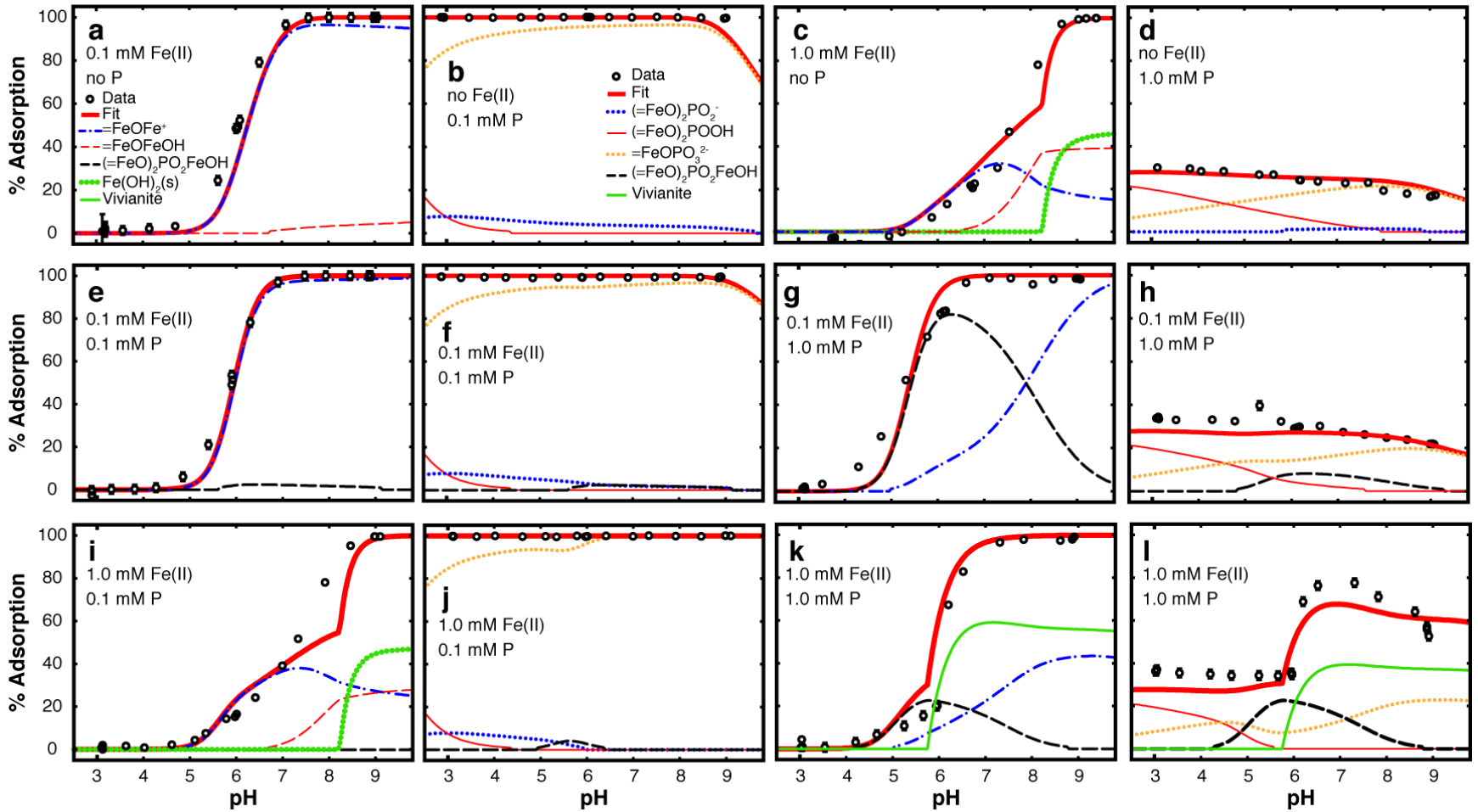

Figure A2.4. Surface complexation modeling fits of Fe(II) and phosphate adsorption onto goethite.

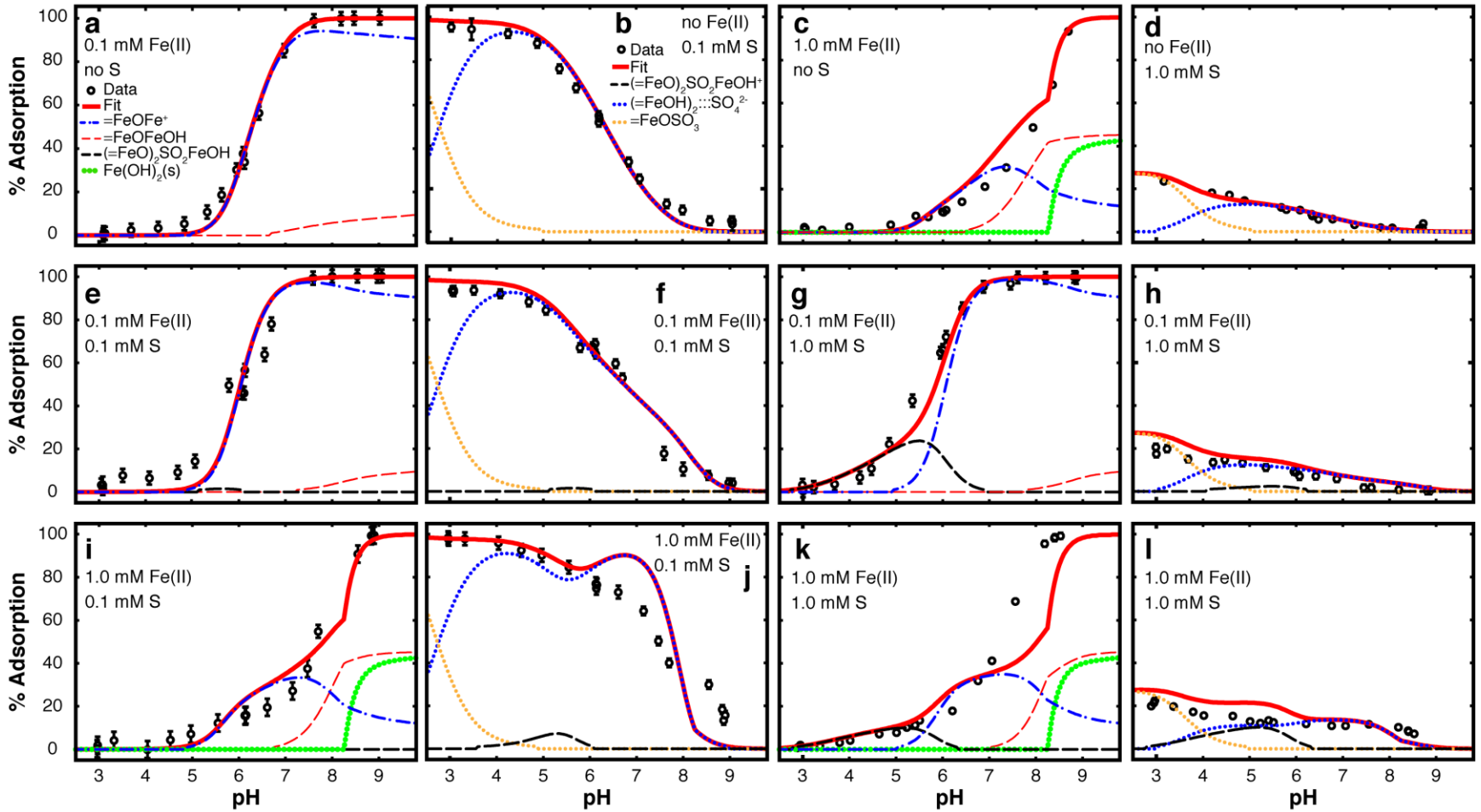

Figure A2.5. Surface complexation modeling fits of Fe(II) and sulfate adsorption onto goethite.

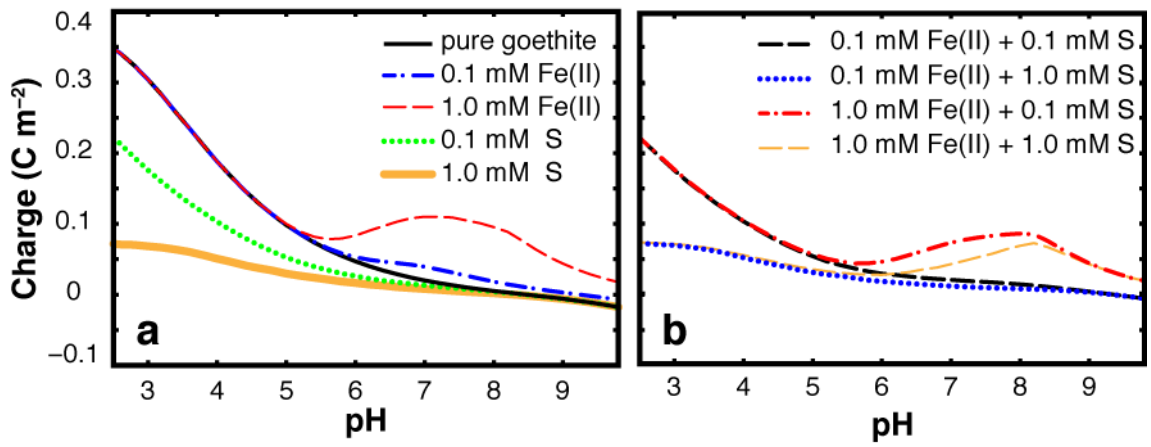

Figure A2.6. SCM calculated surface charge of (a) pure goethite and goethite reacted with 0.1 mM or 1.0 mM Fe(II) or sulfate; and (b) goethite reacted with both Fe(II) and sulfate.

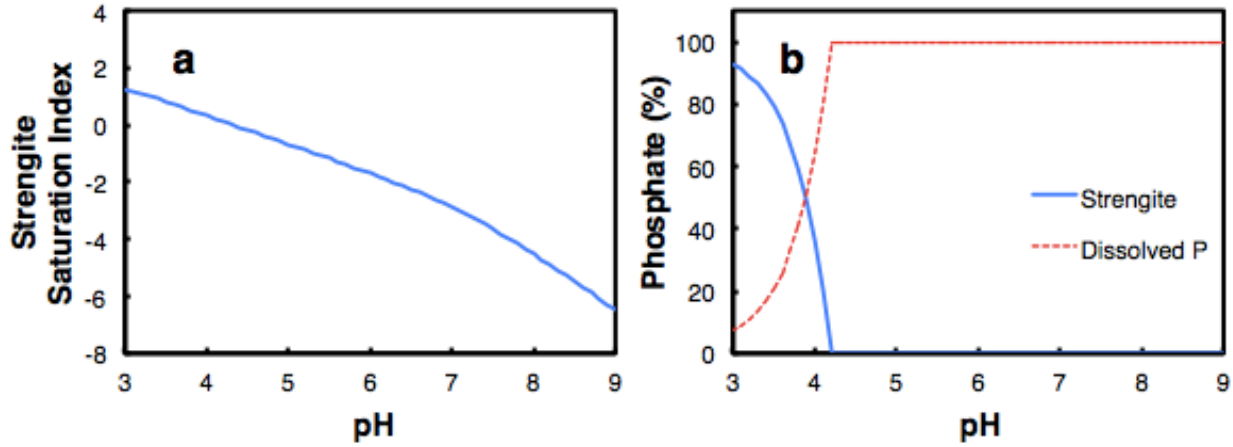

Figure A2.7. Calculation about strengite formation in the presence of 1.0 mM phosphate in equilibrium with goethite (a) Saturation index of strengite, (b) Relative amounts of dissolved and precipitated phosphate.

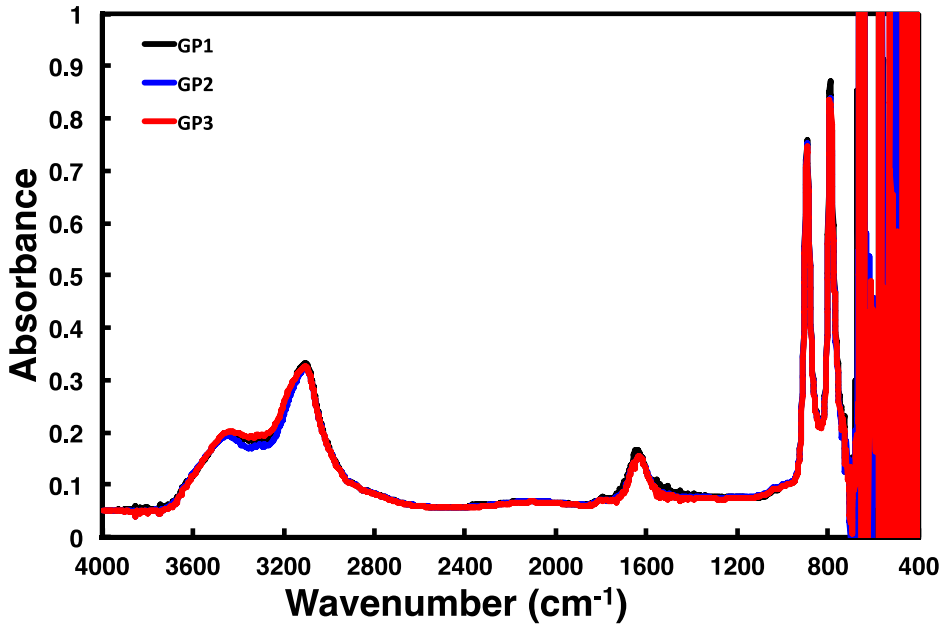

Figure A2.8. ATR-FTIR spectra of phosphate adsorbed onto goethite at pH 7 for the full spectral region examined (without blank goethite spectrum subtracted). Phosphate absorbance for equilibrium conditions of 4 μM PO_4^{3-} with no Fe(II) (black), 4 μM Fe(II) (blue), or 400 μM Fe(II) (red).

2.7 REFERENCES

Al-Borno A. and Tomson M. B. (1994) The temperature-dependence of the solubility product constant of vivianite. *Geochimica et Cosmochimica Acta* **58**, 5373-5378.

Ali M. A. and Dzombak D. A. (1996) Interactions of copper, organic acids, and sulfate in goethite suspensions. *Geochimica et Cosmochimica Acta* **60**, 5045-5053.

Arai Y. and Sparks D. L. (2001) ATR-FTIR spectroscopic investigation on phosphate adsorption mechanisms at the ferrihydrite-water interface. *Journal of Colloid and Interface Science* **241**, 317-326.

Balistrieri L. S. and Murray J. W. (1982) The adsorption of Cu, Pb, Zn, and Cd on goethite from major ion seawater. *Geochimica et Cosmochimica Acta* **40**, 1253-1265.

Baskar S., Baskar R., Lee N., Kaushik A. and Theophilus P. K. (2008) Precipitation of iron in microbial mats of the spring waters of Borra Caves, Vishakapatnam, India: some geomicrobiological aspects. *Environmental Geology* **56**, 237-243.

Beattie D. A., Chapelet J. K., Gräfe M., Skinner W. M. and Smith E. (2008) In situ ATR FTIR studies of SO_4 adsorption on goethite in the presence of copper ions. *Environmental Science & Technology* **42**, 9191-9196.

Benjamin M. M. and Leckie J. O. (1982) Effects of complexation by Cl, SO_4, and S_2O_3 on adsorption behavior of Cd on oxide-surfaces. *Environmental Science & Technology* **16**, 162-170.

Bondietti G., Sinniger J. and Stumm W. (1993) The reactivity of Fe(III) (hydr)oxides: effects of ligands in inhibiting the dissolution. *Colloids and Surfaces A: Physicochemical and Engineering Aspects* **79**, 157-167.

Borch T., Masue, Y., Kukkadapu R. K. and Fendorf S. (2007) Phosphate imposed limitations on biological reduction and alteration of ferrihydrite. *Environmental Science & Technology* **41**, 166-172.

Canfield D. E., Thamdrup B. and Hansen J. W. (1993) The anaerobic degradation of organic matter in Danish coastal sediments: iron reduction, manganese reduction, and sulfate reduction. *Geochimica et Cosmochimica Acta* **57**, 3867-3885.

Catalano J. G., Fenter P., Park C., Zhang Z. and Rosso K. M. (2010) Structure and oxidation state of hematite surfaces reacted with aqueous Fe(II) at acidic and neutral pH. *Geochimica et Cosmochimica Acta* **74**, 1498-1512.

Catalano J. G., Luo Y. and Otemuyiwa B. (2011) Effect of aqueous Fe(II) on arsenate sorption on goethite and hematite. *Environmental Science & Technology* **45**, 8826-8833.

Collins C. R., Ragnarsdottir K. V. and Sherman D. M. (1999) Effect of inorganic and organic ligands on the mechanism of cadmium sorption to goethite. *Geochimica et Cosmochimica*

Acta **63**, 2989-3002.

Crosby H. A., Johnson C. M., Roden E. E. and Beard B. L. (2005) Coupled Fe(II)-Fe(III) electron and atom exchange as a mechanism for Fe isotope fractionation during dissimilatory iron oxide reduction. *Environmental Science & Technology* **39**, 6698-6704.

Diaz-Barrientos E., Madrid L., Contreras M. C. and Morillo E. (1990) Simultaneous adsorption of zinc and phosphate on synthetic lepidocrocite. *Australian Journal of Soil Research* **28**, 549-557.

Dzombak D. A. and Morel F. M. M. (1990) *Surface complexation modeling: Hydrous ferric oxide.* John Wiley & Sons, New York.

Eggleston C. M., Hug S., Stumm W., Sulzberger B. and Dos Santos Afonso M. (1998) Surface complexation of sulfate by hematite surfaces: FTIR and STM observations. *Geochimica et Cosmochimica Acta* **62**, 585-593.

Elzinga E. J., Peak D. and Sparks D. L. (2001) Spectroscopic studies of Pb(II)-sulfate interactions at the goethite-water interface. *Geochimica et Cosmochimica Acta* **65**, 2219-2230.

Elzinga E. J. and Kretzschmar R. (2013) *In situ* ATR-FTIR spectroscopic analysis of the co-adsorption of orthophosphate and Cd(II) onto hematite. *Geochimica et Cosmochimica Acta* **117**, 53-64.

Elzinga E. J. and Sparks D. L. (2007) Phosphate adsorption onto hematite: An in situ ATR-FTIR investigation of the effects of pH and loading level on the mode of phosphate surface complexation. *Journal of Colloid and Interface Science* **308**, 53-70.

Eynard A., Del Campillo M. C., Barrón V. and Torrent J. (1992) Use of vivianite (Fe3 (PO4) 2.8 H2O) to prevent iron chlorosis in calcareous soils. *Fertilizer Research* **31**, 61-67.

Frierdich A. J., Luo Y. and Catalano J. G. (2011) Trace element cycling through iron oxide minerals during redox-driven dynamic recrystallization. *Geology* **39**, 1083-1086.

Frierdich A. J. and Catalano J. G. (2012) Controls on Fe(II)-activated trace element release from goethite and hematite. *Environmental Science & Technology* **46**, 1519-1526.

Fukushi K. and Sverjensky D. A. (2007) A surface complexation model for sulfate and selenate on iron oxides consistent with spectroscopic and theoretical molecular evidence. *Geochimica et Cosmochimica Acta* **71**, 1-24.

Handler R. M., Beard B. L., Johnson C. M. and Scherer M. M. (2009) Atom exchange between aqueous Fe(II) and goethite: an Fe isotope tracer study. *Environmental Science & Technology* **43**, 1102-1107.

Hansel C. M., Benner S. G. and Fendorf S. (2005) Competing Fe(II)-induced mineralization pathways of ferrihydrite. *Environmental Science & Technology* **39**, 7147-7153.

Hezel A. and Ross S. D. (1968) Forbidden transitions in the infra-red spectra of tetrahedral anions--IV. The vibrational spectra (4000-400 cm^{-1}) of some cobalt (M) sulphato- and phosphato-complexes. *Spectrochimica Acta Part A: Molecular Spectroscopy* **24**, 985-992.

Hoins U. (1993) Ligand effect on the adsorption of heavy metals: The sulfate-cadmium-goethite case. *Water, Air, and Soil Pollution* **68**, 241-255.

Hug S. (1997) In situ Fourier transform infrared measurements of sulfate adsorption on hematite in aqueous solutions. *Journal of Colloid and Interface Science* **188**, 415-422.

Jeon B. H., Dempsey B. A., Burgos W. D. and Royer R. A. (2001) Reactions of ferrous iron with hematite. *Colloids and Surfaces A: Physicochemical and Engineering Aspects* **191**, 41-55.

Jeon B. H., Dempsey B. A., Burgos W. D. and Royer R. A. (2003) Sorption kinetics of Fe(II), Zn(II), Co(II), Ni(II), Cd(II), and Fe(II)/Me(II) onto hematite. *Water Research* **37**, 4135-4142.

Johnson D. B., Ghauri M. A. and McGinness S. (1993) Biogeochemical cycling of iron and sulphur in leaching environments. *FEMS Microbiology Reviews* **11**, 63-70.

Juang R. and Wu W. (2002) Adsorption of sulfate and copper(II) on goethite in relation to the changes of zeta potentials. *Journal of Colloid and Interface Science* **249**, 22-29.

Jubb A. M., Verreault D., Posner R., Criscenti L. J., Katz L. E. and Allen H. C. (2013) Sulfate adsorption at the buried hematite/solution interface investigated using total internal reflection (TIR)-Raman spectroscopy. *Journal of Colloid and Interface Science* **400**, 140-146.

Kanematsu M., Young T. M., Fukushi K., Green P. G. and Darby J. L. (2010) Extended triple layer modeling of arsenate and phosphate adsorption on a goethite-based granular porous adsorbent. *Environmental Science & Technology* **44**, 3388-3394.

Kappler A. and Straub K. L. (2005) Geomicrobiological cycling of iron. *Reviews in Mineralogy and Geochemistry* **59**, 85-108.

Larese-Casanova P. and Scherer M. M. (2007) Fe(II) sorption on hematite: new insights based on spectroscopic measurements. *Environmental Science & Technology* **41**, 471-477.

Latta D. E., Bachman J. E. and Scherer M. M. (2012) Fe electron transfer and atom exchange in goethite: Influence of Al-substitution and anion sorption. *Environmental Science & Technology* **46**, 10614-10623.

Lefèvre G. (2004) In situ Fourier-transform infrared spectroscopy studies of inorganic ions adsorption on metal oxides and hydroxides. *Advances in Colloid and Interface Science* **107**, 109-123.

Liger E., Charlet L. and Van Cappellen P. (1999) Surface catalysis of uranium(VI) reduction by iron(II). *Geochimica et Cosmochimica Acta* **63**, 2939-2955.

Luengo C., Brigante M., Antelo J. and Avena M. (2006) Kinetics of phosphate adsorption on goethite: Comparing batch adsorption and ATR-IR measurements. *Journal of Colloid and Interface Science* **300**, 511-518.

Lützenkirchen J., Boily J. F., Lövgren L. and Sjöberg S. (2002) Limitations of the potentiometric titration technique in determining the proton active site density of goethite surfaces. *Geochimica et Cosmochimica Acta* **66**, 3389-3396.

Madrid L., Diaz-Barrientos E. and Contreras M. C. (1991) Relationships between zinc and phosphate adsorption on montmorillonite and an iron oxyhydroxide. *Australian Journal of Soil Research* **29**, 239-247.

Majzlan J. and Myneni S. C. B. (2005) Speciation of iron and sulfate in acid waters: Aqueous clusters to mineral precipitates. *Environmental Science & Technology* **39**, 188-194.

Mathur S. S. and Dzombak D. A. (2006) Surface complexation modeling: Goethite. In *Interface Science and Technology* **11**, pp. 443-468.

Myneni S. C. B., Traina S. J., Waychunas G. A. and Logan T. J. (1998) Experimental and theoretical vibrational spectroscopic evaluation of arsenate coordination in aqueous solutions, solids, and at mineral-water interfaces. *Geochimica et Cosmochimica Acta* **62**, 3285-3300.

Northup D. E., Barns S. M., Yu L. E., Spilde M. N., Schelble R. T., Dano K. E., Crossey L. J., Connolly C. A., Boston P. J., Natvig D. O. and Dahm C. N. (2003) Diverse microbial communities inhabiting ferromanganese deposits in Lechuguilla and Spider Caves. *Environmental Microbiology* **5**, 1071-1086.

Ostergren J. D., Brown G. E., Parks G. A. and Persson P. (2000) Inorganic ligand effects on Pb(II) sorption to goethite (α-FeOOH): II. Sulfate. *Journal of Colloid and Interface Science* **225**, 483-493.

Paul K. W., Borda M. J., Kubicki J. D. and Sparks D. L. (2005) Effect of dehydration on sulfate coordination and speciation at the Fe-(hydr)oxide-water interface: A Molecular Orbital/Density Functional Theory and Fourier transform infrared spectroscopic investigation. *Langmuir* **21**, 11071-11078.

Paul K. W., Kubicki, J. D. and Sparks D. L. (2006) Quantum chemical calculations of sulfate adsorption at the Al- and Fe-(Hydr)oxide-H_2O interface–Estimation of Gibbs free energies. *Environmental Science & Technology* **40**, 7717-7724.

Peak D., Elzinga E. J. and Sparks D. L. (2001) Understanding sulfate adsorption mechanisms on iron(III) oxides and hydroxides: Results from ATR-FTIR spectroscopy. In *Heavy Metals Release in Soils* (ed H. M. Selim). CRC Press LLC, Boca Raton. pp. 167-190.

Peak D., Ford R. G. and Sparks D. L. (1999) An in situ ATR-FTIR investigation of sulfate bonding mechanisms on goethite. *Journal of Colloid and Interface Science* **218**, 289-299.

Persson P. and Lövgren L. (1996) Potentiometric and spectroscopic studies of sulfate complexation at the goethite-water interface. *Geochimica et Cosmochimica Acta* **60**, 2789-2799.

Prasad P. S. R., Shiva Prasad K., Krishna Chaitanya V., Babu E. V. S. S. K., Sreedhar B., Ramana Murthy S. (2006) In situ FTIR study on the dehydration of natural goethite. *Journal of Asian Earth Sciences* **27**, 503-511.

Ronson T. K. and McQuillan A. J. (2002) Infrared spectroscopic study of calcium and phosphate ion coadsorption and of brushite crystallization on TiO2. *Langmuir* **18**, 5019-5022.

Rosso K. M., Yanina S. V., Gorski C. A., Larese-Casanova P. and Scherer M. M. (2010) Connecting observations of hematite (α-Fe_2O_3) growth catalyzed by Fe(II). *Environmental Science & Technology* **44**, 61-67.

Rubasinghege G., Lentz R. W., Scherer M. M. and Grassian V. H. (2010) Simulated atmospheric processing of iron oxyhydroxide minerals at low pH: Roles of particle size and acid anion in iron dissolution. *Proceedings of the National Academy of Sciences of the United States of America* **107**, 6628-6633.

Schecher W. D. and McAvoy D. C. (2007) MINEQL+: A chemical equilibrium modeling system, version 4.6. *MINEQL+: A chemical equilibrium modeling system, version 4.6.*

Schwertmann U. and Cornell R. M. (2000) *Iron oxides in the laboratory: preparation and characterization.* Wiley-VCH, Weinheim.

Singer P. C. (1972) Anaerobic control of phosphate by ferrous iron. *Journal (Water Pollution Control Federation)* **44**, 663-669.

Sobolev D. and Roden E. E. (2002) Evidence for rapid microscale bacterial redox cycling of iron in circumneutral environments. *Antonie Van Leeuwenhoek* **81**, 587-97.

Sposito G. (1989) *The Chemistry of Soils.* Oxford University Press, New York.

Stumm W. (1993) From surface acidity to surface reactivity; inhibition of oxide dissolution. *Aquatic Sciences* **55**, 273-280.

Stumm W. (1997) Reactivity at the mineral-water interface: dissolution and inhibition. *Colloids and Surfaces A: Physicochemical and Engineering Aspects* **120**, 143-166.

Stumm W. and Lee G. F. (1961) Oxygenation of ferrous iron. *Industrial and Engineering Chemistry* **53**, 143-146.

Sverjensky D. A. (2003) Standard states for the activities of mineral surface sites and species. *Geochimica et Cosmochimica Acta* **67**, 17-28.

Swedlund P. J., Webster J. G. and Miskelly G. M. (2003) The effect of SO_4 on the ferrihydrite adsorption of Co, Pb and Cd: ternary complexes and site heterogeneity. *Applied Geochemistry* **18**, 1671-1689.

Swedlund P. J., Webster J. G. and Miskelly G. M. (2009) Goethite adsorption of Cu (II), Pb (II), Cd (II), and Zn (II) in the presence of sulfate: Properties of the ternary complex. *Geochimica et Cosmochimica Acta* **73**, 1548-1562.

Swedlund P. J. and Webster J. G. (2001) Cu and Zn ternary surface complex formation with SO4 on ferrihydrite and schwertmannite. *Applied Geochemistry* **16**, 503-511.

Tejedor-Tejedor M. I. and Anderson M. A. (1990) The protonation of phosphate on the surface of goethite as studied by CIR-FTIR and electrophoretic mobility. *Langmuir* **6**, 602-611.

Thompson A., Chadwick O. A., Rancourt D. G. and Chorover J. (2006) Iron-oxide crystallinity increases during soil redox oscillations. *Geochimica et Cosmochimica Acta* **70**, 1710-1727.

Tickanen L. D., Tejedor-Tejedor M. I. and Anderson M. A. (1991) Quantitative characterization of aqueous suspensions using attenuated total reflection Fourier transform infrared spectroscopy: influence of internal reflection element-particle interactions on spectral absorbance values. *Langmuir* **7**, 451-456.

Tugel J. B., Hines M. E. and Jones G. E. (1986) Microbial iron reduction by enrichment cultures isolated from estuarine sediments. *Applied and Environmental Microbiology* **52**, 1167-72.

Venema P., Hiemstra T. and van Riemsdijk WH (1997) Interaction of Cadmium with Phosphate on Goethite. *Journal of Colloid and Interface Science* **192**, 94-103.

Villalobos M. and Leckie J.O. (2001) Surface complexation modeling and FTIR study of carbonate adsorption to goethite. *Journal of Colloid and Interface Science* **235**, 15-32.

Villalobos M., Trotz M. A. and Leckie J. O. (2003) Variability in goethite surface site density: evidence from proton and carbonate sorption. *Journal of Colloid and Interface Science* **268**, 273-87.

Wang Z. and Giammar D. E. (2013) Mass action expressions for bidentate adsorption in surface complexation modeling: theory and practice. *Environmental Science & Technology* **47**, 3982-96.

Webb S. M. (2005) SIXPack: A Graphical User Interface for XAS Analysis using IFEFFIT. *Physica Scripta* **T115**, 1011-1014.

Weber K. A., Achenbach L. A. and Coates J. D. (2006) Microorganisms pumping iron: anaerobic microbial iron oxidation and reduction. *Nature Reviews Microbiology* **4**, 752-64.

Wijnja H. and Schulthess C. P. (2001) Carbonate adsorption mechanism on goethite studied with ATR-FTIR, DRIFT, and proton coadsorption measurements. *Soil Science Society of America Journal* **65**, 324-330.

Williams A. G. B. and Scherer M. M. (2004) Spectroscopic evidence for Fe(II)-Fe(III) electron transfer at the iron oxide-water interface. *Environmental Science & Technology* **38**, 4782-90.

Xu N., Christodoulatos C. and Braida W. (2006) Modeling the competitive effect of phosphate, sulfate, silicate, and tungstate anions on the adsorption of molybdate onto goethite. *Chemosphere* **64**, 1325-33.

Yanina S. V. and Rosso K. M. (2008) Linked reactivity at mineral-water interfaces through bulk crystal conduction. *Science* **320**, 218-22.

Zhang G. Y. and Peak D. (2007) Studies of Cd (II)--sulfate interactions at the goethite--water interface by ATR-FTIR spectroscopy. *Geochimica et Cosmochimica Acta* **71**, 2158-2169.

Zhu M., Northrup P., Shi C., Billinge S. J., Sparks D. L. and Waychunas G. A. (2014) Structure of sulfate adsorption complexes on ferrihydrite. *Environmental Science & Technology Letters* **1**, 97-101.

CHAPTER 3

EFECT OF PHOSPHATE AND SULFATE ON NI REPARTITIONING DURING FE(II)-CATALYZED FE(III) OXIDE MINERAL RECRYSTALLIZATION

Submitted to *Geochimica et Cosmochimica Acta* as:
Hinkle, M.A.G., Catalano, J.G. (2015) Effect of phosphate and sulfate on Ni repartitioning during Fe(II)-catalyzed Fe(III) oxide mineral recrystallization.

3.1 ABSTRACT

Dissolved Fe(II) activates coupled oxidative growth and reductive dissolution of Fe(III) oxide minerals, causing recrystallization and the repartitioning of structurally-compatible trace metals. Phosphate and sulfate, two ligands common to natural aquatic systems, alter Fe(II) adsorption onto Fe(III) oxides and affect Fe(III) oxide dissolution and precipitation. However, the effect of these oxoanions on trace metal repartitioning during Fe(II)-catalyzed Fe(III) oxide recrystallization is unclear. The effects of phosphate and sulfate on Ni adsorption and Ni repartitioning during Fe(II)-catalyzed Fe(III) oxide recrystallization were investigated as such repartitioning may be affected by both Fe(II)-oxoanion and metal-oxoanion interactions. Phosphate substantially enhances Ni adsorption while decreasing macroscopic Fe(II)-catalyzed release of Ni from hematite and goethite. In contrast, sulfate has little effect on macroscopic Ni adsorption and release of Ni from Fe(III) oxides. Both phosphate and sulfate enhance Fe(II)-catalyzed incorporation of Ni into goethite, with sulfate having a substantially larger effect than phosphate. Conversely, phosphate and sulfate were found to suppress the incorporation of Ni into hematite, with phosphate causing near complete inhibition. This demonstrates that phosphate and sulfate have unique, mineral-specific interactions with Ni during Fe(II)-catalyzed Fe(III) oxide recrystallization. This research suggests that micronutrient bioavailability at redox interfaces in hematite-dominated systems may be especially suppressed by phosphate, while both oxoanions likely have limited effects in goethite-rich soils or sediments. Phosphate may also exert a large control on contaminant fate at redox interfaces, increasing Ni retention on iron oxide surfaces. These results further indicate that trace metal retention by iron oxides during lithification and later repartitioning during diagenesis may be substantially altered in the presence of oxoanions.

3.2 INTRODUCTION

Fe(III) oxide minerals are prevalent in modern and ancient soils and sediments (Cornell and Schwertmann, 2003) and often control the concentrations of trace elements through adsorption processes (Brown et al., 1999; Brown and Parks, 2001). The biogeochemical cycling of Fe results in the coexistence of aqueous Fe(II) and solid Fe(III) oxides at redox interfaces in natural aquatic systems. Such Fe cycling activates secondary abiotic reactions between aqueous Fe(II) and solid Fe(III) oxides, involving the oxidative adsorption of Fe(II) and the subsequent reduction of a structural Fe(III) cation elsewhere on the surface via interfacial electron transfer and atom exchange (ET-AE) processes (Williams and Scherer, 2004; Larese-Casanova and Scherer, 2007; Yanina and Rosso, 2008; Handler et al., 2009; Gorski and Scherer, 2011; Handler et al., 2014). Fe(II)-Fe(III) ET-AE reactions result in spatially separated growth and dissolution, leading to self-recrystallization of crystalline Fe(III) oxides (Handler et al., 2009; Catalano et al., 2010; Handler et al., 2014), Fe isotope fractionation and equilibration (Pedersen et al., 2005; Crosby et al., 2005; Wu et al., 2010; Beard et al., 2010), and metastable Fe oxide phase transitions (Hansel et al., 2003; Hansel et al., 2004; Pedersen et al., 2005; Hansel et al., 2005; Yang et al., 2010).

Previous work has shown that the presence of aqueous Fe(II) leads to the incorporation of structurally compatible trace elements, such as Ni (Frierdich et al., 2011), into goethite and hematite. Conversely, Fe(II) also causes the release to solution of trace metals preincorporated into Fe(III) oxides (Latta et al., 2012b; Frierdich and Catalano, 2012). This dynamic Fe(II)-catalyzed trace element cycling scales with Fe(II) surface coverage (Frierdich and Catalano, 2012), and is fundamentally the result of Fe(III) oxide mineral recrystallization (Pedersen et al., 2005; Handler et al., 2009; Latta et al., 2012b; Gorski et al., 2012; Frierdich et

al., 2014).

Fe(III) oxide recrystallization, dissolution, and precipitation processes are affected by phosphate and sulfate (Bondietti et al., 1993; Stumm, 1997; Eggleston et al., 1998; Majzlan and Myneni, 2005; Borch et al., 2007), two oxoanions common in natural aquatic systems. Isotope tracer experiments show that phosphate enhances the extent of Fe(II)-Fe(III) atom exchange with goethite (Latta et al., 2012a). Recent research shows that both sulfate and phosphate enhance Fe(II) adsorption onto hematite and goethite through a combination of ternary complexation and electrostatic interactions, with the specific interaction dependent on both mineral and oxoanion identity (Hinkle et al., 2015). Processes associated with ET-AE reactions may thus be affected differently by phosphate and sulfate and vary with iron mineralogy.

In this study, we examine how phosphate and sulfate alter Ni repartitioning during Fe(II)-catalyzed Fe(III) oxide recrystallization. To identify how phosphate and sulfate alter Ni redistribution during Fe(III) oxide recrystallization, the effect of these oxoanions on Fe(II)-catalyzed Ni release from and incorporation into hematite and goethite was studied. The effect of phosphate and sulfate on macroscopic Ni adsorption was also investigated, as Ni adsorption is an important intermediate during Ni incorporation into and release from Fe oxides and oxoanions often enhance the adsorption of divalent metal cations, e.g., Cd, Co, Cu, Fe, Pb, and Zn (Benjamin and Bloom, 1981; Balistrieri and Murray, 1982; Diaz-Barrientos et al., 1990; Madrid et al., 1991; Hoins, 1993; Venema et al., 1997; Collins et al., 1999; Jeon et al., 2001; Juang and Wu, 2002; Swedlund et al., 2003; Hinkle et al., 2015). Ni partitioning between adsorbed, incorporated, and aqueous Ni phases was determined through combined X-ray absorption fine structure (XAFS) spectroscopy and mass balance calculations.

3.3 MATERIALS AND METHODS

3.3.1 Fe Oxide Preparation

Pure and Ni-substituted hematite and goethite (Hem, NiHem, Goe, and NiGoe, respectively) were prepared following previously published syntheses (Frierdich et al., 2011; Hinkle et al., 2015), modified from the procedures described in Schwertmann and Cornell (2000). After synthesis, Hem and Goe were rinsed and filtered with deionized (DI) water (>18.2 MΩ·cm) to remove excess electrolytes. The NiHem and NiGoe were filtered and washed with 0.25 M HCl for two hours to remove adsorbed Ni, and were then rinsed and filtered with DI water to remove excess electrolytes. The iron oxides were resuspended in DI water and stored in polypropylene bottles wrapped in aluminum foil.

The mineral suspensions were subsequently moved to an anaerobic chamber (Coy Laboratory Products, Inc., 3% H_2/97% N_2 atmosphere with Pd catalysts) and sparged with the anaerobic chamber atmosphere, as described elsewhere (Hinkle et al., 2015). The mineral suspensions were sparged until a colorimetric indicator test (CHEMets® Kit K-7540) indicated that dissolved O_2 was below the detection limit (2.5 μg L^{-1}). A portion of each mineral suspension was then dried at 70 ^{o}C for mineral characterization by BET analysis (N_2 adsorption, Quantachrome Instruments Autosorb-1) for surface area determination, powder X-ray diffraction (XRD; Bruker D8 Advance X-ray diffractometer, Cu K_α radiation) for phase identification, and fractional and total acid dissolution [described in past research (Frierdich et al., 2011)] for the distribution and extent of Ni substitution. Fluorescence-yield Ni K-edge XAFS spectra were obtained for NiHem and NiGoe wet pastes to ensure consistency with previously published works (Frierdich et al., 2011); the preparation of these samples and collection of these measurements are described below.

3.3.2 Stock Solution Preparation

An Fe(II) stock solution was prepared from $FeCl_2 \cdot 4H_2O$ in the anaerobic chamber using deoxygenated DI water, acidified to pH 2 with HCl, and stored in amber polypropylene bottles to prevent photo-oxidation. Na_2HPO_4, Na_2SO_4, $NiCl_2$, NaCl, and 3-(N-morpholino)propanesulfonic acid hemisodium salt (MOPS) buffer stock solutions were also prepared in the anaerobic chamber using deoxygenated DI water. HCl and NaOH solutions for pH adjustments were transferred to and sparged in the anaerobic chamber more than 90 days before use.

3.3.3 Macroscopic Ni Adsorption Experiments

The effect of phosphate and sulfate on Ni adsorption onto Fe(III) oxides was investigated through a series of adsorption experiments. The experiments consisted of 1 g L^{-1} Hem (or Goe) reacted 0 or 0.1 mM phosphate (or sulfate), 10 mM NaCl (for ionic strength buffering), 1.0 mM MOPS buffer, and varying initial Ni concentrations at pH 7.00 ± 0.05. The experiments were also conducted with mineral-free blanks to assess systematic errors in the initial Ni concentrations and in triplicate for samples reacted with an initial 100 μM Ni. The samples were prepared by adding phosphate (or sulfate), NaCl, MOPS buffer, and Ni to the appropriate amount of deoxygenated DI water in 15 mL conical centrifuge tubes. An aliquot of Hem (or Goe) suspension was then added to the sample, marking the start of the reaction, and the pH of the sample was adjusted to pH 7.00 ± 0.05 using HCl or NaOH. The centrifuge tubes were rotated on end-over-end rotators for five days while wrapped in aluminum foil. The sample pH was checked and adjusted if necessary after 24 hours reaction time. After 5 days of reaction, the pH of each sample was recorded and the samples were filtered (0.22 μm MCE filters; Fisher

Scientific), discarding the first 1 mL of filtrate. The samples were removed from the anaerobic chamber and immediately acidified to 2% HNO_3 (trace metal grade; Fisher Scientific) for inductively coupled plasma-optical emission spectroscopic (ICP-OES; Perkin Elmer Optima 7300 DV) analysis for dissolved P and Ni concentrations. Sulfate concentrations were measured by ion chromatography (IC; Metrohm 881 Compact IC Pro), with samples acidified to 0.5% HCl (trace metal grade; Fisher Scientific). The sample uncertainty (95% confidence level) was calculated for ICP-OES analyses using the triplicate samples and the instrument triplicate measurements.

3.3.4 Ni Release Experiments

The rate and extent of Fe(II)-catalyzed Ni release from NiHem and NiGoe in the absence and presence of phosphate and sulfate were probed by macroscopic Ni release and X-ray absorption near edge structure (XANES) spectroscopy, heretofore collectively referred to as "Ni release experiments." The macroscopic Ni release experiments were conducted following the protocol outlined in Frierdich and Catalano (2012): each sample consisted of 1 g L^{-1} NiHem (or NiGoe), 10 mM NaCl, 1.0 mM MOPS buffer, and 0 or 1.0 mM Fe(II), with samples reacted for 1 hour, 3 hours, 1 day, 2 days, 3 days, 5 days, 8 days, and 14 days. Experiments employed 0 or 0.1 mM phosphate (or sulfate) concentrations; the 14 days samples were prepared in triplicate. The samples were prepared by adding deoxygenated DI water with the appropriate aliquots of NaCl, MOPS buffer, Fe(II), and phosphate (or sulfate). The solutions were adjusted to pH 7.00 ± 0.05. The appropriate amount of NiHem or NiGoe was then added to the solution, marking the beginning of the experiment. Sample pH was checked and adjusted for drift if necessary. The samples were then wrapped in aluminum foil and placed on an end-over-end rotator. At the end

of the prescribed reaction time, the sample pH was recorded and the sample was filtered using 0.22 μm MCE filters (Fisher Scientific). The filtrate samples were acidified and analyzed for dissolved Fe, Ni, and P concentration with ICP-OES and sulfate concentrations with IC following the procedures outlined in the previous section. The macroscopic Ni release data were fit using a second order kinetic model (Appendix), using the approach described by Frierdich and Catalano (2012). To determine how solid-associated Ni partitioning is altered during Ni release in the presence of oxoanions, large batches of the 14 day samples equilibrated at pH 7.5 (to increase the possibility of detecting adsorbed Ni, if present) were filtered and prepared following procedures described below for XAFS spectroscopic measurements. Previous research indicates that increasing pH from 7 to 8 does not alter overall macroscopic Ni release from NiGoe (Frierdich and Catalano, 2012), thus overall macroscopic Ni release likely exhibits the same behavior at pH 7 and 7.5.

3.3.5 Ni Incorporation Experiments

The effect of sulfate and phosphate on Ni incorporation into Hem and Goe in the presence of aqueous Fe(II) was investigated following a previously published procedure (Frierdich et al., 2011). In these experiments, 4 g L^{-1} Hem or Goe was reacted with a solution consisting of 0.2 mM Ni, 10 mM NaCl, 1.0 mM MOPS buffer, and varying concentrations of Fe(II), sulfate or phosphate at pH 7.50 ± 0.05 for 30 days. The sulfate experiment samples were reacted with 1.0 mM Fe(II) and 0, 0.1, or 1.0 mM sulfate. To prevent the precipitation of secondary mineral phases (e.g., vivianite), the phosphate samples were reacted with lower Fe(II) and oxoanion concentrations: 0.5 mM Fe(II) and 0, 0.1, or 0.5 mM phosphate. At the end of the experiment, the suspensions were filtered and prepared for XAFS spectroscopic measurements

following the procedures described below, while the filtrate was collected for ICP-OES analysis. These experiments will be referred to as "Ni incorporation experiments" throughout the paper.

3.3.6 XAFS Spectroscopic Measurements

Fluorescence-yield Ni K-edge XAFS spectra were collected for samples from the Ni release and Ni incorporation experiments, as well as end-member standards: NiHem, NiGoe, and Ni adsorbed onto Hem and Goe in the presence of sulfate and phosphate. For comparison to the two different sets of experiments, Ni adsorbed samples were prepared by reacting the maximum concentration of phosphate (or sulfate) and the appropriate concentration of Hem (or Goe) for the applicable experiment with 0.2 mM Ni, 10 mM NaCl, and 1.0 mM MOPS buffer for 5 days. The samples were filtered (reusable syringe filter; 0.22 μm MCE membrane; Fisher Scientific) to collect both filtered solids and filtrate. The filtered solids were packed as wet pastes in polycarbonate sample holders, sealed with 25 μm Kapton tape, and heat sealed in polyethylene bags to maintain anoxic conditions. Samples were prepared within 48 hours of transport to the Advanced Photon Source (APS) at Argonne National Laboratory. XAFS spectra of samples the standard for the Ni release experiments were collected at beamline 12-BM-B, while XAFS measurements for the Ni incorporation experiment XAFS were made at beamline 9-BM-C. Both beamlines employ Si (111) fixed-offset double-crystal monochromators, which were detuned 30% to reduce the harmonic content of the incident X-ray beam, as well as torroidal focusing and flat harmonic rejection mirrors. The monochromators were calibrated at the Ni K-edge (8333 eV) using a Ni metal foil. Fluorescence-yield spectra were collected using a 12-element energy dispersive Ge detector.

3.3.7 Analysis of XAFS Spectra

XAFS spectra were averaged and normalized using IFEFFIT (Newville, 2001) via the Athena interface (Ravel and Newville, 2005). Linear combination fitting (LCF) of normalized XANES spectra was performed using Athena, with Ni-substituted hematite and goethite (NiHem and NiGoe) and Ni adsorbed onto pure hematite (Hem) and goethite (Goe) as end-member standards. The k^3-weighted extended X-ray absorption fine structure (EXAFS) spectra of Ni adsorbed Hem and Goe standards were quantitatively fit using SixPack (Webb, 2005) using backscattering phase and amplitude functions generated in FEFF 9.6. (Rehr et al., 2010) from the crystal structure of trevorite ($NiFe_2O_4$) (Hill et al., 1979) and sarcopside [$(Ni_{0.89}Fe_{2.11})P_2O_8$] (Ericsson and Nord, 1984). Nonlinear least-squares fits were obtained by refining coordination number (N), interatomic distance (R), and σ^2 (a Debye-Waller type factor) (Table A3.1). The EXAFS spectra were fit in R-space from 1-4.2 Å for Ni adsorbed onto goethite and 1-5 Å for Ni adsorbed onto hematite. S_0^2, the amplitude reduction factor, was fixed to 0.9 (Frierdich et al., 2011). The σ^2 values were determined using a preliminary fit, and were kept constant for each mineral set (e.g., σ^2 of Ni-Fe1 for Hem and Goe is 0.01 and 0.004, respectively; σ^2 of Ni-Fe2 for Hem and Goe is 0.009 and 0.008, respectively) to better compare fits between different conditions and oxoanions.

3.4. RESULTS

3.4.1 Properties of Minerals and Materials

The minerals prepared and used in these experiments have similar properties as those reported in previous studies (Frierdich et al., 2011; Hinkle et al., 2015). BET surface areas for Hem, Goe, NiHem and NiGoe are 30.1, 42.0, 12.0, and 21.7 $m^2\ g^{-1}$, respectively. The Ni content

of NiHem and NiGoe are 1.9 and 1.4 mol %, respectively. The fractional dissolution of Ni and Fe from NiHem and NiGoe is near congruent (Figure A3.1), in agreement with prior studies of Ni substitution in Fe oxides (Sidhu et al., 1978; Lim-Nunez and Gilkes, 1985; Wells et al., 2001; Frierdich and Catalano, 2012). Ni EXAFS spectral fits of the NiHem and NiGoe materials (not shown) are consistent with EXAFS spectra from previous studies, and are described in detail therein (Singh et al., 2002; Frierdich et al., 2011).

3.4.2 Sulfate and Phosphate Coadsorption with Ni

The macroscopic adsorption of Ni onto both Hem and Goe in the presence and absence of phosphate or sulfate are well described by Langmuir isotherms (Figure 3.1, Table 3.1). Consistent with previous research (Arai, 2008), Hem shows a greater affinity for Ni than Goe. The presence of 0.1 mM sulfate has little effect on Ni adsorption onto Goe, but slightly enhances Ni adsorption onto Hem. The addition of 0.1 mM phosphate, however, increases Ni adsorption by ~165% for both the Goe and Hem systems. Ni enhances both phosphate and sulfate adsorption onto Hem to a greater degree than onto Goe (Figures A3.2,A3.3). Phosphate adsorption increases linearly with increasing Ni adsorption ($R^2 > 0.8$) (Figure A3.2B), but there is no clear trend for sulfate adsorption (Figure A3.3B).

The EXAFS spectra of Ni adsorbed onto Hem and Goe in the presence of sulfate or phosphate show little variation with oxoanion or mineral concentration and are well reproduced by structural model fits (Figure 3.2). The local coordination environment of Ni adsorbed to Goe and Hem, with the exception of 1 g L^{-1} Hem reacted with phosphate, are in agreement with the observations of Frierdich et al. (2011) and Arai (2008) for oxoanion-free systems. This indicates that sulfate has little effect on Ni adsorption mechanisms onto Fe(III) oxides. Phosphate also has

no observed effect on Ni adsorption mechanisms on goethite or, at high mineral concentrations (4 g L^{-1}, used for the Ni incorporation experiments), on hematite. However, at low Hem concentration (1 g L^{-1}, used for the Ni release experiments), Ni coordination changes, suggesting the presence of a Ni-PO_4 ternary complexes. This is supported by the need to include a P neighbor at ~3.8 Å to reproduce the EXAFS spectrum of this sample (Table A3.1). In addition, the corner-sharing Ni complex (interatomic Ni-Fe distance of ~4.10 Å) does not appear due to a low availability of surface sites. These large effects on Ni adsorption in the presence of phosphate indicate that Ni-phosphate ternary complexes form, while the effect of sulfate is less substantial, suggesting that Ni-sulfate interactions may be dominated by electrostatic interactions.

3.4.3 Effect of Sulfate and Phosphate on Ni Release

NiHem and NiGoe were reacted in the presence and absence of sulfate, phosphate, and Fe(II) to investigate how oxoanions alter Ni release to solution. In the absence of aqueous Fe(II) and oxoanions, 0.8 and 0.7 μM Ni is released from NiHem and NiGoe, respectively, to solution over 14 days, corresponding to 0.32 and 0.44% of the total incorporated Ni being released (Figure 3.3). Sulfate does not affect Ni release from either mineral in the Fe(II)-free system. The presence of phosphate, however, suppresses Ni release from NiGoe to 0.31 μM Ni and inhibits Ni release from NiHem, with the amount of Ni released below the detection limit (0.1 μM).

The presence of aqueous Fe(II) greatly increases Ni release from Ni-substituted Fe(III) oxides (Frierdich et al., 2011; Frierdich and Catalano, 2012) due to Fe(II)-Fe(III) ET-AE reactions increasing the rate of iron oxide recrystallization (Pedersen et al., 2005; Handler et al., 2009; Latta et al., 2012b; Gorski et al., 2012; Frierdich et al., 2014). The addition of oxoanions

does not appear to alter the rate of Ni release from Fe(III) oxides, but the overall amount of Ni released is substantially suppressed by phosphate. Fe(II)-catalyzed Ni release from NiHem and NiGoe in the presence and absence of oxoanions is consistent with a second-order rate reaction, in agreement with past research of oxoanion-free systems (Frierdich and Catalano, 2012). The second-order rate reaction describing the Ni release data in the current paper was confirmed following the integral method (Brantley and Conrad, 2008). The kinetic fit parameters (Table 3.2) show that the overall amount of Ni released is less for NiHem than for NiGoe in the absence of oxoanions (with 1.3% and 9% of substituted Ni released, respectively), consistent with past research (Frierdich et al., 2011; Frierdich and Catalano, 2012). The addition of 0.1 mM sulfate has no effect on Ni release from NiHem and NiGoe, with the fit results within error of those for the oxoanion-free system. Phosphate suppresses the total Ni released from NiHem and NiGoe to just 0.64% and 1.6%, respectively, meaning that an additional 0.66% and 7.4% of the preincorporated Ni remains associated with the solid phase relative to the oxoanion-free experiments.

To investigate the origin of the increase in solid-associated Ni upon phosphate addition during these Ni release experiment, the relative amounts of incorporated and adsorbed Ni were determined with XANES spectroscopy. The percent of Ni associated with the solid that remains incorporated at the end of the Ni release experiments was calculated by least-squares linear combination fitting (LCF) of the XANES data, using the Ni substituted Fe(III) oxides and Ni adsorbed onto Fe (III) oxides as end-member standards. The LCF results (Figure 3.4, Table 3.2) show that there is no change in the percent of Ni incorporated, when in the absence or presence of oxoanions, for either the NiHem or NiGoe systems, with 100% and ~98%, respectively, of solid-associated Ni remaining incorporated at the end of the release experiments. These results

show that Ni is not accumulating as an adsorbed layer during Ni release; any Ni that readsorbs to the surface is reincorporated during Fe(II)-catalyzed Fe(III) oxide recrystallization. Thus, these results show that the decrease in macroscopic Ni release from Goe with phosphate cannot solely be due to enhanced readsorption, because that scenario requires 7.4% of the solid-associated Ni to be adsorbed, well in excess of the LCF uncertainty (± 2%). In the hematite system, the LCF uncertainty is greater than the increase in Ni adsorption needed to explain the decrease in macroscopic Ni release from NiHem with phosphate. However, Ni adsorption onto both Hem and Goe increases substantially upon phosphate addition and it is thus unlikely that buildup of adsorbed Ni during Ni release is an important process for Hem but is irrelevant in the Goe system.

3.4.4 Effect of Sulfate and Phosphate on Ni Incorporation

XAFS spectroscopy was also used to assess the effect of sulfate and phosphate on the reverse process, Fe(II)-catalyzed Ni incorporation into pure Hem and Goe (Figure 3.5). The presence of three isosbestic points when comparing the XANES spectra of the experimental samples and the adsorbed Ni and Ni substituted Fe(III) oxide standards (not shown) suggest that the samples contain mixtures of adsorbed and incorporated Ni. This is consistent with previous findings of Fe(II)-catalyzed Ni incorporation into Hem and Goe (Frierdich et al., 2011). Fitting of the experimental XANES spectra (Table 3.3) quantified the percentage of solid-associated Ni that is incorporated versus adsorbed. These fitting results are combined with the total concentration of Ni associated with the solid, obtained from the filtrate ICP-OES data, to calculate by mass balance the concentration of incorporated and adsorbed Ni (Table 3.3). The uncertainties in the calculated incorporated and adsorbed Ni concentrations were obtained using

both the uncertainty in the triplicate ICP-OES measurements and the uncertainty in the LCF calculations. In the absence of Fe(II), ~85% of the initial Ni reacted with Hem and Goe is associated with the solid phase at the end of the 30 day reaction. Of that solid-associated Ni, 0 and 17% are incorporated into Hem and Goe, respectively, consistent with past studies of Ni incorporation into goethite in natural and aged synthetic samples (Manceau et al., 2000; Singh et al., 2002; Carvalho-e-Silva et al., 2003). The addition of sulfate increases overall Ni incorporation into Hem and Goe. In contrast, addition of phosphate suppresses Ni incorporation into Goe; Ni incorporation into Hem is within error of zero regardless of the amount of phosphate present. These results indicate that Ni incorporation into Fe(III) oxide minerals in the absence of Fe(II) is affected by oxoanions.

The addition of Fe(II) substantially increases Ni incorporation into Goe, but suppresses the overall amount of sorbed Ni in the Goe system, indicative of competitive adsorption between aqueous Fe(II) and Ni (Table 3.3). Aqueous Fe(II) does not alter the total amount of sorbed Ni in the Hem system, but does increase Ni incorporation. The lack of competitive adsorption effects between Ni and Fe(II) on Hem suggests that the Ni binding affinity for Hem is greater than for Goe, consistent with the adsorption isotherm measurements (Figure 3.1) and past observations (Arai, 2008). In the presence of 1.0 mM Fe(II), ~50% of the total solid-associated Ni incorporates into the solid phase and ~50% adsorbs to the mineral surface for both Goe and Hem. Addition of 0.5 mM Fe(II) (used in the phosphate experiments to prevent vivianite precipitation) results in less Ni incorporation, with 36% and 44% solid-associated Ni incorporated into Hem and Goe, respectively.

Sulfate modifies the partitioning of Ni during Fe(II)-catalyzed Hem and Goe recrystallization. The co-addition of 0.1 mM sulfate and 1.0 mM Fe(II) to a Goe suspension

increases the overall concentration of Ni associated with the solid as a result of increased Ni incorporation (Table 3.3). The addition of 1.0 mM sulfate to this system slightly reduces Ni incorporation relative to the 0.1 mM sulfate experiment. In both Goe experiments, Ni adsorption remains statistically invariant. In contrast, 0.1 mM sulfate has no effect on Ni incorporation into or adsorption onto Hem in the presence of 1.0 mM Fe(II), while 1.0 mM sulfate causes a reduction in Ni incorporation but an increase in Ni adsorption.

Phosphate also affects Ni partitioning during Fe(II)-catalyzed recrystallization of Hem and Goe, but these effects are distinct from the changes caused by sulfate. The addition of 0.5 mM phosphate and Fe(II) decreases the percentage of solid-associated Ni that is incorporated into Goe compared to the oxoanion-free system. However, this apparent decrease in Ni incorporation is due to a substantial increase in Ni adsorption; phosphate actually also enhances the amount of Ni incorporated into Goe (Table 3.3). In the Hem system, however, the addition of phosphate substantially decreases Ni incorporation, with 0.5 mM phosphate causing complete inhibition.

3.5. DISCUSSION

3.5.1 Oxoanion- and Mineral-Specific Effects on Ni Repartitioning

Mechanisms of Oxoanion Effects on Ni Repartitioning

Phosphate in general has a substantially greater effect on Ni repartitioning during Fe(II)-catalyzed recrystallization than sulfate. In the hematite system, phosphate strongly suppresses Ni incorporation into and release from the mineral while sulfate only slightly alters the behavior seen in oxoanion-free systems. Fe(II)-catalyzed Ni repartitioning in Fe(III) oxides is fundamentally controlled by adsorption reactions and the effects of oxoanions on this process are

likely the result of molecular interactions of adsorbates on mineral surfaces. Both phosphate and sulfate form surface complexes with bidentate symmetry on hematite (Paul et al., 2005; Elzinga and Kretzschmar, 2013; Jubb et al., 2013; Hinkle et al., 2015). While phosphate clearly forms bidentate binuclear surface complexes, the nature of sulfate surfaces complexes is unclear regarding whether these are inner- or outer-sphere (or a mixture). The formation of bidentate binuclear surface complexes likely suppresses hematite dissolution and growth (Bondietti et al., 1993; Stumm, 1997). Therefore phosphate surface complexes may effectively prevent hematite recrystallization, inhibiting Fe(II)-catalyzed Ni repartitioning. Adsorbate inhibition of recrystallization, however, cannot be a dominant process in the sulfate-hematite system because Ni incorporation into hematite in the absence of Fe(II) actually increases upon addition of sulfate. The subsequent decrease in Ni incorporation into hematite when 1.0 mM sulfate and 1.0 mM Fe(II) are added thus suggests that Fe(II)-sulfate-hematite interactions, which include the formation of Fe(II)-sulfate ternary surface complexes (Hinkle et al., 2015), are likely responsible for the observed effect.

Oxoanion-Fe(II) interactions are also important in controlling Ni repartitioning behavior in the phosphate-goethite system, as phosphate suppresses Ni incorporation in the absence of Fe(II) but enhances Ni incorporation in the presence of Fe(II) (Table 3.3). The Fe(II)-free experiments are in agreement with previous research finding that phosphate suppresses goethite dissolution in the absence of Fe(II) (Stumm, 1993; Biber et al., 1994). The effect of phosphate in the Fe(II) system is consistent with a recent isotope exchange study demonstrating that phosphate enhances the rate and extent of Fe atom exchange between goethite and aqueous Fe(II) (Latta et al., 2012a). Increased Fe(II)-catalyzed goethite recrystallization upon phosphate addition should lead to increased macroscopic Ni release. In phosphate-free Fe(II)-catalyzed Ni

release experiments, most (>85%) of the Ni released is actually reincorporated into goethite rather than remaining in the aqueous phase (Frierdich et al., 2012). Because phosphate substantially increases Ni adsorption (Figure 3.1; Table 3.1) (a necessary intermediate during incorporation), phosphate likely increases Ni reincorporation during Fe(II)-catalyzed goethite recrystallization, thereby decreasing macroscopic Ni release. Phosphate thus enhances Ni incorporation into goethite in both the Fe(II)-catalyzed Ni release and Ni incorporation experiments by increasing Fe(II)-catalyzed goethite recrystallization (Latta et al., 2012a) through increased Fe(II) surface coverage (Hinkle et al., 2015), and by substantially increasing Ni (re)adsorption to (and therefore Ni (re)incorporation into) the surface.

Although sulfate also enhances Fe(II)-catalyzed Ni incorporation into goethite, its effect on Ni release differs substantially from the phosphate-goethite system. Interestingly, sulfate exhibits different effects on total macroscopic Ni sorption onto goethite in the absence (Figure 3.1; Table 3.1) and presence of Fe(II) (Table 3.3). These results suggest that sulfate moderates Ni-Fe(II) competitive adsorption on goethite, preferentially increasing overall Ni sorption without affecting Fe(II) surface coverage. By lessening Ni-Fe(II) competitive adsorption effects on goethite, sulfate allows more Ni to adsorb to the surface and thus become incorporated into goethite. Competitive adsorption of Ni and Fe(II) is likely less substantial in the Ni release experiments because of the lower Ni concentrations. As a result, sulfate does not appreciably affect Ni release.

Mineral-Specific Effects

Although the mechanisms through which each oxoanion alters Ni cycling in Fe(III) oxides differ depending on the specific oxoanion-mineral system, goethite- and hematite-specific

effects are observed, suggesting these minerals exhibit distinct behaviors during biogeochemical Fe cycling in the presence of oxoanions. Both oxoanions decrease Fe(II)-catalyzed incorporation of Ni into hematite and phosphate suppresses Ni release from this mineral. These observations suggest that Fe(II)-catalyzed Ni cycling through hematite is inhibited by oxoanions because such species alter Fe(II) adsorption mechanisms and hematite recrystallization. Conversely, this research indicates that phosphate and sulfate do not prevent Ni repartitioning during Fe(II)-catalyzed goethite recrystallization, suggesting that these oxoanions do not interfere with Fe(II)-Fe(III) ET-AE processes. Instead, phosphate and sulfate largely affect Ni cycling through goethite by increasing the extent of Ni adsorption. These results suggest that the mineral identity is an important controlling factor in predicting how oxoanions may alter processes associated with Fe(II)-Fe(III) ET-AE reactions.

3.5.2 Environmental and Geological Implications of Trace Element Fate

This study demonstrates that oxoanions common to aquatic systems affect trace element fate at redox interfaces in environmental and geological systems. Because trace metals are often associated with (Singh and Gilkes, 1992; Manceau et al., 2002; Cornell and Schwertmann, 2003) and incorporated into (Singh and Gilkes, 1992; Manceau et al., 2000; Carvalho-e-Silva et al., 2003) naturally-occurring iron oxides, micronutrient bioavailability is often limited by the extractability of these trace metals from iron oxides. Phosphate suppresses net Fe(II)-catalyzed Ni release from hematite. Therefore Ni bioavailability in hematite-dominated environments with Fe redox gradients may be lower in systems with substantial phosphate uptake by iron oxides [e.g., hydrothermal vents (Froelich et al., 1982; Berner et al., 1993) and waterlogged subtropical or tropical soils (Parfitt, 1989; Chacon, 2006)]. However, Ni bioavailability in systems with large

reactive goethite fractions and coexisting aqueous Fe(II) [e.g., soils, lacustrine and marine sediments (Drodt et al., 1997; Cornell and Schwertmann, 2003; van der Zee et al., 2003)] will likely not be affected by oxoanion concentration, as phosphate and sulfate do not impede Ni cycling through goethite.

Heavy metal contamination of soils and aquatic systems is often mediated by iron or manganese oxide adsorption processes (Mench et al., 1994; Fuller and Harvey, 2000; Sowder et al., 2003; Isaure et al., 2005; Waychunas et al., 2005; Tankere-Muller et al., 2007). Phosphate exerts a large effect on macroscopic Ni adsorption onto both hematite and goethite, resulting in decreased Ni concentrations in the aqueous phase. Thus, phosphate may exert a substantial control on Ni retention in riparian soils by increasing Ni adsorption to iron oxide minerals, an important control on the contamination of nearby soils (Sowder et al., 2003). Further entrapment of Ni by incorporation into hematite may, however, be prevented by phosphate and sulfate in these systems. Conversely, enhanced Ni incorporation into goethite by sulfate and phosphate does not translate into increased Ni entrapment, as Ni cycling is not obstructed by either oxoanion.

This research shows that Ni cycling in iron oxides is altered by phosphate and sulfate differently depending on both the mineral identity and the concentration and identity of the oxoanions, which may have important ramifications for the preservation of Ni in the rock record. For example, these results indicate that the amount of Ni incorporated into banded iron formations (BIFs), which formed in oceans containing dissolved Fe(II) (Holland, 1973; Holland, 1984; Derry and Jacobsen, 1990; Holland, 2006), was likely dependent on a number of factors, including the oceanic sulfate and phosphate concentrations. The results of this research also indicate that the retention of Ni may have been affected by the identity of minerals formed

through phase transformations of initial iron (oxyhydr)oxide precipitates during BIF deposition, burial, and lithification. Phosphate could further affect the amount of Ni incorporated into BIFs during lithification by preferentially enhancing Ni adsorption onto iron oxides. Phosphate and sulfate may also alter trace element partitioning during diagenesis and fluid flow through sediments. Thus, the relationship between Ni concentrations in BIFs and ancient seawater is almost certainly not straightforward, as has been assumed in prior studies, e.g., (Konhauser et al., 2009). Instead, recorded Ni concentrations will have a highly non-linear dependence on fluid composition, mineral properties, and depositional and post-depositional processes. The present work clearly shows that species incompatible with Fe(III) oxide structures, such as phosphate and sulfate, still have substantial impacts on the partitioning of structurally compatible metals in a variety of environments, potentially altering micronutrient bioavailability, contaminant sequestration, and geochemical proxies.

3.6 ACKNOWLEDGMENTS

This research was supported by the National Science Foundation (NSF), Division of Earth Sciences, Geobiology and Low-Temperature Geochemistry Program through Grant No. EAR-1056480. ICP-OES analyses were conducted at the Nano Research Facility at Washington University, supported by the NSF through award no. ECS-0335765. Use of the Bruker D8 Advance XRD at Washington University in St. Louis is supported by the National Science Foundation through award no. EAR-1161543. XAFS spectra were collected at beamlines 9-BM-C and 12-BM-B at the Advanced Photon Source, an Office of Science User Facility operated for the U.S. Department of Energy (DOE) Office of Science by Argonne National Laboratory, which is supported by the U.S. DOE under Contract No. DE-AC02-06CH11357.

The authors thank Jennifer Houghton and Sanmathi Chavalmane for their help with collecting IC and ICP-OES analyses, respectively.

Table 3.1. Langmuir isotherm parameters determined for Ni adsorption to goethite and hematite.

Sample	Γ_{max} (μmol g^{-1})	K (mL μmol^{-1})
Hematite		
Oxoanion-free	44 ± 6	12 ± 4
0.1 mM SO_4	58 ± 7	11 ± 3
0.1 mM PO_4	117 ± 2	82 ± 6
Goethite		
Oxoanion-free	15 ± 2	80 ± 40
0.1 mM SO_4	16 ± 2	110 ± 60
0.1 mM PO_4	40 ± 2	250 ± 70

Table 3.2. Kinetic fit parameters, extent of Ni release, and final solid phase Ni speciation following reaction of 1.0 mM Fe(II) with Ni-substituted Fe(III) oxides.

Sample	k_{obs} (μM d^{-1})[a]	$[Ni]_{eq}$ (μM)[a]	Total Release (%)[b]	Ni incorporated (%)[c]
NiHem				
Oxoanion-free	1.3 ± 0.9	3.2 ± 0.3	1.3 ± 0.1	100.0 ± 0.1
0.1 mM SO_4	0.8 ± 0.6	3.4 ± 0.4	1.4 ± 0.1	100.0 ± 0.1
0.1 mM PO_4	21 ± 13	1.6 ± 0.2	0.64 ± 0.04	100 ± 3
NiGoe				
Oxoanion-free	0.03 ± 0.02	14 ± 2	9 ± 1	98 ± 2
0.1 mM SO_4	0.04 ± 0.02	13 ± 1	8 ± 1	98 ± 2
0.1 mM PO_4	90 ± 75	2.6 ± 0.2	1.61 ± 0.06	99 ± 2

[a] Second order kinetics fitting parameters for Fe(II)-catalyzed Ni release from Fe(III) oxides (see Appendix).
[b] Percentage of initial incorporated Ni released from the mineral during reaction.
[c] Speciation of solid-associated Ni at the end of reaction as determined by LCF of Ni XANES spectra.

Table 3.3. Final percent of solid-associated Ni, corresponding Ni distributions, and Fe concentrations in the Ni incorporation experiments.

Sample	Ni incorporated(%)[a]	$[Ni]_{inc}$ (μM)[b]	$[Ni]_{ads}$ (μM)[b]	$[Fe]_{aq}$ (μM)[c]
Hematite Fe(II)-free				
Oxoanion-free	0.4 ± 0.2	1 ± 4	174 ± 4	5 ± 1
0.1 mM PO_4	0 ± 3	0 ± 6	190 ± 6	BDL[d]
0.5 mM PO_4	2 ± 3	3 ± 5	196 ± 5	BDL
0.1 mM SO_4	2 ± 2	3 ± 3	170 ± 3	BDL
1.0 mM SO_4	9 ± 2	18 ± 4	170 ± 4	BDL
Hematite + 0.5 mM Fe(II)				
Oxoanion-free	36 ± 2	67 ± 4	118 ± 4	195 ± 7
0.1 mM PO_4	17 ± 4	32 ± 7	158 ± 7	115 ± 3
0.5 mM PO_4	5 ± 2	10 ± 4	189 ± 4	6.4 ± 0.1
Hematite + 1.0 mM Fe(II)				
Oxoanion-free	50 ± 3	92 ± 6	93 ± 6	403 ± 3
0.1 mM SO_4	48 ± 3	89 ± 6	96 ± 6	545 ± 5
1.0 mM SO_4	40 ± 3	75 ± 5	112 ± 5	430 ± 6
Goethite Fe(II)-free				
Oxoanion-free	17 ± 2	27 ± 3	138 ± 3	BDL
0.1 mM PO_4	14 ± 3	22 ± 6	138 ± 7	BDL
0.5 mM PO_4	4 ± 3	7 ± 5	180 ± 6	BDL
0.1 mM SO_4	25 ± 2	40 ± 3	120 ± 3	8 ± 1
1.0 mM SO_4	19 ± 3	29 ± 4	125 ± 4	23.9 ± 0.5
Goethite + 0.5 mM Fe(II)				
Oxoanion-free	44 ± 2	49 ± 3	63 ± 3	234 ± 5
0.1 mM PO_4	44 ± 3	52 ± 4	66 ± 4	214 ± 5
0.5 mM PO_4	32 ± 2	58 ± 4	126 ± 6	32.5 ± 0.4
Goethite + 1.0 mM Fe(II)				
Oxoanion-free	50 ± 3	52 ± 3	52 ± 3	638 ± 16
0.1 mM SO_4	62 ± 3	83 ± 4	50 ± 4	674 ± 15
1.0 mM SO_4	58 ± 2	74 ± 4	54 ± 4	657 ± 9

[a] Percentage of solid-associated Ni incorporated into the Fe(III) oxide, calculated by LCF of XANES spectra

[b] Concentration of Ni that is incorporated or adsorbed, calculated using final aqueous Ni concentrations determined by ICP-OES and the LCF XANES spectral fits.

[c] Concentration of Fe remaining in solution at the end of the 30-day Ni incorporation experiments, determined by ICP-OES of the filtrate.

[d] Measured analyte below detection limit (BDL)

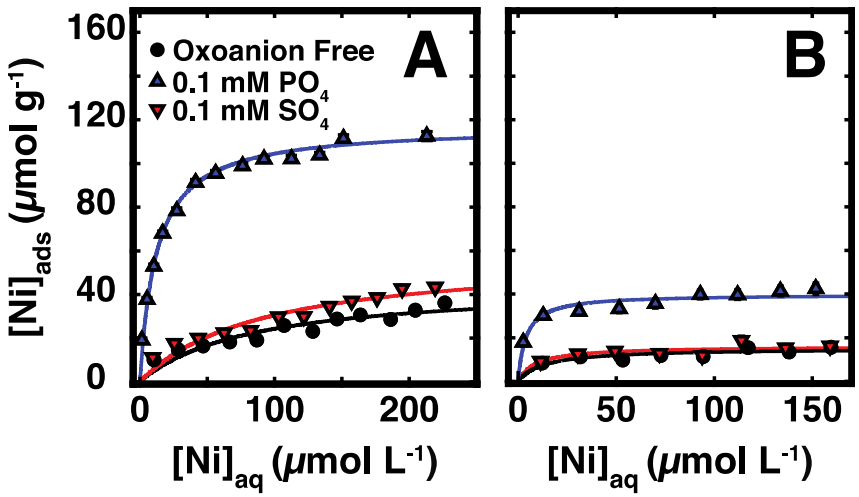

Figure 3.1. Ni adsorption isotherms at pH 7 on Hem (A) and Goe (B). Lines represent Langmuir isotherm fits to the data.

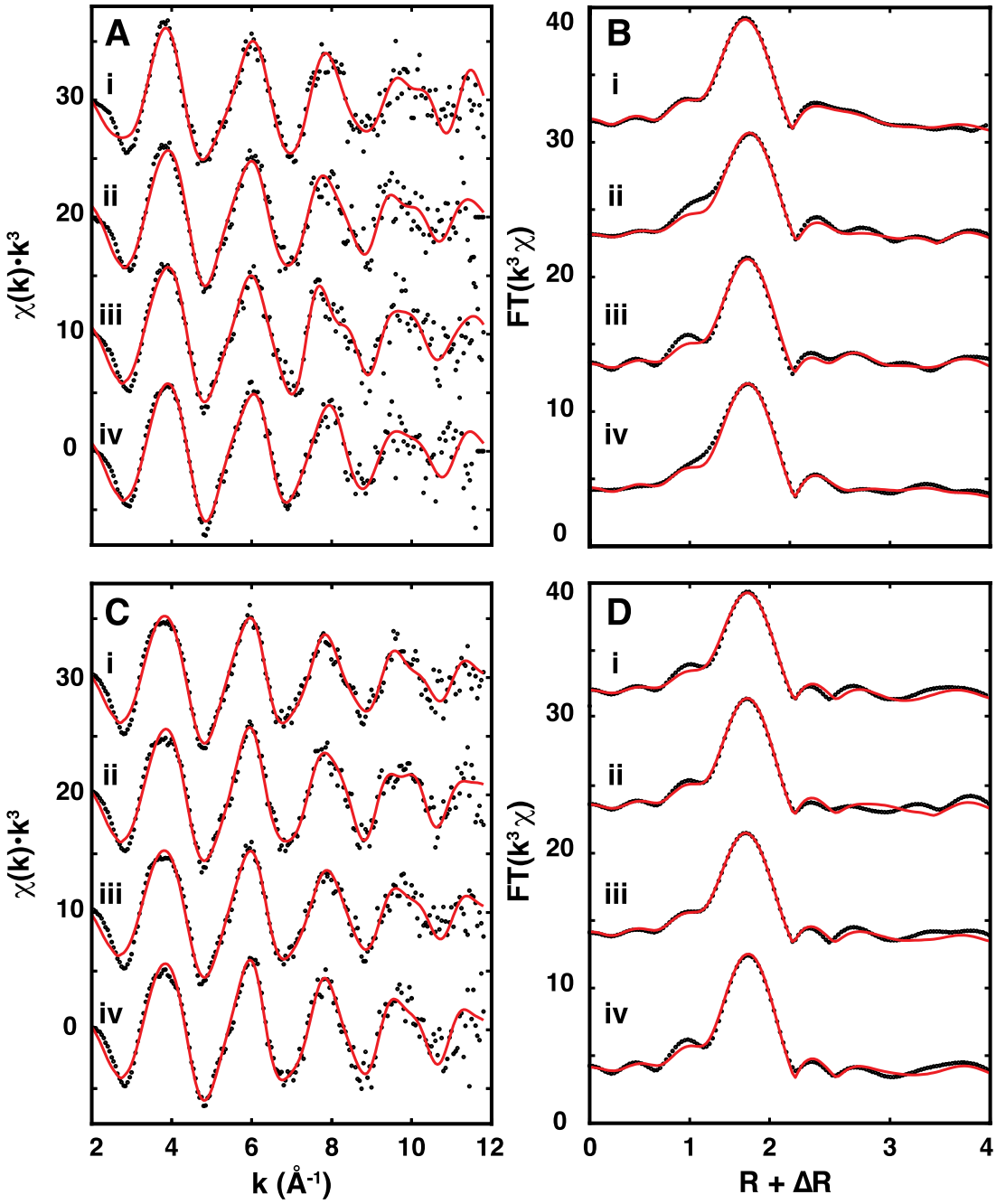

Figure 3.2. Ni fluorescence EXAFS spectra (points) and structural model fits (red lines) for Ni adsorbed onto hematite (A, B) and goethite (C, D) with (i) 0.1 mM phosphate and 1 g L^{-1} Fe(III) oxide, (ii) 0.5 mM phosphate and 4 g L^{-1} Fe(III) oxide, (iii) 0.1 mM sulfate and 1 g L^{-1} Fe(III) oxide, and (iv) 1.0 mM sulfate and 4 g L^{-1} Fe(III) oxide.

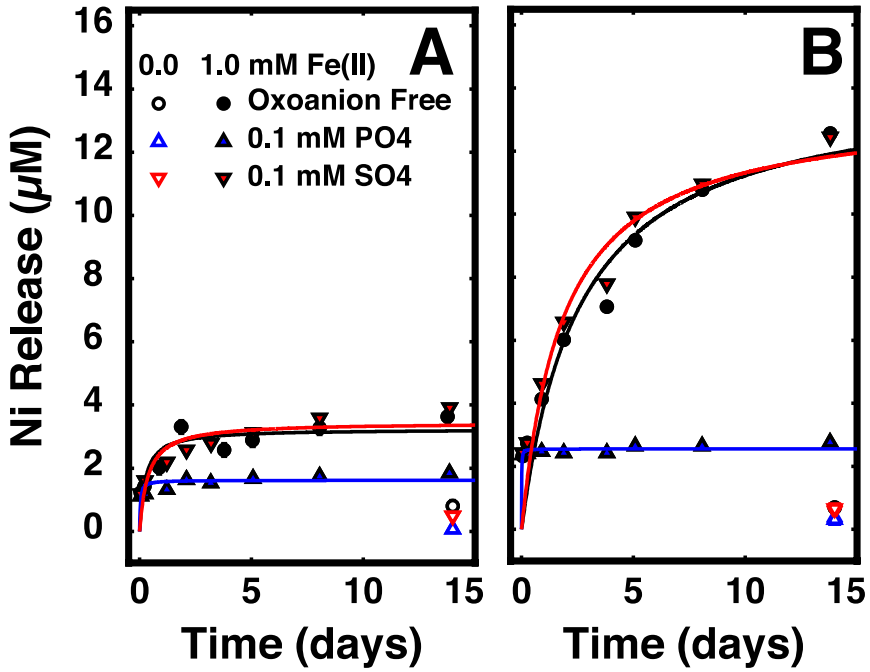

Figure 3.3. Ni release at pH 7 from NiHem (A) and NiGoe (B). Filled symbols represent samples reacted with 1 mM Fe(II); open symbols represent samples reacted in the absence of Fe(II). Lines represent second-order kinetic fits to the data.

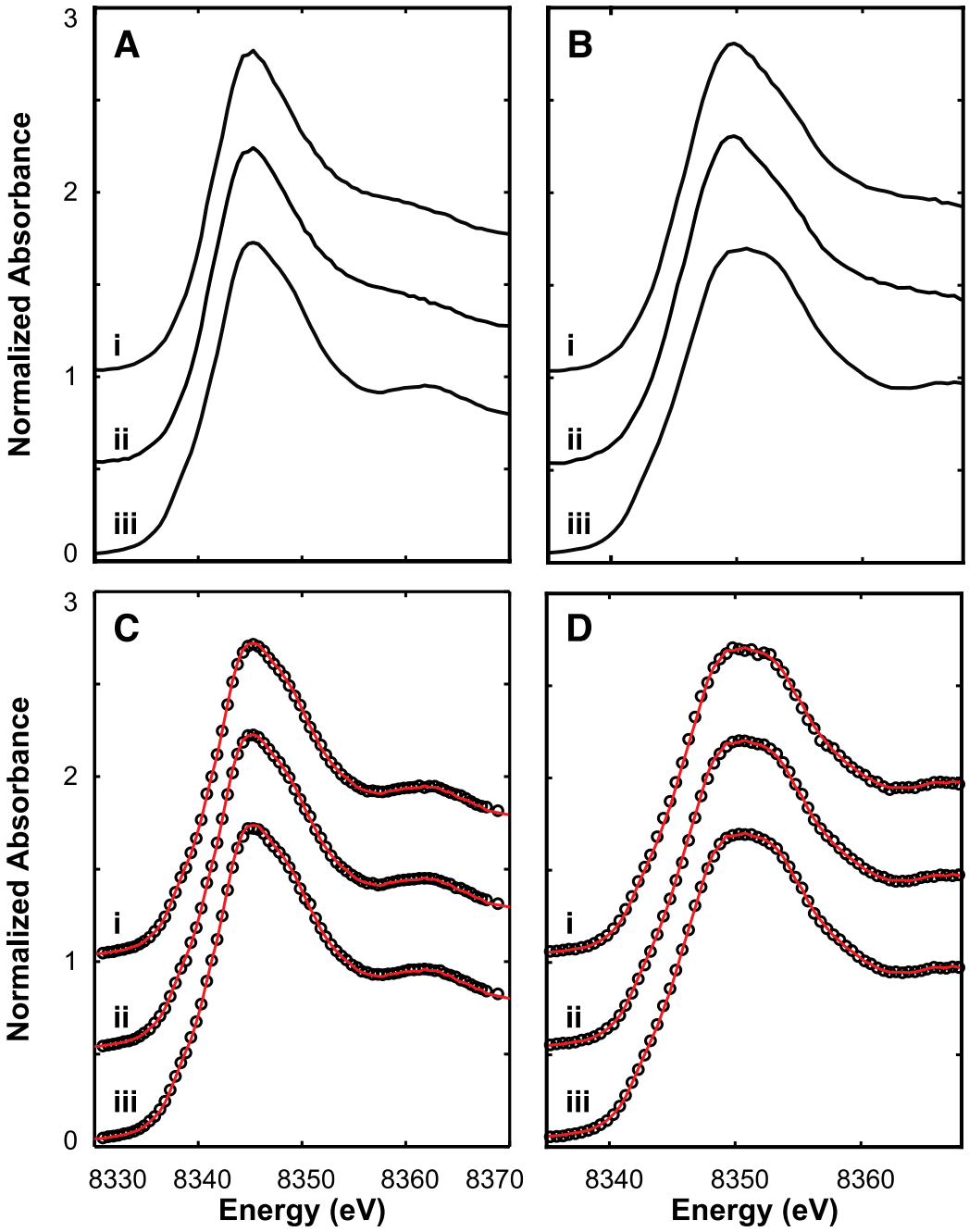

Figure 3.4. Ni fluorescence XANES of standards used for LCF fitting of Ni release experiments with goethite (A) or hematite (B): Adsorbed Ni with 0.1 mM phosphate (i) or 0.1 mM sulfate (ii), and incorporated Ni (iii); and XANES (points) and LCF fits (red lines) for solids collected at the end of Ni release experiments at pH 7.5 with NiGoe (C) and NiHem (D) for samples reacted with 0.1 mM phosphate (i), with 0.1 mM sulfate (ii), and without oxoanions (iii).

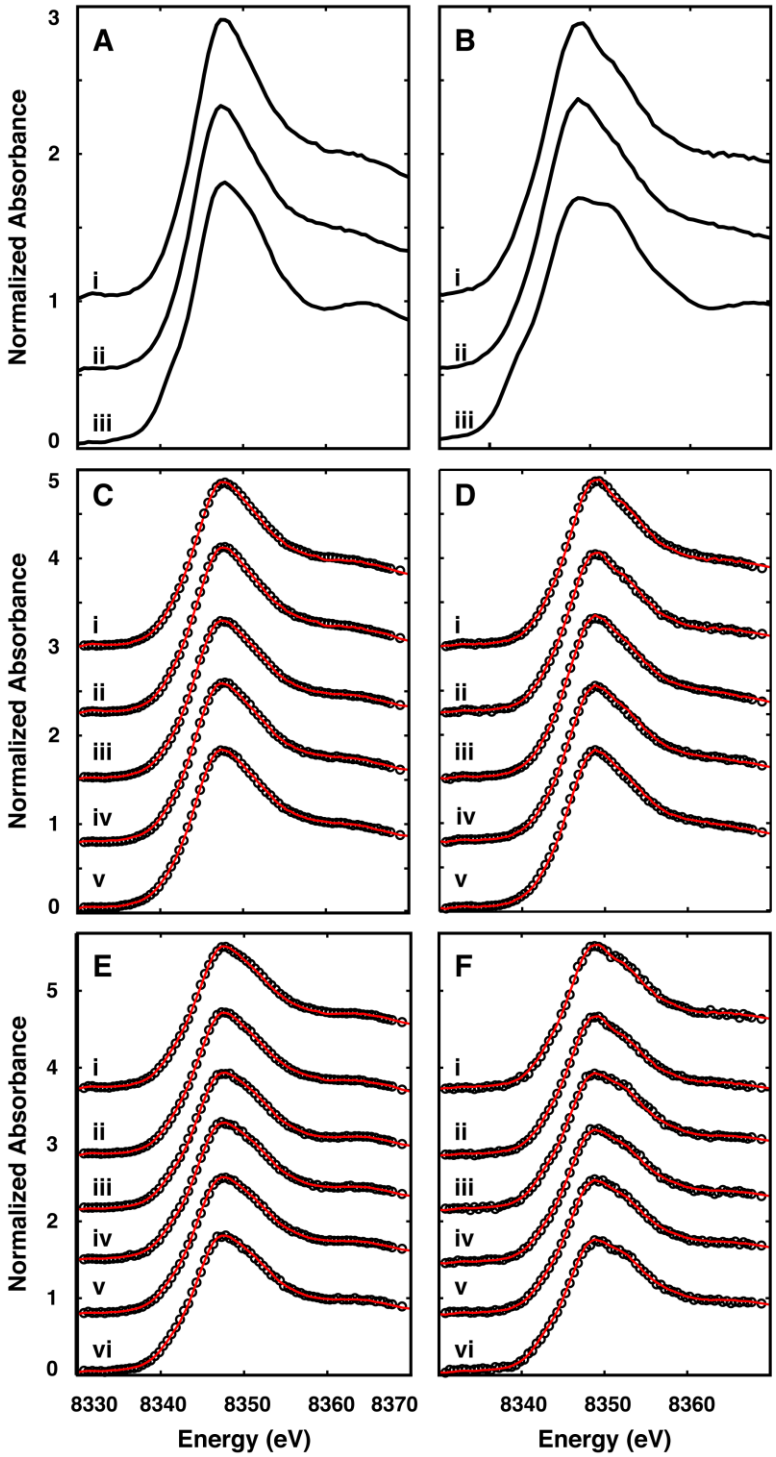

Figure 3.5. Ni XANES spectra of standards used for LCF fitting of Ni incorporation experiments with goethite (A) or hematite (B): Adsorbed Ni with 0.5 mM phosphate (i) or 1.0 mM sulfate (ii), and incorporated Ni (iii); XANES spectra (points) and LCF fits (red lines) for Ni incorporation experiments at pH 7.5 without Fe(II) [Goe (C) and Hem (D)] and with Fe(II) [Goe (E) and Hem (F)] reacted for 30 days with 0.1 mM phosphate (i), 0.5 mM phosphate (ii), 0.1 mM sulfate (iii), 1.0 mM sulfate (iv), without oxoanions (v) [and 0.5 mM Fe(II) in E and F], or (vi) without oxoanions and 1.0 mM Fe(II).

3.7 APPENDIX

3.7.1 Second Order Kinetic Fits of Macroscopic Ni Release Data

The results from the macroscopic Ni release experiments were modeled using a mineral dissolution second-order rate law, as Fe(II)-catalyzed Ni release from Ni-substituted iron oxides occurs during mineral dissolution and follows a second-order rate reaction (Frierdich and Catalano, 2012):

$$\text{rate} = \frac{d[\text{Ni}]}{dt} = k_{\text{obs}}([\text{Ni}]_{\text{ss}} - [\text{Ni}])^2 \qquad (1)$$

Where "[Ni]" is the nickel concentration (μM) at time "*t*," "$[\text{Ni}]_{\text{ss}}$" is the steady state nickel concentration (μM), and k_{obs} is a pseudo second-order rate constant ($\mu M^{-1}\ d^{-1}$). Integrating the rate law leads to:

$$\frac{1}{[\text{Ni}]_{\text{ss}} - [\text{Ni}]} = k_{\text{obs}}t + C \qquad (2)$$

The fact that [Ni] = 0 at t = 0 is used to calculate the integration constant, "C":

$$C = \frac{1}{[\text{Ni}]_{\text{eq}}} \qquad (3)$$

Substituting Eq. (3) into Eq. (2) leads to the following equation for time-dependent Ni concentration:

$$[\text{Ni}] = \frac{[\text{Ni}]_{\text{ss}}^2 k_{\text{obs}} t}{1 + [\text{Ni}]_{\text{ss}} k_{\text{obs}} t} \qquad (4)$$

Eq. (4) was used to model the rate of Ni release from NiHem and NiGoe in the presence of aqueous Fe(II) with and without sulfate and phosphate.

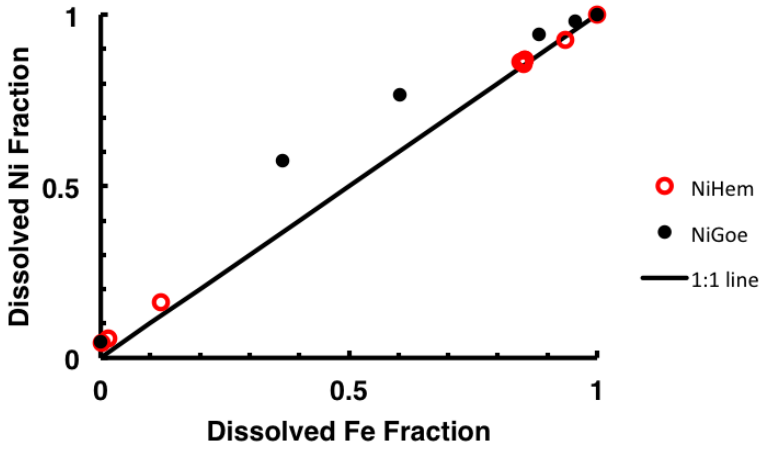

Figure A3.1. Fraction of Ni dissolved during acid dissolution of NiHem and NiGoe (points) compared against a 1:1 dissolution (line).

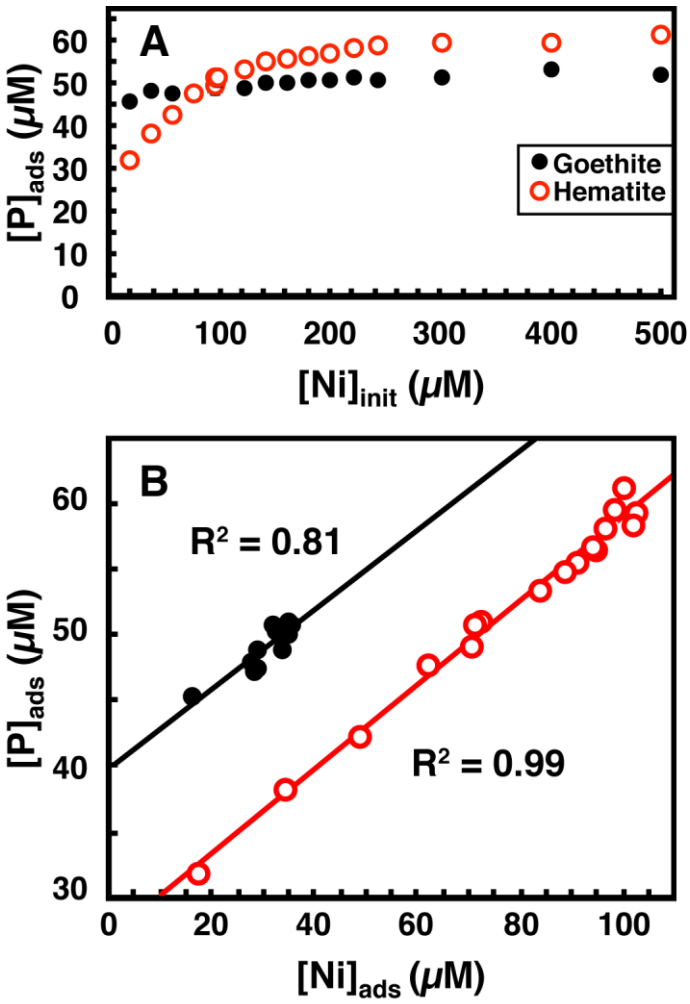

Figure A3.2. Phosphate adsorption as a function of initial Ni concentrations (A) and adsorbed Ni with correlation lines and corresponding coefficients of determination (B).

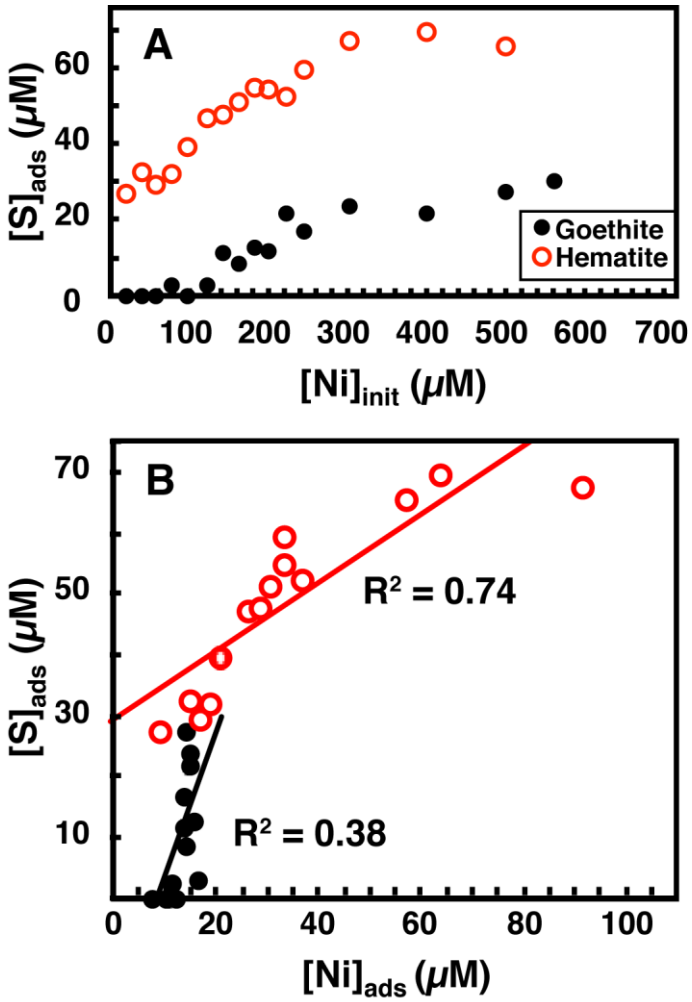

Figure A3.3. Sulfate adsorption as a function of initial Ni concentrations (A) and adsorbed Ni, with correlation lines and corresponding coefficients of determination (B).

Table A3.1. Spectral fitting results for Ni fluorescence EXAFS for Ni adsorbed onto Fe(III) oxides.

Sample	Shell	N[a]	R (Å)[b]	σ^2 (Å^2)[c]	ΔE_0 (eV)[d]	S_0^2 [e]	χ_ν^2 [f]
1 g L^{-1} Hematite							
0.1 mM PO_4	Ni-O	6	2.032(8)[g]	0.0068(5)	2(1)	0.9	5.46
	Ni-Fe1	0.6(2)	2.88(2)	0.005[h]			
	Ni-Fe2	1.6(5)	3.45(3)	0.008			
	Ni-P	2.4(8)	3.83(3)	0.005			
0.1 mM SO_4							
	Ni-O	6	2.044(8)	0.0068(5)	1(1)	0.9	5.79
	Ni-Fe1	0.4(2)	2.95(4)	0.005			
	Ni-Fe2	1.0(5)	3.42(3)	0.008			
	Ni-Fe3	2.5(9)	4.14(3)	0.01			
4 g L^{-1} Hematite							
0.5 mM PO_4	Ni-O	6	2.058(9)	0.0073(6)	3(1)	0.9	3.73
	Ni-Fe1	0.3(2)	2.90(5)	0.005			
	Ni-Fe2	0.9(5)	3.48(3)	0.008			
	Ni-Fe3	1.5(9)	4.12(4)	0.01			
1.0 mM SO4							
	Ni-O	6	2.045(7)	0.0068(5)	1(1)	0.9	5.83
	Ni-Fe1	0.3(2)	2.87(3)	0.005			
	Ni-Fe2	1.0(4)	3.49(3)	0.008			
	Ni-Fe3	1.0(7)	4.03(5)	0.01			
1 g L^{-1} Goethite							
0.1 mM PO_4	Ni-O	6	2.049(6)	0.0071(4)	0(1)	0.9	11.09
	Ni-Fe1	0.3(2)	3.48(4)	0.004			
	Ni-Fe2	1.4(5)	4.06(2)	0.008			
0.1 mM SO_4							
	Ni-O	6	2.038(7)	0.0068(4)	-2(1)	0.9	9.48
	Ni-Fe1	0.4(2)	3.48(3)	0.004			
	Ni-Fe2	1.1(5)	4.05(3)	0.008			
4 g L^{-1} Goethite							
0.5 mM PO_4	Ni-O	6	2.046(7)	0.0064(4)	0(1)	0.9	7.90
	Ni-Fe1	0.6(2)	3.52(3)	0.004			
	Ni-Fe2	1.6(6)	4.13(3)	0.008			
1.0 mM SO_4							
	Ni-O	6	2.051(6)	0.0057(4)	0.3(9)	0.9	6.40
	Ni-Fe1	0.4(2)	3.52(3)	0.004			
	Ni-Fe2	1.7(5)	4.09(2)	0.008			

[a] Coordination number.
[b] Interatomic distance.
[c] Debye-Waller factor.
[d] Difference in the threshold Fermi level between data and theory.
[e] Amplitude reduction factor.
[f] Goodness of fit parameters (Kelly et al., 2008).
[g] Statistical uncertainties at the 68% confidence level are reported in parentheses. Any parameters without reported uncertainties were held constant during fitting.
[h] σ^2 was fixed for all Fe shells.

3.8 REFERENCES

Arai Y. (2008) Spectroscopic evidence for Ni(II) surface speciation at the iron oxyhydroxides−water interface. *Environmental Science & Technology* **42,** 1151-1156.

Balistrieri L. S. and Murray J. W. (1982) The adsorption of Cu, Pb, Zn, and Cd on goethite from major ion seawater. *Geochimica et Cosmochimica Acta* **40,** 1253-1265.

Beard B. L., Handler R. M., Scherer M. M., Wu L., Czaja A. D., Heimann A. and Johnson C. M. (2010) Iron isotope fractionation between aqueous ferrous iron and goethite. *Earth and Planetary Science Letters* **295,** 241-250.

Benjamin M. M. and Bloom N. S. (1981) Effects of strong binding of anionic adsorbates on adsorption of trace metals on amorphous iron oxyhydroxide. In *Adsorption From Aqueous Solutions* (ed. P.H. Tewari), Plenum Press, New York. pp. 41-60.

Berner R. A., Ruttenberg K. C., Ingall E. D. and Rao, J. L. (1993) The nature of phosphorus burial in modern marine sediments. In *Interactions of C, N, P, and S Biogeochemical Cycles and Global Change* (eds. R. Wollast, F.T. Mackenzie and L. Chou), Springer-Verlag, Berlin. pp. 365-378.

Biber M. V., dos Santos Afonso M. and Stumm W. (1994) The coordination chemistry of weathering: IV. Inhibition of the dissolution of oxide minerals. *Geochimica et Cosmochimica Acta* **58,** 1999-2010.

Bondietti G., Sinniger J. and Stumm W. (1993) The reactivity of Fe(III) (hydr)oxides: effects of ligands in inhibiting the dissolution. *Colloids and Surfaces A: Physicochemical and Engineering Aspects* **79,** 157-167.

Borch T., Masue, Y., Kukkadapu R. K. and Fendorf S. (2007) Phosphate imposed limitations on biological reduction and alteration of ferrihydrite. *Environmental Science & Technology* **41,** 166-172.

Brantley S. L. and Conrad C. F. (2008) Analysis of Rates of Geochemical Reactions, In *Kinetics of Water-Rock Interaction* (eds. J.D. Kubicki and A.F. White). Springer, New York. pp. 1-37.

Brown G. E., Henrich V., Casey W., Clark D. and Eggleston C. M. (1999) Metal oxide surfaces and their interactions with aqueous solutions and microbial organisms. *Chemical Reviews* **99,** 77-174.

Brown G. E. and Parks G. A. (2001) Sorption of trace elements on mineral surfaces: Modern perspectives from spectroscopic studies, and comments on sorption in the marine environment. *International Geology Review* **43,** 963-1073.

Carvalho-e-Silva M. L., Ramos A. Y., Tolentino H. C. N., Enzweiler J., Netto S. M. and Alves M. D. C. M. (2003) Incorporation of Ni into natural goethite: An investigation by X-ray absorption spectroscopy. *American Mineralogist* **88,** 876-882.

Catalano J. G., Fenter P., Park C., Zhang Z. and Rosso K. M. (2010) Structure and oxidation state of hematite surfaces reacted with aqueous Fe(II) at acidic and neutral pH. *Geochimica et Cosmochimica Acta* **74,** 1498-1512.

Chacon N., Silver W. L., Dubinsky E. A. and Cusak D. F. (2006) Iron reduction and soil phosphorus solubilization in humid tropical forests soils: The roles of labile carbon pools and an electron shuttle compound. *Biogeochemistry* **78,** 67-84.

Collins C. R., Ragnarsdottir K. V. and Sherman D. M. (1999) Effect of inorganic and organic ligands on the mechanism of cadmium sorption to goethite. *Geochimica et Cosmochimica Acta* **63,** 2989-3002.

Cornell R. M. and Schwertmann U. (2003) *The iron oxides: Structure, properties, reactions, occurrences and uses*. WILEY-VCH Verlag GmbH & Co. KGaA, Weinheim.

Crosby H. A., Johnson C. M., Roden E. E. and Beard B. L. (2005) Coupled Fe(II)-Fe(III) electron and atom exchange as a mechanism for Fe isotope fractionation during dissimilatory iron oxide reduction. *Environmental Science & Technology* **39,** 6698-6704.

Derry L. A. and Jacobsen S. B. (1990) The chemical evolution of Precambrian seawater: Evidence from REEs in banded iron formations. *Geochimica et Cosmochimica Acta* **54,** 2965-2977.

Diaz-Barrientos E., Madrid L., Contreras M. C. and Morillo E. (1990) Simultaneous adsorption of zinc and phosphate on synthetic lepidocrocite. *Australian Journal of Soil Research* **28,** 549-557.

Drodt M., Trautwein A. X., König I., Suess E. and Koch C. B. (1997) Mössbauer spectroscopic studies on the iron forms of deep-sea sediments. *Physics and Chemistry of Minerals* **24,** 281-293.

Eggleston C. M., Hug S., Stumm W., Sulzberger B. and Dos Santos Afonso M. (1998) Surface complexation of sulfate by hematite surfaces: FTIR and STM observations. *Geochimica et Cosmochimica Acta* **62,** 585-593.

Elzinga E. J. and Kretzschmar R. (2013) *In situ* ATR-FTIR spectroscopic analysis of the co-adsorption of orthophosphate and Cd(II) onto hematite. *Geochimica et Cosmochimica Acta* **117,** 53-64.

Ericsson T. and Nord A. G. (1984) Strong cation ordering in olivine-related (Ni, Fe)-sarcopsides: A combined Mössbauer, X-ray and neutron diffraction study. *American Mineralogist* **69,** 889-895.

Frierdich A. J., Beard B. L., Reddy T. R., Scherer M. M. and Johnson C. M. (2014) Iron isotope fractionation between aqueous Fe(II) and goethite revisited: New insights based on a multi-direction approach to equilibrium and isotopic exchange rate modification. *Geochimica et Cosmochimica Acta* **139,** 383-398.

Frierdich A. J. and Catalano J. G. (2012) Controls on Fe(II)-activated trace element release from goethite and hematite. *Environmental Science & Technology* **46,** 1519-1526.

Frierdich A. J., Luo Y. and Catalano J. G. (2011) Trace element cycling through iron oxide minerals during redox-driven dynamic recrystallization. *Geology* **39,** 1083-1086.

Frierdich A. J., Scherer M. M., Bachman J. E., Engelhard M. H., Rapponotti B. W. and Catalano J. G. (2012) Inhibition of trace element release during Fe(II)-activated recrystallization of Al-, Cr-, and Sn-substituted goethite and hematite. *Environmental Science & Technology* **46,** 10031-10039.

Froelich P. N., Bender M. L. and Luedtke N. A. (1982) The marine phosphorus cycle. *American Journal of Science* **282,** 474-511.

Fuller C. C. and Harvey J. W. (2000) Reactive uptake of trace metals in the hyporheic zone of a mining-contaminated stream, Pinal Creek, Arizona. *Environmental Science & Technology* **34,** 1150-1155.

Gorski C. A., Handler R. M., Beard B. L., Pasakarnis T., Johnson C. M. and Scherer M. M. (2012) Fe atom exchange between aqueous Fe^{2+} and magnetite. *Environmental Science & Technology* **46,** 12399-12407.

Gorski C. A. and Scherer M. M. (2011) Fe2+ sorption at the Fe oxide-water interface: A revised conceptual framework. *Aquatic Redox Chemistry* **1071,** 477-517.

Handler R. M., Beard B. L., Johnson C. M. and Scherer M. M. (2009) Atom exchange between aqueous Fe(II) and goethite: an Fe isotope tracer study. *Environmental Science & Technology* **43,** 1102-1107.

Handler R. M., Frierdich A. J., Johnson C. M., Rosso K. M., Beard B. L., Wang C., Latta D. E., Neumann A., Pasakarnis T. and Premaratne W. (2014) Fe (II)-catalyzed recrystallization of goethite revisited. *Environmental Science & Technology* **48,** 11302-11311.

Hansel C. M., Benner S. G. and Fendorf S. (2005) Competing Fe(II)-induced mineralization pathways of ferrihydrite. *Environmental Science & Technology* **39,** 7147-7153.

Hansel C. M., Benner S. G., Neiss J., Dohnalkova A., Kukkadapu R. K. and Fendorf S. (2003) Secondary mineralization pathways induced by dissimilatory iron reduction of ferrihydrite under advective flow. *Geochimica et Cosmochimica Acta* **67,** 2977-2992.

Hansel C. M., Benner S. G., Nico P. and Fendorf S. (2004) Structural constrains of ferric (hydr)oxides on dissimilatory iron reduction and the fate of Fe(II). *Geochimica et Cosmochimica Acta* **68,** 3217-3229.

Hill R. J., Craig, J. R. and Gibbs, G. V. (1979) Systematics of the spinel structure type. *Physics and Chemistry of Minerals* **4,** 317-339.

Hinkle M. A. G., Wang Z., Giammar D. E. and Catalano J. G. (2015) Interaction of Fe(II) with

phosphate and sulfate on iron oxide surfaces. *Geochimica et Cosmochimica Acta* **158,** 130-146.

Hoins U. (1993) Ligand effect on the adsorption of heavy metals: The sulfate-cadmium-goethite case. *Water, Air, and Soil Pollution* **68,** 241-255.

Holland H. D. (1973) The Oceans; A Possible Source of Iron in Iron-Formations. *Economic Geology* **68,** 1169-1172.

Holland H. D. (1984) *The chemical evolution of the atmosphere and oceans*. Princeton University Press, New Jersey.

Holland H. D. (2006) The oxygenation of the atmosphere and oceans. *Philosophical Transactions of the Royal Society B: Biological Sciences* **361,** 903-915.

Isaure M. -P., Manceau A., Geoffroy N., Laboudigue A., Tamura N. and Marcus M. A. (2005) Zinc mobility and speciation in soil covered by contaminated dredged sediment using micrometer-scale and bulk-averaging X-ray fluorescence, absorption and diffraction techniques. *Geochimica et Cosmochimica Acta* **69,** 1173-1198.

Jeon B. H., Dempsey B. A., Burgos W. D. and Royer R. A. (2001) Reactions of ferrous iron with hematite. *Colloids and Surfaces A: Physicochemical and Engineering Aspects* **191,** 41-55.

Juang R. and Wu W. (2002) Adsorption of sulfate and copper(II) on goethite in relation to the changes of zeta potentials. *Journal of Colloid and Interface Science* **249,** 22-29.

Jubb A. M., Verreault D., Posner R., Criscenti L. J., Katz L. E. and Allen H. C. (2013) Sulfate adsorption at the buried hematite/solution interface investigated using total internal reflection (TIR)-Raman spectroscopy. *Journal of Colloid and Interface Science* **400,** 140-146.

Kelly S. D., Hesterberg D. and Ravel B. (2008). Analysis of soils and minerals using X-ray absorption spectroscopy. In *Methods of Soil Analysis. Part 5 - Mineralogical Methods* (eds. L.R. Drees and A.L. Ulery). Soil Science Society of America, Madison, WI. pp. 387-463.

Konhauser K., Pecoits E., Lalonde S. V., Papineau D., Nisbet E. G., Barley M. E., Arndt N. T., Zahnle K. and Kamber B. S. (2009) Oceanic nickel depletion and a methanogen famine before the Great Oxidation Event. *Nature* **458,** 750-753.

Larese-Casanova P. and Scherer M. M. (2007) Fe(II) sorption on hematite: New insights based on spectroscopic measurements. *Environmental Science & Technology* **41,** 471-477.

Latta D. E., Bachman J. E. and Scherer M. M. (2012a) Fe electron transfer and atom exchange in goethite: Influence of Al-substitution and anion sorption. *Environmental Science & Technology* **46,** 10614-10623.

Latta D. E., Gorski C. A. and Scherer M. M. (2012b) Influence of Fe^{2+}-catalyzed iron oxide recrystallization on metal cycling. *Biochemical Society Transactions* **40,** 1191-7.

Lim-Nunez R. and Gilkes R. J. (1985) Acid dissolution of synthetic metal-containing goethites and hematites. In *Proceedings of the International Clay Conference,* pp. 197-204.

Madrid L., Diaz-Barrientos E. and Contreras M. C. (1991) Relationships between zinc and phosphate adsorption on montmorillonite and an iron oxyhydroxide. *Australian Journal of Soil Research* **29,** 239-247.

Majzlan J. and Myneni S. C. B. (2005) Speciation of iron and sulfate in acid waters: Aqueous clusters to mineral precipitates. *Environmental Science & Technology* **39,** 188-194.

Manceau A., Schlegel M. L., Musso M., Sole V. A., Gauthier C., Petit P. E. and Trolard F. (2000) Crystal chemistry of trace elements in natural and synthetic goethite. *Geochimica et Cosmochimica Acta* **64,** 3643-3661.

Manceau A., Tamura N., Celestre R. S., MacDowell A. A., Geoffroy N., Sposito G. and Padmore H. A. (2002) Molecular-scale speciation of Zn and Ni in soil ferromanganese nodules from loess soils of the Mississippi Basin. *Environmental Science & Technology* **37,** 75-80.

Mench M. J., Didier V. L., Loffler M., Gomez A. and Masson P. (1994) A mimicked in situ remediation study of metal-contaminated soils with emphasis on cadmium lead. *Journal of Environmental Quality* **23,** 58-63.

Newville M. (2001) IFEFFIT: interactive EXAFS analysis and FEFF fitting. *Journal of Synchrotron Radiation* **8,** 322-324.

Parfitt R. L., Hume L. J. and Sparling G.P. (1989) Loss of availability of phosphate in New Zealand soils. *Journal of Soil Science* **40,** 371-382.

Paul K. W., Borda M. J., Kubicki J. D. and Sparks D. L. (2005) Effect of dehydration on sulfate coordination and speciation at the Fe-(hydr)oxide-water interface: A Molecular Orbital/Density Functional Theory and Fourier transform infrared spectroscopic investigation. *Langmuir* **21,** 11071-11078.

Pedersen H. D., Postma D., Jakobsen R. and Larsen O. (2005) Fast transformation of iron oxyhydroxides by the catalytic action of aqueous Fe(II). *Geochimica et Cosmochimica Acta* **69,** 3967-3977.

Ravel B. and Newville M. (2005) ATHENA, ARTEMIS, HEPHAESTUS: data analysis for X-ray absorption spectroscopy using IFEFFIT. *Journal of Synchrotron Radiation* **12,** 537-541.

Rehr J. J., Kas J. J., Vila F. D., Prange M. P. and Jorissen K. (2010) Parameter-free calculations of x-ray spectra with FEFF9. *Physical Chemistry Chemical Physics* **12,** 5503-5513.

Schwertmann U. and Cornell R. M. (2000) *Iron oxides in the laboratory: preparation and characterization*. Wiley-VCH, Weinheim.

Sidhu P. S., Gilkes R. J. and Posner A. M. (1978) The synthesis and some properties of Co, Ni, Zn, Cu, Mn and Cd substituted magnetites. *Journal of Inorganic and Nuclear Chemistry* **40,** 429-435.

Singh B. and Gilkes R. J. (1992) Properties and distribution of iron oxides and their association with minor elements in the soils of south-western Australia. *Journal of Soil Science* **43,** 77-98.

Singh B., Sherman D. M., Gilkes R. J., Wells M. A. and Mosselmans J. F. W. (2002) Incorporation of Cr, Mn and Ni into goethite (α-FeOOH): mechanism from extended X-ray absorption fine structure spectroscopy. *Clay Minerals* **37,** 639-649.

Sowder A. G., Bertsch P. M. and Morris P. J. (2003) Partitioning and availability of uranium and nickel in contaminated riparian sediments. *Journal of Environmental Quality* **32,** 885-898.

Stumm W. (1993) From surface acidity to surface reactivity; inhibition of oxide dissolution. *Aquatic Sciences* **55,** 273-280.

Stumm W. (1997) Reactivity at the mineral-water interface: dissolution and inhibition. *Colloids and Surfaces A: Physicochemical and Engineering Aspects* **120,** 143-166.

Swedlund P. J., Webster J. G. and Miskelly G. M. (2003) The effect of SO_4 on the ferrihydrite adsorption of Co, Pb and Cd: ternary complexes and site heterogeneity. *Applied Geochemistry* **18,** 1671-1689.

Tankere-Muller S., Zhang H., Davison W., Finke N., Larsen O., Stahl H. and Glud R. N. (2007) Fine scale remobilisation of Fe, Mn, Co, Ni, Cu and Cd in contaminated marine sediment. *Marine Chemistry* **106,** 192-207.

van der Zee C., Roberts D. R., Rancourt D. G. and Slomp C. P. (2003) Nanogoethite is the dominant reactive oxyhydroxide phase in lake and marine sediments. *Geology* **31,** 993-996.

Venema P., Hiemstra T. and van Riemsdijk W. H. (1997) Interaction of Cadmium with Phosphate on Goethite. *Journal of Colloid and Interface Science* **192,** 94-103.

Waychunas G. A., Kim C. S. and Banfield J. F. (2005) Nanoparticulate iron oxide minerals in soils and sediments: unique properties and contaminant scavenging mechanisms. *Journal of Nanoparticle Research.* **7,** 409-433.

Webb S. M. (2005) SIXPack: A Graphical User Interface for XAS Analysis using IFEFFIT. *Physica Scripta* **T115,** 1011-1014.

Wells M. A., Gilkes R. J. and Fitzpatrick R. W. (2001) Properties and acid dissolution of metal-

substituted hematites. *Clays and Clay Minerals* **49,** 60-72.

Williams A. G. B. and Scherer M. M. (2004) Spectroscopic evidence for Fe(II)-Fe(III) electron transfer at the iron oxide-water interface. *Environmental Science & Technology* **38,** 4782-90.

Wu L., Beard B. L., Roden E. E., Kennedy C. B. and Johnson C. M. (2010) Stable Fe isotope fractionations produced by aqueous Fe(II)-hematite surface interactions. *Geochimica et Cosmochimica Acta* **74,** 4249-4265.

Yang L., Steefel C. I., Marcus M. A. and Bargar J. R. (2010) Kinetics of Fe (II)-catalyzed transformation of 6-line ferrihydrite under anaerobic flow conditions. *Environmental Science & Technology* **44,** 5469-5475.

Yanina S. V. and Rosso K. M. (2008) Linked reactivity at mineral-water interfaces through bulk crystal conduction. *Science* **320,** 218-22.

CHAPTER 4

EFFECT OF AGING AND MN(II) ON MANGANESE OXIDE STRUCTURES

To be submitted to *Environmental Science & Technology* as:
Hinkle, M.A.G., Catalano, J.G. (2015) Effect of aging and Mn(II) on manganese oxide structures.

4.1 ABSTRACT

Naturally occurring Mn(IV/III) oxides are often formed through microbial Mn(II) oxidation, resulting in highly reactive phyllomanganates with varying Mn(IV) and Mn(III) contents. Residual aqueous Mn(II), like other cations, may adsorb in the interlayer of phyllomanganates above vacancies in their octahedral sheets. The potential for interlayer Mn(II)-layer Mn(IV) comproportionation reactions and subsequent formation of structural Mn(III) suggests that aqueous Mn(II) may cause manganese oxide structural changes that could alter mineral reactivity. Here we examine the effects of Mn(II) adsorption at pH 4 and 7 on the structure of phyllomanganates with varying initial vacancy and Mn(III) content: δ-MnO_2 has high vacancy content; hexagonal birnessite has vacancies and Mn(III); triclinic birnessite has high Mn(III) substitution. The mineral stacking behaviors also differ, with δ-MnO_2 and hexagonal birnessite having turbostratic stacking while triclinic birnessite has ordered layer stacking. Mn(II) adsorption exhibits a dependence on vacancy content at pH 4, but does not follow any such trend at pH 7. Both powder X-ray diffraction and X-ray absorption fine structure spectroscopy suggest that Mn(II) adsorbs above phyllomanganate sheet vacancies and promotes the formation of phyllomanganates with mixed orthogonal and hexagonal sheets arranged into supercells that are rotationally ordered at pH 4. At pH 7, aqueous Mn(II) exhibits differing effects on the different phyllomanganates, with Mn(II)-Mn(IV) comproportionation reactions altering δ-MnO_2 sheets, while changes to the sheet structures of hexagonal and triclinic birnessite are minimal. These results suggest that Mn(III) content plays an important role in the extent of aqueous Mn(II)-induced structural alterations and that pH largely controls the stability of phyllomanganate structures.

4.2 INTRODUCTION

Many naturally-occurring manganese oxides are nanoparticulate, poorly crystalline, and highly reactive minerals (Krumbein and Jens, 1981; Emerson et al., 1982; Villalobos et al., 2003; Saratovsky et al., 2006; Bargar et al., 2009; Clement et al., 2009; Dick et al., 2009; Grangeon et al., 2010; Tan et al., 2010). Manganese oxide formation in natural systems is often controlled by microbial Mn(II) oxidation, as abiotic Mn(II) oxidation is kinetically slow (Morgan and Stumm, 1964; Nealson et al., 1988; Tebo, 1991; Wehrli et al., 1995; Tebo et al., 1997; Von Langen et al., 1997; Bargar et al., 2000; Nelson and Lion, 2003; Morgan, 2005). Biogenic manganese oxides are typically phyllomanganates with birnessite-type structures, consisting of negatively charged octahedral sheets separated by hydrated interlayers (Krumbein and Jens, 1981; Emerson et al., 1982; Villalobos et al., 2003; Bargar et al., 2005; Webb et al., 2005a; Saratovsky et al., 2006; Bargar et al., 2009; Clement et al., 2009; Dick et al., 2009; Grangeon et al., 2010; Tan et al., 2010; Santelli et al., 2011). The negative charge develops as a result of Mn(IV) vacancies, Mn(III) substitutions, or a combination thereof, with varying vacancy and Mn(III) content depending on the mineral phase. To compensate the negative charge, exchangeable cations are adsorbed into the interlayer. These poorly crystalline phyllomanganates exhibit high adsorption capacities for many cations, including Mn(II) (Morgan and Stumm, 1964; McKenzie, 1980; Murray et al., 1984), which often adsorb above vacant sites within the interlayer (Toner et al., 2006; Peacock and Sherman, 2007; Manceau et al., 2007b; Peacock, 2009; Zhu et al., 2010b) and can enter into the phyllomanganate sheet vacancies over time (Peacock, 2009).

Phyllomanganates coexist with aqueous Mn(II) in regions with active manganese cycling; for example, at hydrothermal vents, redox interfaces in soils or sediments, or in oxic regions of stratified soils, sediments, and water columns as a result of upward diffusion of Mn(II) (Graybeal

and Heath, 1984; Rajendran et al., 1992; Burdige, 1993; Van Cappellen et al., 1998; Tebo et al., 2004; Tebo et al., 2005). Abiotic reactions involving Mn(II) adsorption onto phyllomanganates are likely common in these environments (Shimmield and Price, 1986; Canfield et al., 1993), and could involve Mn(II) incorporation into vacant sites or electron transfer via Mn(II)-Mn(IV) comproportionation reactions resulting in increased structural Jahn-Teller distorted Mn(III). A recent study has identified that Mn isotope exchange occurs between aqueous Mn(II) and a solid Mn(IV) oxide, likely involving Mn(II)-Mn(IV) comproportionation reactions, the formation of the metastable Mn(III) oxyhydroxide feitknechtite and subsequent phase transformation to manganite (Elzinga and Kustka, 2015). Several recent studies have also identified that Mn(II) induces phyllomanganate phase transformations to hausmannite (Lefkowitz et al., 2013) or manganite (Elzinga, 2011; Lefkowitz et al., 2013; Elzinga and Kustka, 2015) under anoxic conditions, with the final product dependent on the pH of the system (7.0-7.5 or 8.0-8.5, respectively). Under abiotic oxic conditions, reacting Mn(II) with Mn(IV/III) phyllomanganates results in phase transformations to a number of different Mn(III) or Mn(IV/III) oxide minerals, such as cryptomelane, groutite, manganite, manjiroite, nsutite, ramsdellite (Tu et al., 1994), and feitknechtite (Bargar et al., 2005), showing that a wide range of phase transformation products can form.

Natural systems with active Mn cycling, however, are typically associated with Mn(IV/III) phyllomanganates, not with Mn(III) oxyhydroxide phases like feitknechtite, manganite, or hausmannite, even under conditions with elevated aqueous Mn(II) concentrations (Wehrli et al., 1995; Friedl et al., 1997; Manceau et al., 2007a; Manceau et al., 2007b; Dick et al., 2009; Tan et al., 2010; Frierdich and Catalano, 2012). Research on Mn(II)-Mn(IV) interactions in which phyllomanganates do not undergo phase transformations is limited, but

some studies do indicate that Mn(II) alters sheet stacking behaviors (Lefkowitz et al., 2013) and symmetries (Bargar et al., 2005; Zhu et al., 2010a), suggestive of the formation of additional structural Jahn-Teller distorted Mn(III). However, there is no established systematic relationship between the presence of Mn(II) and phyllomanganate structural changes that do not involve mineral phase transformations. Mn oxide reactivity, scavenging ability, and trace metal sorption behavior are largely controlled by the Mn oxide structure (Post, 1999).

In this paper, aqueous Mn(II)-induced changes to phyllomanganate structures are examined. Because Mn(II) likely adsorbs above vacancies, three birnessite-type phyllomanganates with varying vacancy content and layer stacking are investigated. δ-MnO_2, the synthetic analogue of vernadite [(Ca,Na,K)(Mn^{4+},□)O_2•nH_2O] (Villalobos et al., 2006), has high vacancy content and turbostratic stacking; c-disordered H^+ birnessite (a hexagonal-type birnessite) [(Ca,Na,K)(Mn^{4+},Mn^{3+},□)O_2•nH_2O] has vacancies (Silvester et al., 1997; Lanson et al., 2000), Mn(III) substitution, and turbostratic stacking; triclinic birnessite [(Ca,Na,K)($Mn^{4+}_x Mn^{3+}_{1-x}$)O_2•nH_2O] has primarily Mn(III) substitution, few vacancies, and ordered layer stacking (Post and Veblen, 1990; Drits et al., 1997; Post et al., 2002; Lopano et al., 2007). The role of pH is also examined because Mn(II)-Mn(IV) comproportionation reactions exhibit a pH dependence, with comproportionation promoted with increasing pH (Mandernack et al., 1995). Mn(II) adsorption onto the solids at differing pH values was investigated through macroscopic adsorption isotherms, while the effects of Mn(II) on phyllomanganate sheet structures over longer time scales (i.e., 25 days) was explored using X-ray absorption fine structure (XAFS) spectroscopy and powder X-ray diffraction (XRD).

4.3 METHODS AND MATERIALS

4.3.1 Manganese Oxide Syntheses

Manganese oxide minerals were synthesized following modified previously published procedures, as described in detail in the Appendix. δ-MnO_2 and hexagonal birnessite (or 'c-disordered H^+ birnessite') (HexB) were synthesized using a redox method, which involves the reduction of $KMnO_4$ and the oxidation of $MnCl_2$ under alkaline conditions, following the procedures of Villalobos (2003). Triclinic birnessite (TriB) was prepared following the synthesis for Na-birnessite outlined in Lopano et al. (2007), based on procedures described by Post and Veblen (1990) and Golden et al. (1986; 1987). Excess electrolytes were removed from the synthesized phyllomanganates either by suspending in NaCl and deionized water followed by centrifugation and decanting the fluid (δ-MnO_2 and HexB) or by rinsing with deionized water during vacuum filtration (TriB). After synthesis, the minerals were resuspended in DI water, transferred to an anaerobic chamber (Coy Laboratory Products, Inc., 3% H_2/97% N_2 atmosphere with Pd catalysts) and sparged for at least 24 hours with a gas filtration system (Hinkle et al., 2015) to remove dissolved O_2 from the suspensions. The minerals were stored within the anaerobic chamber as suspensions in deionized water in aluminum foil-wrapped polypropylene bottles. Mineral aliquots were dried at 70 ^oC for BET (N_2 adsorption, Quantachrome Instruments Autosorb-1) and XRD (Bruker D8 Advance X-ray diffractometer, Cu K_α radiation) characterization.

4.3.2 Reagent Preparation

All stock solutions for experiments conducted in this study were prepared in the anaerobic chamber using deoxygenated deionized water. The Mn(II) stock solution was prepared

from $MnCl_2 \cdot 4H_2O$ and stored in an amber polypropylene bottle to prevent photo-oxidation. NaCl and 2-(4-morpholino)ethanesulfonic acid (MES) stock solutions were also prepared. For experiments conducted at pH 7, a stock solution comprised of both NaCl and MES was prepared and adjusted to pH 7 using HCl or NaOH solutions, which were sparged using the gas filtration systems more than six months prior to use. The HCl and NaOH solutions were also used to adjust experiment sample pH.

4.3.3 Macroscopic Mn(II) Adsorption Experiments

Macroscopic Mn(II) adsorption isotherms were measured for each phyllomanganate mineral. All experiments were conducted within the anaerobic chamber with 10 mM NaCl (to buffer ionic strength), 2.5 g L^{-1} phyllomanganate, and 0.02 – 20 mM aqueous Mn(II) at pH 4 or 7. The samples for the pH 7 experiments also included 1 mM MES buffer. Samples at 0.10 mM Mn(II) were prepared in triplicate and as mineral-free blanks to assess systematic experimental errors. The experiments were conducted by first adding NaCl, MES buffer, and Mn(II) to deoxygenated deionized water in a 15 mL conical centrifuge tube. While the mineral suspension was stirring to ensure thorough mixing, the appropriate amount of δ-MnO_2, HexB, or TriB was then added to each sample. The samples were allowed to equilibrate for approximately an hour, at which point the pH of each sample was adjusted using HCl or NaOH. The samples were wrapped in aluminum foil and rotated on end-over-end rotators for two days. The sample pH was checked and adjusted if necessary throughout the reaction period.

At the end of the experiments, the pH of the samples were recorded and the samples were filtered (0.22 μm MCE filters; Fisher Scientific). Any samples with final pH that deviated more than 0.5 pH units from the target pH were discarded from the final reported isotherms. The

filtrate was collected after discarding the first 1 mL of filtrate and acidified to 2% HNO_3 (trace metal grade; Fisher Scientific) immediately after removal from the anaerobic chamber. Aliquots of the acidified filtrate were diluted using 2% HNO_3 and analyzed for Mn concentrations by inductively coupled plasma-optical emission spectroscopy (ICP-OES; Perkin Elmer Optima 7300 DV). Sample uncertainty (95% confidence level) was calculated for these samples by the triplicate instrument analyses and propagating the standard deviations from the triplicate experiment samples to the entire sample set.

4.3.4 Solid Mn(IV/III) Oxide Aging Experiments

The effect of Mn(II) on phyllomanganate sheet structures was explored by collecting XAFS spectra and XRD patterns on phyllomanganates reacted with varying concentrations of Mn(II). In these experiments, 10 mM NaCl, 1 mM MES buffer (for pH 7 experiments), and 0, 0.75, or 7.5 mM Mn(II) were reacted with 2.5 g L^{-1} δ-MnO_2, HexB, or TriB at pH 4 or 7 for 25 days. Samples were prepared in 15 mL or 50 mL conical centrifuge tubes for the XAFS and XRD analyses, respectively. The pH of the samples were monitored throughout the experiments. At the end of 25 days, the final pH of each sample was recorded and the samples were filtered (reusable syringe filter; 0.22 μm membrane; Fisher Scientific), collecting the solids and filtrate. The filtrate was prepared for ICP-OES measurements as described in the previous section.

For XRD analyses, the samples were dried at ambient temperature (22±1°C) in a vacuum desiccator in the anaerobic chamber, then ground with an agate mortar and pestle and stored within glass vials. XRD slides were prepared in the anaerobic chamber and sealed with an airtight dome. XRD patterns were collected for all samples reacted with 7.5 mM Mn(II) with and without the dome to test the stability of these materials under oxic conditions for the duration of

an XRD pattern collection (approximately 40 minutes). No changes were observed between XRD patterns collected with and without the dome for these high Mn(II) experiments, consistent with the known slow kinetics of Mn(II) oxidation by O_2 (Morgan, 2005), thus all samples were assumed to be air-stable during XRD analysis. Samples were transferred to the XRD instrument within the airtight dome, which was removed immediately before XRD analysis. XRD patterns were collected from 5-80^o 2θ with 0.04^o 2θ steps at 3 seconds step^{-1} with Cu K_α radiation, a LynxExeXE detector, a 0.6 mm anti-scatter slit, and a 2.5^o soller slit, with the X-ray tube voltage and current set to 40 kV and 40 mA, respectively. No Ni pre-filter was used.

Samples prepared for XAFS spectroscopic analyses, however, were packed as wet pastes between Kapton film and 25 µm acrylic Kapton tape, with the filter used as backing immediately following sample filtration. Each XAFS sample was heat sealed in a polyethylene bag with a damp KimWipe to maintain anoxic and hydrated conditions during transport to the Advanced Photon Source (APS) at Argonne National Laboratory. Hydrated conditions were further ensured by filtering and preparing the solids for transport within 48 hours of transport to the APS. Wet pastes of synthesized, unreacted δ-MnO_2, HexB, and TriB were also filtered and prepared for XAFS spectroscopic measurements as described above. All XAFS spectra were collected at beamline 5-BM-D. Specific measurement details are described in the Appendix.

4.3.5 XAFS Spectral Fitting

The XAFS spectra were averaged, processed, and normalized using the Athena (Ravel and Newville, 2005) interface to IFEFFIT (Newville, 2001). The average Mn oxidation state for each sample was calculated using linear combination fitting (LCF) of the normalized XANES spectra in Athena with the following Mn oxidation state standards: $MnCl_2$•$4H_2O$, Mn_2O_3, Mn_3O_4

powders (Sigma Aldrich), and the four Mn(IV) standards in the database provided in Manceau et al. (2012) (Figure A4.1). The Sigma Aldrich manganese oxides were determined by XRD to be primarily bixbyite, and hausmannite, respectively (not shown). The solid powders were prepared for XAFS spectroscopy by grinding with an agate mortar and pestle for approximately 15 minutes and spreading the resulting fine powder on Scotch tape. These calculations followed a modified approach described Manceau et al. (2012), in which six or fewer reference oxidation state standards with non-negative loadings are fit to a sample using LCF. The accuracy of these Mn oxidation valence state fits are difficult to calculate through traditional methods, but are estimated to be 0.04 v.u., with decreasing accuracy with increasing $Mn^{3+/2+}$ content (Manceau et al., 2012).

Structural fitting of the k^3-weighted EXAFS spectra was conducted using SixPack (Webb, 2005) using a model similar to that described in detail by Webb et al. (2005a). A Na-birnessite (phyllomanganate) structure (Post and Veblen, 1990) was used to calculate FEFF backscattering phase and amplitude functions using FEFF 9.6 (Rehr et al., 2010). The EXAFS spectra were fit over a k range of 3 – 15.3 $Å^{-1}$ and an R range of 1 – 6 Å. The amplitude reduction factor (S_0^2) was fixed to 0.835 following Webb et al. (2005a). The model employed three Mn-O shells and three Mn-Mn shells, with each shell including two paths to account for potential Mn(III)-induced Jahn-Teller distortions of the phyllomanganate sheet. Corner-sharing Mn-Mn (likely Mn^{2+} or Mn^{3+} bound above sheet vacancies) and interlayer Mn-Na were also included in the model. All five possible Mn-Mn multiple scattering (MS) paths for the long-distance (third) Mn-Mn shell were included in the model, but did not contribute additional fitting variables to the fit as their coordination numbers, distances, and σ^2 values could be constrained fully using the constituent single scattering (SS) paths. The σ^2 values between linked

paths were fixed, and second and third shell Mn-Mn distances were fixed based on the geometrical constrains defined by the first Mn-Mn shell. Every Mn-Mn scattering path included a parameter to account for vacancy effects on the amplitude, f_{occ}: the fraction of Mn sites occupied in the phyllomanganate sheet.

4.4 RESULTS AND DISCUSSION

4.4.1 Synthesized Materials

The three phyllomanganates used in this study, δ-MnO_2, HexB, and TriB, exhibit properties consistent with past studies (Villalobos et al., 2003; Webb et al., 2005a). The BET surface areas are similar to those reported by Villalobos et al. (2003), with HexB (167.8 m^2 g^{-1}) and δ-MnO_2 (116.4 m^2 g^{-1}) having much larger surface areas than TriB (24.8 m^2 g^{-1}). The average Mn oxidation state (AMOS) (Table 4.1) also differs among the manganese oxides, with TriB < HexB < δ-MnO_2, consistent with the observed edge energy shifts in the XANES spectra (Figures 4.1, A4.2) and previous studies (Villalobos et al., 2003). The XRD patterns of δ-MnO_2 and HexB (Figures 4.2A, A4.3) exhibit broad, low-intensity (001) and (002) peaks near 12.3 and 24.8^o 2θ, respectively, indicating that few sheets are stacked along the *c*-axis (Villalobos et al., 2003). The δ-MnO_2 and HexB XRD patterns also contain asymmetric (20,11) and (02,31) bands near 37 and 65^o 2θ, respectively, characteristic of turbostratic phyllomanganates (Villalobos et al., 2003; Webb et al., 2005a; Webb et al., 2005b), with d-spacing ratios in close agreement with the value expected for phyllomanganates with hexagonal symmetry (i.e., 1.73 = √3) (Villalobos et al., 2003; Villalobos et al., 2006; Grangeon et al., 2010). The TriB XRD pattern (Figures 4.2A, A4.4), on the other hand, is consistent with orthogonally symmetric sheets and has intense, sharp (001) and (002) peaks, indicative of many layers stacked along the *c*-axis (Brindley and Brown,

1980).

The EXAFS spectra (Figure 4.1) also indicate that δ-MnO_2 and HexB (Figure 4.1B,E) have hexagonal symmetry, while TriB is orthogonal (Figure 4.1H). Positive antinodes at ~8.1 and 9.2 $Å^{-1}$ in k^3-weighted spectra broaden, split, and shift to the left when moving from hexagonal to orthogonal symmetry (Marcus et al., 2004; Manceau et al., 2005; Zhu et al., 2010a). These antinodes are clearly shifted and split in the TriB EXAFS spectrum (Figure 4.1H), in contrast with the sharp single peaks at 8.1 and 9.2 $Å^{-1}$ in the HexB and δ-MnO_2 spectra (Figure 4.1B,E). In addition, the positive antinode at ~6.8 $Å^{-1}$ [characteristic of layered manganese oxides (McKeown and Post, 2001)] in the HexB and δ-MnO_2 spectra (Figure 4.1B,E) is shifted to the left in the TriB spectrum (Figure 4.1H), consistent with past research (Webb et al., 2005a; Yu et al., 2012). In R-space, the Mn MS peak at 5.2 Å (R+ΔR) in TriB is attenuated, which is consistent with sheet bending arising from Jahn-Teller distorted Mn(III) substitution (Webb et al., 2005a; Bargar et al., 2009). The distance (R) for Mn adsorbed above vacant sites, modeled by Mn-Mn_{crnr} in the fit (Table A4.1), is shorter in TriB (3.33 Å) than in HexB or δ-MnO_2 (~3.46 Å). These R values likely scale with the ionic radii of the adsorbing cation [in this case, Mn(II) or Mn(III)] (Silvester et al., 1997; Zhu et al., 2010a), and thus indicate that of the adsorbed Mn, more Mn(III) is present in TriB than in HexB or δ-MnO_2, which likely have more adsorbed Mn(II) than Mn(III) (Silvester et al., 1997; Zhu et al., 2010a). These conclusions regarding the valence of adsorbed Mn for the HexB and TriB systems are supported by the presence and lack of, respectively, a shoulder at 6553 eV in the XANES spectra (Figure 4.1D,G) corresponding to sorbed Mn^{2+} (Bargar et al., 2000; Villalobos et al., 2003; Webb et al., 2005a). The absence of the shoulder at 6553 eV in the δ-MnO_2 XANES spectrum (Figure 4.2A), along with the AMOS of 4.00 (Table 4.1), indicate that the amount of Mn^{2+} adsorbed onto δ-MnO_2 is minimal. It should

be noted that no interpretation of phyllomanganate structures will be made based solely on the Mn-Mn_{crnr} coordination number, as there is large uncertainty associated with calculating this parameter, as has been previously discussed (Webb et al., 2005a).

4.4.2 Macroscopic Mn(II) Adsorption onto Phyllomanganates

Langmuir isotherms were used to describe aqueous Mn(II) adsorption behavior onto TriB, HexB, and δ-MnO_2 (Figure 4.3; Table A4.2). Mn(II) adsorption is enhanced at higher pH, consistent with past research (Lefkowitz et al., 2013). The effect of adsorbent identity, however, differs depending on the pH. For example, Mn(II) adsorption increases with decreasing Mn(III) content at pH 4 (i.e., Mn(II) adsorption onto δ-MnO_2 > HexB > TriB), but follows no such trend at pH 7. Rather, at pH 7 Mn(II) surface coverage is greatest on TriB and is approximately the same on δ-MnO_2 and HexB. The increase in Mn(II) adsorption onto TriB at pH 7 relative to the other phyllomanganates is particularly surprising given the large disparity in BET surface areas. It should be noted that the precipitation of secondary minerals does not necessarily follow expected isotherm trends (i.e., two distinct plateaus) in Mn(II)-birnessite systems above pH 7 (Elzinga, 2011; Lefkowitz et al., 2013), thus it is possible that precipitation occurs in the pH 7 isotherm presented here. These results suggest that phyllomanganate structures may be affected by Mn(II) differently depending on the pH as well as the vacancy content of the adsorbent.

4.4.3 Effect of Mn(II) on Turbostratic Phyllomanganates

pH 4

δ-MnO_2 and HexB sheet structures change substantially after 25 days of aging at pH 4 in both the absence and presence of aqueous Mn(II). The AMOS decreases with increasing initial

aqueous Mn(II) (Table 4.1; Figure 4.1A,D,G), consistent with the substantial sorption of Mn(II) onto the phyllomanganates during the 25 day reaction (Table A4.2; Figure A4.5). Interestingly, the amount of Mn(II) sorbed onto HexB after 25 days of reaction with 0.75 mM Mn(II) at pH 4 (Table 4.1) does not reach the equilibrium Mn(II) surface coverage calculated for the 48-hour Mn(II) adsorption experiment Langmuir isotherms (Table A4.2; Figure A4.5), suggesting that Mn is ejected from the sheet during aging and subsequently competes for surface sites with the added Mn(II).

The weak basal (001) and (002) reflections in the δ-MnO_2 XRD patterns suggest dispersion of some phyllomanganate sheets upon aging (Figure 4.2B). The XRD patterns of δ-MnO_2 reacted with 0 and 0.75 mM Mn(II) exhibit more pronounced minimums on the high angle side of the (11,20) band near ~46^o 2θ relative to the unreacted δ-MnO_2 sample, consistent with increasing Mn adsorption over vacancies (Villalobos et al., 2006; Grangeon et al., 2010; Grangeon et al., 2012). This change in the minimum near ~46^o 2θ in XRD, along with the reduction in the f_{occ} value (Table A4.3) for the 0 mM Mn(II) sample relative to the unreacted sample suggests that some interlayer Mn(IV) migrates out of the phyllomanganate sheet and adsorbs over vacancies upon aging δ-MnO_2. Because the Mn-Mn_{crnr} interatomic distance is relatively short (Table A4.3) and the AMOS is 4.00 (Table 4.1) in the 0 mM Mn(II) 25 day δ-MnO_2 sample, it is likely that the adsorbed Mn remains Mn(IV). A similar trend in the Mn-Mn_{crnr} interatomic distance occurs in the HexB system. The Mn-Mn_{crnr} interatomic distance and the AMOS value for the 0.75 mM Mn(II) δ-MnO_2 sample, however, are consistent with the sorption of Mn(II).

The XRD patterns of the 7.5 mM Mn(II) δ-MnO_2 pH 4 sample and all HexB samples aged at pH 4 exhibit similar changes. These patterns show splitting of the (11,20) and (31,02)

reflections to individual peaks and the appearance of additional peaks in the 20-70^{o} 2θ region (Figure 4.2B,C). These additional peaks do not correspond with the XRD patterns of known Mn oxides (Table A4.4). In addition, the EXAFS spectra (Figure 4.1) and fits (Table A4.3) demonstrate that the local structures are consistent with phyllomanganates. Thus, it is unlikely that the additional XRD peaks are the result of a secondary manganese oxide mineral phase. Instead, the peaks between ~35-70^{o} 2θ are consistent with the XRD patterns of an H-exchanged hexagonal birnessite ('HBi') formed by equilibration of triclinic Na-buserite at pH 5 (Lanson et al., 2000) and of HBi with Zn adsorbed over vacancies (Lanson et al., 2002; Drits et al., 2007). These studies identified, based on Drits and McCarty's (1996) initial observation, that the *hkl* peak positions of interstratified defective layer structures lie between the *hkl* positions of the layer-types present in the material (Lanson et al., 2000; Lanson et al., 2002; Drits et al., 2007). In these studies, XRD patterns were fit using simulated patterns calculated by structural models and were best described by models consisting of mixed sheet symmetries, with hexagonal sheets interspersed with monoclinic layers and each sheet displaced along the a axis by +a/3 (Lanson et al., 2000; Lanson et al., 2002), analogous to the chalcophanite structure (Post and Appleman, 1988). This structure minimizes electrostatic repulsion arising from high valence Mn in adjacent layers, maximizing the distance between layer Mn in neighboring sheets and the distance between layer Mn and interlayer Mn (Lanson et al., 2000; Lanson et al., 2002).

In a related paper, Drits et al., (2002) analyzed Zn adsorbed HBi with selected-area electron diffraction, finding that the phyllomanganate sheets are ordered in supercells. Earlier research (Drits et al., 1998) found that the presence of supercells in a phyllomanganate gives rise to additional XRD peaks with positions similar to those observed in the 20-26^{o} 2θ region in the current study. As these peaks (as well as the peaks ~30-34^{o} 2θ) do not correspond with any

known manganese oxide (Table A4.4), it is plausible that they are supercell reflections arising from long range ordering. These results suggest that the phyllomanganate sheet structure formed after δ-MnO_2 reacts with 7.5 mM Mn(II) at pH 4 and HexB is aged at pH 4 is likely a mixture of hexagonal and orthogonal phyllomanganate sheets with rotated stacking behaviors ordered into supercells. The fact that the XRD patterns of HexB aged at pH 4 in the absence and presence of Mn(II) exhibit changes that are only seen in the δ-MnO_2 system upon reaction with high Mn(II) loadings indicates that Mn(III) content may act as a threshold, below which rotational ordering and supercell formation do not occur upon aging.

The 7.5 mM Mn(II) δ-MnO_2 k^3-weighted EXAFS spectrum (Figure 4.1B) supports the conclusion that Mn(II) promotes the formation of a phyllomanganate with mixed sheet symmetries, as the 6.8 and 9.2 $Å^{-1}$ features are dampened and slightly broadened relative to the other δ-MnO_2 pH 4 samples, consistent with a mixture of hexagonal to orthogonal symmetry. The XAFS model fit indicates that the first shell Mn-O splitting (Mn-O_{1a} and Mn-O_{1b}; Table A4.3) decreases with 7.5 mM initial Mn(II). However, the shell splitting between other shells (e.g., Mn-$Mn_{1a,b}$ and Mn-$O_{2a,b}$) is not affected, and the σ^2 value for Mn-O_{1a} (the equatorial Mn-O shell) is much larger than other δ-MnO_2 samples. Therefore, the modeled decrease in Mn-O_{1a} and Mn-O_{1b} splitting may be due to increased disorder of the equatorial Mn-O shell, possibly as a result of multiple sheet symmetries.

pH 7

δ-MnO_2 and HexB aged at pH 7 exhibit substantially different behavior than when reacted at pH 4. Changes in both the δ-MnO_2 and the HexB XRD patterns indicate that "heavy" cations (e.g., Ni, Zn, Mn, etc.) cap a substantial fraction of layer vacancies after aging for 25

days at pH 7 in the absence of Mn(II). In particular, the minimum at 46^{o} 2θ and the broad hump at 55^{o} 2θ both become more prominent (Figure 4.2B,C) (Villalobos et al., 2006; Grangeon et al., 2010; Grangeon et al., 2012). These changes in the XRD patterns suggest that some layer Mn ejects from the phyllomanganate sheet and readsorbs above vacancies over time. The (001) and (002) reflections in the δ-MnO_2 system are substantially sharper after 25 days reaction at pH 7.

The addition of 0.75 mM Mn(II) to δ-MnO_2 increases the intensity of the (001) and (002) reflections, suggesting that δ-MnO_2 sheet stacking increases during reaction at pH 7. The EXAFS model parameters (Table A4.3) are relatively stable in the δ-MnO_2 system, with the exception of the first and second Mn-O shells splitting, both of which which increase in the presence of 0.75 mM Mn(II). These results indicate that layer Mn(III) increases upon addition of aqueous Mn(II). The only change from the unreacted HexB XAFS spectrum with the addition of 0.75 mM Mn(II) is related to Mn adsorption behavior: an increase in the Fourier Transform XAFS peak amplitude at ~3.0 Å (Figure 4.1F). XRD clearly shows that feitknechtite (β-$Mn^{III}OOH$) precipitates in the presence of 7.5 mM Mn(II) for all minerals explored in this study at pH 7 (Figure A4.6), thus the remaining discussions for pH 7 systems will focus on the lower initial Mn(II) experiments.

4.4.4 Effect of Mn(II) on TriB

pH 4

XRD and XAFS results show that TriB undergoes substantial structural changes when reacted at pH 4 for 25 days in the absence or presence of aqueous Mn(II). The XRD pattern shows that TriB aged at pH 4 results in a hexagonally symmetric material with weaker rotational ordering than the unreacted sample (Figure 4.2D). The d-spacing ratio between reflections in all

pH 4 reacted TriB samples is ~1.73, in agreement with a hexagonal unit cell (Villalobos et al., 2003; Villalobos et al., 2006; Grangeon et al., 2010). The k^3-weighted EXAFS spectra clearly show that TriB reacted at pH 4 no longer possesses orthogonal sheet symmetry, as the maxima centered at 6.8, 8.1, and 9.2 $Å^{-1}$ in hexagonally symmetric phyllomanganates are not shifted to lower k values as in unreacted TriB, and each is a single positive antinode. The Mn-Mn_{crnr} distance increased from 3.33 Å in unreacted TriB to ~3.49 Å in TriB aged at pH 4 in the absence and presence of Mn(II), indicating that Mn adsorbed above vacancies shifts from predominately Mn(III) to Mn(II) after 25 days of reaction (Zhu et al., 2010a). The presence of adsorbed Mn(II) is further supported by the appearance of a shoulder at ~6553 eV in the pH 4 aged TriB XANES spectra (Bargar et al., 2000; Villalobos et al., 2003; Webb et al., 2005a). Furthermore, the amount of Mn(II) remaining in solution at the end of the 0 mM and 0.75 mM Mn(II) 25 day experiments is greater than the initial amount of Mn(II) reacted with the systems, indicating that some Mn(II) is released to solution via structural Mn(III) disproportionation during aging at pH 4. These observations are consistent with TriB transitioning to a phyllomanganate with hexagonal symmetry as a result of pH-promoted Mn(III) disproportionation forming interlayer Mn(II), layer Mn(IV), and sheet vacancies (Lanson et al., 2000).

Although there is little variation in the XANES and k^3-weighted EXAFS spectra between TriB reacted with differing amounts of aqueous Mn(II), some changes in the XRD patterns and the XAFS Fourier Transforms at pH 4 are observed. The XAFS Fourier Transforms (Figure 4.1I) show a slight shift in the first Mn-Mn shell position with 7.5 mM Mn(II), as well as an increase the ~3.0 Å feature corresponding to the Mn-Mn_{crnr} shell. Increasing aqueous Mn(II) shifts the XRD (001) and (002) peak positions to the right relative to the unreacted sample (Figure 4.2D). Additionally, XRD peaks in the 35-70^o 2θ region shift in a systematic way with the addition of

aqueous Mn(II) (Figures 4.2D, A4.7), indicating that the addition of Mn(II) alters the sheet stacking or interlayer displacement, as has been invoked to explain XRD peak shifts in this current and past studies (Lanson et al., 2002; Drits et al., 2007). The addition of 0.75 and 7.5 mM Mn(II) also leads to the appearance of new, low intensity XRD peaks in the 30-34^{o} 2θ region, and increases the intensity of peaks in the 20-26^{o} 2θ region, both of which correspond with the peaks likely associated with supercells discussed above. The presence of these peaks in all triclinic birnessite and 7.5 mM Mn(II) pH 4 sample XRD patterns further supports the conclusion that the addition of Mn(II) induces long range ordering resulting in a supercell, and that this ordering is particularly promoted in Mn(III)-rich materials.

pH 7

XRD patterns show that the TriB sheet structure is much more stable at pH 7 than at pH 4, with little to no difference between the unreacted and the TriB aged in the absence of Mn(II) patterns (Figure 4.2D). The XAFS spectra, however, suggest that some restructuring of TriB occurs after aging at pH 7 for 25 days. The k^3-weighted XAFS spectra show that the peak centered at 8.1 Å^{-1} in hexagonal materials but shifted to the left and split in unreacted TriB is no longer split or shifted, and is more intense upon aging at pH 7 (Figure 4.1H). However, the positive antinodes centered at 6.8 and 9.2 Å^{-1} in hexagonal materials are shifted to the left in the TriB samples reacted for 25 days at pH 7, consistent with unreacted TriB (Figure 4.1H). It is unclear if the decrease in the first shell Mn-O splitting (Mn-O_{1a} and MnO_{1b}; Table A4.3) is indicative of less Mn(III) in the sheet, as splitting between other shells remains similar to that of unreacted TriB. The σ^2 value for the first equatorial Mn-O shell (Mn-O_{1a}) is much larger than for unreacted TriB, thus the apparent lack of splitting in the Mn-O_{1a} and Mn-O_{1b} shells may be the

result of increased disorder in the distribution of the Mn-O_{1a} distance.

The addition of 0.75 mM Mn(II) leads to additional changes in the XAFS spectrum of TriB, although it is unclear if these changes are the result of a minor feitknechtite component observable in the XRD pattern (Figure 4.2D). The k^3-weighted EXAFS spectrum (Figure 4.1H) shows changes to the 6.8 and 9.25 $Å^{-1}$ peaks upon addition of 0.75 mM Mn(II). In this spectrum, the peak at 6.8 $Å^{-1}$ shifts toward the right relative to unreacted TriB and the peak at 9.25 $Å^{-1}$ increases in intensity and has decreased splitting. These peaks are still much broader than those in the pH 4 system, but are consistent with a transition toward hexagonal symmetry, possibly due to the formation of hexagonal sheets or feitknechtite precipitation, as feitknechtite also has hexagonal symmetry (Meldau et al., 1973).

4.4.5 Mechanism of Mn(II)-Induced Phyllomanganate Structural Changes

These results indicate that at pH 4 in the absence of Mn(II), some structural Mn is ejected from the interlayer and adsorbs above vacancies in turbostratic phyllomanganates, while structural Mn(III) in TriB disproportionates to aqueous Mn(II) and layer Mn(IV). Mn(III) disproportionation, which serves to relax Jahn-Teller induced sheet strain, leads to the formation of a hexagonally-symmetric material in the TriB pH 4 system. The addition of Mn(II) promotes the reverse reaction, Mn(II)-Mn(IV) comproportionation, resulting in a phyllomanganate with mixed orthogonal and hexagonal sheet symmetries when TriB is aged at pH 4. However, the pH is so low the addition of Mn(II) is unable to revert the structure back to full rotational ordering. In the HexB system, however, aging at pH 4 results in the ejection of some layer Mn(IV) and the redistribution of structural Mn(III) to ordered rows in some sheets, resulting in a phyllomanganate with rotationally ordered, interspersed hexagonal and orthogonal sheets. The

presence of aqueous Mn(II), which adsorbs onto turbostratic phyllomanganate sheet vacancies as indicated by our XRD and XAFS results, promotes the formation of a phyllomanganate with mixed sheet symmetries in the δ-MnO_2 and HexB systems. In these cases, orthogonal and hexagonal layers are intermixed and the sheets are rotationally ordered to minimize repulsion between high valence Mn in adjacent layers and Mn in the interlayer (Lanson et al., 2002). Thus, increasing interlayer Mn(II/III) adsorption over vacancies could increase electrostatic repulsion with layer Mn(IV), which would promote rotated sheet stacking behaviors. Alternatively, increasing Mn(II) adsorption may lead to some structural Mn(III) formation through comproportionation reactions, thereby promoting the formation of orthogonal layers. Mn(II) also promotes long range ordering of the phyllomanganates into supercells. It is probable that the supercell ordering is not along the *c*-axis, as the (001) reflections for these materials appear weaker, not more intense as would be expected. Instead, the supercell may form due to adsorbing cations capping vacancies in an ordered manner or ordering of orthogonal and hexagonal domains within the sheets. Both scenarios could explain the evident Mn(III) threshold, as Mn(III) can drive orthogonal ordering and can more readily act as an adsorbing cation than Mn(IV).

At pH 7, phyllomanganates with substantial vacancy content are more likely to be affected by aqueous Mn(II) than those with few vacancies and more structural Mn(III). For example, the addition of aqueous Mn(II) to the δ-MnO_2 system increases structural Mn(III), likely through Mn(IV)-Mn(II) comproportionation, and increases sheet stacking. In the HexB system, however, aqueous Mn(II) does not appear to alter the manganese oxide structure, restricting its interaction to adsorption over vacant sites. It should also be noted that, in the absence of aqueous Mn(II), phyllomanganates with more vacancies were less stable at pH 7 than

those with more structural Mn(III). These results suggest that Mn(III) is more stable against Mn(III) disproportionation at this pH. However, increased structural Mn(III) with the addition of aqueous Mn(II) only occurs in phyllomanganates with large numbers of vacancies (i.e., δ-MnO_2). Phyllomanganates with fewer vacancies, such as HexB and TriB are not as affected by Mn(II).

4.4.6 Comparison to Prior Work

Research on phyllomanganates at acidic conditions have found that sheet structures undergo structural changes consistent with those observed in this study in the absence of Mn(II) (Lanson et al., 2000; Manceau et al., 2013). Recent research using high-energy X-ray scattering and pair distribution function analysis demonstrated that structural Mn migrates into the interlayers in δ-MnO_2 upon equilibration at low pH, resulting in increased vacancy content and the formation of a supercell either through long range ordering of sheet vacancies or ordering of interlayer Mn (Manceau et al., 2013). In the current study, we also find that some layer Mn(IV) is ejected from δ-MnO_2 sheets after aging at pH 4 and that a supercell may form in HexB aged at pH 4. Previous research on the structures of Na-birnessite [an orthogonal, triclinic birnessite (Post et al., 2002)] observed that the phyllomanganate becomes increasingly hexagonally symmetric with increasing acidity (Drits et al., 1997; Silvester et al., 1997; Lanson et al., 2000), consistent with our observation that TriB maintains its orthogonal sheets after aging at pH 7 but forms hexagonal sheets at pH 4.

Although most studies on aqueous Mn(II)-solid Mn oxide interactions in abiotic systems have largely focused on phase transformation behaviors, some have indicated that Mn(II) can affect phyllomanganate sheet structures (Bargar et al., 2005; Zhu et al., 2010a; Lefkowitz et al.,

2013). Previous research identified that Mn(II) adsorbs above vacancies in a biogenic hexagonally symmetric manganese oxide and, at high pH, that Mn(II) likely oxidizes via Mn(II)-Mn(IV) comproportionation and enters the phyllomanganate sheet as Mn(III) (Zhu et al., 2010a). Other research has found that the fraction of Na birnessite [an orthogonal triclinic birnessite (Post et al., 2002)] in LCF of XANES spectra increased with increasing length of time that δ-MnO_2 was reacted with 100 µM Mn(II) at pH 8 (Bargar et al., 2005). Our research also finds that the addition of aqueous Mn(II) causes phyllomanganate sheet symmetries to become more orthogonal at low pH and causes structural Mn(III) content to increase in the high pH δ-MnO_2 system, consistent with the findings of these previous studies (Bargar et al., 2005; Zhu et al., 2010a). Sheet stacking in hexagonal birnessite has also been observed to decrease upon addition of aqueous Mn(II) (Lefkowitz et al., 2013). While the opposite trend is observed in our pH 7 δ-MnO_2 experiments, sheet stacking does appear to decrease in the presence of aqueous Mn(II) in the pH 4 δ-MnO_2 and hexagonal birnessite systems.

The addition of 7.5 mM Mn(II) to all mineral systems at pH 7 resulted in the precipitation of feitknechtite in the current study. These samples all have AMOS near 3.25 (Table 4.1, Figure A4.8) and have similar XRD patterns indicative of mixed crystalline manganese oxides, dominated by feitknechtite. The transformation of phyllomanganates to feitknechtite at pH 7 with high Mn(II) concentrations is consistent with past research (Elzinga, 2011; Lefkowitz et al., 2013), although our experiments were conducted with aqueous Mn(II) to solid Mn(IV) oxide ratios much lower (3 mmol Mn(II) g^{-1}) than those previously observed to not precipitate feitknechtite at pH 7 (8 mmol Mn(II) g^{-1}) (Lefkowitz et al., 2013). Our solids have surface areas similar to or much larger than those used in the previous studies, thus the precipitation of feitknechtite below previously identified thresholds is surprising. One possible explanation is

that reaction times in this current study were longer than in prior work (25 versus 8 days), and mineral precipitation processes are often kinetically limited. This present study also found that feitknechtite precipitated at pH 7 with TriB at low initial Mn(II) concentrations (0.75 mM Mn(II); 0.3 mmol Mn(II) g^{-1}). This suggests that the initial structural Mn(III) content is an important factor in Mn(II)-induced phase transformations.

4.4.7 Environmental Significance

The results of this study suggest that aqueous Mn(II) alters phyllomanganate sheet structures, with varied effects depending on the initial phyllomanganate vacancy content, the reaction pH, and the concentration of aqueous Mn(II). Aqueous Mn(II) concentrations exhibit spatial and temporal variations in natural systems, with large Mn(II) concentrations in many environments (Graybeal and Heath, 1984; Rajendran et al., 1992; Burdige, 1993; Van Cappellen et al., 1998; Tebo et al., 2004; Tebo et al., 2005). Abiotic Mn(II)-phyllomanganate interactions are likely prevalent in such systems, and at low pH involve the adsorption of Mn(II) over vacant sites and the restructuring and rotational ordering of phyllomanganate sheets. These structural changes as well as capping of vacant sites may alter trace metal adsorption, possibly causing the reduction in trace metal sorption. For example, recent research indicates that higher aqueous Mn(II) concentrations are associated with manganese oxides with lower metal content in a cave system (Frierdich and Catalano, 2012).

In environments at circumneutral to high pH such as marine sediments and suboxic soils, aqueous Mn(II) interactions with trace metals on phyllomanganates with high initial structural Mn(III) contents may be limited to competitive adsorption effects. Alternatively, aqueous Mn(II) may increase structural Mn(III) in phyllomanganates like δ-MnO_2, potentially decreasing surface

sites available for trace metal adsorption (Toner et al., 2006; Peacock and Sherman, 2007; Manceau et al., 2007b; Peacock, 2009; Zhu et al., 2010b) and later incorporation (Peacock and Sherman, 2007). Because the structural changes induced by aqueous Mn(II) likely alters the overall Mn oxidation state of the phyllomanganate sheet, aqueous Mn(II) may lead to different reactivities between phyllomanganates and redox active adsorbates. The results of this study suggest that aqueous Mn(II) can control phyllomanganate sheet structures, potentially impacting the sorption behavior and reactivities of naturally-occurring phyllomanganates.

4.5 ACKNOWLEDGEMENTS

The National Science Foundation (NSF), Division of Earth Sciences, Geobiology and Low-Temperature Geochemistry Program supported this research through Grant No. EAR-1056480. The facilities and instruments maintained by the Nano Research Facility at Washington University, supported by the NSF through Award No. ECS-0335765, were used to conduct ICP-OES analyses. XRD patterns were collected with the Bruker D8 Advance XRD instrument at Washington University in St. Louis, supported by the NSF through Award No. EAR-1161543. XAFS spectra presented in this manuscript were collected at beamline 5-BM-D at the APS, an Office of Science User Facility run by the U.S. Department of Energy (DOE) Office of Science by Argonne National Laboratory, supported by the U.S. DOE through Contract No. DE-AC02-06CH11357. Preliminary XAFS spectra were collected at beamline 12-BM-B, also at the APS at Argonne National Laboratory. The authors would particularly like to thank Sungsik Lee and Benjamin Reinhart for their support in running at beamline 12-BM-B, and Qing Ma for his help in setting up and collecting XAFS spectra at 5-BM-D.

Table 4.1. Properties of synthesized and reacted phyllomanganates, and reaction conditions and final solution concentrations for 25-day experiments.

Sample ID	Mn Oxide	pH	$[Mn(II)]_{initial}$ (mM)	AMOS[a]	$[Mn]_{soln}$ (mM)	$[Mn]_{ads}$ (mmol g^{-1})
Unreacted:						
Synthδ	δ-MnO_2			3.99		
SynthHB	HexB			3.82		
SynthTB	TriB			3.66		
25-day Samples:						
4δno	δ-MnO_2	4	0	4.00	0.012 ± 0.001	-[b]
4δlow	δ-MnO_2	4	0.75	3.91	BDL[c]	0.30
4δhigh	δ-MnO_2	4	7.5	3.69	4.4 ± 0.1	1.24
7δno	δ-MnO_2	7	0	3.74	BDL	-
7δlow	δ-MnO_2	7	0.75	3.75	BDL	0.30
7δhigh	δ-MnO_2	7	7.5	3.29	BDL	3.00
4HBno	HexB	4	0	3.84	BDL	-
4HBlow	HexB	4	0.75	3.69	0.48 ± 0.02	0.11
4HBhigh	HexB	4	7.5	--[d]	6.8 ± 0.2	0.28
7HBno	HexB	7	0	3.76	BDL	-
7HBlow	HexB	7	0.75	3.72	BDL	0.30
7HBhigh	HexB	7	7.5	3.28	BDL	3.00
4TBno	TriB	4	0	3.77	0.43 ± 0.01[c]	-
4TBlow	TriB	4	0.75	3.74	0.88 ± 0.03[c]	0.00
4TBhigh	TriB	4	7.5	3.73	6.70 ± 0.08	0.32
7TBno	TriB	7	0	3.66	BDL	-
7TBlow	TriB	7	0.75	3.61	BDL	0.30
7TBhigh	TriB	7	7.5	3.17	BDL	3.00

[a] Average manganese oxidation state. Errors are estimated to be approximately 0.04 v.u. in accordance with past studies (Manceau et al., 2012).
[b] (-) Denotes no aqueous Mn(II) added to the sample, so this parameter is not reported.
[c] BDL denotes any samples with $[Mn]_{soln}$ below detection limit (0.006 mM).
[d] No XAFS data is presented for this sample because it was damaged prior to analysis.

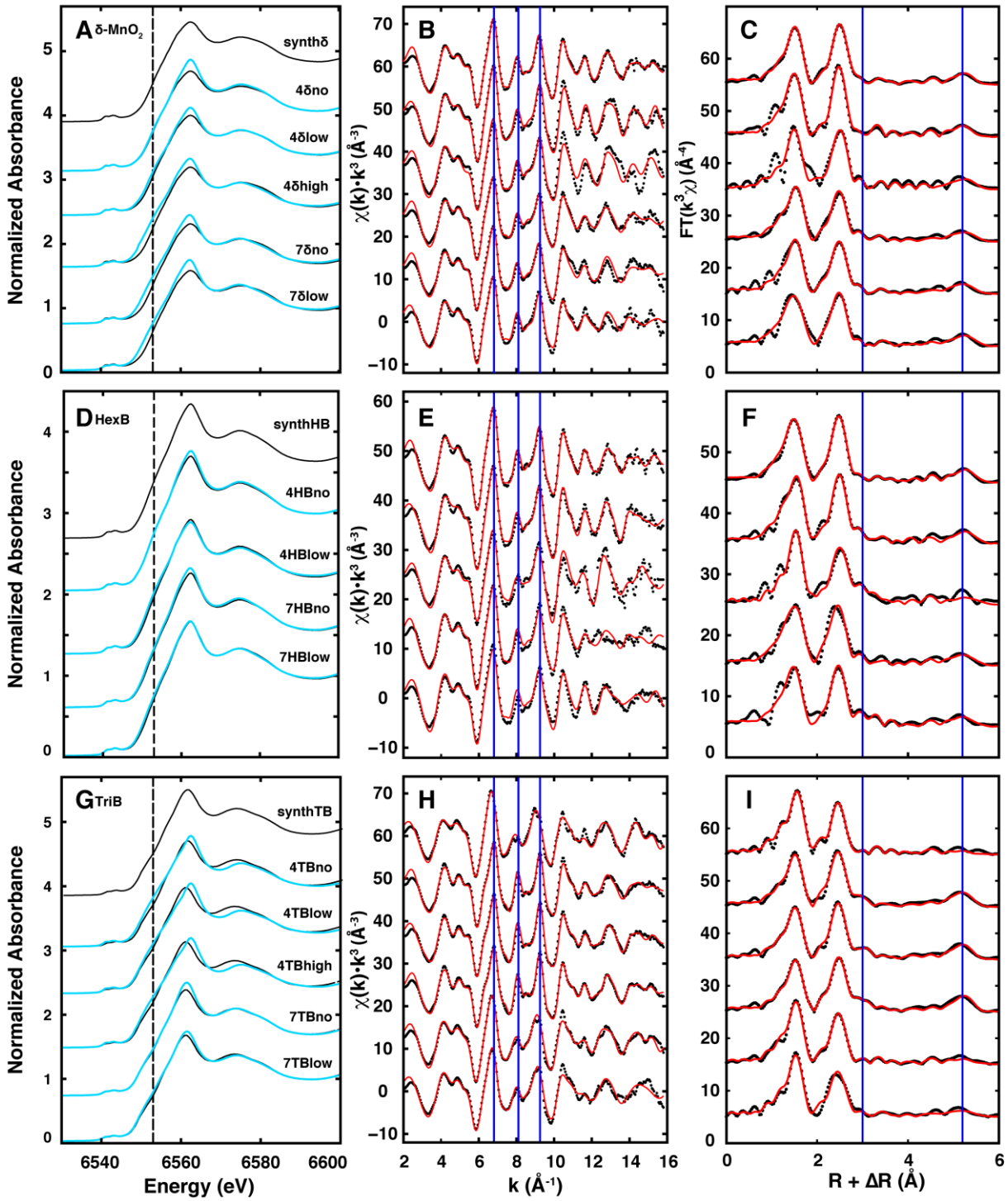

Figure 4.1. Mn XAFS spectra for the δ-MnO_2 (A-C), HexB (D-F), and TriB (G-I) systems. XANES spectra (A,D,G) of 25-day reacted samples (blue lines) are overplotted the XANES spectra for the corresponding synthesized, unreacted manganese oxide (thin black lines). EXAFS model fits (red lines) are overplotted the EXAFS spectra (points). Diagnostic features at 6553 Ev in the XANES spectra, 6.8, 8.1, and 9.2 $Å^{-1}$ in k space, and at 3.0 and 5.2 Å in R space are denoted by vertical lines.

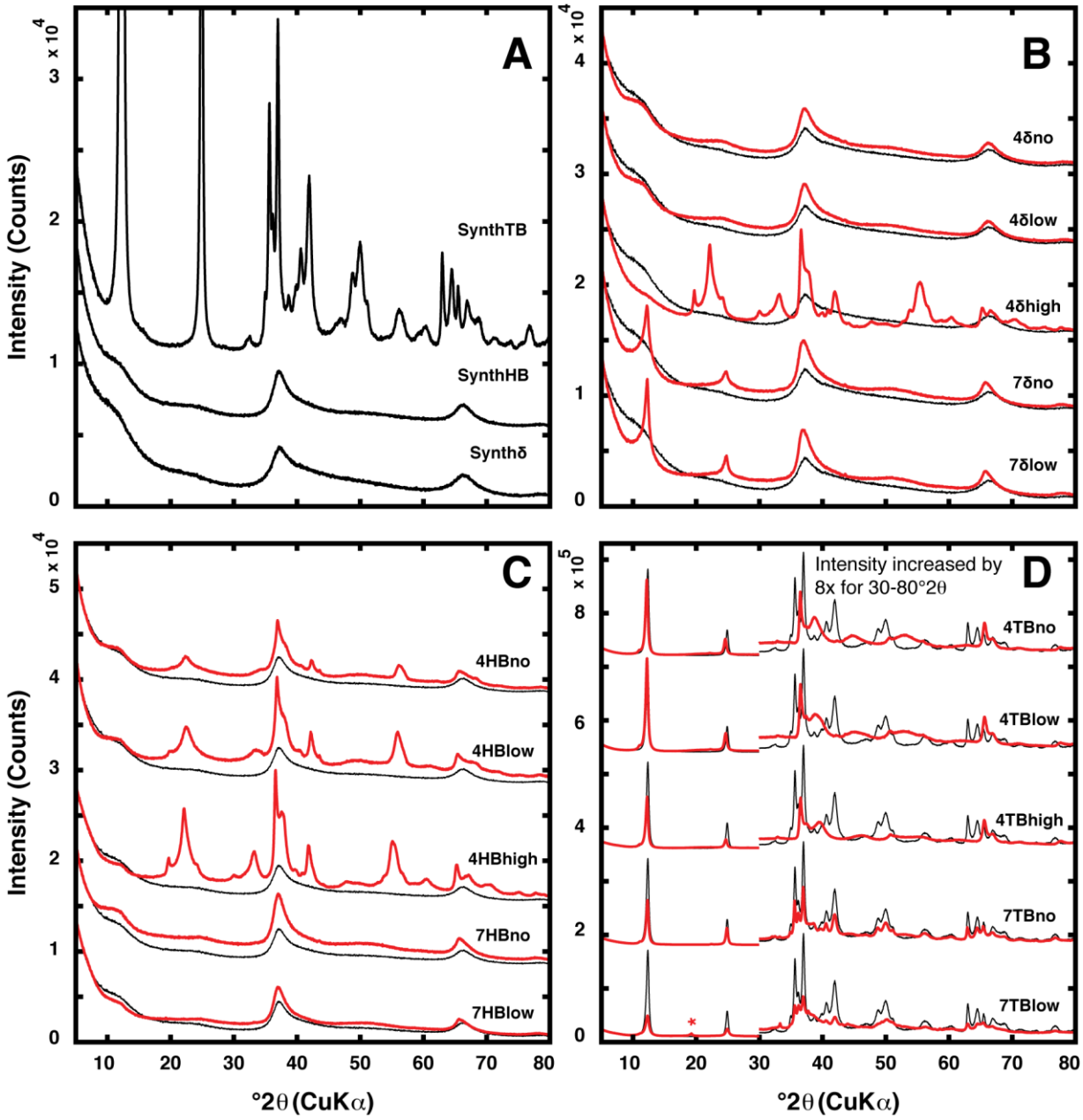

Figure 4.2. XRD patterns of unreacted, synthesized manganese oxides (A) and δ-MnO2 (B), HexB (C), and TriB (D): red line overplots are samples reacted for 25 days, solid black lines are the unreacted, synthesized phyllomanganate for comparison. Peak corresponding to feitknechtite is denoted by a red asterisk above the corresponding peak in (D). See Appendix for full plot of synthTB (001) and (002) intensities.

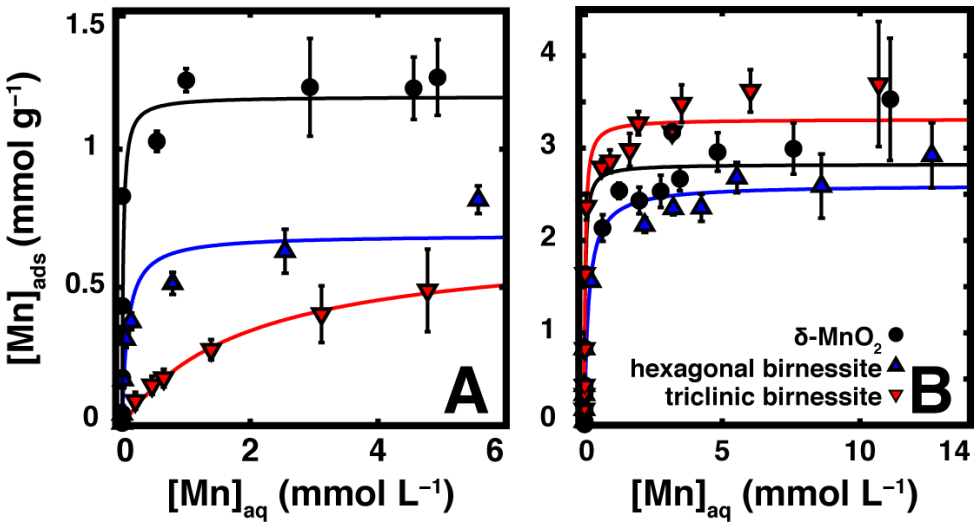

Figure 4.3. Mn(II) adsorption isotherms at pH 4 (A) and pH 7 (B). Lines represent Langmuir isotherm fits to the data.

4.6 APPENDIX

4.6.1 Manganese Oxide Syntheses

Manganese oxide minerals were synthesized following modified previously published procedures, as described in detail below. δ-MnO_2 was synthesized using a redox method, which involves the reduction of $KMnO_4$ and the oxidation of $MnCl_2$ under alkaline conditions, outlined by Villalobos (2003). Briefly, a solution of 2.50 g $KMnO_4$ in 80 mL deionized water (>18.2 MΩ·cm) was added to a solution of 1.75 g NaOH in 90 mL deionized water over approximately five minutes. While stirring this mixture vigorously, a solution of 4.70 g $MnCl_2$•$4H_2O$ in 80 mL deionized water was added slowly, over approximately 35 minutes. The mixture was allowed to settle for four hours, after which point the pH of the suspension was checked to ensure it was around a pH of 7, and the suspension was centrifuged, discarding the supernatant. The suspension was subjected to at least four 1 M NaCl washes, as described in Villalobos (2003), followed by at least six deionized water washes.

A poorly crystalline hexagonal birnessite was synthesized following the c-disordered H^+-birnessite synthesis procedure described in Villalobos (2003). This synthesis is similar to the δ-MnO_2 synthesis described above, except the NaOH solution consisted of 1.83 g NaOH in 90 mL deionized water and the Mn(II) solution consisted of 5.82 g $MnCl_2$•$4H_2O$ in 80 mL deionized water, and the pH of the suspension prior to centrifugation was near 3.1.

Triclinic birnessite was prepared following the synthesis for Na-birnessite outlined in Lopano et al. (2007), based on the synthesis procedures described by Post and Veblen (1990) and Golden et al. (1986; 1987). In this synthesis, a 5.5 M NaOH solution and a 0.5 M $MnCl_2$•$4H_2O$ solution were chilled in an ice bath while air was vigorously bubbled through the Mn(II)

solution. Once the solutions were chilled to 5 ^{o}C, the NaOH solution was added to the Mn(II) solution over approximately 3 minutes under a fume hood. The resulting suspension was bubbled with air overnight in the fume hood. The suspension was washed by an initial centrifugation to remove the basic supernatant, followed by filtration (0.45 µm nylon membrane, Whatman ®) and washing with deionized water until the pH of the filtrate was below 10. The synthesized Mn(IV/III) oxides were stored as mineral suspensions in deionized water in aluminum foil-wrapped polypropylene bottles.

4.6.2 XAFS Spectroscopy Data Collection

XAFS spectra were collected at beamline 5-BM-D at the Advanced Photon Source (APS) at Argonne National Laboratory. This beamline uses a Si (111) fixed-offset double-crystal monochromator, which was detuned by 40% to decrease harmonics in the incident X-ray beam. Rh-coated Si mirrors collimate the beam and further reduce the harmonic content. A Mn metal foil was used to calibrate the monochromators to the Mn K-edge (6539 eV). All measurements were collected in transmission mode.

Table A4.1. Spectral fitting results for Mn transmission EXAFS for phyllomanganate standards.

Sample	Shell	N[a]	R (Å)[b]	σ^2 (Å^2)[c]	ΔE_0 (eV)[d]	$S0^2$ [e]	χ_v^2 [f]	f_{occ}	R-factor
δ-MnO₂									
	$Mn\text{-}O_{1a}$	4	1.900(4)[g]	0.0040(3)	10.8(6)	0.835	34.46	0.78(4)	0.0051
	$Mn\text{-}O_{1b}$	2	1.97(2)	0.012(3)					
	$Mn\text{-}Mn_{1a}$	2	2.853(7)	0.0052(4)					
	$Mn\text{-}Mn_{1b}$	4	2.893(4)	0.0052[h]					
	$Mn\text{-}O_{2a}$	4	3.58(3)	0.004(3)					
	$Mn\text{-}O_{2b}$	2	3.71(3)	0.004					
	$Mn\text{-}Mn_{crnr}$	2.4(9)	3.47(2)	0.0052					
	$Mn\text{-}Na_{int}$	1.0(7)	4.07(4)	0.0052					
	$Mn\text{-}O_{3a}$	4	4.49(3)	0.006(2)					
	$Mn\text{-}O_{3b}$	8	4.70(2)	0.006					
	$Mn\text{-}Mn_{2a}$	4	4.92	0.007(2)					
	$Mn\text{-}Mn_{2b}$	2	5.03	0.007					
	$Mn\text{-}Mn_{3a}$	2	5.71	0.016(5)					
	$Mn\text{-}Mn_{3b}$	4	5.79	0.016					
	$Mn\text{-}Mn_{MS3a}$	2	5.71	0.003(2)					
	$Mn\text{-}Mn_{MS3b}$	4	5.79	0.003					
	$Mn\text{-}Mn_{MS3c}$	4	5.71	0.016					
	$Mn\text{-}Mn_{MS3d}$	8	5.79	0.016					
	$Mn\text{-}Mn_{MS4a}$	2	5.71	0.003					
	$Mn\text{-}Mn_{MS4b}$	4	5.79	0.003					
	$Mn\text{-}Mn_{MS4c}$	2	5.71	0.003					
	$Mn\text{-}Mn_{MS4d}$	4	5.79	0.003					
	$Mn\text{-}Mn_{MS4e}$	2	5.71	0.016					
	$Mn\text{-}Mn_{MS4f}$	4	5.79	0.016					
HexB									
	$Mn\text{-}O_{1a}$	4	1.870(6)	0.0039(7)	8.4(8)	0.835	53.6	0.75(7)	0.0097
	$Mn\text{-}O_{1b}$	2	1.97(1)	0.003(1)					
	$Mn\text{-}Mn_{1a}$	2	2.84(1)	0.0053(5)					
	$Mn\text{-}Mn_{1b}$	4	2.880(5)	0.0053					
	$Mn\text{-}O_{2a}$	4	3.55(6)	0.01(2)					
	$Mn\text{-}O_{2b}$	2	3.7(2)	0.01					
	$Mn\text{-}Mn_{crnr}$	2(2)	3.44(2)	0.0053					
	$Mn\text{-}Na_{int}$	0.4(1.1)	3.8(4)	0.0053					
	$Mn\text{-}O_{3a}$	4	4.51(3)	0.004(2)					
	$Mn\text{-}O_{3b}$	8	4.69(2)	0.004					
	$Mn\text{-}Mn_{2a}$	4	4.90	0.007(3)					
	$Mn\text{-}Mn_{2b}$	2	5.00	0.007					
	$Mn\text{-}Mn_{3a}$	2	5.68	0.008(1)					
	$Mn\text{-}Mn_{3b}$	4	5.76	0.008					
	$Mn\text{-}Mn_{MS3a}$	2	5.68	0.02(1)					
	$Mn\text{-}Mn_{MS3b}$	4	5.76	0.02					
	$Mn\text{-}Mn_{MS3c}$	4	5.68	0.008					
	$Mn\text{-}Mn_{MS3d}$	8	5.76	0.008					
	$Mn\text{-}Mn_{MS4a}$	2	5.68	0.02					
	$Mn\text{-}Mn_{MS4b}$	4	5.76	0.02					
	$Mn\text{-}Mn_{MS4c}$	2	5.68	0.02					
	$Mn\text{-}Mn_{MS4d}$	4	5.76	0.02					
	$Mn\text{-}Mn_{MS4e}$	2	5.68	0.008					
	$Mn\text{-}Mn_{MS4f}$	4	5.76	0.008					

Table A4.1

Sample	Shell	N[a]	R (Å)[b]	σ^2 (Å^2)[c]	ΔE_0 (eV)[d]	$S0^2$ [e]	χ_v^2 [f]	f_{occ}	R-factor
TriB									
	Mn-O_{1a}	4	1.88(2)	0.006(1)	6(2)	0.835	266	0.8(1)	0.028
	Mn-O_{1b}	2	1.92(1)	0.002(1)					
	Mn-Mn_{1a}	2	2.86(1)	0.007(1)					
	Mn-Mn_{1b}	4	2.89(2)	0.007					
	Mn-O_{2a}	4	3.46(3)	0.003(2)					
	Mn-O_{2b}	2	3.66(4)	0.003					
	Mn-Mn_{crnr}	1.6(8)	3.33(5)	0.007					
	Mn-Na_{int}	0.6(2.2)	4.1(2)	0.007					
	Mn-O_{3a}	4	4.50(8)	0.006(4)					
	Mn-O_{3b}	8	4.69(4)	0.006					
	Mn-Mn_{2a}	4	4.94	0.010(7)					
	Mn-Mn_{2b}	2	5.03	0.010					
	Mn-Mn_{3a}	2	5.73	0.02(2)					
	Mn-Mn_{3b}	4	5.78	0.02					
	Mn-Mn_{MS3a}	2	5.73	0.02(2)					
	Mn-Mn_{MS3b}	4	5.78	0.02					
	Mn-Mn_{MS3c}	4	5.73	0.02					
	Mn-Mn_{MS3d}	8	5.78	0.02					
	Mn-Mn_{MS4a}	2	5.73	0.02					
	Mn-Mn_{MS4b}	4	5.78	0.02					
	Mn-Mn_{MS4c}	2	5.73	0.02					
	Mn-Mn_{MS4d}	4	5.78	0.02					
	Mn-Mn_{MS4e}	2	5.73	0.02					
	Mn-Mn_{MS4f}	4	5.78	0.02					

[a] Coordination Number.
[b] Interatomic distance.
[c] Debye-Waller factor.
[d] Difference in the threshold Fermi level between data and theory.
[e] Amplitude reduction factor.
[f] Goodness of fit parameters [see (Kelly et al., 2008)].
[g] Statistical uncertainties at the 68% confidence level are reported in parentheses. Any parameters without reported uncertainties were not allowed to vary during fitting.
[h] σ^2 fixed for all linked shells, denoted by those without uncertainties reported.

Table A4.2. Langmuir isotherm parameters determined for Mn(II) adsorption onto Mn oxides.

Sample	Γ_{max} (mmol g^{-1})	K (mL mmol^{-1})
pH 4		
δ-MnO_2	1.2 ± 0.2	55 ± 480
HexB	0.69 ± 0.06	12 ± 5
TriB	0.67 ± 0.06	0.5 ± 0.1
pH 7		
δ-MnO_2	2.8 ± 0.2	31 ± 20
HexB	2.6 ± 0.2	7 ± 4
TriB	3.3 ± 0.1	29 ± 5

Table A4.3. Spectral fitting results for Mn transmission EXAFS for 25-day reacted phyllomanganate samples.

Sample	Shell	N[a]	R (Å)[b]	σ^2 (Å^2)[c]	ΔE_0 (eV)[d]	$S0^2$ [e]	χ_v^2 [f]	f_{occ}	R-factor
δ-MnO₂	Mn-O_{1a}	4	1.87(2)[g]	0.003(1)	8(1)	0.835	186.7	0.6(1)	0.0212
pH4	Mn-O_{1b}	2	1.96(3)	0.004(3)					
0 mM	Mn-Mn_{1a}	2	2.83(1)	0.0031(8)					
Mn(II)	Mn-Mn_{1b}	4	2.872(8)	0.0031[h]					
25 days	Mn-O_{2a}	4	3.41(4)	0.003(2)					
	Mn-O_{2b}	2	3.68(4)	0.003					
	Mn-Mn_{crnr}	0.8(6)	3.28(3)	0.0031					
	Mn-Na_{int}	1(1)	4.11(7)	0.0031					
	Mn-O_{3a}	4	4.46(5)	0.004(3)					
	Mn-O_{3b}	8	4.66(3)	0.004					
	Mn-Mn_{2a}	4	4.87	0.004(3)					
	Mn-Mn_{2b}	2	5.00	0.004					
	Mn-Mn_{3a}	2	5.66	0.011(9)					
	Mn-Mn_{3b}	4	5.74	0.011					
	Mn-Mn_{MS3a}	2	5.66	0.002(6)					
	Mn-Mn_{MS3b}	4	5.74	0.002					
	Mn-Mn_{MS3c}	4	5.66	0.011					
	Mn-Mn_{MS3d}	8	5.74	0.011					
	Mn-Mn_{MS4a}	2	5.66	0.002					
	Mn-Mn_{MS4b}	4	5.74	0.002					
	Mn-Mn_{MS4c}	2	5.66	0.002					
	Mn-Mn_{MS4d}	4	5.74	0.002					
	Mn-Mn_{MS4e}	2	5.66	0.011					
	Mn-Mn_{MS4f}	4	5.74	0.011					
δ-MnO₂									
pH4	Mn-O_{1a}	4	1.87(1)	0.0020(8)	9(3)	0.835	467	0.7(1)	0.068
0.75 mM	Mn-O_{1b}	2	2.00(2)	0.0020					
Mn(II)	Mn-Mn_{1a}	2	2.83(2)	0.004(1)					
25 days	Mn-Mn_{1b}	4	2.88(1)	0.004					
	Mn-O_{2a}	4	3.50(4)	0.001(3)					
	Mn-O_{2b}	2	3.66(6)	0.001					
	Mn-Mn_{crnr}	2(1)	3.40(4)	0.004					
	Mn-Na_{int}	2(3)	4.10(8)	0.004					
	Mn-O_{3a}	4	4.4(2)	0.01(1)					
	Mn-O_{3b}	8	4.6(1)	0.01					
	Mn-Mn_{2a}	4	4.86	0.007(9)					
	Mn-Mn_{2b}	2	5.03	0.007					
	Mn-Mn_{3a}	2	5.66	0.01(1)					
	Mn-Mn_{3b}	4	5.77	0.01					
	Mn-Mn_{MS3a}	2	5.66	0.01(2)					
	Mn-Mn_{MS3b}	4	5.77	0.01					
	Mn-Mn_{MS3c}	4	5.66	0.01					
	Mn-Mn_{MS3d}	8	5.77	0.01					
	Mn-Mn_{MS4a}	2	5.66	0.01					
	Mn-Mn_{MS4b}	4	5.77	0.01					
	Mn-Mn_{MS4c}	2	5.66	0.01					
	Mn-Mn_{MS4d}	4	5.77	0.01					
	Mn-Mn_{MS4e}	2	5.66	0.01					
	Mn-Mn_{MS4f}	4	5.77	0.01					
δ-MnO₂									
pH 4	Mn-O_{1a}	4	1.90(2)	0.009(2)	10(1)	0.835	105	0.74(8)	0.019
7.5 mM	Mn-O_{1b}	2	1.916(9)	0.0023(6)					

Table A4.3

Sample	Shell	N[a]	R (Å)[b]	σ^2 (Å^2)[c]	ΔE_0 (eV)[d]	$S0^2$ [e]	χ_v^2 [f]	f_{occ}	R-factor
Mn(II)	$Mn\text{-}Mn_{1a}$	2	2.85(2)	0.0059(8)					
25 days	$Mn\text{-}Mn_{1b}$	4	2.890(9)	0.0059					
	$Mn\text{-}O_{2a}$	4	3.54(3)	0.001(2)					
	$Mn\text{-}O_{2b}$	2	3.67(4)	0.001					
	$Mn\text{-}Mn_{crnr}$	4(1)	3.44(2)	0.0059					
	$Mn\text{-}Na_{int}$	1(1)	4.1(2)	0.0059					
	$Mn\text{-}O_{3a}$	4	4.48(9)	0.008(6)					
	$Mn\text{-}O_{3b}$	8	4.67(5)	0.008					
	$Mn\text{-}Mn_{2a}$	4	4.91	0.010(8)					
	$Mn\text{-}Mn_{2b}$	2	5.03	0.10					
	$Mn\text{-}Mn_{3a}$	2	5.70	0.010(5)					
	$Mn\text{-}Mn_{3b}$	4	5.78	0.010					
	$Mn\text{-}Mn_{MS3a}$	2	5.70	0.01(1)					
	$Mn\text{-}Mn_{MS3b}$	4	5.78	0.01					
	$Mn\text{-}Mn_{MS3c}$	4	5.70	0.010					
	$Mn\text{-}Mn_{MS3d}$	8	5.78	0.010					
	$Mn\text{-}Mn_{MS4a}$	2	5.70	0.01					
	$Mn\text{-}Mn_{MS4b}$	4	5.78	0.01					
	$Mn\text{-}Mn_{MS4c}$	2	5.70	0.01					
	$Mn\text{-}Mn_{MS4d}$	4	5.78	0.01					
	$Mn\text{-}Mn_{MS4e}$	2	5.70	0.010					
	$Mn\text{-}Mn_{MS4f}$	4	5.78	0.010					
δ-MnO$_2$									
pH 7	$Mn\text{-}O_{1a}$	4	1.903(6)	0.0038(5)	10(1)	0.835	185.9	0.77(9)	0.024
0 mM	$Mn\text{-}O_{1b}$	2	1.96(7)	0.019(8)					
Mn(II)	$Mn\text{-}Mn_{1a}$	2	2.86(3)	0.006(1)					
25 days	$Mn\text{-}Mn_{1b}$	4	2.89(2)	0.006					
	$Mn\text{-}O_{2a}$	4	3.55(4)	0.001(2)					
	$Mn\text{-}O_{2b}$	2	3.68(5)	0.001					
	$Mn\text{-}Mn_{crnr}$	3(1)	3.45(3)	0.006					
	$Mn\text{-}Na_{int}$	0.6(1.7)	4.1(2)	0.006					
	$Mn\text{-}O_{3a}$	4	4.5(1)	0.009(9)					
	$Mn\text{-}O_{3b}$	8	4.68(7)	0.009					
	$Mn\text{-}Mn_{2a}$	4	4.93	0.012(9)					
	$Mn\text{-}Mn_{2b}$	2	5.02	0.012					
	$Mn\text{-}Mn_{3a}$	2	5.72	0.014(9)					
	$Mn\text{-}Mn_{3b}$	4	5.78	0.014					
	$Mn\text{-}Mn_{MS3a}$	2	5.72	0.005(7)					
	$Mn\text{-}Mn_{MS3b}$	4	5.78	0.005					
	$Mn\text{-}Mn_{MS3c}$	4	5.72	0.014					
	$Mn\text{-}Mn_{MS3d}$	8	5.78	0.014					
	$Mn\text{-}Mn_{MS4a}$	2	5.72	0.005					
	$Mn\text{-}Mn_{MS4b}$	4	5.78	0.005					
	$Mn\text{-}Mn_{MS4c}$	2	5.72	0.005					
	$Mn\text{-}Mn_{MS4d}$	4	5.78	0.005					
	$Mn\text{-}Mn_{MS4e}$	2	5.72	0.014					
	$Mn\text{-}Mn_{MS4f}$	4	5.78	0.014					
δ-MnO$_2$									
pH 7	$Mn\text{-}O_{1a}$	4	1.865(7)	0.0041(7)	8(1)	0.835	133.4	0.8(1)	0.034
0.75 mM	$Mn\text{-}O_{1b}$	2	1.97(1)	0.002(1)					
Mn(II)	$Mn\text{-}Mn_{1a}$	2	2.85(4)	0.006(1)					
25 days	$Mn\text{-}Mn_{1b}$	4	2.88(1)	0.006					
	$Mn\text{-}O_{2a}$	4	3.54(7)	0.005(3)					

Table A4.3

Sample	Shell	N[a]	R (Å)[b]	σ^2 (Å^2)[c]	ΔE_0 (eV)[d]	$S0^2$ [e]	χ_v^2 [f]	f_{occ}	R-factor
	$Mn\text{-}O_{2b}$	2	3.79(7)	0.005					
	$Mn\text{-}Mn_{crnr}$	2(1)	3.43(6)	0.006					
	$Mn\text{-}Na_{int}$	0.6(1.9)	4.0(2)	0.006					
	$Mn\text{-}O_{3a}$	4	4.5(1)	0.008(8)					
	$Mn\text{-}O_{3b}$	8	4.68(7)	0.008					
	$Mn\text{-}Mn_{2a}$	4	4.91	0.01(1)					
	$Mn\text{-}Mn_{2b}$	2	5.01	0.01					
	$Mn\text{-}Mn_{3a}$	2	5.69	0.009(4)					
	$Mn\text{-}Mn_{3b}$	4	5.76	0.009					
	$Mn\text{-}Mn_{MS3a}$	2	5.69	0.02(2)					
	$Mn\text{-}Mn_{MS3b}$	4	5.76	0.02					
	$Mn\text{-}Mn_{MS3c}$	4	5.69	0.009					
	$Mn\text{-}Mn_{MS3d}$	8	5.76	0.009					
	$Mn\text{-}Mn_{MS4a}$	2	5.69	0.016					
	$Mn\text{-}Mn_{MS4b}$	4	5.76	0.016					
	$Mn\text{-}Mn_{MS4c}$	2	5.69	0.016					
	$Mn\text{-}Mn_{MS4d}$	4	5.76	0.016					
	$Mn\text{-}Mn_{MS4e}$	2	5.69	0.009					
	$Mn\text{-}Mn_{MS4f}$	4	5.76	0.009					
HexBirn									
pH 4	$Mn\text{-}O_{1a}$	4	1.86(2)	0.006(2)	7(2)	0.835	120.8	0.6(1)	0.0198
0 mM	$Mn\text{-}O_{1b}$	2	1.93(1)	0.0013(8)					
Mn(II)	$Mn\text{-}Mn_{1a}$	2	2.84(2)	0.005(1)					
25 days	$Mn\text{-}Mn_{1b}$	4	2.88(1)	0.005					
	$Mn\text{-}O_{2a}$	4	3.34(6)	0.003(3)					
	$Mn\text{-}O_{2b}$	2	3.73(3)	0.003					
	$Mn\text{-}Mn_{crnr}$	2(2)	3.18(4)	0.005					
	$Mn\text{-}Na_{int}$	1(2)	3.4(2)	0.005					
	$Mn\text{-}O_{3a}$	4	4.46(5)	0.005(3)					
	$Mn\text{-}O_{3b}$	8	4.68(3)	0.005					
	$Mn\text{-}Mn_{2a}$	4	4.90	0.007(5)					
	$Mn\text{-}Mn_{2b}$	2	5.00	0.007					
	$Mn\text{-}Mn_{3a}$	2	5.68	0.007(2)					
	$Mn\text{-}Mn_{3b}$	4	5.75	0.007					
	$Mn\text{-}Mn_{MS3a}$	2	5.68	0.02(4)					
	$Mn\text{-}Mn_{MS3b}$	4	5.75	0.02					
	$Mn\text{-}Mn_{MS3c}$	4	5.68	0.007					
	$Mn\text{-}Mn_{MS3d}$	8	5.75	0.007					
	$Mn\text{-}Mn_{MS4a}$	2	5.68	0.02					
	$Mn\text{-}Mn_{MS4b}$	4	5.75	0.02					
	$Mn\text{-}Mn_{MS4c}$	2	5.68	0.02					
	$Mn\text{-}Mn_{MS4d}$	4	5.75	0.02					
	$Mn\text{-}Mn_{MS4e}$	2	5.68	0.007					
	$Mn\text{-}Mn_{MS4f}$	4	5.75	0.007					
HexBirn									
pH 4	$Mn\text{-}O_{1a}$	4	1.904(8)	0.0022(5)	12(3)	0.835	72.91	1[m]	0.0502
0.75 mM	$Mn\text{-}O_{1b}$	2	2.08(4)	0.010 (8)					
Mn(II)	$Mn\text{-}Mn_{1a}$	2	2.88(2)	0.009(3)					
25 days	$Mn\text{-}Mn_{1b}$	4	2.93(2)	0.009					
	$Mn\text{-}O_{2a}$	4	3.39(3)	0.003(3)					
	$Mn\text{-}O_{2b}$	2	3.73(5)	0.003					
	$Mn\text{-}Mn_{crnr}$	3(2)	3.17(2)	0.009					
	$Mn\text{-}Na_{int}$	2(3)	4.2(1)	0.009					

Table A4.3

Sample	Shell	N[a]	R (Å)[b]	σ^2 (Å^2)[c]	ΔE_0 (eV)[d]	$S0^2$ [e]	χ_v^2 [f]	f_{occ}	R-factor
	Mn-O_{3a}	4	4.47(7)	0.005(4)					
	Mn-O_{3b}	8	4.68(4)	0.005					
	Mn-Mn_{2a}	4	4.95	0.010(9)					
	Mn-Mn_{2b}	2	5.10	0.010					
	Mn-Mn_{3a}	2	5.75	0.015(8)					
	Mn-Mn_{3b}	4	5.85	0.015					
	Mn-Mn_{MS3a}	2	5.75	0.02(7)					
	Mn-Mn_{MS3b}	4	5.85	0.02					
	Mn-Mn_{MS3c}	4	5.75	0.015					
	Mn-Mn_{MS3d}	8	5.85	0.015					
	Mn-Mn_{MS4a}	2	5.75	0.02					
	Mn-Mn_{MS4b}	4	5.85	0.02					
	Mn-Mn_{MS4c}	2	5.75	0.02					
	Mn-Mn_{MS4d}	4	5.85	0.02					
	Mn-Mn_{MS4e}	2	5.75	0.015					
	Mn-Mn_{MS4f}	4	5.85	0.015					
HexBirn									
pH 7	Mn-O_{1a}	4	1.87(2)	0.004(2)	8(2)	0.835	387.9	1.0(2)	0.0522
0 mM	Mn-O_{1b}	2	1.96(2)	0.002(2)					
Mn(II)	Mn-Mn_{1a}	2	2.84(2)	0.007(1)					
25 days	Mn-Mn_{1b}	4	2.88(1)	0.007					
	Mn-O_{2a}	4	3.58(5)	0.001(4)					
	Mn-O_{2b}	2	3.7(1)	0.001					
	Mn-Mn_{crnr}	4(2)	3.47(3)	0.007					
	Mn-Na_{int}	1(3)	4.0(2)	0.007					
	Mn-O_{3a}	4	4.48(9)	0.005(5)					
	Mn-O_{3b}	8	4.67(6)	0.005					
	Mn-Mn_{2a}	4	4.88	0.01(1)					
	Mn-Mn_{2b}	2	5.02	0.01					
	Mn-Mn_{3a}	2	5.67	0.010(5)					
	Mn-Mn_{3b}	4	5.76	0.010					
	Mn-Mn_{MS3a}	2	5.67	0.02(2)					
	Mn-Mn_{MS3b}	4	5.76	0.02					
	Mn-Mn_{MS3c}	4	5.67	0.010					
	Mn-Mn_{MS3d}	8	5.76	0.010					
	Mn-Mn_{MS4a}	2	5.67	0.02					
	Mn-Mn_{MS4b}	4	5.76	0.02					
	Mn-Mn_{MS4c}	2	5.67	0.02					
	Mn-Mn_{MS4d}	4	5.76	0.02					
	Mn-Mn_{MS4e}	2	5.67	0.010					
	Mn-Mn_{MS4f}	4	5.76	0.010					
HexBirn									
pH 7	Mn-O_{1a}	4	1.88(2)	0.004(2)	9(2)	0.835	268.6	0.7(1)	0.0520
0.75 mM	Mn-O_{1b}	2	1.98(3)	0.004(4)					
Mn(II)	Mn-Mn_{1a}	2	2.85(3)	0.006(1)					
25 days	Mn-Mn_{1b}	4	2.89(2)	0.006					
	Mn-O_{2a}	4	3.4(2)	0.002(3)					
	Mn-O_{2b}	2	3.6(2)	0.002					
	Mn-Mn_{crnr}	0.4(1.6)	3.47(2)	0.006					
	Mn-Na_{int}	1(2)	4.1(1)	0.006					
	Mn-O_{3a}	4	4.4(1)	0.006(6)					
	Mn-O_{3b}	8	4.66(5)	0.006					
	Mn-Mn_{2a}	4	4.91	0.01(1)					

Table A4.3

Sample	Shell	N[a]	R (Å)[b]	σ^2 (Å^2)[c]	ΔE_0 (eV)[d]	$S0^2$ [e]	χ_ν^2 [f]	f_{occ}	R-factor
	Mn-Mn_{2b}	2	5.02	0.01					
	Mn-Mn_{3a}	2	5.70	0.01(1)					
	Mn-Mn_{3b}	4	5.77	0.01					
	Mn-Mn_{MS3a}	2	5.70	0.01(1)					
	Mn-Mn_{MS3b}	4	5.77	0.01					
	Mn-Mn_{MS3c}	4	5.70	0.01					
	Mn-Mn_{MS3d}	8	5.77	0.01					
	Mn-Mn_{MS4a}	2	5.70	0.01					
	Mn-Mn_{MS4b}	4	5.77	0.01					
	Mn-Mn_{MS4c}	2	5.70	0.01					
	Mn-Mn_{MS4d}	4	5.77	0.01					
	Mn-Mn_{MS4e}	2	5.70	0.01					
	Mn-Mn_{MS4f}	4	5.77	0.01					
TriBirn									
pH 4	Mn-O_{1a}	4	1.899(5)	0.0039(4)	9(1)	0.835	507.6	0.89(9)	0.0199
0 mM	Mn-O_{1b}	2	1.94(7)	0.022(9)					
Mn(II)	Mn-Mn_{1a}	2	2.83(2)	0.0064(8)					
25 days	Mn-Mn_{1b}	4	2.878(7)	0.0064					
	Mn-O_{2a}	4	3.56(6)	0.002(4)					
	Mn-O_{2b}	2	3.67(9)	0.002					
	Mn-Mn_{crnr}	3(2)	3.48(3)	0.0064					
	Mn-Na_{int}	0.5(1.8)	4.0(2)	0.0064					
	Mn-O_{3a}	4	4.48(7)	0.006(5)					
	Mn-O_{3b}	8	4.66(4)	0.006					
	Mn-Mn_{2a}	4	4.88	0.009(6)					
	Mn-Mn_{2b}	2	5.01	0.009					
	Mn-Mn_{3a}	2	5.67	0.012(6)					
	Mn-Mn_{3b}	4	5.76	0.012					
	Mn-Mn_{MS3a}	2	5.67	0.002(4)					
	Mn-Mn_{MS3b}	4	5.76	0.002					
	Mn-Mn_{MS3c}	4	5.67	0.012					
	Mn-Mn_{MS3d}	8	5.76	0.012					
	Mn-Mn_{MS4a}	2	5.67	0.002					
	Mn-Mn_{MS4b}	4	5.76	0.002					
	Mn-Mn_{MS4c}	2	5.67	0.002					
	Mn-Mn_{MS4d}	4	5.76	0.002					
	Mn-Mn_{MS4e}	2	5.67	0.012					
	Mn-Mn_{MS4f}	4	5.76	0.012					
TriBirn									
pH 4	Mn-O_{1a}	4	1.896(4)	0.0038(3)	9(1)	0.835	258.6	0.77(7)	0.0131
0.75 mM	Mn-O_{1b}	2	1.99(8)	0.03(1)					
Mn(II)	Mn-Mn_{1a}	2	2.83(1)	0.0056(6)					
25 days	Mn-Mn_{1b}	4	2.875(5)	0.0056					
	Mn-O_{2a}	4	3.6(1)	0.009(9)					
	Mn-O_{2b}	2	3.8(1)	0.009					
	Mn-Mn_{crnr}	2(2)	3.50(3)	0.0056					
	Mn-Na_{int}	0.8(1.3)	4.0(1)	0.0056					
	Mn-O_{3a}	4	4.48(5)	0.006(3)					
	Mn-O_{3b}	8	4.68(3)	0.006					
	Mn-Mn_{2a}	4	4.88	0.007(4)					
	Mn-Mn_{2b}	2	5.00	0.007					
	Mn-Mn_{3a}	2	5.66	0.011(4)					
	Mn-Mn_{3b}	4	5.75	0.011					

Table A4.3

Sample	Shell	N[a]	R (Å)[b]	σ^2 (Å^2)[c]	ΔE_0 (eV)[d]	$S0^2$ [e]	χ_ν^2 [f]	f_{occ}	R-factor
	Mn-Mn_{MS3a}	2	5.66	0.001(3)					
	Mn-Mn_{MS3b}	4	5.75	0.001					
	Mn-Mn_{MS3c}	4	5.66	0.011					
	Mn-Mn_{MS3d}	8	5.75	0.011					
	Mn-Mn_{MS4a}	2	5.66	0.001					
	Mn-Mn_{MS4b}	4	5.75	0.001					
	Mn-Mn_{MS4c}	2	5.66	0.001					
	Mn-Mn_{MS4d}	4	5.75	0.001					
	Mn-Mn_{MS4e}	2	5.66	0.011					
	Mn-Mn_{MS4f}	4	5.75	0.011					
TriBirn									
pH 4	Mn-O_{1a}	4	1.905(3)	0.0036(2)	11(1)	0.835	347.9	0.79(5)	0.0067
7.5 mM	Mn-O_{1b}	2	2.07(5)	0.03(1)					
Mn(II)	Mn-Mn_{1a}	2	2.847(9)	0.0058(4)					
25 days	Mn-Mn_{1b}	4	2.886(4)	0.0058					
	Mn-O_{2a}	4	3.56(3)	0.001(1)					
	Mn-O_{2b}	2	3.67(4)	0.001					
	Mn-Mn_{crnr}	3.9(9)	3.48(2)	0.0058					
	Mn-Na_{int}	0.4(8)	4.0(1)	0.0058					
	Mn-O_{3a}	4	4.50(4)	0.006(3)					
	Mn-O_{3b}	8	4.70(2)	0.006					
	Mn-Mn_{2a}	4	4.91	0.008(3)					
	Mn-Mn_{2b}	2	5.02	0.008					
	Mn-Mn_{3a}	2	5.69	0.013(3)					
	Mn-Mn_{3b}	4	5.77	0.013					
	Mn-Mn_{MS3a}	2	5.69	0.001(2)					
	Mn-Mn_{MS3b}	4	5.77	0.001					
	Mn-Mn_{MS3c}	4	5.69	0.013					
	Mn-Mn_{MS3d}	8	5.77	0.013					
	Mn-Mn_{MS4a}	2	5.69	0.001					
	Mn-Mn_{MS4b}	4	5.77	0.001					
	Mn-Mn_{MS4c}	2	5.69	0.001					
	Mn-Mn_{MS4d}	4	5.77	0.001					
	Mn-Mn_{MS4e}	2	5.69	0.013					
	Mn-Mn_{MS4f}	4	5.77	0.013					
TriBirn									
pH 7	Mn-O_{1a}	4	1.90(2)	0.009(1)	8(1)	0.835	601.5	0.9(1)	0.0216
0 mM	Mn-O_{1b}	2	1.907(7)	0.0013(6)					
Mn(II)	Mn-Mn_{1a}	2	2.86(2)	0.007(1)					
25 days	Mn-Mn_{1b}	4	2.90(1)	0.007					
	Mn-O_{2a}	4	3.49(2)	0.001(2)					
	Mn-O_{2b}	2	3.64(4)	0.001					
	Mn-Mn_{crnr}	2(1)	3.39(3)	0.007					
	Mn-Na_{int}	0.5(2.0)	4.2(2)	0.007					
	Mn-O_{3a}	4	4.49(5)	0.005(3)					
	Mn-O_{3b}	8	4.68(3)	0.005					
	Mn-Mn_{2a}	4	4.93	0.010(7)					
	Mn-Mn_{2b}	2	5.05	0.010					
	Mn-Mn_{3a}	2	5.72	0.02(1)					
	Mn-Mn_{3b}	4	5.80	0.02					
	Mn-Mn_{MS3a}	2	5.72	0.01(2)					
	Mn-Mn_{MS3b}	4	5.80	0.01					
	Mn-Mn_{MS3c}	4	5.72	0.02					

Table A4.3

Sample	Shell	N[a]	R (Å)[b]	σ^2 (Å^2)[c]	ΔE_0 (eV)[d]	$S0^2$ [e]	χ_v^2 [f]	f_{occ}	R-factor
	Mn-Mn_{MS3d}	8	5.80	0.02					
	Mn-Mn_{MS4a}	2	5.72	0.01					
	Mn-Mn_{MS4b}	4	5.80	0.01					
	Mn-Mn_{MS4c}	2	5.72	0.01					
	Mn-Mn_{MS4d}	4	5.80	0.01					
	Mn-Mn_{MS4e}	2	5.72	0.02					
	Mn-Mn_{MS4f}	4	5.80	0.02					
TriBirn									
pH 7	Mn-O_{1a}	4	1.90(3)	0.010(2)	7(2)	0.835	238.4	0.9(2)	0.0417
0.75 mM	Mn-O_{1b}	2	1.901(8)	0.0012(7)					
Mn(II)	Mn-Mn_{1a}	2	2.86(7)	0.009(2)					
25 days	Mn-Mn_{1b}	4	2.89(3)	0.009					
	Mn-O_{2a}	4	3.5(1)	0.008(8)					
	Mn-O_{2b}	2	3.8(9)	0.008					
	Mn-Mn_{crnr}	0.4(8.2)	3.7(9)	0.009					
	Mn-Na_{int}	1(4)	4.1(2)	0.009					
	Mn-O_{3a}	4	4.4(2)	0.01(1)					
	Mn-O_{3b}	8	4.7(1)	0.01					
	Mn-Mn_{2a}	4	4.93	0.02(2)					
	Mn-Mn_{2b}	2	5.02	0.02					
	Mn-Mn_{3a}	2	5.72	0.014(8)					
	Mn-Mn_{3b}	4	5.78	0.014					
	Mn-Mn_{MS3a}	2	5.72	0.02(4)					
	Mn-Mn_{MS3b}	4	5.78	0.02					
	Mn-Mn_{MS3c}	4	5.72	0.01					
	Mn-Mn_{MS3d}	8	5.78	0.01					
	Mn-Mn_{MS4a}	2	5.72	0.02					
	Mn-Mn_{MS4b}	4	5.78	0.02					
	Mn-Mn_{MS4c}	2	5.72	0.02					
	Mn-Mn_{MS4d}	4	5.78	0.02					
	Mn-Mn_{MS4e}	2	5.72	0.01					
	Mn-Mn_{MS4f}	4	5.78	0.01					

[a] Coordination Number.
[b] Interatomic distance.
[c] Debye-Waller factor.
[d] Difference in the threshold Fermi level between data and theory.
[e] Amplitude reduction factor.
[f] Goodness of fit parameters [see (Kelly et al., 2008)].
[g] Statistical uncertainties at the 68% confidence level are reported in parentheses. Any parameters without reported uncertainties were not allowed to vary during fitting.
[h] σ^2 fixed for all linked shells, denoted by those without uncertainties reported.
[i] f_{occ} parameter fixed to 1 as it refined to within error of 1 with large uncertainty when allowed to freely vary.

Table A4.4. List of diffraction lines for relevant Mn (hydr)oxides.[a]

Mn Oxide	°2θ	Intensity	d-spacing	Reference
Pyrolusite	28.72	100.00	3.1084	(Wyckoff, 1963)[b]
	37.41	54.73	2.4038	
	42.88	13.30	2.1091	
	56.75	52.46	1.6221	
	59.47	14.91	1.5542	
	72.41	16.05	1.3052	
Ramsdellite	21.87	100	4.0644	(Post and Heaney, 2004)[b]
	35.17	32.89	2.5519	
	36.89	25.32	2.4365	
	38.45	27.37	2.341	
	47.74	16.26	1.9052	
	55.44	28.7	1.6573	
	56.88	15.53	1.6186	
Todorokite	9.08	91.06	9.7393	(Post et al., 2003)[b]
	9.28	100.00	9.5309	
	13.5	32.38	6.5610	
	18.22	52.68	4.8696	
	18.62	49.68	4.7655	
	21.12	42.91	4.2056	
	29.76	39.31	3.0025	
	37.39	58.28	2.4054	
	38.29	44.04	2.3509	
Manganite	26.340	100.00	3.3830	(Buerger, 1936)[b]
	34.220	23.52	2.6200	
	35.870	12.90	2.5036	
	37.520	15.48	2.3968	
	37.520	15.48	2.3968	
	55.380	17.27	1.6589	
	55.380	17.27	1.6589	
Hausmannite	18.01	23.09	4.9255	(Baron et al., 1998) [b]
	28.90	36.98	3.0892	
	32.35	74.66	2.7671	
	36.08	100.00	2.4891	
	44.41	20.04	2.0397	
	50.78	23.38	1.7979	
	58.50	29.36	1.5777	
	59.88	52.16	1.5446	
Bixbyite	23.27	16.33	3.8232	(Pauling and Shappell, 1930)[b]
	33.14	100.00	2.7034	
	38.45	15.44	2.3412	
	55.51	45.08	1.6555	
	66.19	22.52	1.4118	
Groutellite	21.06	100	4.2184	(Post and Heaney, 2004)[b]
	34.09	40.71	2.6302	
	36.62	20.87	2.454	
	37.97	23.6	2.3697	
	53.99	17.9	1.6984	

Table A4.4

Mn Oxide	°2θ	Intensity	d-spacing	Reference
Manganosite	34.96	63.67	2.5663	(Pacalo and Graham, 1991)[b]
	40.59	100	2.2225	
	58.75	53.63	1.5715	
	70.23	21.53	1.3402	
	73.86	15.02	1.2831	
Groutite	21.18	100	4.1949	(Wyckoff, 1963)[b]
	31.85	43.63	2.8094	
	33.5	17.28	2.675	
	35.7	20.99	2.5154	
	38.18	48.99	2.3574	
	54.3	35.19	1.6893	
	57.52	20.85	1.6022	
Hollandite	28.08	49.42	3.1778	(Post et al., 1982)[b]
	28.4	100	3.1429	
	28.79	99.52	3.1015	
	29.1	49.83	3.069	
	37.27	62.77	2.4124	
	37.31	48.8	2.4098	
	41.4	47.27	2.1807	
	41.97	44.54	2.1525	
	50.06	38.9	1.822	
	59.59	42.21	1.5514	
Cryptomelane	12.63	50.75	7.0072	(Post et al., 1982)[b]
	12.84	51.98	6.892	
	17.82	55.02	4.9773	
	18.28	71.69	4.8523	
	28.57	99.79	3.1239	
	28.88	100	3.0916	
	37.41	52.37	2.404	
	37.58	46.9	2.3931	
	41.6	51.21	2.1709	
	42.08	48.73	2.1471	
Coronadite	25.4	33.88	3.507	(Post and Bish, 1989)[b]
	25.57	29.49	3.4832	
	28.37	33.3	3.1457	
	28.49	100	3.1328	
	28.62	69.05	3.1193	
	28.74	57.72	3.1067	
	37.31	21.54	2.4101	
	37.37	19.8	2.4062	
	37.38	20.77	2.4056	
	56.12	20.83	1.639	
Romanechite	22.83	63.37	3.8951	(Turner and Post, 1988)[b]
	25.6	79.14	3.4792	
	26.87	77.26	3.3181	
	27.61	58.19	3.2311	
	31.06	78.15	2.8792	
	37.37	83.57	2.4067	

Table A4.4

Mn Oxide	$^{o}2\theta$	Intensity	d-spacing	Reference
Romanechite, cont.	38.05	74	2.3651	
	39.99	50.41	2.2546	
	41.27	100	2.1874	
	50.09	71.86	1.8211	
Pyrochroite	18.96	77.71	4.68	(Wyckoff, 1963)[b]
	30.91	31.51	2.8925	
	36.52	90.18	2.4605	
	50.14	22.86	1.8192	
	50.14	22.86	1.8192	
	54.98	23.52	1.67	
	58.7	16.43	1.5729	
Nsutite	22.21	95	4.00	(Faulring, 1965)[c]
	34.605	20	2.59	
	37.12	65	2.42	
	38.61	70	2.33	
	42.40	45	2.13	
	56.22	100	1.635	
	57.44	45	1.603	
	62.82	25	1.478	
	68.60	40	1.367	
	72.35	20	1.205	

[a]List includes ten most intense diffraction lines and/or lines above 15% intensity.
[b]X-ray diffraction data obtained from XPOW database [Downs and Hall-Wallace (2003)].
[c]X-ray diffraction data obtained from PDF 00-017-0510.

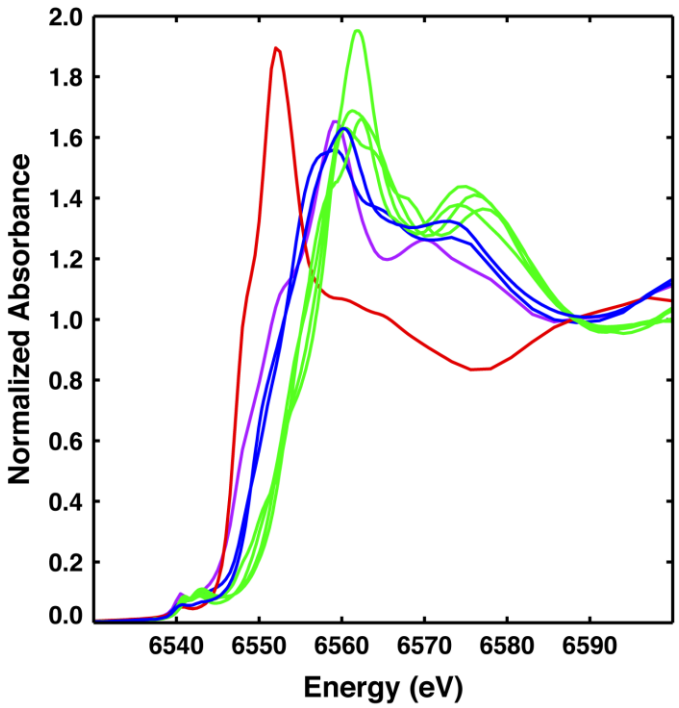

Figure A4.1. XANES spectra of manganese oxidation state standards used in linear combination fits to calculate average manganese oxidation state for experiment samples: Mn(II) standard ($MnCl_2$•$4H_2O$; Sigma Aldrich) (red), Mn(II,III) standard (hausmannite; Sigma Aldrich) (purple), Mn(III) standards (feitknechtite, bixbyite; Sigma Aldrich) (blue), Mn(IV) standards (ramsdellite, pyrolusite, KBi, $Ca_2Mn_3O_8$) (green). XANES of feitknechtite and all Mn(IV) standards are obtained from the database provided in Manceau et al. (2012).

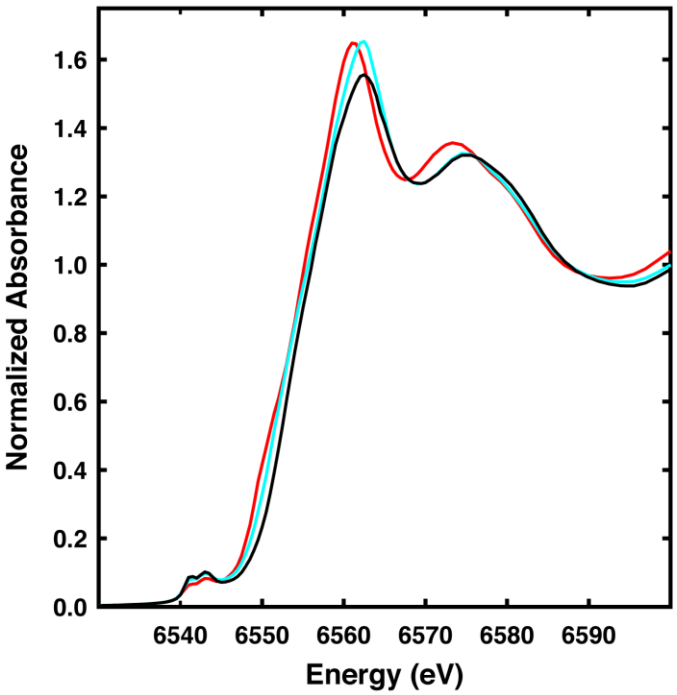

Figure A4.2. XANES spectra of unreacted synthesized turbostratic phyllomanganates δ-MnO_2 (black), HexB (B) (blue), and TriB (red).

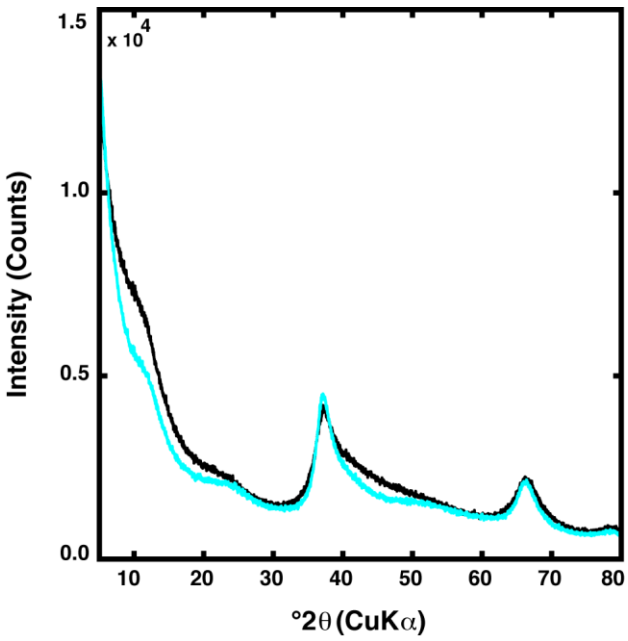

Figure A4.3. XRD patterns of unreacted synthesized turbostratic phyllomanganates δ-MnO_2 (black line) and HexB (blue line).

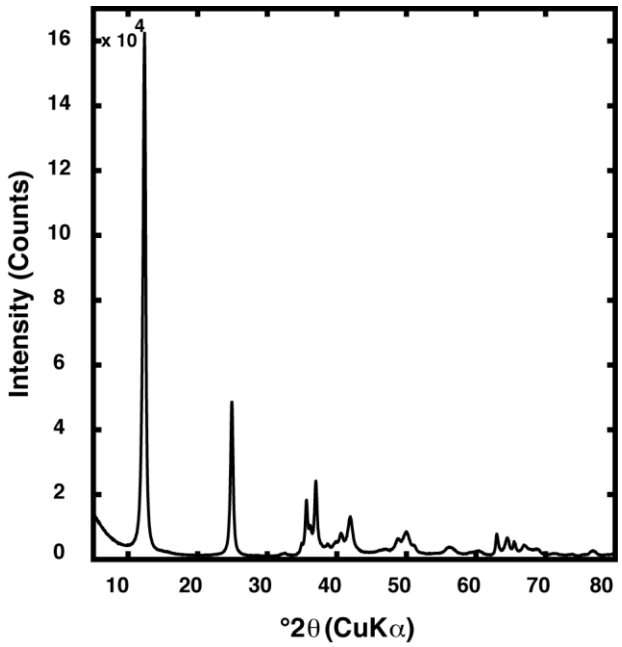

Figure A4.4. XRD pattern of unreacted synthesized TriB.

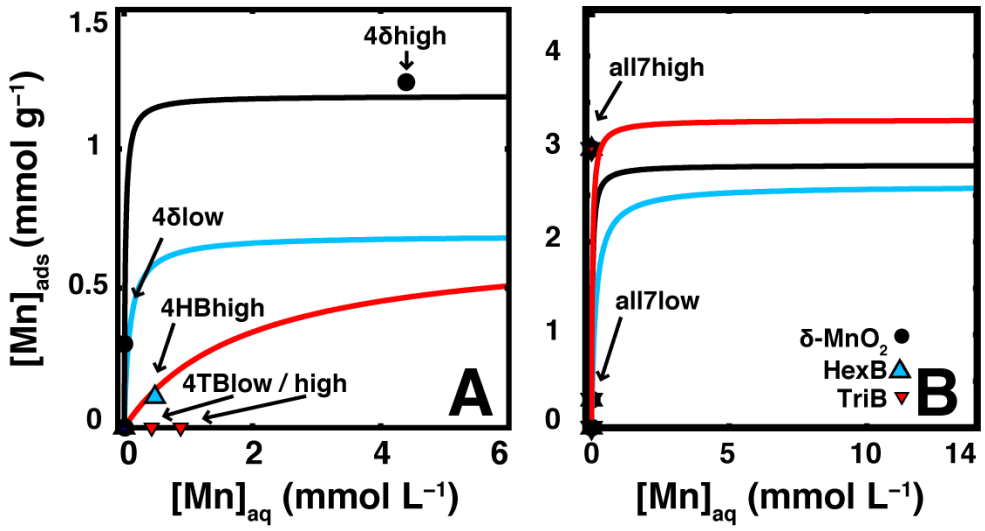

Figure A4.5. Mn(II) adsorption onto phyllomanganates after 25 days of reaction (see Table 4.1) at pH 4 (A) and pH 7 (B) with lines representing Langmuir isotherm fits to the 24 hour Mn(II) adsorption isotherms (see Figure 4.3).

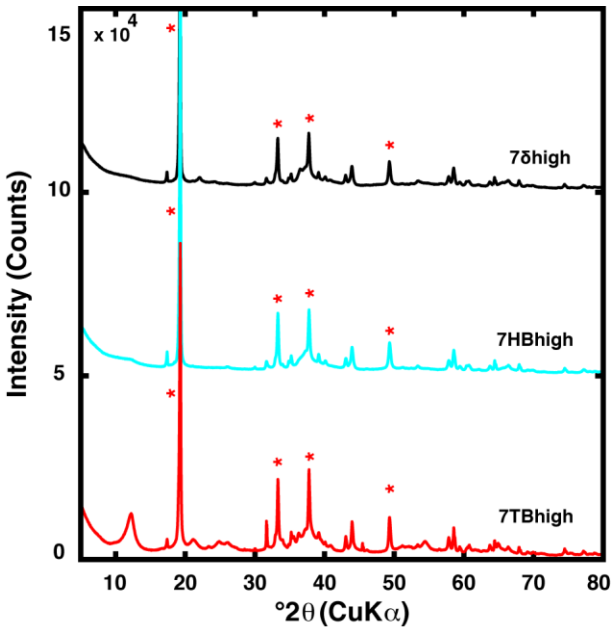

Figure A4.6. XRD patterns of phyllomanganates reacted for 25 days with 7.5 mM Mn(II). Peaks corresponding to feitknechtite are denoted by red asterisks above (or immediately to the left of) the corresponding peaks in (D).

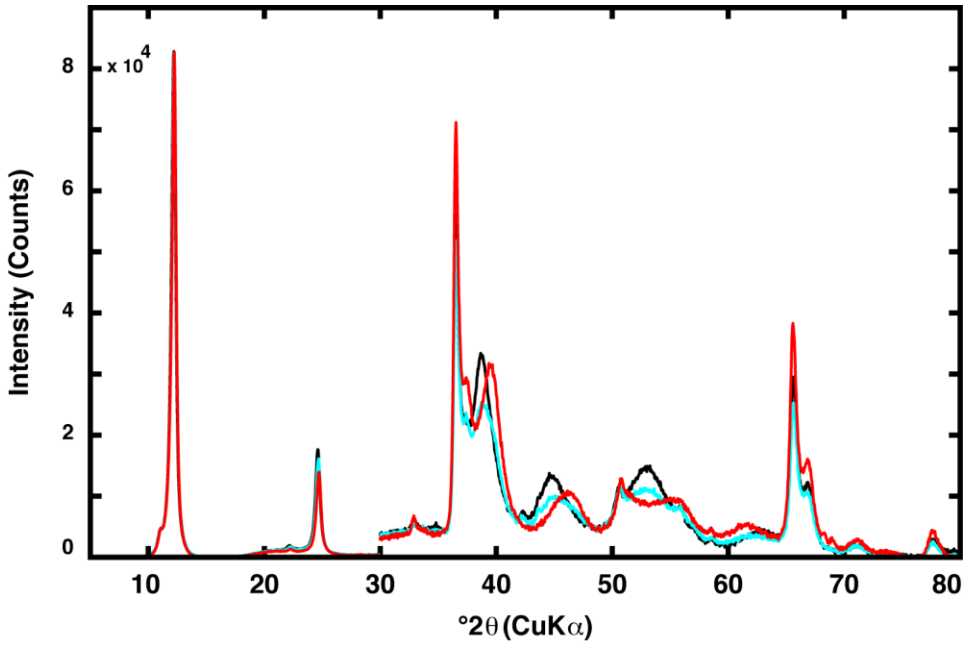

Figure A4.7. Background subtracted XRD patterns of TriB reacted for 25 days at pH 4, with 0 mM Mn(II) (black), 0.75 mM Mn(II) (blue), or 7.5 mM Mn(II) (red).

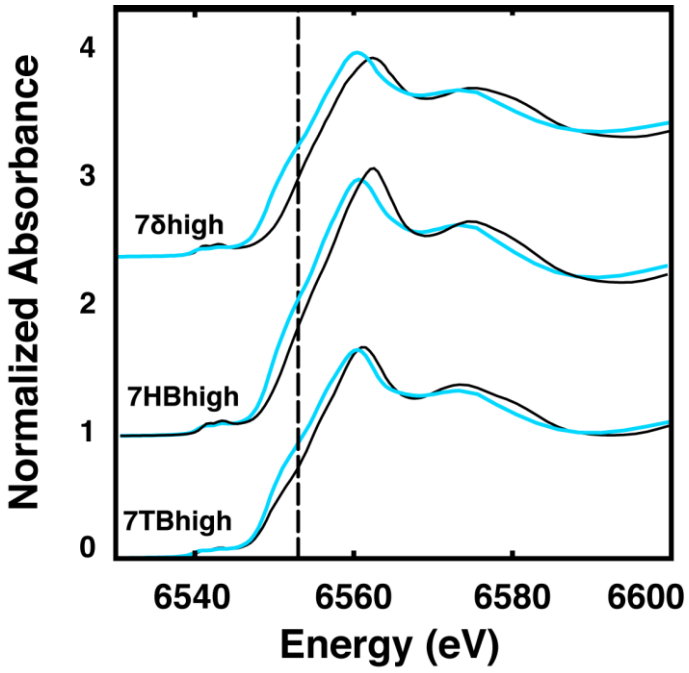

Figure A4.8. XANES spectra for samples reacted for 25 days at pH 7, with 7.5 mM Mn(II) (blue lines), overplotted with the corresponding synthesized, unreacted phyllomanganate (thin black lines). Dashed line denotes 6553 eV corresponding to adsorbed Mn(II).

4.7 REFERENCES

Bargar J. R., Fuller C. C., Marcus M. A., Brearley A. J., de la Rosa M. P., Webb S. M. and Caldwell W. A. (2009) Structural characterization of terrestrial microbial Mn oxides from Pinal Creek, AZ. *Geochimica et Cosmochimica Acta* **73,** 889-910.

Bargar J. R., Tebo B. M., Bergmann U., Webb S. M., Glatzel P., Chiu V. Q. and Villalobos M. (2005) Biotic and abiotic products of Mn(II) oxidation by spores of the marine *Bacillus sp.* strain SG-1. *American Mineralogist* **90,** 143-154.

Bargar J. R., Tebo B. M. and Villinski J. E. (2000) In situ characterization of Mn (II) oxidation by spores of the marine *Bacillus* sp. strain SG-1. *Geochimica et Cosmochimica Acta* **64,** 2775-2778.

Baron V., Gutzmer J., Rundlo H. and Tellgren R. (1998) The influence of iron substitution on the magnetic properties of hausmannite, $Mn^{2+}(Fe, Mn)_2{}^{3+}O_4$. *American Mineralogist* **83,** 786-793.

Brindley G. W. and Brown G. (1980) Crystal structures of clay minerals and their X-ray identification. *Mineralogical Society, London* 361-410.

Buerger M. J. (1936) The symmetry and crystal structure of manganite, Mn (OH) O. *Zeitschrift Für Kristallographie-Crystalline Materials* **95,** 163-174.

Burdige D. J. (1993) The biogeochemistry of manganese and iron reduction in marine sediments. *Earth-Science Reviews* **35,** 249-284.

Canfield D. E., Thamdrup B. and Hansen J. W. (1993) The anaerobic degradation of organic matter in Danish coastal sediments: iron reduction, manganese reduction, and sulfate reduction. *Geochimica et Cosmochimica Acta* **57,** 3867-3885.

Clement B. G., Luther III G. W. and Tebo B. M. (2009) Rapid, oxygen-dependent microbial Mn(II) oxidation kinetics at sub-micromolar oxygen concentrations in the Black Sea suboxic zone. *Geochimica et Cosmochimica Acta* **73,** 1878-1889.

Dick G. J., Clement B. G., Webb S. M., Fodrie F. J., Bargar J. R. and Tebo B. M. (2009) Enzymatic microbial Mn(II) oxidation and Mn biooxide production in the Guaymas Basin deep-sea hydrothermal plume. *Geochimica et Cosmochimica Acta* **73,** 6517-6530.

Downs, R. T. and Hall-Wallace, M. (2003) The *American Mineralogist* crystal structure database. *American Mineralogist* **88,** 247-250.

Drits V. A., Lanson B., Bougerol-Chaillout C., Gorshkov A. I. and Manceau A. (2002) Structure of heavy-metal sorbed birnessite: Part 2. Results from electron diffraction. *American Mineralogist* **87,** 1646-1661.

Drits V. A., Lanson B. and Gaillot A. -C. (2007) Birnessite polytype systematics and identification by powder X-ray diffraction. *American Mineralogist* **92,** 771-788.

Drits V. A., Lanson B., Gorshkov A. I. and Manceau A. (1998) Substructure and superstructure of four-layer Ca-exchanged birnessite. *American Mineralogist* **83,** 97-118.

Drits V. A. and McCarty D. K. (1996) The nature of diffraction effects from illite and illite-smectite consisting of interstratified trans-vacant and cis-vacant 2:1 layers: A semiquantitative technique for determination of layer-type content. *American Mineralogist* **81,** 852-863.

Drits V. A., Silvester E., Gorshkov A. I. and Manceau A. (1997) Structure of synthetic monoclinic Na-rich birnessite and hexagonal birnessite: I. Results from X-ray diffraction and selected-area electron diffraction. *American Mineralogist* **82,** 946-961.

Elzinga E. J. (2011) Reductive transformation of birnessite by aqueous Mn (II). *Environmental Science & Technology* **45,** 6366-6372.

Elzinga E. J. and Kustka A. B. (2015) A Mn-54 radiotracer study of Mn isotope solid-liquid exchange during reductive transformation of vernadite (δ-MnO2) by aqueous Mn (II). *Environmental Science & Technology* doi: 10.1021/acs.est.5b00022.

Emerson S., Kalhorn S., Jacobs L., Tebo B. M., Nealson K. H. and Rosson R. A. (1982) Environmental oxidation rate of manganese(II): bacterial catalysis. *Geochimica et Cosmochimica Acta* **46,** 1073-1079.

Faulring, G. M. (1965) Unit cell determination and thermal transformations of nsutite. *American Mineralogist* **50,** 170.

Friedl G., Wehrli B. and Manceau A. (1997) Solid phases in the cycling of manganese in eutrophic lakes: New insights from EXAFS spectroscopy. *Geochimica et Cosmochimica Acta* **61,** 275-290.

Frierdich A. J. and Catalano J. G. (2012) Distribution and speciation of trace elements in iron and manganese oxide cave deposits. *Geochimica et Cosmochimica Acta* **91,** 240-253.

Golden D. C., Chen C. C. and Dixon J. B. (1987) Transformation of birnessite to buserite, todorokite, and manganite under mild hydrothermal treatment. *Clays and Clay Minerals* **35,** 271-280.

Golden D. C., Dixon J. B. and Chen C. C. (1986) Ion exchange, thermal transformations, and oxidizing properties of birnessite. *Clays and Clay Minerals* **34,** 511-520.

Grangeon S., Lanson B., Miyata N., Tani Y. and Manceau A. (2010) Structure of nanocrystalline phyllomanganates produced by freshwater fungi. *American Mineralogist* **95,** 1608-1616.

Grangeon S., Manceau A., Guilhermet J., Gaillot A. C., Lanson M. and Lanson B. (2012) Zn sorption modifies dynamically the layer and interlayer structure of vernadite. *Geochimica et Cosmochimica Acta* **85,** 302-313.

Graybeal A. L. and Heath G. R. (1984) Remobilization of transition metals in surficial pelagic sediments from the eastern Pacific. *Geochimica et Cosmochimica Acta* **48,** 965-975.

Hinkle M. A. G., Wang Z., Giammar D. E. and Catalano J. G. (2015) Interaction of Fe(II) with phosphate and sulfate on iron oxide surfaces. *Geochimica et Cosmochimica Acta* **158,** 130-146.

Kelly S. D., Hesterberg D. and Ravel B. Analysis of soils and minerals using X-ray absorption spectroscopy, In *Methods of Soil Analysis. Part 5 - Mineralogical Methods,* L.R. Drees and A.L. Ulery (Eds.), Soil Science Society of America, Madison, WI, 2008; pp. 387-463.

Krumbein W. E. and Jens K. (1981) Biogenic rock varnishes of the Negev Desert (Israel) and ecological study of iron and magnanese transformation by cyanobacteria and fungi. *Oceologia* **50,** 25-38.

Lanson B., Drits V. A., Gaillot A. -C., Silvester E., Plançon A. and Manceau A. (2002) Structure of heavy-metal sorbed birnessite: Part 1. Results from X-ray diffraction. *American Mineralogist* **87,** 1631-1645.

Lanson B., Drits V. A., Silvester E. and Manceau A. (2000) Structure of H-exchanged hexagonal birnessite and its mechanism of formation from Na-rich monoclinic buserite at low pH. *American Mineralogist* **85,** 826-838.

Lefkowitz J. P., Rouff A. A. and Elzinga E. J. (2013) Influence of pH on the reductive transformation of birnessite by aqueous Mn(II). *Environmental Science & Technology* **47,** 10364-10371.

Lopano C. L., Heaney P. J., Post J. E., Hanson J. and Komarneni S. (2007) Time-resolved structural analysis of K- and Ba-exchange reactions with synthetic Na-birnessite using synchrotron X-ray diffraction. *American Mineralogist* **92,** 380-387.

Manceau A., Kersten M., Marcus M. A., Geoffroy N. and Granina L. (2007a) Ba and Ni speciation in a nodule of binary Mn oxide phase composition from Lake Baikal. *Geochimica et Cosmochimica Acta* **71,** 1967-1981.

Manceau A., Lanson M. and Geoffroy N. (2007b) Natural speciation of Ni, Zn, Ba, and As in ferromanganese coatings on quartz using X-ray fluorescence, absorption, and diffraction. *Geochimica et Cosmochimica Acta* **71,** 95-128.

Manceau A., Marcus M. A. and Grangeon S. (2012) Determination of Mn valence states in mixed-valent manganates by XANES spectroscopy. *American Mineralogist* **97,** 816-827.

Manceau A., Marcus M. A., Grangeon S., Lanson M., Lanson B., Gaillot A. -C., Skanthakumar S. and Soderholm L. (2013) Short-range and long-range order of phyllomanganate nanoparticles determined using high-energy X-ray scattering. *Journal of Applied Crystallography* **46,** 193-209.

Manceau A., Tommaseo C., Rihs S., Geoffroy N., Chateigner D., Schlegel M., Tisserand D., Marcus M. A., Tamura N. and Chen Z. -S. (2005) Natural speciation of Mn, Ni, and Zn at the micrometer scale in a clayey paddy soil using X-ray fluorescence, absorption, and diffraction. *Geochimica et Cosmochimica Acta* **69,** 4007-4034.

Mandernack K. W., Post J. E. and Tebo B. M. (1995) Manganese mineral formation by bacterial spores of a marine *Bacillus*, strain SG-1: Evidence for the direct oxidation of Mn(II) to MN(IV). *Geochimica et Cosmochimica Acta* **59,** 4393-4408.

Marcus M. A., Manceau A. and Kersten M. (2004) Mn, Fe, Zn and As speciation in a fast-growing ferromanganese marine nodule. *Geochimica et Cosmochimica Acta* **68,** 3125-3136.

McKenzie R. M. (1980) The adsorption of lead and other heavy metals on oxides of manganese and iron. *Soil Research* **18,** 61-73.

McKeown D. A. and Post J. E. (2001) Characterization of manganese oxide mineralogy in rock varnish and dendrites using X-ray absorption spectroscopy. *American Mineralogist* **86,** 701-713.

Meldau R., Newesely H. and Strunz H. (1973) Zur Kristallchemie von Feitknechtit, β-MnOOH. *Naturwissenschaften* **60,** 387-387.

Morgan J. J. (2005) Kinetics of reaction between O_2 and Mn (II) species in aqueous solutions. *Geochimica et Cosmochimica Acta* **69,** 35-48.

Morgan J. J. and Stumm W. (1964) Colloid-chemical properties of manganese dioxide. *Journal of Colloid Science* **19,** 347-359.

Murray J. W., Balistrieri L. S. and Paul B. (1984) The oxidation state of manganese in marine sediments and ferromanganese nodules. *Geochimica et Cosmochimica Acta* **48,** 1237-1247.

Nealson K. H., Tebo B. M. and Rosson R. A. (1988) Occurrence and mechanisms of microbial oxidation of manganese. *Advances in Applied Microbiology* **33,** 2027-2035.

Nelson Y. M. and Lion L. W. (2003) Formation of biogenic manganese oxides and their influence on the scavenging of toxic trace elements. *Geochemical and Hydrological Reactivity of Heavy Metals in Soils. CRC Press* **200,** 169-186.

Newville M. (2001) IFEFFIT: interactive EXAFS analysis and FEFF fitting. *Journal of Synchrotron Radiation* **8,** 322-324.

Pacalo R. E. and Graham E. K. (1991) Pressure and temperature dependence of the elastic properties of synthetic MnO. *Physics and Chemistry of Minerals* **18,** 69-80.

Pauling L. and Shappell M. D. (1930) The crystal structure of bixbyite and the C-modification of the sesquioxides. *Zeitschrift für Kristallographie* **75,** 128-142.

Peacock C. L. (2009) Physiochemical controls on the crystal-chemistry of Ni in birnessite: Genetic implications for ferromanganese precipitates. *Geochimica et Cosmochimica Acta* **73,** 3568-3578.

Peacock C. L. and Sherman D. M. (2007) Crystal-chemistry of Ni in marine ferromanganese crusts and nodules. *American Mineralogist* **92,** 1087-1092.

Post J. E. (1999) Manganese oxide minerals: Crystal structures and economic and environmental significance. *Proceedings of the National Academy of Sciences of the United States of America* **96,** 3447-3454.

Post J. E. and Appleman D. E. (1988) Chalcophanite, $ZnMn_3O_7$-$3H_2O$: New crystal-structure determinations. *American Mineralogist* **73,** 1401-1404.

Post J. E. and Bish D. L. (1989) Rietveld refinement of the coronadite structure. *American Mineralogist* **74,** 913-917.

Post J. E. and Heaney P. J. (2004) Neutron and synchrotron X-ray diffraction study of the structures and dehydration behaviors of ramsdellite and groutellite. *American Mineralogist* **89,** 969-975.

Post J. E., Heaney P. J. and Hanson J. (2002) Rietveld refinement of a triclinic structure for synthetic Na-birnessite using synchrotron powder diffraction data. *Powder Diffraction* **17,** 218-221.

Post J. E., Heaney P. J. and Hanson J. (2003) Synchrotron X-ray diffraction study of the structure and dehydration behavior of todorokite. *American Mineralogist* **88,** 142-150.

Post J. E. and Veblen D. R. (1990) Crystal structure determinations of synthetic sodium, magnesium, and potassium birnessite using TEM and the Rietveld method. *American Mineralogist* **75,** 477-489.

Post J. E., Von Dreele R. B. and Buseck P. R. (1982) Symmetry and cation displacements in hollandites: structure refinements of hollandite, cryptomelane and priderite. *Acta Crystallographica Section B: Structural Crystallography and Crystal Chemistry* **38,** 1056-1065.

Rajendran A., Kumar M. D. and Bakker J. F. (1992) Control of manganese and iron in Skagerrak sediments (northeastern North Sea). *Chemical Geology* **98,** 111-129.

Ravel B. and Newville M. (2005) ATHENA, ARTEMIS, HEPHAESTUS: data analysis for X-ray absorption spectroscopy using IFEFFIT. *Journal of Synchrotron Radiation* **12,** 537-541.

Rehr J. J., Kas J. J., Vila F. D., Prange M. P. and Jorissen K. (2010) Parameter-free calculations of x-ray spectra with FEFF9. *Physical Chemistry Chemical Physics* **12,** 5503-5513.

Santelli C. M., Webb S. M., Dohnalkova A. C. and Hansel C. M. (2011) Diversity of Mn oxides produced by Mn(II)-oxidizing fungi. *Geochimica et Cosmochimica Acta* **75,** 2762-2776.

Saratovsky I., Wightman P. G., Pasten P. A., Gaillard J. F. and Poeppelmeier K. R. (2006) Manganese oxides: Parallels between abiotic and biotic structures. *Journal of the American Chemical Society* **128,** 11188-11198.

Shimmield G. B. and Price N. B. (1986) The behaviour of molybdenum and manganese during early sediment diagenesisoffshore Baja California, Mexico. *Marine Chemistry* **19,** 261-280.

Silvester E., Manceau M. and Drits V. A. (1997) Structure of synthetic monoclinic Na-rich birnessite and hexagonal birnessite: II. Results from chemical studies and EXAFS spectroscopy. *American Mineralogist* **82,** 962-978.

Tan H., Zhang G., Heaney P. J., Webb S. M. and Burgos W. D. (2010) Characterization of manganese oxide precipitates from Appalachian coal mine drainage treatment systems. *Applied Geochemistry* **25,** 389-399.

Tebo B. M. (1991) Manganese (II) oxidation in the suboxic zone of the Black Sea. *Deep Sea Research Part A. Oceanographic Research Papers* **38,** S883-S905.

Tebo B. M., Bargar J. R., Clement B. G., Dick G. J., Murray K. J., Parker D., Verity R. and Webb S. M. (2004) Biogenic manganese oxides: Properties and mechanisms of formation. *Annual Review of Earth and Planetary Sciences* **32,** 287-328.

Tebo B. M., Ghiorse W. C., van Waasbergen L. G., Siering P. L. and Caspi R. (1997) Bacterially mediated mineral formation; insights into manganese (II) oxidation from molecular genetic and biochemical studies. *Reviews in Mineralogy and Geochemistry* **35,** 225-266.

Tebo B. M., Johnson H. A., McCarthy J. K. and Templeton A. S. (2005) Geomicrobiology of manganese(II) oxidation. *TRENDS in Microbiology* **13,** 421-428.

Toner B., Manceau A., Webb S. M. and Sposito G. (2006) Zinc sorption by biogenic hexagonal birnessite particles within a hydrated bacterial biofilm. *Geochimica et Cosmochimica Acta* **70,** 27-43.

Turner S. and Post J. E. (1988) Refinement of the substructure and superstructure of romanechite. *American Mineralogist* **73,** 1155-1161.

Tu S., Racz G. J. and Goh T. B. (1994) Transformations of synthetic birnessite as affected by pH and manganese concentration. *Clays and Clay Minerals* **42,** 321-330.

Van Cappellen P., Viollier E., Roychoudhury A., Clark L., Ingall E., Lowe K. and Dichristina T. (1998) Biogeochemical cycles of manganese and iron at the oxic-anoxic transition of a stratified marine basin (Orca Basin, Gulf of Mexico). *Environmental Science & Technology* **32,** 2931-2939.

Villalobos M., Lanson B., Manceau A., Toner B. and Sposito G. (2006) Structural model for the biogenic Mn oxide produced by Pseudomonas putida. *American Mineralogist* **91,** 489-502.

Villalobos M., Toner B., Bargar J. R. and Sposito G. (2003) Characterization of the manganese oxide produced by *pseudomonas putida* strain MnB1. *Geochimica et Cosmochimica Acta* **67,** 2649-2662.

Von Langen P. J., Johnson K. S., Coale K. H. and Elrod V. A. (1997) Oxidation kinetics of manganese (II) in seawater at nanomolar concentrations. *Geochimica et Cosmochimica Acta* **61,** 4945-4954.

Webb S. M. (2005) SIXPack: A Graphical User Interface for XAS Analysis using IFEFFIT. *Physica Scripta* **T115,** 1011-1014.

Webb S. M., Tebo B. M. and Bargar J. R. (2005a) Structural characterization of biogenic Mn oxides produced in seawater by the marine *bacillus sp.* strain SG-1. *American Mineralogist* **90,** 1342-1357.

Webb S. M., Tebo B. M. and Bargar J. R. (2005b) Structural influences of sodium and calcium ions on the biogenic manganese oxides produced by the marine *Bacillus sp.*, strain SG-1. *Geomicrobiology Journal* **22,** 181-193.

Wehrli B., Friedl G. and Manceau A. (1995) Reaction rates and products of manganese oxidation at the sediment-water interface, In *Advances in Chemistry*, pp. 111-134.

Wyckoff R. W. G. Crystal Structures 1, 2nd edition, Interscience Publishers, New York, 1963.

Yu Q., Sasaki K., Tanaka K., Ohnuki T. and Hirajima T. (2012) Structural factors of biogenic birnessite produced by fungus *Paraconiothyrium* sp. WL-2 strain affecting sorption of Co^{2+}. *Chemical Geology* **310-311,** 106-113.

Zhu M., Ginder-Vogel M., Parikh S. J., Feng X. H. and Sparks D. L. (2010a) Cation effects on the layer structure of biogenic Mn-oxides. *Environmental Science & Technology* **44,** 4465-4471.

Zhu M., Ginder-Vogel M. and Sparks D. L. (2010b) Ni(II) sorption on biogenic Mn-oxides with varying Mn octahedral layer structure. *Environmental Science & Technology* **44,** 4472-4478.

CHAPTER 5

IMPACT OF MN(II)-MANGANESE OXIDE REACTIONS ON TRACE ELEMENT FATE

To be submitted to *Environmental Science & Technology* as:
Hinkle, M.A.G., Becker, K.G., Catalano, J.G. (2015) Impact of Mn(II)-manganese oxide reactions on trace element fate.

5.1 ABSTRACT

Phyllomanganate minerals affect trace metal fate in many natural systems via adsorption and structural incorporation. Several such metals (e.g., Ni, Zn) preferentially adsorb above vacancies within the phyllomanganate interlayer. Some metals, such as Ni, can subsequently enter the phyllomanganate sheet, occupying a previously vacant site. Mn(II) also adsorbs above phyllomanganate sheet vacancies and can cause changes in phyllomanganate sheet structure. This suggests that Mn(II) may thus alter trace metal adsorption on or incorporation into Mn oxides. In this study, we investigate the effect of Mn(II) on Ni and Zn sorption behaviors in phyllomanganates of varying initial vacancy content (δ-MnO_2, hexagonal birnessite, and triclinic birnessite) at pH 4 and 7. Extended X-ray absorption fine structure spectroscopy demonstrates that at pH 4 Mn(II) alters Ni and Zn adsorption mechanisms by decreasing Ni and Zn binding at vacancy sites, promoting Ni and Zn adsorption at sheet edges, and increasing the fraction of adsorbed Zn that is tetrahedrally coordinated. At pH 7, Ni adsorption mechanisms are not affected by Mn(II), but Ni incorporation into δ-MnO_2 is altered as a result of increased Mn(III) sheet content. Mn(II) has little to no effect at pH 7 on Ni incorporation in phyllomanganates with higher Mn(III) contents, suggesting that initial phyllomanganate Mn(III) content is an important controlling factor in trace metal incorporation behavior in the presence of Mn(II). Adsorbed Zn coordination state and adsorption behaviors are similarly unaffected by Mn(II) at pH 7. This study indicates that aqueous Mn(II) can alter metal speciation in phyllomanganate systems by altering manganese oxide structures, and that the pH of the system exerts a dominant control on the resulting metal sorption behavior.

5.2 INTRODUCTION

Manganese oxides are highly reactive and widespread minerals, often acting as heavy metal scavengers in marine, lacustrine, riverine, and cave systems due to their large adsorptive capacities and redox behavior (Goldberg, 1954; Jenne, 1968; Singh et al., 1999; Brown and Parks, 2001; Li et al., 2001; Tebo et al., 2004; Miyata et al., 2007; White et al., 2009; Frierdich and Catalano, 2012). As a result, manganese oxide minerals can exert substantial controls on the concentrations and speciation of many trace metals (e.g., Ni and Zn) in natural systems and mine drainage remediation sites (Jenne, 1968; Tebo et al., 1997; Manceau et al., 2002; Tebo et al., 2004). Manganese oxide reactivity, scavenging ability, and sorptive behavior are largely controlled by the structure and stability of the host manganese oxide (Siegel and Turner, 1983; Post, 1999), which can be affected by cation adsorption onto, and incorporation into, the manganese oxide structure (Paterson et al., 1986; Shen et al., 1994; Ching et al., 1999; Cai et al., 2002; Bodeï et al., 2007; Boonfueng et al., 2009; Zhu et al., 2010a; Zhu et al., 2010b; Grangeon et al., 2012; Yin et al., 2012; Yu et al., 2013). Aqueous Mn(II), like other cations, can also affect manganese oxide structures, but results in distinct effects due to the unique capacity for Mn(II)-Mn(IV) comproportionation reactions. Recent research shows that Mn(II) promotes Mn(IV/III) oxide phase transformations to the Mn(III) and Mn(III/II) oxides, manganite and hausmannite, involving a feitknechtite intermediary (Elzinga, 2011; Lefkowitz et al., 2013; Elzinga and Kustka, 2015). However, such mineral phases are not prevalent in environmental systems, which are typically dominated by Mn(IV/III) phyllomanganates (Wehrli et al., 1995; Friedl et al., 1997; Manceau et al., 2007; Manceau et al., 2007; Dick et al., 2009; Tan et al., 2010; Frierdich and Catalano, 2012). Mn(II):Mn(IV) ratios lower than those that lead to mineral phase transformations alter Mn(IV/III) oxide sheet structures and layer stacking (Hinkle and

Catalano, 2015). The effect of Mn(II) on manganese oxide structures is dependent on the ratio of Mn(II):Mn(IV), pH, reaction time, and the initial manganese oxide mineral composition and structure (Elzinga, 2011; Lefkowitz et al., 2013; Hinkle and Catalano, 2015).

The effects of Mn(II) on Mn oxide structure suggests that metals may display distinct sorption behavior to such minerals in regions with coexisting aqueous Mn(II), such as at redox interfaces in soils, sediments, and water columns, coal mine drainage remediation sites, or regions with active biogeochemical manganese cycling. Manganese oxides in most natural systems are phyllomanganates with interlayer cations accommodating negative layer charge resulting from Mn(IV) vacancies or Mn(III) substitutions. Many cations (e.g., Mn(II), Ni, Zn) bind to the basal plane by adsorbing over vacant sites within the interlayer (Marcus et al., 2004; Manceau et al., 2005; Toner et al., 2006; Peacock and Sherman, 2007a; Peacock and Sherman, 2007b; Peacock, 2009; Hinkle and Catalano, 2015). Over time, structurally compatible cations become progressively incorporated into the phyllomanganate sheet vacancies (Peacock, 2009). Thus, Mn(II) may cause cations to be redistributed in or ejected from phyllomanganate sheets due to Mn(II)-induced manganese oxide structural changes, or alter cation adsorptive mechanisms due to competition for adsorption sites above or below vacancies.

In this study, the effect of Mn(II) on Ni and Zn sorption behaviors is examined. The role of mineral vacancy content and pH are investigated, as both of these factors are important controls on Mn(II)-induced phyllomanganate structural changes (Hinkle and Catalano, 2015). Furthermore, Ni and Zn typically adsorb over vacancies and their adsorption increases with increasing pH (Toner et al., 2006; Manceau et al., 2007; Peacock and Sherman, 2007b; Peacock, 2009). The manganese oxides examined in this study are: δ-MnO_2 (the synthetic analogue of vernadite) which has vacancies, triclinic birnessite which has predominantly Mn(III)

substitutions, and c-disordered H^+ birnessite (a birnessite with hexagonal symmetry) which has both vacancies and Mn(III) substitutions (Villalobos et al., 2003; Lopano et al., 2007). Macroscopic Ni adsorption in the absence and presence of Mn(II) was investigated to assess the extent of metal-Mn(II) competitive adsorption effects. The effect of Mn(II) on Ni and Zn sorption behaviors was investigated by X-ray absorption fine structure (XAFS) spectroscopy.

5.3 METHODS AND MATERIALS

5.3.1. Mineral and Reagent Preparation

The phyllomanganates prepared for this study were synthesized using previously published procedures (Hinkle and Catalano, 2015). The δ-MnO_2 and hexagonal birnessite syntheses were modified from the those described by Villalobos et al. (2003) for the "redox" method δ-MnO2 and c-disordered H^+ birnessite (termed 'HexB' in this paper). The synthesis used to prepare triclinic birnessite (TriB) was based on the Na-birnessite synthesis described by Lopano et al. (2007). After synthesis, excess electrolytes were washed from the minerals following procedures described elsewhere (Hinkle and Catalano, 2015). Mineral suspensions were stored in polypropylene bottles wrapped in aluminum foil in an anaerobic chamber (Coy Laboratory Products, Inc., 3% H_2/97% N_2 atmosphere with Pd catalysts). The mineral suspensions were sparged with a gas filtration system (Hinkle et al., 2015) or a minimum of 24 hours prior to use to remove dissolved O_2. X-ray diffraction (XRD) (Bruker D8 Advance X-ray diffractometers, Cu K_α radiation) and surface area determinations by BET N_2 gas adsorption (Quantachrome Instruments Autosorb-1) were performed on samples dried at 70^o C.

NaCl, 2-(4-morpholino)ethanesulfonic acid (MES), $NiCl_2$•$6H_2O$, $ZnCl_2$, and $MnCl_2$•$4H_2O$ stock solutions were made in the anaerobic chamber with deoxygenated deionized

water. Experiments conducted at pH 7 used a solution consisting of NaCl and MES preadjusted to pH 7, also prepared within the anaerobic chamber. All pH adjustments were made using HCl or NaOH solutions.

5.3.2 Molecular-Scale Ni and Zn Sorption Experiments

Sample Preparation

Ni and Zn sorption onto phyllomanganates in the presence and absence of Mn(II) was investigated by Ni and Zn K-edge XAFS spectroscopy. These experiments consisted of reacting 0.23 mM Ni(II) or Zn(II) with 10 mM NaCl, 1 mM MES (for pH 7 samples), 2.5 g L^{-1} δ-MnO2, TriB, or HexB, and 0, 0.75, or 7.5 mM Mn(II) for 25 days. The 7.5 mM Mn(II) experiments were conducted at pH 4 only, as feitknechitite precipitation occurs at this Mn(II):Mn(IV) ratio at pH 7 (Hinkle and Catalano, 2015) and the impact of phase transformations on Ni and Zn speciation is beyond the scope of this study. After the mineral suspension was added to the samples, marking the start of the experiment, the samples were allowed to equilibrate for approximately 1 hour, at which point the pH of the samples was adjusted to pH 4 or 7 with HCl and NaOH. The samples were placed on end-over-end rotators wrapped in aluminum foil. Sample pH was checked, and adjusted if necessary, throughout the duration of the experiment. At the end of the experiment, the samples were filtered (reusable syringe filter; 0.22 µm MCE membrane; Fisher Scientific), discarding the first 1 mL of filtrate and collecting the solid as a wet paste. The filtered samples were removed from the anaerobic chamber and promptly acidified to 2% HNO_3 (trace metal grade; OmniTrace® Ultra™). The acidified filtrates were diluted with 2% HNO_3 for inductively coupled plasma-optical emission spectroscopy (ICP-OES; Perkin Elmer Optima 7300 DV) analysis for Ni, Zn, and Mn concentrations. Uncertainty (95% confidence level) was determined

using the standard deviations from the triplicate instrument analyses and the triplicate experiment samples.

Additional Mn(II)-free samples of Ni and Zn adsorbed onto phyllomanganates, reacted for just 48 hours, were also prepared for XAFS spectroscopic measurements. These samples involved the same experimental parameters described above. Phyllomanganates coprecipitated with Ni and Zn were synthesized and analyzed by XAFS spectroscopy as well. These samples were synthesized following the procedures described above for metal-free phyllomanganate syntheses, but with Ni(II) or Zn(II) (using a $NiCl_2 \cdot 6H_2O$ or $ZnCl_2$) substituting for a portion of the $MnCl_2 \cdot 4H_2O$ starting solution [Ni:Mn and Zn:Mn= 0.02]. All syntheses were successful in producing the intended phyllomanganate with approximately 2 mol% Ni or Zn, with the exception of Zn-coprecipitated TriB. All attempts to synthesize Zn-coprecipitated TriB resulted in the formation of a triclinic birnessite-hetaerolite mixture, even at lower initial Zn contents (e.g., 0.2 mol% Zn), as evidenced by XRD patterns and XANES spectra (not shown). The precipitation of hetaerolite ($ZnMn_2O_4$) is consistent with a recent study that observed the precipitation of hetaerolite upon reacting HexB with aqueous Mn(II) and Zn (Lefkowitz and Elzinga, 2015).

XAFS samples for the solids (as wet pastes) were prepared following methods described in detail elsewhere (Hinkle and Catalano, 2015). Samples analyzed at the Advanced Photon Source (APS) at Argonne National Laboratory were prepared a maximum of 48 hours prior to transport to prevent drying out. Samples analyzed at the Stanford Synchrotron Radiation Lightsource (SSRL) at the SLAC National Accelerator Laboratory were prepared a maximum of 120 hours prior to transport, as sample shipment was required.

XAFS Spectroscopic Measurements

XAFS spectra were collected at APS beamline 20-BM-B and SSRL beamline 4-1. Beamline 20-BM-B at the APS uses a Si (111) fixed-offset double-crystal monochromator, detuned by 10% to attenuate harmonics. Rh-coated Si mirrors were used for focusing and further harmonic rejection. Fluorescence yield Ni and Zn K-edge XAFS spectra were collected with a 12-element energy dispersive solid-state Ge array detector. Beamline 4-1 at SSRL uses a Si (220) double crystal monochromator, which was detuned by 40% to attenuate beam harmonics. Fluorescence yield Ni and Zn K-edge XAFS spectra were collected with a 15-element energy dispersive solid-state Ge array detector. Ni and Zn metal foils was used to calibrate the monochromators to the Ni and Zn K-edges, respectively (8333 eV and 9659 eV).

XAFS Fitting

The Athena (Ravel and Newville, 2005) graphical user interface to IFEFFIT (Newville, 2001), in conjunction with SamView via the SixPack interface (Webb, 2005) were used to average, process, deadtime correct, and normalize the XAFS spectra. SixPack was also used for spectral fitting, largely following models described in past research (Peacock and Sherman, 2007a; Manceau et al., 2007; Peacock, 2009; Zhu et al., 2010b) for Ni and Zn adsorption onto phyllomanganates. The chalcophanite structure (Post and Appleman, 1988) was used to calculate backscattering phase and amplitude functions for the Zn system using FEFF 9.6 (Rehr et al., 2010), and Ni substituted for Zn within the chalcophanite structure was used to calculate these functions for the Ni system. The k^3-weighted EXAFS spectra were fit over a k range of 3 – 11.1 $Å^{-1}$ and an R range of 1 – 4.0 Å, with the amplitude reduction factor (S_0^2) fixed to 0.94 for all Ni samples (Zhu et al., 2010b) and 0.86 for all Zn samples (Toner et al., 2006). In the model fits,

Ni-O coordination numbers were fixed at 6, while Zn-O coordination numbers were allowed to vary due to potential for mixed tetrahedral and octahedral Zn (^{IV}Zn and ^{VI}Zn) coordination states.

5.3.3 Macroscopic Ni(II) Adsorption Experiments

A series of Ni(II) adsorption experiments were conducted for the δ-MnO2, HexB, and TriB mineral systems in the absence and presence of Mn(II) at pH 4 and pH 7. All experiments were conducted within the anaerobic chamber. Each 10 mL sample consisted of 10 mM NaCl (an ionic strength buffer), 2.5 g L^{-1} phyllomanganate, 1 mM MES buffer (if conducted at pH 7), and 0.02 - 10 mM Ni(II) at pH 4 or 7 with or without 0.75 mM Mn(II). Triplicate samples were prepared for 0.10 mM Ni(II) to estimate experimental uncertainty. Similar methods as those described in the prior section regarding the addition of the mineral suspension, pH adjustments, and experiment conditions were followed in these experiments. After approximately 24 hours of reaction, the final pH of the samples was recorded and samples were filtered (0.22 µm MCE filters; Santa Cruz Biotechnology), discarding the first 1 mL of filtrate. If the final sample pH substantially diverged from the target pH (i.e., more than ±0.5 pH units from the target pH), the sample results were not included in the isotherm. ICP-OES was conducted on the filtrate, diluted and acidified as described above.

5.4 RESULTS AND DISCUSSION

5.4.1 Synthesized Metal-Free Materials

The chemical and physical properties of the metal-free phyllomanganates used for this research are described in detail elsewhere (Hinkle and Catalano, 2015). Briefly, the δ-MnO_2 and HexB used in this study are turbostratic phyllomanganates with hexagonal sheet symmetry and

high surface areas (116.4 m^2 g^{-1} and 167.8 m^2 g^{-1}, respectively), while TriB is a more crystalline phyllomanganate with orthogonal sheet symmetry, rotationally ordered layer stacking, and lower surface area (24.8 m^2 g^{-1}). The materials used in this study were analyzed by XRD and XAFS spectroscopy (Hinkle and Catalano, 2015), confirming that these materials are consistent with those characterized extensively in previous studies, with the negative layer charge in δ-MnO2, HexB, and TriB predominantly arising from vacancies, a mixture of vacancies and Mn(III) substitutions, and only Mn(III) substitution, respectively (Villalobos et al., 2003; Lopano et al., 2007).

5.4.2 Effect of Adsorption Versus Coprecipitation on Metal Binding Mechanisms

Recent research has found that aqueous Mn(II) induces phyllomanganate structural changes (Elzinga, 2011; Lefkowitz et al., 2013; Hinkle and Catalano, 2015). Thus, it is possible that phyllomanganates dissolve and reprecipitate in the presence of aqueous Mn(II). To explore the possibility of Mn(II)-induced phyllomanganate recrystallization and the subsequent impact on metal speciation, it is beneficial to first understand metal binding modes during adsorption and coprecipitation in the absence of aqueous Mn(II).

EXAFS spectra (s 5.1) and model fits (Tables 5.1) show that Ni adsorption behaviors vary substantially depending on the mineral structure and pH. The Ni XAFS spectra for all three Ni-adsorbed phyllomanganates (Figure 5.1) at pH 4 exhibit clear peaks in the Fourier transform at ~3.1 Å, corresponding to Ni adsorbed as a double-corner (DC) or triple-corner (TC) sharing complex (Manceau et al., 2007; Peacock, 2009). The DC and TC complexes both have Ni-Mn interatomic distances of ~3.48 Å (which yield a ~3.1 Å feature in the Fourier transform) but the TC complexes have coordination numbers (CNs) of ~6 because they adsorb above vacancies

within the interlayer (Zhu et al., 2010b) while the DC complexes, which adsorb at sheet edges, have CNs of ~2. Because the Ni-$Mn_{DC/TC}$ CNs are relatively high (Table 5.1), the adsorbed Ni in these 48 hour pH 4 Ni adsorption samples are likely TC complexes. The Ni XAFS spectrum for Ni adsorbed onto TriB at pH 4 also contains a peak in the Fourier transform at ~2.4 Å (Figure 5.1F), corresponding to Ni incorporated into the phyllomanganate sheet (Peacock and Sherman, 2007a; Manceau et al., 2007; Peacock and Sherman, 2007b; Peacock, 2009). Ni sorption at pH 7 in the δ-MnO_2 system also involves Ni incorporation (in addition to a TC complex), consistent with past research finding that adsorbed Ni incorporates into vacancy-rich phyllomanganate sheets as pH increases (Manceau et al., 2007; Peacock and Sherman, 2007b; Peacock, 2009). Attempts to fit a Ni-Mn_{incor} shell in the HexB system resulted in larger reduced-chi-square (χ_v^2) values (not shown), thus there is no statistical justification for the inclusion of incorporated Ni in the HexB model. Rather, Ni sorption is simply described by a TC complex at pH 7 HexB surfaces (Table 5.1; Figure 5.1C,D). Ni adsorption onto TriB at pH 7, however, is consistent with a tridentate edge-sharing (TE) complex (Table 5.1), as has been previously identified in Ni-triclinic birnessite systems at pH 7 (Peacock and Sherman, 2007b; Zhu et al., 2010b).

Ni sorption behavior when coprecipitated with phyllomanganates is most similar to the pH 4 adsorbed system, with the addition of some Ni incorporation. The Ni-coprecipitated phyllomanganate EXAFS spectra were well characterized by models accounting for Ni-Mn shells associated with both incorporated Ni and adsorbed Ni at interatomic distances of ~2.90 Å and 3.50 Å, respectively (Table 5.1). The adsorbed Ni in these samples are likely TC complexes, based on their high CNs (~6).

Zn adsorption exhibits similar behavior to Ni in the δ-MnO_2 and TriB systems, with the exception of no Zn incorporation into phyllomanganate sheets, and the potential for both

octahedrally- and tetrahedrally-coordinated Zn. These two coordination states can be differentiated by their Zn-O and Zn-Mn interatomic distances [Zn-O = ~2.15 Å (^{VI}Zn) or ~2.00 (^{IV}Zn); TC Zn-Mn = ~3.53 Å (^{VI}Zn) or ~3.35 Å (^{IV}Zn)] (Manceau et al., 2002; Toner et al., 2006; Manceau et al., 2007). Intermediate values (e.g., Zn-O distance of ~2.07 Å and Zn-Mn distance of ~3.47 Å) are indicative of mixed but spectrally unresolved tetrahedral and octahedral Zn contributions. ^{VI}Zn can also be differentiated from ^{IV}Zn in the EXAFS spectrum, with increasing ^{IV}Zn resulting in increased splitting of the positive antinode at k = ~6.1 Å^{-1}. The relative amount of ^{VI}Zn/^{IV}Zn is sensitive to Zn surface coverage and sheet stacking, with ^{VI}Zn favored by high Zn loadings and increased phyllomanganate sheet stacking (Lanson et al., 2002; Manceau et al., 2002; Grangeon et al., 2012).

As with Ni, Zn adsorbs onto δ-MnO_2 as TC $^{IV/VI}$Zn at both pH 4 and 7 (Table 5.2). CN values for Zn-$Mn_{DC/TC}$ shells in the HexB system at both pH are much lower than those expected for TC Zn (Table 5.2), indicating that Zn either adsorbs as a DC complex to the edge of a phyllomanganate sheet or that there are multiple, spectrally unresolved Zn surface complexes present. For the latter case, destructive interference between the spectral contributions of two Zn-Mn shells would reduce the apparent amplitude of the Fourier transform feature. The Zn-Mn distances in the HexB system are consistent with mixed $^{IV/VI}$Zn at pH 4 and ^{IV}Zn at pH 7 (Table 5.2). Zn and Ni behave similarly in the TriB system (although no Zn incorporation occurs), with Zn forming TC $^{IV/VI}$Zn complexes at pH 4 and TE $^{IV/VI}$Zn complexes at pH 7.

Zn sorption in the coprecipitated samples is also limited to adsorption, with no evidence of incorporation into the phyllomanganate sheets, as there is no Zn-Mn feature in the Fourier transform near 2.4 Å like that observed in the Ni system (Figures 5.1, 5.2). This is not wholly unexpected, as Zn is not observed to enter vacant sites (Manceau et al., 2002; Marcus et al.,

2004; Toner et al., 2006; Fuller and Bargar, 2014) [even in the Zn-bearing phyllomanganate mineral chalcophanite (Post and Appleman, 1988)]. Recent density functional theory calculations also indicate that Zn does not readily enter into phyllomanganate vacancy sites (Kwon et al., 2013). The fact that Zn does not enter into phyllomanganate sheets suggests that Mn(II)-Zn interactions will be predominantly related to surface interactions.

Adsorbed Zn complexes can be used to model the Zn-coprecipitated HexB and δ-MnO_2 EXAFS spectra. Zn-coprecipitated δ-MnO_2 is consistent with TC adsorbed $^{IV/VI}$Zn, requiring two separate Zn-Mn shells to adequately fit the spectrum (Table 5.2). The shorter Zn-Mn distance (3.39 Å) and lower CN (2.3) modeled for Zn-coprecipitated HexB is consistent with DC ^{IV}Zn. In the TriB system, however, EXAFS spectroscopy indicates that Zn formed the spinel phase hetaerolite ($ZnMn_2O_4$) instead of binding to the Mn oxide sheet structure (not shown).

These results show that metal sorption behaviors when reacted over short (i.e., 48 hour) time scales with or coprecipitated with phyllomanganates are similar, with the exception that Ni incorporation is more prevalent in the coprecipitation samples. These results indicate that Ni and Zn sorption behaviors are largely controlled by the vacancy content and the system pH. The presence of TC Ni and Zn complexes on TriB at pH 4 but not at pH 7 suggests that a substantial vacancy content has developed in this material at pH 4. Previous research has found that aging TriB at pH 4 results in a reduction of Mn(III) content, the creation of sheet vacancies, and a transition to hexagonal sheet symmetry, likely as a result of acidic conditions promoting Mn(III) disproportionation reactions (Lanson et al., 2000; Hinkle and Catalano, 2015). Such proton-promoted structural changes in TriB at low pH could explain the presence of TC Ni and Zn as well as incorporated Ni in the TriB pH 4 sample. Previous observations that Ni

incorporation into phyllomanganates increases with increasing pH may, therefore, only apply to manganese oxides with high initial vacancy contents (e.g., δ-MnO_2 and HexB).

5.4.3 Effect of Mn(II) on Metal Binding Mechanisms

pH 4

Aging the Ni-sorbed phyllomanganates at pH 4 for 25 days in the absence of Mn(II) does not affect the Ni speciation relative to the 48-hour samples (Figure 5.1; Table 5.1). Upon addition of aqueous Mn(II), however, Ni binding mechanisms onto phyllomanganates at pH 4 after 25 days of reaction are altered (Figure 5.1; Table 5.1). Similarly, XANES spectra of 25-day reacted Zn-sorbed manganese oxides are unaltered in the absence of Mn(II) at pH 4 (Figure 5.3), indicating that Zn speciation does not change with aging in Mn(II)-free systems at this pH. No change is observed in the Ni and Zn sorbed δ-MnO_2 EXAFS (Figure 5.1A,B) and XANES (Figure 5.3A) δ-MnO_2 spectra, respectively, between the absence and presence of 0.75 mM Mn(II), but the addition of 7.5 mM Mn(II) substantially decreases the Fourier transform feature at ~3.1 Å (Figures 5.1B, 5.2B). The decrease in CN associated with this shell (Tables 5.1, 5.2) is consistent with a transition from TC to DC metal adsorption. In the Zn δ-MnO_2 system, increased splitting in the 6.1 $Å^{-1}$ peak in the k^3-weighted EXAFS spectrum in the 7.5 mM Mn(II) sample further indicates that Mn(II) increases ^{IV}Zn (Toner et al., 2006; Grangeon et al., 2012). The presence of ^{IV}Zn is confirmed by the model fit Zn-O and Zn-Mn interatomic distances, which are consistent with ^{IV}Zn (2.02 Å and 3.37 Å, respectively).

In the Ni HexB system, the Fourier transform feature at ~3.1 Å decreases in amplitude (Figure 5.1D) with increasing aqueous Mn(II) concentration, consistent with a conversion of TC Ni to DC Ni. Aqueous Mn(II) also promotes ^{IV}Zn over ^{VI}Zn adsorption onto HexB, with Zn

predominantly adsorbing as a DC complex. The Zn-O feature in the Fourier transform of the EXAFS spectrum of the Zn-reacted HexB clearly shifts to shorter distance with increasing Mn(II) (Figure 5.2D), indicative of an increased ^{IV}Zn content. The model fit for the Zn-reacted HexB sample reacted with 7.5 mM Mn(II) requires the inclusion of two Zn-O and Zn-Mn shells corresponding to ^{IV}Zn and ^{VI}Zn (Table 5.2), further supporting the conclusion that ^{IV}Zn complexes are promoted by aqueous Mn(II).

In the TriB system, the amplitude of the Ni-Mn shell associated with incorporated Ni decreases with the addition of 0.75 mM Mn(II), but increases substantially in the presence of 7.5 mM Mn(II) (Figure 5.1F). No change is observed in the Ni-Mn shell at 3.48 Å, indicating that adsorbed TC Ni is not affected by aqueous Mn(II). However, the presence of multiple adsorbed Ni species is suggested by the decrease in Ni-O shell interatomic distance (Table 5.1) and amplitude with 7.5 mM Mn(II) (Figure 5.1F). Adding additional Ni-Mn and Ni-O shells to account for other Ni surface species or split shells does not improve the spectral fit, therefore conclusively identifying the additional Ni surface species that form in the presence of aqueous Mn(II) is not tenable. However, changes in Zn sorption mechanisms in the TriB system are more straightforward. The CNs for the TC Zn-Mn shell progressively decrease with increasing Mn(II), indicating a transition from Zn adsorption over vacant sites (TC) to sheet edges (DC). Features in the Fourier transform of the EXAFS spectra associated with Zn-O and Zn-Mn shells also shift to shorter distances with increasing Mn(II) (Figure 5.6; Table 5.2), consistent with a transition from mixed $^{IV/VI}$Zn toward predominantly ^{IV}Zn upon Mn(II) addition.

Mechanism of Mn(II)-Induced Metal Speciation Changes at pH 4

These results indicate that aqueous Mn(II) causes the redistribution of adsorbed Ni and

Zn from vacant sites (TC complexes) to sheet edges (DC complexes) at pH 4. In the majority of systems studied, the addition of aqueous Mn(II) decreases TC Ni and Zn adsorption, promoting DC complexes instead. In the δ-MnO_2 system, the transition from predominantly TC to DC Ni and Zn only occurs at high Mn(II) loadings, while the transition occurs at lower Mn(II) loadings in the HexB system. This transition from TC to DC Ni and Zn correlates with Mn(II)-induced rotational ordering and the formation of intermixed hexagonal and orthogonal sheets with long range ordering, which occur at lower Mn(II) loadings in the HexB system relative to the δ-MnO_2 system under similar experimental conditions (Hinkle and Catalano, 2015). Edge-binding complexes like DC and TE species may be promoted by the formation of orthogonal phyllomanganate sheet symmetries, as these sheets have more ordered structural Mn(III) and fewer vacancies relative to hexagonal sheets (Lanson et al., 2000; Drits et al., 2007), and therefore possess fewer vacant sites for TC adsorption.

The current research also finds that aqueous Mn(II) consistently promotes ^{IV}Zn over ^{VI}Zn adsorption onto phyllomanganates at pH 4, suggesting that ^{IV}Zn preferentially forms when driven to edge sites. Past research has found that ^{VI}Zn is promoted over ^{IV}Zn on δ-MnO_2 surfaces with increasing Zn:Mn ratios, which also corresponds with decreased structural Mn(III) (Grangeon et al., 2012). Thus, the formation of rotationally ordered phyllomanganates with intermixed orthogonal and hexagonal sheets upon Mn(II) addition could promote ^{IV}Zn over ^{VI}Zn adsorption and also lead to increased edge-binding complexes like DC and TE species.

pH 7

In contrast to the pH 4 δ-MnO_2 system, aging samples at pH 7 for 25 days in the absence of Mn(II) alters Zn sorption relative to the 48 hour experiments (Figures 5.2, 5.3), although no

substantial changes are observed in the Ni adsorption behavior (Figure 5.1A,B). The model fit parameters for the 0.75 mM Mn(II) Ni δ-MnO_2 sample are within error of those for the Mn(II)-free sample (Table 5.1). However, it is clear that the Ni-Mn_{incor} shell amplitude decreases in the Fourier Transform upon addition of 0.75 mM Mn(II) (Figure 5.1B), which could be due to decreased Ni incorporation or interference from multiple Ni-Mn_{incor} shells arising from the presence of both Mn(IV) and Mn(III) in the sheet (Hinkle and Catalano, 2015). In fitting both the Zn pH 7 δ-MnO_2 and HexB systems, two Zn-O and Zn-Mn shells are required to account for contributions from both ^{IV}Zn and ^{VI}Zn (Table 5.2). While the δ-MnO_2 samples reacted for 25 days at pH 7 exhibit substantial decreases in the TC Zn-Mn shell amplitude relative to the 48 hour adsorbed standard (Figure 5.2B), the CNs for ^{IV}Zn- and ^{VI}Zn-Mn shells sum to ~6, indicating that the observed decrease in the Zn-Mn peak is due to interference from the two $^{IV/VI}$Zn contributions rather than a transition from TC to DC adsorbed Zn.

The Ni HexB EXAFS spectra indicate that reacting Ni at pH 7 for 25 days may lead to some Ni incorporation into the phyllomanganate sheets (Figure 5.1C,D). Fitting the data with an additional Ni-Mn_{incor} shell does improve the fit of the 0 mM Mn(II) sample (Table 5.1), but the change is not statistically significant (Kelly et al., 2008b). However, including the Ni-Mn_{incor} shell in the 0.75 mM Mn(II) pH 7 HexB sample fit is a statistically significant improvement. Because the EXAFS spectra for the 0 and 0.75 mM Mn(II) Ni HexB samples are very similar in the 2.4 Å region (corresponding to the Ni-Mn_{incor} shell) (Figure 5.1D), it is likely that some Ni is incorporated into the phyllomanganate sheet after 25 days of reaction at pH 7, even in the absence of Mn(II). Comparing the 0 and 0.75 mM Mn(II) HexB model fits that include Ni-Mn_{incor} shells shows that the addition of Mn(II) does not alter Ni binding mechanisms at pH 7. The appearance of incorporated Ni after 25 days of reaction is consistent with past research,

which found that Ni becomes progressively incorporated into phyllomanganates over time at circumneutral pH (Peacock, 2009).

Like HexB, Ni and Zn speciation in the TriB system exhibits only minor changes upon reaction at pH 7 for 25 days. Ni adsorption can be described entirely by a TE Ni surface complex in the 25-day pH 7 TriB samples, and is unaffected by the addition of Mn(II) (Table 5.1; Figure 5.1E,F). In the Zn system, the Fourier transform peak at ~2.7 Å corresponding to the TE Zn complex is substantially dampened in the absence of Mn(II) (Figure 5.2F). Attempts to model the Mn(II)-free TriB pH 7 EXAFS spectrum using the Zn-Mn_{TE} shell resulted in CNs refined to within error of zero, but the data can be well described by DC Zn with a Zn-$Mn_{DC/TC}$ interatomic distance of 3.45 Å (Table 5.2). It is possible that DC/TC and TE Zn surface complexes are all present in the Mn(II)-free TriB sample, but destructive interference between the Zn-Mn shells reduce the amplitude of the Fourier transform features. Upon addition of 0.75 mM Mn(II), the peak associated with Zn-Mn_{TE} becomes apparent in the Fourier transform (Figure 5.2F), and is required to fit the EXAFS spectrum (Table 5.2). These results suggest that Mn(II) alters Zn and Ni speciation differently at pH 7, predominantly affecting Ni incorporation into vacancy-rich phyllomanganates and Zn adsorption onto TriB.

Mechanism of Mn(II)-Induced Metal Speciation Changes at pH 7

Aqueous Mn(II) has less effect on Ni and Zn speciation in phyllomanganates at pH 7 than at pH 4, with a more substantial effect in the δ-MnO_2 system than the HexB or TriB systems. Aqueous Mn(II) increases structural Mn(III) in δ-MnO_2 at pH 7 under similar conditions (Hinkle and Catalano, 2015), while Mn(II) effects on HexB and TriB structures are minimal. Thus, the apparent decrease in the peak at ~2.4 Å associated with Ni-Mn_{incor} in δ-MnO_2 with aqueous

Mn(II) can be attributed to either decreased Ni incorporation due to decreased Mn(IV) vacancies or multiple Ni-Mn_{incor} interatomic distances due to the presence of both Mn(III) and Mn(IV) in the sheets. Ni and Zn speciation in the HexB system is largely unaffected by the addition of Mn(II), consistent with the finding that Mn(II) does not alter the HexB structure (Hinkle and Catalano, 2015). While Ni adsorption onto TriB is not altered by Mn(II), Zn adsorption is affected relative to the 25-day Mn(II)-free sample. Zn adsorption onto TriB at pH 7 in the 25-day Mn(II)-free sample is consistent with a DC Zn complex. The reappearance of TE Zn upon addition of Mn(II), consistent with the 48-hour Zn TriB sample, may be due to Mn(II) outcompeting Zn for DC adsorption sites.

Effect of Mn(II) on Macroscopic Metal Uptake

The addition of Mn(II) at pH 4 decreases macroscopic Ni and Zn uptake in the 25-day experiments for most systems (Table 5.3). In particular, Ni and Zn sorption substantially decrease in the presence of 7.5 mM Mn(II) at pH 4, suggesting that competitive adsorption effects occurs at high Mn(II) loadings. It should be noted that Mn(II) concentrations in the TriB system were larger than the initial Mn(II) added, likely due to structural Mn(III) disproportionating and producing aqueous Mn(II) and layer Mn(IV), as has been previously observed (Hinkle and Catalano, 2015). No suppression of Ni and Zn uptake occurs in the pH 7 system (Table 5.4), as 100% of the initial Ni and Zn is associated with the solid at the end of the 25 day reaction period with or without Mn(II). It follows, therefore, that while metals and Mn(II) may compete for specific types of adsorption sites (e.g., competition for DC sites in TriB), total metal uptake is not affected.

5.4.4 Effect of Mn(II) on Macroscopic Metal Adsorption

In order to determine if the limited effect of 0.75 mM Mn(II) on metal uptake after 25 days is the result of weak competition for surface sites or re-equilibration upon aging, Ni adsorption in the absence and presence of Mn(II) was examined in a series of 48-hour macroscopic adsorption experiments. In these short time scale experiments, macroscopic Ni adsorption (Figure 5.4) and corresponding Langmuir isotherm fit parameters (Table 5.4) indicate that Mn(II) does not substantially alter macroscopic Ni adsorption. Ni adsorption onto δ-MnO_2 is slightly suppressed upon addition of 0.75 mM Mn(II) at pH 4 (Figure 5.4A), but not at low Ni concentrations comparable to those examined in the 25-day experiments (Figure 5.4D). Ni adsorption in the pH 7 HexB system is not affected by Mn(II) at low initial Ni concentrations (Figure 5.4E), but is enhanced at higher Ni loadings (~2 mM initial Ni) with 0.75 mM Mn(II). Mn(II) has no effect on Ni adsorption onto TriB at both pH 4 and 7 (Figure 5.4C,F).

Although Mn(II) has a minimal effect on Ni adsorption even at low initial Ni concentrations, aqueous Mn concentrations indicate that Ni causes Mn(II/III) to eject from the phyllomanganate interlayer or sheets (Figure 5.5). If Mn(III) is ejected from the interlayer to the aqueous phase in the absence of a chelating agent, disproportionation will occur, forming aqueous Mn(II) (Glenn et al., 1986). In the pH 4 HexB and TriB mineral systems, aqueous Mn(II) reaches concentrations above the initial 0.75 mM Mn(II) added, and is present in appreciable amounts even in the Mn(II)-free experiments. Mn(II) released to solution in the δ-MnO_2 pH 4 system is much less substantial, likely due to the lower initial layer and interlayer Mn(III) content. This is consistent with previous research finding that Ni and Zn adsorption leads to the formation of vacancy-rich phyllomanganates as a result of the ejection of layer Mn(III) from the phyllomanganate sheets (Zhu et al., 2010b; Grangeon et al., 2012), and that sorption of

Co(II) and Cu(II) onto birnessite can result in the release of Mn(II) to solution (Traina and Doner, 1985). No substantial changes are observed in the Ni binding mechanisms between the 48-hour and 25-day Mn(II) free pH 4 experiments, as discussed above, suggesting that Ni-induced structural changes persist over long time scales. These results suggest that the slight effect of 0.75 mM Mn(II) on macroscopic metal uptake during the 25-day reactions at pH 4 is not the result of re-equilibration, but is due to competitive adsorption effects or altered phyllomanganate sheet compositions.

5.4.5 Environmental Implications

This study shows that Mn(II) alters trace metal speciation in phyllomanganates, with differing effects at acidic and circumneutral pH. Trace metals such as Ni and Zn commonly coexist with phyllomanganates and aqueous Mn(II) in acid and coal mine drainage sites, marine sediments, and anoxic soils (Graybeal and Heath, 1984; Kay et al., 2001; Tebo et al., 2004; Tebo et al., 2005; Cravotta III, 2008; Tan et al., 2010). At acidic pH, Mn(II) redistributes Ni and Zn surface complexes from capping vacancies within the interlayer to binding at more exposed edge sites and, at high loadings, suppresses overall Ni and Zn uptake by the solid. Therefore, phyllomanganates may not sequester trace metals as effectively in acidic soils and acid mine drainage sites with appreciable concentrations of aqueous Mn(II). In more alkaline marine sediments or calcareous coal mine drainage sites, Mn(II) may serve to alter the long-term behavior of incorporated structurally compatible metals, such as Ni, in phyllomanganates with high initial vacancy contents. In fact, heavy metal uptake by phyllomanganates in a karst cave system has been shown to decrease with increased aqueous Mn(II), potentially due to decreased sheet vacancy content upon Mn(II) exposure (Frierdich and Catalano, 2012). These results

demonstrate that when phyllomanganates are exposed to Mn(II)-rich fluids, trace metals exhibit altered speciation and coordination behaviors.

5.5 ACKNOWLEDGEMENTS

This research was supported by the National Science Foundation (NSF), Division of Earth Sciences, Geobiology and Low-Temperature Geochemistry Program with Grant No. EAR-1056480. ICP-OES analyses were conducted at the Nano Research Facility at Washington University, which is supported through NSF Award No. ECS-0335765. XAFS spectra were collected at beamline 20-BM-B at the APS, an Office of Science User Facility run by the U.S. Department of Energy (DOE) Office of Science by Argonne National Laboratory, supported by the U.S. DOE through Contract No. DE-AC02-06CH11357 and at beamline 4-1 at SSRL, operated by SLAC National Accelerator Laboratory with support from the DOE Office of Science through Contract No. DE-AC02-76SF00515. XRD patterns were collected with the Bruker D8 Advance XRD instrument at Washington University in St. Louis, supported by the NSF through Award No. EAR-1161543. We would particularly like to thank Dale Brewe, John Bargar, and Ryan Davis for their help and support in collecting the XAFS spectra presented in this paper.

Table 5.1. Spectral fitting results for Ni EXAFS spectra of Ni incorporated into, adsorbed onto, or reacted with phyllomanganates.

Sample	Shell	N[a]	R (Å)[b]	σ^2 (Å^2)[c]	ΔE_0 (eV)[d]	χ_v^2[f]
Ni Coprecipitated						
δ-MnO_2	Ni-O	6	2.032(6)[g]	0.0066(5)	2(1)	9.08
	Ni-Mn_{incor1}	2.4(8)	2.89(1)	0.006(2)		
	Ni-$Mn_{DC/TC}$	6(3)	3.493(9)	0.013(4)		
HexBirn	Ni-O	6	2.03(1)	0.007(1)	2(2)	26.97
	Ni-Mn_{incor1}	2(1)	2.86(1)	0.003(3)		
	Ni-$Mn_{DC/TC}$	8(5)	3.48(2)	0.013(7)		
TriBirn	Ni-O	6	2.027(6)	0.0061(5)	1(1)	18.58
	Ni-Mn_{incor1}	2.8(9)	2.88(1)	0.006(2)		
	Ni-$Mn_{DC/TC}$	5(4)	3.50(2)	0.017(9)		
Ni 48 hr Rxn pH 4						
δ-MnO_2	Ni-O	6	2.051(5)	0.0066(4)	3(1)	9.20
	Ni-$Mn_{DC/TC}$	8(1)	3.498(7)	0.09(1)		
HexBirn	Ni-O	6	2.043(4)	0.0063(3)	2.5(6)	2.36
	Ni-$Mn_{DC/TC}$	7.5(9)	3.489(6)	0.011(1)		
TriBirn	Ni-O	6	2.044(6)	0.0070(5)	2(1)	5.14
	Ni-Mn_{incor1}	0.3(3)	2.88(2)	0.002(7)		
	Ni-$Mn_{DC/TC}$	5(1)	3.489(8)	0.008(2)		
Ni 48 hr Rxn pH 7						
δ-MnO_2	Ni-O	6	2.038(6)	0.0064(5)	2(1)	9.75
	Ni-Mn_{incor1}	1.5(7)	2.86(1)	0.005(3)		
	Ni-$Mn_{DC/TC}$	7(2)	3.483(9)	0.009(2)		
HexBirn	Ni-O	6	2.04(1)	0.0053(7)	3(2)	16.09
	Ni-$Mn_{DC/TC}$	7(2)	3.49(1)	0.009(3)		
TriBirn	Ni-O	6	2.052(8)	0.0063(5)	4(1)	2.50
	Ni-Mn_{TE}	4(2)	3.07(2)	0.019(7)		
Ni 25 day Rxn pH 4						
δ-MnO_2	Ni-O	6	2.046(5)	0.0063(4)	3(1)	2.50
Mn(II)-free	Ni-$Mn_{DC/TC}$	8(1)	3.493(7)	0.009(1)		
δ-MnO_2	Ni-O	6	2.047(5)	0.0064(4)	3(1)	6.46
0.75 mM Mn(II)	Ni-$Mn_{DC/TC}$	8(1)	3.497(7)	0.009(1)		
δ-MnO_2						
7.5 mM Mn(II)	Ni-O	6	2.043(7)	0.0065(5)	2(1)	2.25
	Ni-$Mn_{DC/TC}$	4(2)	3.48(1)	0.012(4)		
HexBirn	Ni-O	6	2.043(6)	0.0065(5)	2(1)	5.96
Mn(II)-free	Ni-$Mn_{DC/TC}$	7(1)	3.488(8)	0.010(2)		
HexBirn	Ni-O	6	2.040(8)	0.0068(6)	2(1)	8.61
0.75 mM Mn(II)	Ni-$Mn_{DC/TC}$	6(2)	3.48(1)	0.011(3)		
HexBirn	Ni-O	6	2.046(6)	0.0062(4)	3(1)	3.57
7.5 mM Mn(II)	Ni-$Mn_{DC/TC}$	4(1)	3.48(1)	0.012(3)		

TriBirn	Ni-O	6	2.039(8)	0.0065(6)	2(1)	16.69
Mn(II)-free	Ni-Mn_{incor1}	0.3(1)	2.89(3)	0.010(5)		
	Ni-$Mn_{DC/TC}$	5(2)	3.48(1)	0.007(2)		
TriBirn	Ni-O	6	2.043(8)	0.0073(6)	2(1)	3.62
0.75 mM Mn(II)	Ni-Mn_{incor1}	1(1)	2.9(1)	0.01(5)		
	Ni-$Mn_{DC/TC}$	8(2)	3.50(1)	0.010(2)		
TriBirn	Ni-O	6	2.04(1)	0.007(1)	2(2)	25.19
7.5 mM Mn(II)	Ni-Mn_{incor1}	0.5(2)	2.85(3)	0.001(3)		
	Ni-$Mn_{DC/TC}$	7(3)	3.47(2)	0.010(3)		
Ni 25 day Rxn pH 7						
δ-MnO_2	Ni-O	6	2.040(8)	0.0065(7)	2(1)	15.26
Mn(II)-free	Ni-Mn_{incor}	1.1(7)	2.86(1)	0.002(3)		
	Ni-$Mn_{DC/TC}$	7(2)	3.49(1)	0.010(3)		
δ-MnO_2	Ni-O	6	2.040(5)	0.0064(5)	3(1)	10.23
0.75 mM Mn(II)	Ni-Mn_{incor}	1.0(6)	2.86(1)	0.005(4)		
	Ni-$Mn_{DC/TC}$	7(2)	3.483(7)	0.009(2)		
HexBirn	Ni-O	6	2.039(6)	0.0055(5)	2(1)	5.46
Mn(II)-free	Ni-Mn_{incor}	0.3(4)	2.86(3)	0.001(0.01)		
Ni-Mn_{incor} included	Ni-$Mn_{DC/TC}$	7(2)	3.48(1)	0.010(2)		
HexBirn	Ni-O	6	2.042(7)	0.0057(5)	2(1)	7.08
Mn(II)-free	Ni-$Mn_{DC/TC}$	7(2)	3.48(1)	0.010(2)		
No Ni-Mn_{incor}						
HexBirn	Ni-O	6	2.044(5)	0.0067(4)	3(1)	5.26
0.75 mM Mn(II)	Ni-Mn_{incor}	0.4(1)	2.87(2)	0.004(1)		
Ni-Mn_{incor} included	Ni-$Mn_{DC/TC}$	6(1)	3.483(7)	0.011(2)		
HexBirn	Ni-O	6	2.046(8)	0.0068(6)	3(1)	11.88
0.75 mM Mn(II)	Ni-$Mn_{DC/TC}$	6(2)	3.49(1)	0.011(2)		
No Ni-Mn_{incor}						
TriBirn	Ni-O	6	2.052(5)	0.0063(4)	4(1)	5.88
Mn(II)-free	Ni-Mn_{TE}	5(2)	3.07(1)	0.016(3)		
TriBirn	Ni-O	6	2.051(5)	0.0062(4)	3(1)	5.89
0.75 mM Mn(II)	Ni-Mn_{TE}	5(2)	3.07(2)	0.020(5)		

[a] Coordination Number.
[b] Interatomic distance.
[c] Debye-Waller factor.
[d] Difference in the threshold Fermi level between data and theory.
[e] Amplitude reduction factor.
[f] Goodness of fit parameters (see (Kelly et al., 2008a))
[g] Statistical uncertainties at the 68% confidence level are reported in parentheses. Any parameters without reported uncertainties were not allowed to vary during fitting.

Table 5.2. Spectral fitting results for Zn EXAFS spectra of Zn incorporated into, adsorbed onto, or reacted with phyllomanganates.

Sample	Shell	N[a]	R (Å)[b]	σ^2 (Å^2)[c]	ΔE_0 (eV)[d]	χ_v^2[f]
Zn-Coprecipitated						
δ-MnO_2	Zn-O	6.1(6)	2.040(8)[g]	0.012(1)	0(1)	12.55
	Zn-$Mn_{DC/TC1}$	2.2(6)	3.34(3)	0.01[h]		
	Zn-$Mn_{DC/TC2}$	4.2(7)	3.49(2)	0.01		
HexBirn	Zn-O	5.2(5)	2.012(9)	0.010(1)	0(1)	14.55
	Zn-$Mn_{DC/TC}$	2.3(4)	3.39(1)	0.01		
Zn 48 hr Rxn pH 4						
δ-MnO_2	Zn-O	7.4(8)	2.095(7)	0.009(1)	2(1)	15.86
	Zn-$Mn_{DC/TC}$	7.6(5)	3.530(9)	0.01		
HexBirn	Zn-O	7.4(4)	2.096(5)	0.0098(7)	2.2(7)	12.32
	Zn-$Mn_{DC/TC}$	2.7(3)	3.517(9)	0.01		
TriBirn	Zn-O	7.1(9)	2.090(9)	0.011(2)	3(1)	31.12
	Zn-$Mn_{DC/TC}$	6.0(5)	3.50(1)	0.01		
Zn 48 hr Rxn pH 7						
δ-MnO_2	Zn-O	6.8(8)	2.078(9)	0.011(2)	2(1)	67.93
	Zn-$Mn_{DC/TC}$	5.4(5)	3.50(1)	0.01		
HexBirn	Zn-O	5.3(6)	2.002(8)	0.010(1)	-1(1)	28.87
	Zn-$Mn_{DC/TC}$	2.2(3)	3.35(1)	0.01		
TriBirn	Zn-O	7.7(6)	2.073(7)	0.012(1)	0.7(9)	11.89
	Zn-Mn_{TE}	1.1(2)	3.08(2)	0.01		
Zn 25 day Rxn pH 4						
δ-MnO_2	Zn-O	7.5(7)	2.100(7)	0.009(1)	3(1)	19.46
0.75 mM Mn(II)	Zn-$Mn_{DC/TC}$	7.5(5)	3.532(8)	0.01		
δ-MnO_2	Zn-O	6.1(6)	2.023(9)	0.012(1)	4(1)	11.45
7.5 mM Mn(II)	Zn-$Mn_{DC/TC}$	2.2(3)	3.37(1)	0.01		
HexBirn	Zn-O	8.1(7)	2.089(8)	0.012(1)	3(1)	4.55
0.75 mM Mn(II)	Zn-$Mn_{DC/TC}$	1.2(4)	3.47(2)	0.01		
HexBirn	Zn-O_1	4.4(8)	2.01(1)	0.007(2)	6(1)	8.03
7.5 mM Mn(II)	Zn-O_2	2.3(3)	2.17(3)	0.007[i]		
	Zn-$Mn_{DC/TC1}$	3(2)	3.32(4)	0.013(8)		
	Zn-$Mn_{DC/TC2}$	2.3(8)	3.48(4)	0.013		
TriBirn	Zn-O	6.9(9)	2.07(1)	0.011(2)	2(1)	22.47
0.75 mM Mn(II)	Zn-$Mn_{DC/TC}$	4.8(5)	3.48(1)	0.01		
TriBirn	Zn-O	6.0(7)	2.044(9)	0.011(1)	2(1)	20.29
7.5 mM Mn(II)	Zn-$Mn_{DC/TC}$	3.2(4)	3.41(1)	0.01		
Zn 25 day Rxn pH 7						
δ-MnO_2	Zn-O_1	2.7(4)	1.97(1)	0.003(2)	6(1)	2.3
Mn(II)-free	Zn-O_2	3.5(2)	2.13(1)	0.003		
	Zn-$Mn_{DC/TC1}$	1.8(6)	3.30(5)	0.012(4)		
	Zn-$Mn_{DC/TC2}$	5(2)	3.48(2)	0.012		

δ-MnO_2	Zn-O_1	5(2)	2.02(3)	0.010(4)	6(2)	8.82
0.75 mM Mn(II)	Zn-O_2	1(1)	2.19(9)	0.01		
	Zn-$Mn_{DC/TC1}$	2.2(6)	3.34(3)	0.009(5)		
	Zn-$Mn_{DC/TC2}$	3(1)	3.50(3)	0.009		
HexBirn	Zn-O_1	3.1(7)	1.99(2)	0.004(2)	7(2)	2.73
Mn(II)-free	Zn-O_2	2.2(2)	2.15(2)	0.004		
	Zn-$Mn_{DC/TC1}$	2.0(8)	3.30(4)	0.011(6)		
	Zn-$Mn_{DC/TC2}$	4(2)	3.47(3)	0.011		
HexBirn	Zn-O_1	4(1)	2.00(2)	0.007(2)	6(2)	8.94
0.75 mM Mn(II)	Zn-O_2	1.6(5)	2.17(5)	0.007		
	Zn-$Mn_{DC/TC1}$	1.9(7)	3.27(5)	0.013(7)		
	Zn-$Mn_{DC/TC2}$	4(2)	3.44(3)	0.013		
TriBirn	Zn-O	6.3(7)	2.052(9)	0.012(1)	5(1)	9.03
Mn(II)-free	Zn-$Mn_{DC/TC}$	1.3(4)	3.45(2)	0.01		
TriBirn	Zn-O	6.4(8)	2.06(1)	0.010(1)	5(1)	11.94
0.75 mM Mn(II)	Zn-Mn_{TE}	1.3(3)	3.06(2)	0.01		

[a] Coordination Number.
[b] Interatomic distance.
[c] Debye-Waller factor.
[d] Difference in the threshold Fermi level between data and theory.
[e] Amplitude reduction factor.
[f] Goodness of fit parameters (see (Kelly et al., 2008a))
[g] Statistical uncertainties at the 68% confidence level are reported in parentheses. Any parameters without reported uncertainties were not allowed to vary during fitting.
[h] σ^2 fixed for all Zn adsorbed Zn-Mn shells when one Zn-Mn shell is present.
[i] σ^2 fixed for all linked Zn-O and Zn-Mn shells, denoted by those with no uncertainties reported.

Table 5.3. Amount of metal (Me) and Mn(II) remaining in solution, and amount of metal and Mn(II) associated with the solid phase after 25 days of reaction.

Sample ID	Mn Oxide	pH	$[Me]_{soln}$ (mmol L^{-1})	$[Me]_{ads}$ (mmol g^{-1})	$[Mn]_{soln}$ (mmol L^{-1})	$[Mn]_{ads}$ (mmol g^{-1})
Ni(II):						
Ni4δno	δ-MnO_2	4	BDL	0.092	BDL	-
Ni4δlow	δ-MnO_2	4	BDL	0.092	BDL	0.30
Ni4δhigh	δ-MnO_2	4	1.56 ± 0.01 [c]	-[c]	36.0 ± 0.4	-[c]
Ni4HBno	HexB	4	BDL	0.092	BDL	-
Ni4HBlow	HexB	4	0.018 ± 0.006	0.085	0.106 ± 0.006	0.26
Ni4HBhigh	HexB	4	0.16 ± 0.01	0.028	5.7 ± 0.1	0.72
Ni4TBno	TriB	4	0.060 ± 0.008	0.068	0.42 ± 0.01	-[d]
Ni4TBlow	TriB	4	0.059 ± 0.007	0.068	0.87 ± 0.01	-[d]
Ni4TBhigh	TriB	4	0.11 ± 0.005	0.048	6.9 ± 0.2	0.24
Ni7δno	δ-MnO_2	7	BDL	0.092	BDL	-
Ni7δno	δ-MnO_2	7	BDL	0.092	BDL	0.30
Ni7HBno	HexB	7	BDL	0.092	BDL	-
Ni7HBlow	HexB	7	BDL	0.092	BDL	0.30
Ni7TBno	TriB	7	BDL	0.092	BDL	-
Ni7TBlow	TriB	7	BDL	0.092	0.023 ± 0.006	0.29
Zn(II):						
Zn4δno	δ-MnO_2	4	BDL	0.092	0.034 ± 0.005	-
Zn4δlow	δ-MnO_2	4	BDL	0.092	BDL	0.30
Zn4δhigh	δ-MnO_2	4	0.217 ± 0.008	0.005	4.29 ± 0.07	1.28
Zn4HBno	HexB	4	BDL	0.092	0.006 ± 0.005	-
Zn4HBlow	HexB	4	0.036 ± 0.01	0.078	0.084 ± 0.008	0.27
Zn4HBhigh	HexB	4	0.21 ± 0.01	0.008	5.7 ± 0.2	0.72
Zn4TBno	TriB	4	0.038 ± 0.008	0.077	0.43 ± 0.007	-[d]
Zn4TBlow	TriB	4	0.072 ± 0.006	0.063	1.02 ± 0.01	-[d]
Zn4TBhigh	TriB	4	0.181 ± 0.008	0.020	6.6 ± 0.1	0.36
Zn7δno	δ-MnO_2	7	BDL	0.092	BDL	-
Zn7δno	δ-MnO_2	7	BDL	0.092	BDL	0.30
Zn7HBno	HexB	7	BDL	0.092	BDL	-
Zn7HBlow	HexB	7	BDL	0.092	BDL	0.30
Zn7TBno	TriB	7	BDL	0.092	BDL	-
Zn7TBlow	TriB	7	BDL	0.092	BDL	0.30

[a] (-) Denotes no aqueous Mn(II) added to the sample, so this parameter is not reported.
[b] BDL denotes any samples with $[Ni]_{soln}$, $[Zn]_{soln,}$ or $[Mn]_{soln}$ below detection limit (0.006 mM; 0.035 mM; and 0.006 mM, respectively).
[c] Particles may have passed through filters, leading to excess metal and Mn(II) in solution. Thus, calculations for amount adsorbed are not reported for this sample.

Table 5.4. Langmuir isotherm parameters determined for Ni(II) adsorption onto Mn oxides.

Sample	**Γ_{max} (mmol g^{-1})**	**K (mL $mmol^{-1}$)**
pH 4		
δ-MnO_2, Mn(II)-free	1.02 ± 0.08	1400 ± 800
δ-MnO_2, 0.75 mM Mn(II)	0.84 ± 0.05	670 ± 260
HexB, Mn(II)-free	0.57 ± 0.05	19 ± 9
HexB, 0.75 mM Mn(II)	0.52 ± 0.04	5 ± 2
TriB, Mn(II)-free	1.6 ± 0.2	0.4 ± 0.1
TriB, 0.75 mM Mn(II)	1.4 ± 0.2	0.8 ± 0.3
pH 7		
δ-MnO_2, Mn(II)-free	1.6 ± 0.2	2000 ± 800
δ-MnO_2, 0.75 mM Mn(II)	1.6 ± 0.1	1800 ± 840
HexB, Mn(II)-free	1.1 ± 0.2	16 ± 7
HexB, 0.75 mM Mn(II)	1.5 ± 0.1	160 ± 70
TriB, Mn(II)-free	2.6 ± 0.1	190 ± 30
TriB, 0.75 mM Mn(II)	2.6 ± 0.08	380 ± 70

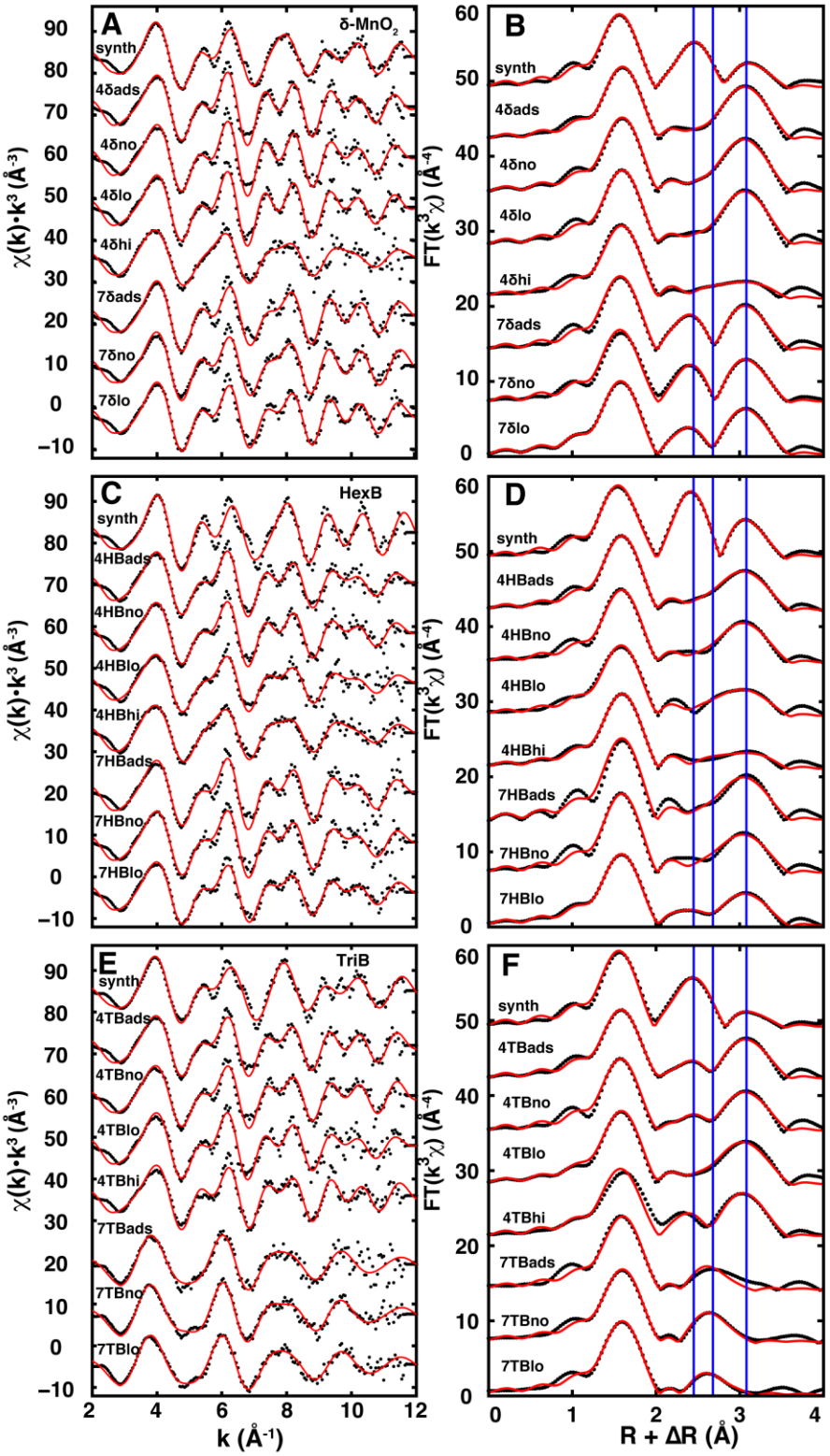

Figure 5.1. Ni EXAFS spectra (points) and model fits (red lines) for the δ-MnO_2 (A,B), HexB (C,D), and TriB (E,F) systems. Diagnostic features at 2.5, 2.7 and 3.1 Å (R + ΔR) in R space (corresponding to Ni-Mn shells for incorporated Ni at 2.88 Å, TE Ni at 3.08 Å, and DC/TC Ni at 3.48 Å, respectively) are denoted by blue lines.

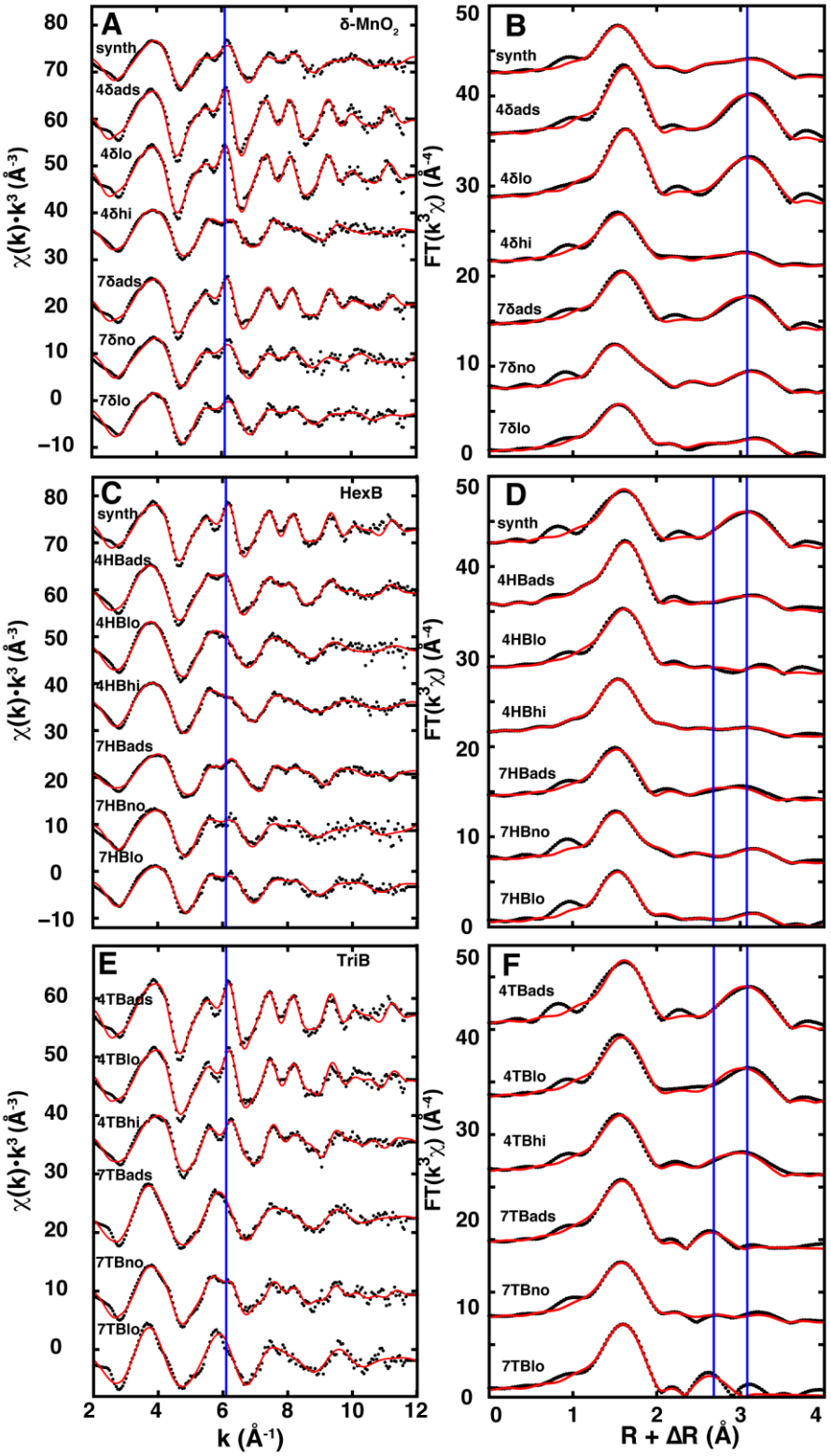

Figure 5.2. Zn EXAFS spectra (points) and model fits (red lines) for the δ-MnO_2 (A,B), HexB (C,D), and TriB (E,F) systems. Diagnostic features at 6.1 $Å^{-1}$ in k space (^{VI}Zn versus ^{IV}Zn) and at 2.7 Å and 3.1 Å (R + ΔR) in R space (Zn-Mn shells for TE Zn at 3.1 Å and DC/TC Zn at 3.48 Å, respectively) are denoted by blue lines.

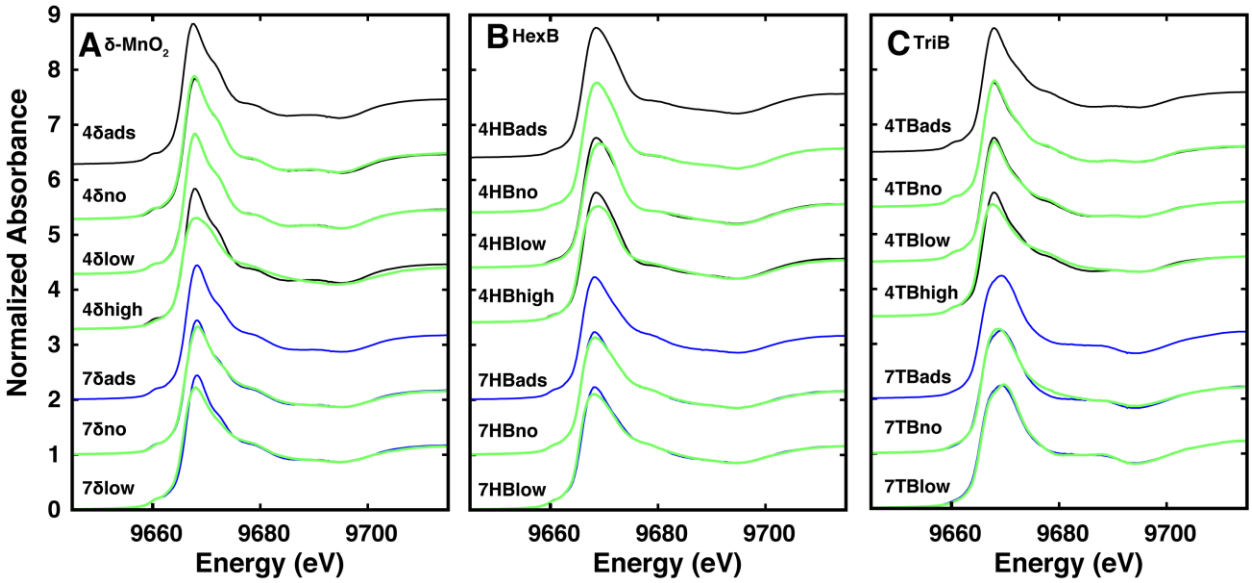

Figure 5.3. Zn XANES spectra for the δ-MnO_2 (A), HexB (B), and TriB (C) systems. 25-day reacted samples (thick green lines) are overplotted the XANES spectra for the corresponding sample reacted for 48 hours ('ads') with no aqueous Mn(II) added (thin black (pH 4) or blue (pH 7) line.

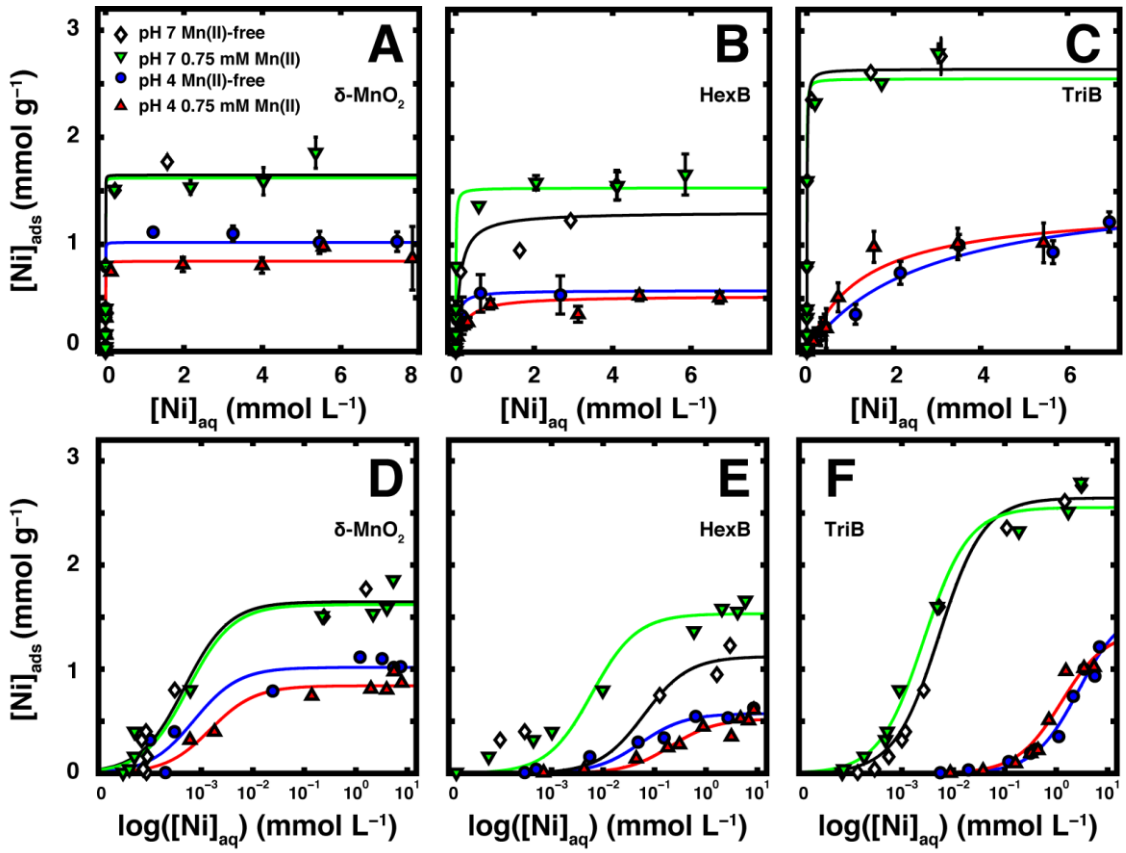

Figure 5.4. Ni(II) adsorption onto δ-MnO_2 (A), HexB (B), and TriB (C) at pH 4 without Mn(II) (blue circles) and with 0.75 mM Mn(II) (red triangles) or at pH 7 without Mn(II) (diamonds) and with 0.75 mM Mn(II) (green triangles). Lines represent Langmuir isotherm fits to the data. Corresponding semilog scale plots for δ-MnO_2 (D), HexB (E), and TriB (F) systems.

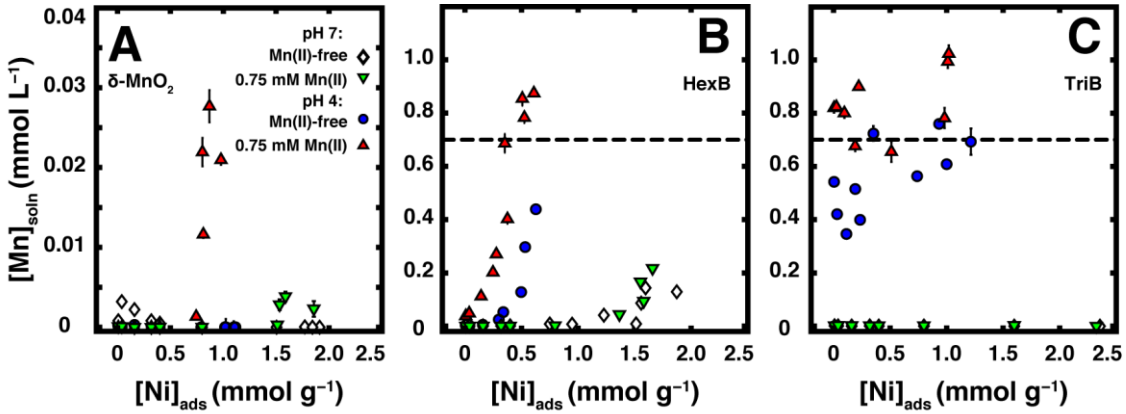

Figure 5.5. Amount of Mn in solution as a function of adsorbed Ni(II) on δ-MnO_2 (A), HexB (B), and TriB (C) systems at pH 4 without added Mn(II) (blue circles) and with 0.75 mM Mn(II) (red triangles) or at pH 7 without added Mn(II) (diamonds) and with 0.75 mM Mn(II) (green triangles). Horizontal dashed line corresponds to the initial amount of Mn(II) added in the experiments conducted with added Mn(II).

5.7 REFERENCES

Bodeï S., Manceau A., Geoffroy N., Baronnet A. and Buatier M. (2007) Formation of todorokite from vernadite in Ni-rich hemipelagic sediments. *Geochimica et Cosmochimica Acta* **71,** 5698-5716.

Boonfueng T., Axe L., Yee N., Hahn D. and Ndiba P. K. (2009) Zn sorption mechanisms onto sheathed *Leptothrix discophora* and the impact of the nanoparticulate biogenic Mn oxide coating. *Journal of Colloid and Interface Science* **333,** 439-447.

Brown G. E. and Parks G. A. (2001) Sorption of trace elements on mineral surfaces: Modern perspectives from spectroscopic studies, and comments on sorption in the marine environment. *International Geology Review* **43,** 963-1073.

Cai J., Liu J. and Suib S. L. (2002) Preparative parameters and framework dopant effects in the synthesis of layer-structure birnessite by air oxidation. *Chemistry of Materials* **14,** 2071-2077.

Ching S., Krukowska K. S. and Suib S. L. (1999) A new synthetic route to todorokite-type manganese oxides. *Inorganica Chimica Acta* **294,** 123-132.

Cravotta III C. A. (2008) Dissolved metals and associated constituents in abandoned coal-mine discharges, Pennsylvania, USA. Part 1: Constituent quantities and correlations. *Applied Geochemistry* **23,** 166-202.

Dick G. J., Clement B. G., Webb S. M., Fodrie F. J., Bargar J. R. and Tebo B. M. (2009) Enzymatic microbial Mn(II) oxidation and Mn biooxide production in the Guaymas Basin deep-sea hydrothermal plume. *Geochimica et Cosmochimica Acta* **73,** 6517-6530.

Drits V. A., Lanson B. and Gaillot A. -C. (2007) Birnessite polytype systematics and identification by powder X-ray diffraction. *American Mineralogist* **92,** 771-788.

Elzinga E. J. (2011) Reductive transformation of birnessite by aqueous Mn (II). *Environmental Science & Technology* **45,** 6366-6372.

Elzinga E. J. and Kustka A. B. (2015) A Mn-54 radiotracer study of Mn isotope solid-liquid exchange during reductive transformation of vernadite (δ-MnO2) by aqueous Mn (II). *Environmental Science & Technology* doi:10.1021/acs.est.5b00022.

Friedl G., Wehrli B. and Manceau A. (1997) Solid phases in the cycling of manganese in eutrophic lakes: New insights from EXAFS spectroscopy. *Geochimica et Cosmochimica Acta* **61,** 275-290.

Frierdich A. J. and Catalano J. G. (2012) Distribution and speciation of trace elements in iron and manganese oxide cave deposits. *Geochimica et Cosmochimica Acta* **91,** 240-253.

Fuller C. C. and Bargar J. R. (2014) Processes of Zinc Attenuation by Biogenic Manganese Oxides Forming in the Hyporheic Zone of Pinal Creek, Arizona. *Environmental Science & Technology* **48,** 2165-2172.

Glenn J. K., Akileswaran L. and Gold M. H. (1986) Mn (II) oxidation is the principal function of the extracellular Mn-peroxidase from *Phanerochaete chrysosporium*. *Archives of Biochemistry and Biophysics* **251,** 688-696.

Goldberg E. D. (1954) Marine Geochemistry 1. Chemical scavengers of the sea. *The Journal of Geology* **62,** 249-265.

Grangeon S., Manceau A., Guilhermet J., Gaillot A. C., Lanson M. and Lanson B. (2012) Zn sorption modifies dynamically the layer and interlayer structure of vernadite. *Geochimica et Cosmochimica Acta* **85,** 302-313.

Graybeal A. L. and Heath G. R. (1984) Remobilization of transition metals in surficial pelagic sediments from the eastern Pacific. *Geochimica et Cosmochimica Acta* **48,** 965-975.

Hinkle M. A. G. and Catalano J. G. (2015) Effect of aging and Mn(II) on manganese oxide sheet structures, In *Ion Interactions at the Mineral-Water Interface During Biogeochemical Iron and Manganese Cycling,* Washington University in St. Louis, St. Louis, MO.

Hinkle M. A. G., Wang Z., Giammar D. E. and Catalano J. G. (2015) Interaction of Fe(II) with phosphate and sulfate on iron oxide surfaces. *Geochimica et Cosmochimica Acta* **158,** 130-146.

Jenne E. A. Controls on Mn, Fe, Co, Ni, Cu, and Zn concentrations in soils and water: The significant role of hydrous Mn and Fe oxides, In *Advances in Chemistry,* American Chemical Society, 1968; pp. 337-387.

Kay J. T., Conklin M. H., Fuller C. C. and O'Day P. A. (2001) Processes of nickel and cobalt uptake by a manganese oxide forming sediment in Pinal Cree, Globe Mining District, Arizona. *Environmental Science & Technology* **35,** 4719-4725.

Kelly S. D., Hesterberg D. and Ravel B. Analysis of soils and minerals using X-ray absorption spectroscopy, In *Methods of Soil Analysis. Part 5 - Mineralogical Methods,* L.R. Drees and A.L. Ulery (Eds.), Soil Science Society of America, Madison, WI, 2008a; pp. 387-463.

Kelly S. D., Hesterberg D. and Ravel B. Analysis of soils and minerals using X-ray absorption spectroscopy, In *Methods of Soil Analysis, Part 5. Mineralogical Methods,* A.L. Ulery and L.R. Drees (Eds.), Soil Science Society of America, Madison, WI USA, 2008b; pp. 387-463.

Kwon K. D., Refson K. and Sposito G. (2013) Understanding the trends in transition metal sorption by vacancy sites in birnessite. *Geochimica et Cosmochimica Acta* **101,** 222-232.

Lanson B., Drits V. A., Gaillot A. -C., Silvester E., Plançon A. and Manceau A. (2002) Structure of heavy-metal sorbed birnessite: Part 1. Results from X-ray diffraction. *American Mineralogist* **87,** 1631-1645.

Lanson B., Drits V. A., Silvester E. and Manceau A. (2000) Structure of H-exchanged hexagonal birnessite and its mechanism of formation from Na-rich monoclinic buserite at low pH. *American Mineralogist* **85,** 826-838.

Lefkowitz J. P. and Elzinga E. J. (2015) Impacts of Aqueous Mn(II) on the Sorption of Zn(II) by Hexagonal Birnessite. *Environmental Science & Technology* doi: 10.1021/es506019j.

Lefkowitz J. P., Rouff A. A. and Elzinga E. J. (2013) Influence of pH on the reductive transformation of birnessite by aqueous Mn(II). *Environmental Science & Technology* **47,** 10364-10371.

Li X., Shen Z., Wai O. W. H. and Li Y. Z. (2001) Chemical forms of Pb, Zn and Cu in the sediments profiles of the Pearl River Estuary. *Marine Pollution Bulletin* **42,** 215-223.

Lopano C. L., Heaney P. J., Post J. E., Hanson J. and Komarneni S. (2007) Time-resolved structural analysis of K- and Ba-exchange reactions with synthetic Na-birnessite using synchrotron X-ray diffraction. *American Mineralogist* **92,** 380-387.

Manceau A., Kersten M., Marcus M. A., Geoffroy N. and Granina L. (2007) Ba and Ni speciation in a nodule of binary Mn oxide phase composition from Lake Baikal. *Geochimica et Cosmochimica Acta* **71,** 1967-1981.

Manceau A., Lanson B. and Drits V. A. (2002) Structure of heavy metal sorbed birnessite. Part III: Results from powder and polarized extended X-ray absorption fine structure spectroscopy. *Geochimica et Cosmochimica Acta* **66,** 2639-2663.

Manceau A., Lanson M. and Geoffroy N. (2007) Natural speciation of Ni, Zn, Ba, and As in ferromanganese coatings on quartz using X-ray fluorescence, absorption, and diffraction. *Geochimica et Cosmochimica Acta* **71,** 95-128.

Manceau A., Tamura N., Marcus M. A., MacDowell A. A., Celestre R. S., Sublett R. E., Sposito G. and Padmore H. A. (2002) Deciphering Ni sequestration in soil ferromanganese nodules by combining X-ray fluorescence, absorption, and diffraction at micrometer scales of resolution. *American Mineralogist* **87,** 1494-1499.

Manceau A., Tommaseo C., Rihs S., Geoffroy N., Chateigner D., Schlegel M., Tisserand D., Marcus M. A., Tamura N. and Chen Z. -S. (2005) Natural speciation of Mn, Ni, and Zn at the micrometer scale in a clayey paddy soil using X-ray fluorescence, absorption, and diffraction. *Geochimica et Cosmochimica Acta* **69,** 4007-4034.

Marcus M. A., Manceau A. and Kersten M. (2004) Mn, Fe, Zn and As speciation in a fast-growing ferromanganese marine nodule. *Geochimica et Cosmochimica Acta* **68,** 3125-3136.

Miyata N., Tani Y., Sakata M. and Iwahori K. (2007) Microbial manganese oxide formation and interaction with toxic metal ions. *Journal of Bioscience and Bioengineering* **104,** 1-8.

Newville M. (2001) IFEFFIT: interactive EXAFS analysis and FEFF fitting. *Journal of Synchrotron Radiation* **8,** 322-324.

Paterson E., Bunch J. L. and Clark D. R. (1986) Cation exchange in synthetic manganates: I. Alkylammonium exchange in a synthetic phyllomanganate. *Clay Minerals* **21,** 949-955.

Peacock C. L. (2009) Physiochemical controls on the crystal-chemistry of Ni in birnessite: Genetic implications for ferromanganese precipitates. *Geochimica et Cosmochimica Acta* **73,** 3568-3578.

Peacock C. L. and Sherman D. M. (2007a) Crystal-chemistry of Ni in marine ferromanganese crusts and nodules. *American Mineralogist* **92,** 1087-1092.

Peacock C. L. and Sherman D. M. (2007b) Sorption of Ni by birnessite: Equilibrium controls on Ni in seawater. *Chemical Geology* **238,** 94-106.

Post J. E. (1999) Manganese oxide minerals: Crystal structures and economic and environmental significance. *Proceedings of the National Academy of Sciences of the United States of America* **96,** 3447-3454.

Post J. E. and Appleman D. E. (1988) Chalcophanite, ZnMn3O7-3H2O: New crystal-structure determinations. *American Mineralogist* **73,** 1401-1404.

Ravel B. and Newville M. (2005) ATHENA, ARTEMIS, HEPHAESTUS: data analysis for X-ray absorption spectroscopy using IFEFFIT. *Journal of Synchrotron Radiation* **12,** 537-541.

Rehr J. J., Kas J. J., Vila F. D., Prange M. P. and Jorissen K. (2010) Parameter-free calculations of x-ray spectra with FEFF9. *Physical Chemistry Chemical Physics* **12,** 5503-5513.

Shen Y. -F., Suib S. L. and O'Young C. -L. (1994) Effects of inorganic cation templates on octahedral molecular sieves of manganese oxide. *Journal of the American Chemical Society* **116,** 11020-11029.

Siegel M. D. and Turner S. (1983) Crystalline todorokite associated with biogenic debris in manganese nodules. *Science* **219,** 172-174.

Singh A. K., Hasnain S. I. and Banerjee D. K. (1999) Grain size and geochimical partitioning of heavy metals in sediments of the Damodar River--a tributary of the lower Ganga, India. *Environmental Geology* **39,** 90-98.

Tan H., Zhang G., Heaney P. J., Webb S. M. and Burgos W. D. (2010) Characterization of manganese oxide precipitates from Appalachian coal mine drainage treatment systems. *Applied Geochemistry* **25,** 389-399.

Tebo B. M., Bargar J. R., Clement B. G., Dick G. J., Murray K. J., Parker D., Verity R. and Webb S. M. (2004) Biogenic manganese oxides: Properties and mechanisms of formation. *Annual Review of Earth and Planetary Sciences* **32,** 287-328.

Tebo B. M., Ghiorse W. C., van Waasbergen L. G., Siering P. L. and Caspi R. (1997) Bacterially mediated mineral formation; insights into manganese (II) oxidation from molecular genetic and biochemical studies. *Reviews in Mineralogy and Geochemistry* **35,** 225-266.

Tebo B. M., Johnson H. A., McCarthy J. K. and Templeton A. S. (2005) Geomicrobiology of manganese(II) oxidation. *TRENDS in Microbiology* **13,** 421-428.

Toner B., Manceau A., Webb S. M. and Sposito G. (2006) Zinc sorption by biogenic hexagonal birnessite particles within a hydrated bacterial biofilm. *Geochimica et Cosmochimica Acta* **70,** 27-43.

Traina S. J. and Doner H. E. (1985) Heavy metal induced releases of manganese (II) from a hydrous manganese dioxide. *Soil Science Society of America Journal* **49,** 317-321.

Villalobos M., Toner B., Bargar J. R. and Sposito G. (2003) Characterization of the manganese oxide produced by *pseudomonas putida* strain MnB1. *Geochimica et Cosmochimica Acta* **67,** 2649-2662.

Webb S. M. (2005) SIXPack: A Graphical User Interface for XAS Analysis using IFEFFIT. *Physica Scripta* **T115,** 1011-1014.

Wehrli B., Friedl G. and Manceau A. Reaction rates and products of manganese oxidation at the sediment-water interface, In *Advances in Chemistry*, 1995; pp. 111-134.

White W. B., Vito C. and Scheetz B. E. (2009) The mineralogy and trace element chemistry of black manganese oxide deposits from caves. *Journal of Cave and Karst Studies* **71,** 136-143.

Yin H., Tan W., Zheng L., Cui H., Qiu G., Liu F. and Feng X. (2012) Characterization of Ni-rich hexagonal birnessite and its geochemical effects on aqueous Pb^{2+}/Zn^{2+} and As(III). *Geochimica et Cosmochimica Acta* **93,** 47-62.

Yu Q., Sasaki K., Tanaka K., Ohnuki T. and Hirajima T. (2013) Zinc sorption during bio-oxidation and precipitation of manganese modifies the layer stacking of biogenic birnessite. *Geomicrobiology Journal* **30,** 829-839.

Zhu M., Ginder-Vogel M., Parikh S. J., Feng X. H. and Sparks D. L. (2010a) Cation effects on the layer structure of biogenic Mn-oxides. *Environmental Science & Technology* **44,** 4465-4471.

Zhu M., Ginder-Vogel M. and Sparks D. L. (2010b) Ni(II) sorption on biogenic Mn-oxides with varying Mn octahedral layer structure. *Environmental Science & Technology* **44,** 4472-4478.